Institut für Erd- und Umweltwissenschaften

Mathematisch-Naturwissenschaftliche Fakultät

Universität Potsdam

1D shallow sedimentary subsurface imaging using ambient noise and active seismic data

Kumulative Dissertation zur Erlangung des akademischen Grades "doctor rerum naturalium"

(Dr. rer. nat.) in der Wissenschaftsdisziplin "Geophysics"

eingereicht an der Mathematisch-Naturwissenschaftlichen Fakultät der Universität Potsdam

Von

Agostiny Marrios Lontsi

Potsdam, den 23.08.2016

Published online at the
Institutional Repository of the University of Potsdam:
URN urn:nbn:de:kobv:517-opus4-103807
http://nbn-resolving.de/urn:nbn:de:kobv:517-opus4-103807

Declaration of Authorship for the Thesis

I, Agostiny Marrios Lontsi, declare that this thesis titled, "**1D shallow sedimentary subsurface imaging using ambient noise and active seismic data**" and the work presented in it are my own. I confirm that:

- This work was done wholly while in candidature for a research degree (doctor rerum naturalium - Dr. rer. nat.) at the University of Potsdam.
- To my knowledge, no any part of this thesis has previously been submitted for a degree or any other qualification at this University or any other institution.
- Where I have consulted the published work of others, this is always clearly attributed.
- Where I have quoted from the work of others, the source is always given. With the exception of such quotations, this thesis is entirely my own work.
- I have acknowledged all main sources of help.
- Where the thesis is based on work done by myself jointly with others, I have made clear exactly what I have contributed myself (Please see next page).

Agostiny Marrios Lontsi

Author

apl. Prof. Dr. Frank Krüger

Supervisor

Place, date and signature

Place, date and signature

Declaration of Authorship for the Publications

For the four publications presented in this thesis, the author did the following:

- Publication 1
  - Contributed to the seismic array design, the passive (ambient vibrations) and active (hammer source) data acquisition and the quality control;
  - Estimated virtual active seismic data from passive recordings using interferometric principles;
  - Processed all data sets and interpreted the estimated phase velocity dispersion curves;
  - Correlated the estimated velocity profiles with the geological log information;
  - Wrote about 95% of the manuscript.
- Publication 2
  - Contributed to extending the H/V theory, based on the diffuse field assumption and the interferometric principles, to the interpretation of the observation at depth;
  - Contributed to the ambient noise data acquisition and the quality control;
  - Processed the data and interpreted the observed H/V(z, f);
  - Correlated the estimated velocity depth profiles with the geological log information;
  - Wrote about 95% of the manuscript.
- Publication 3
  - Performed a literature review on the potential of the H/V spectral ratio technique as subsea exploration and geohazard estimation tool;
  - Debugged the new H/V(z, f) spectral modeling code for marine application;
  - Modeled and interpreted the effect of the water column on the H/V spectral ratio estimated at sea- and subseafloor;
  - Wrote about 95% of the manuscript.
- Publication 4
  - Interpreted the phase velocity dispersion curves information from array methods and the microtremors H/V(z, f) information;
  - Highlighted the difference in the spectral content of the two measures;
  - Jointly inverted the two data sets (dispersion curves and H/V(z, f));

– Correlated the resulting velocity depth profiles with the geological log information;

– Wrote about 95% of the manuscript.

Agostiny Marrios Lontsi

Author

apl. Prof. Dr. Frank Krüger

Supervisor

Place, date and signature

Place, date and signature

Zusammenfassung

Oberflächennahe Sedimente wirken oft als Verstärker für einfallende seismische Wellenfelder. Im Rahmen meiner Doktorarbeit konzentriere ich mich auf die Eigenschaften des oberflächennahen Untergrundes von einigen zehn bis zu hundert Metern Sedimentabdeckung. Dabei leite ich Tiefenprofile (1D) der seismische Scherwellengeschwindigkeit (Vs) und wenn möglich auch der Kompressionswellengeschwindigkeit (Vp) aus seismischen Daten ab. Diese Informationen sind nicht nur für jede Erdbebenrisikobewertung, Geotechnik- oder Mikrozonierungsaktivität erforderlich, sondern sind auch für die seismische Erkundung und globale Seismologie von Bedeutung, da Standorteffekte in seismischen Wellenformmodellierungen oft vernachlässigt werden.

Zuerst wird die herkömmliche Frequenz-Wellenzahl (f - k) Technik verwendet, um die Dispersionskurven der Phasengeschwindigkeit von Oberflächenwellen abzuleiten. Die zugrundeliegenden Daten stammen von Seismometerarrays in unterschiedlichen 1D- und 2D-Konfigurationen. In einem weiteren Schritt wird die Green's Funktion zwischen verschiedenen Empfängerpaaren aus den Daten des seismischen Arrays geschätzt. Dabei wird die Kreuzkorrelationstechnik verwendet. In einem virtuellen 1D Experiment der aktiven Seismik werden die abgeleiteten Green's Funktionen der Interstationsdistanz nach geordnet. Dann wird die f-k Technik verwendet um wiederum Dispersionskurven abzuleiten. Dieser integrierte Ansatz ermöglicht die Analyse einer grösseren Bandbreite für die Dispersionskurven und daher eine verbesserte Auflösung des 1D Tiefenprofils der Scherwellengeschwindigkeit (Vs).

In einem zweiten Schritt wird ein neuer Ansatz, basierend auf der diffusen Wellenfeldannahme (engl., Diffuse Field Assumption, DFA), zur Interpretation beobachteter horizontal zu vertikalen Spektralamplitudenverhältnissen (H/V-Spektralverhältnisse), die aus allgemeiner Bodenunruhe abgeleited wurden, genutzt. Diese Theorie wurde im Rahmen der vorliegenden Arbeit erweitert, um nicht nur an der Oberfläche gemessene H/V- Spektralverhältnisse interpretieren zu können sondern auch Messungen in der Tiefe (Bohrloch) und in mariner Umgebung (Ozeanboden). Eine Modellierung und Inversion von synthetischen HV- Spektralverhältnissen für vordefinierte, einfache geologische Strukturen zeigt eine nahezu perfekte Identifikation/Rekonstruktion der Modellparameter (im wesentlichen Vs und in geringerem Maße Vp), wenn die zusätzliche Information von HV- Spektralverhältnissen eines Empfängers in der Tiefe bei der Inversion berücksichtigt wird.

Letztlich wurden (i) Phasengeschwindigkeiten von Rayleighwellen, die aus einem Arraydatensatz geschätzt wurden, mit (ii) H/V-Spektralverhältnissen einer Einzelstation kombiniert invertiert, um Tiefenprofile seismischer Geschwindigkeiten (Vs, Vp) zu bestimmen. Die Ergebnisse deuten daraufhin, dass sich mit einer kombinierte Inversion seismische Geschwindigkeiten bis in größere Tiefen bestimmen lassen, verglichen mit der Inversion von nur Phasengeschwindigkeiten allein. Die geschätzte Gesamtmächtigkeit von Oberflächensedimenten aufgrund der kombinierten Inversion ist vergleichbar mit der, abgleitet von nur H/V-Spektralverhältnissen.

Summary

The Earth's shallow subsurface with sedimentary cover acts as a waveguide to any incoming wavefield. Within the framework of my thesis, I focused on the characterization of this shallow subsurface within tens to few hundreds of meters of sediment cover. I imaged the seismic 1D shear wave velocity (and possibly the 1D compressional wave velocity). This information is not only required for any seismic risk assessment, geotechnical engineering or microzonation activities, but also for exploration and global seismology where site effects are often neglected in seismic waveform modeling.

First, the conventional frequency-wavenumber (f - k) technique is used to derive the dispersion characteristic of the propagating surface waves recorded using distinct arrays of seismometers in 1D and 2D configurations. Further, the cross-correlation technique is applied to seismic array data to estimate the Green's function between receivers pairs combination assuming one is the source and the other the receiver. With the consideration of a 1D media, the estimated cross-correlation Green's functions are sorted with interstation distance in a virtual 1D active seismic experiment. The f - k technique is then used to estimate the dispersion curves. This integrated analysis is important for the interpretation of a large bandwidth of the phase velocity dispersion curves and therefore improving the resolution of the estimated 1D Vs profile.

Second, the new theoretical approach based on the Diffuse Field Assumption (DFA) is used for the interpretation of the observed microtremors H/V spectral ratio. The theory is further extended in this research work to include not only the interpretation of the H/V measured at the surface, but also the H/V measured at depths and in marine environments. A modeling and inversion of synthetic H/V spectral ratio curves on simple predefined geological structures shows an almost perfect recovery of the model parameters (mainly Vs and to a lesser extent Vp). These results are obtained after information from a receiver at depth has been considered in the inversion.

Finally, the Rayleigh wave phase velocity information, estimated from array data, and the H/V(z, f) spectral ratio, estimated from a single station data, are combined and inverted for the velocity profile information. Obtained results indicate an improved depth resolution in comparison to estimations using the phase velocity dispersion curves only. The overall estimated sediment thickness is comparable to estimations obtained by inverting the full micortremor H/V spectral ratio.

Dedication

To **Simone Sterole**, my daughter, with whom I spent little time during my thesis years.
To **Victorine**, my Mum.
To **Elisabeth**, my Grand-Mum, who passed away in the course of my thesis work.

Acknowledgments

I would like to express my profound gratitude to my thesis advisor, apl. Prof. Dr. Frank Krüger, for his confidence in me when filling this doctoral position at the time. Our permanent scientific discussion, together with Dr. Matthias Ohrnberger, has given me an integrated vision (array deployment, data processing and interpretation) of the Earth subsurface structure.

The strong collaboration with Prof. Francisco José Sánchez-Sesma (Paco) and Dr. Juan Camilo Molina-Villegas has played a significant role in the present methodological development.

I would also like to thank the evaluation commission at the University of Potsdam, the external and internal reviewers of this thesis for their time and comments.

Partial or full proofreading from different parties helped improving the quality of the thesis. In this regards, special thanks go to Galina Kulikova, Stefanie Donner, Cecilia Nyamwandha, Annabel Händel, Swenja Rosenwinkel, Amelie Stolle, Jeanne Marie Mbebi, Christian Molkenthin and Saskia Ruttor.

Having completed my PhD within the MuSaWa project (MuSaWa: Multiskalige S-Wellentomografie zur Exploration und der Risikoabschätzung bei der Baugrunduntersuchug - *Multi-scale S-wave Tomography for Exploration and Risk Assessment of Development Sites*) via the Geotechnologien special call has provided me the adequate knowledge for career start, the state of the art knowledge in the shallow subsurface characterization using seismic/seismological methods. I would like to take this opportunity to thank all project members for the friendly working atmosphere during the multiple project milestones and field campaigns. They include: (WP: Working Package): (WP1) Hendrik Paasche, Jens Tronicke, Michael Rumpf (WP2) Matthias Ohrnberger, Frank Krüger, Katrin Hannemann; (WP3) Jörg Hausmann, Ulrike Werban, Peter Dietrich; (WP4) Thomas Fechner. Laboratory technicians are also thanked for preparing the field instruments. Any help during the multiple field campaigns (e.g. sensors deployement/collection, car driving) was also positively regarded.

Fundings have played a significant role toward the completion of the current research work. The thesis was initially funded by the Geotechnologien program of the BMBF/DFG under grant No. 03G0745A, followed by the DFG Graduiertenkollegs GRK 1364, the completion scholarship (Abschlussstipendium) offered by the University of Potsdam, the grant from the UP transfer Gmbh and more recently the scholarship from the University of Potsdam initiative: "Research Focus in Earth Science".

Thanks go to all institute members for supporting my stay in one way or another. I would like to particularly thank all colleagues with whom I have shared an office (House 27, am Mühlenberg, House 12) and in general all Geophysics colleagues (Array seismology, General geophysics & Applied geophysics) for the pleasant working atmosphere.

I will not forget all my friends in the students dormitory T1-3 (Kaiser Friedrich Str. 133-135), Potsdam, with whom recreative activities have unccountlessly been organized; an opportunity which also helped increasing the German Language skills.

I would also like to take this opportunity to thank all friends and institutions who/which have contributed to my scientific cognitive development. Special thank go to the International Centre for Theoretical physics (ICTP), Trieste/Italy for the intensive training received while attending the Diploma courses

in Physics and in Earth System Physics.

Today's accomplishment is the continuity of a work started at the university, secondary and primary school in Cameroon. In this regard, I would like to express my deep gratitude to my friends Dr. Ing. Eric Tala-Tebue, Dr. Patrice Kenfack, (Ing.) Serge Ghislain Kanko, Ing. Marius Tatchou, and many others at the university of Yaounde 1 and at the Ecole Normale Supérieure de Yaoundé 1. I would also like to thank Ing. Symphorien Kanouo, Ing. Sylvain Faha Tamebou, Figaro Tamoka and many others at the High School level in Bafoussam, Cameroon. I won't forget my best friend Tamokoue Tagne Romeo from the Ecole Normale des Instituteurs de l'Enseignement General in Bafoussam, Cameroon.

Thanks also go to my mentors, Prof. Timoleon Kofane and Prof. Paul Waofo both at the Department of Physics of the University of Yaounde 1 and Prof. Aurelien J. Kenfack at the Ecole Normale Supérieure de Yaoundé in Cameroon.

I would also like to acknowledge any person who has financially or morally supported me to date.

Last but not least, I would like to thank all family members and relatives who should all recognize themselves in these words: *Ah Pong fe ndeu - It all starts home* (Source: Groupe Takam 2).

Contents

List of Figures

List of Tables

Chapter 1

Introduction

1.1 State-of-the-art and open research questions

Knowledge regarding the average 1D distribution of seismic shear velocity (Vs) and compressional velocity (Vp) in the shallow (depth range of few tens of meters) or middle deep sediment layer (depth range of few hundreds of meters) and bedrock is necessary for any geotechnical activity and seismic exploration. In geotechnical engineering, Vs is the most important parameter. It relates to the material shear strength and is a necessary prerequisite for the evaluation of the structural safety of buildings. This information is needed not only in the immediate local geotechnical pre-exploration of a specific locality, but also in the analysis of the regional seismic hazard and risk. In seismic exploration, the knowledge of the subsurface Vs and Vp distribution is a prerequisite for building an appropriate velocity model. Using this information could significantly improve the quality of the reservoir image.

Among geophysical methods for the determination of the subsurface seismic velocity are body wave methods (seismic reflection & refraction) and surface wave methods (phase/group velocity dispersion curve inversion, tomography, H/V spectral ratio). In practice, discriminating primary body waves, the corresponding multiples/converted waves/seismic phases and surface waves from seismic recordings is often (if not always) a challenging task. The full waveform analysis is a relatively new approach for site investigation that seeks the interpretation of the full time series or spectrum of the recorded data.

For local site investigation, surface wave methods such as the Spatial Auto-Correlation (SPAC; Aki, 1957) and the frequency-wavenumber methods (f - k; e.g Toksöz, 1964; Capon, 1969) are used to extract the phase velocity dispersion characteristic of the Rayleigh waves contained in the active and/or passive seismic recordings.

The SPAC method is mainly used to estimate the similarities between microtremor (also known as ambient vibration or simply passive seismic) data assuming they are stationary both in time and space (Aki, 1957). It follows from the theoretical investigation that the azimuthal average of the correlation ρ between multiple receiver-pairs located at a distance r for a given frequency f is proportional to the 0^{th} order Bessel function with argument proportional to the phase slowness of the propagating surface waves.

The f - k method applies to both active (Stokoe et al., 1994; Park et al., 1999) and passive seismic data (Horike, 1985) to estimate the dispersion character. Depending on the seismic source characteristic, the spatial setting of the receivers and the construction approach of the phase velocity dispersion curves of the propagating surface waves, two terminologies are often used: The Spectral Analysis of Surface Waves (SASW; Stokoe et al., 1994) and the Multichannel Analysis of Surface Waves (MASW; Park et al., 1999).

In the SASW method, the response of the subsurface to harmonic excitation is recorded by a pair of geophones with known interstation spacing. The distance from the source to the first geophone is

set so as to minimize the nearfield effect. In practice, this source-to-first receiver geophone spacing is considered at least two times the maximum interpretable wavelength. The recorded time series gives the estimation of the cross-power spectra, from which the phase angle is estimated. The phase angle is then used to derive the wavelength/wavenumber and the corresponding phase velocity. The experiment is then repeated for different interstation geophone pairs. The estimated phase velocity dispersion curve is interpreted "only" as fundamental mode. The MASW emerged in the 90s as an improved active seismic method to the commonly used two-station SASW method.

In the MASW experiment, the response of the subsurface to an impulse excitation (multi-frequency) is recorded by equally spaced geophones. Similar to the data survey in the SASW experiment, surface waves recording from the MASW methods are also prone to nearfield effects. This effect is considered reduced for the source-to-first receiver offset equal to at least two times the maximum interpretable wavelength (as in the SASW experiment). Through a grid search or wavefield decomposition for a given wavenumber and frequency combination, the power spectrum of the array output is estimated and the frequency slowness diagram is derived. In comparison to the SASW method, the approach has the power to provide information regarding waves propagating with different energy at a given frequency (overtones).

It is important to point out that the active generation of shear waves with deep penetration and for large distances is still costly, hard to do in urban areas, and presents a high risk of damaging the structure close to the source. Passive monitoring of the natural ambient noise wavefield with seismological array techniques allows obtaining phase velocity curves of surface waves rather cost efficient. From these curves, 1D shear wave velocity models can be constructed. Depending on the source spectrum and the subsurface structure, shallow as well as middle deep sediment structure can be analyzed. The geometries of the used arrays have to be adjusted for each wavelength to achieve optimal resolution and should be supplemented by active shear wave velocity measurements if possible (e.g. Renalier et al., 2009). These hypothesis were tested by combining several array techniques in various EU projects (SESAME 2001-2004, `http://sesame.geopsy.org/`; SISMOVALP 2003-2006, `http://risknat.org/projets/sismovalp/`; NERIES 2006-2010, `http://www.neries-eu.org/`; Last accessed February 23, 2017), in internationally organized blind studies (Asten & Boore, 2005; Cornou et al., 2006) with synthetic and real data sets and in the inter-comparison of methods for site parameter and velocity profile characterization project (Inter-PACIFIC 2014-2015; Garofalo et al., 2016b,a).

A new method emerging from the field of seismic interferometry (Lobkis & Weaver, 2001; Shapiro & Campillo, 2004; Snieder et al., 2007; Gouédard et al., 2008b; Stehly et al., 2008) combines the advantages of the active source methods and passive seismic data in the so called enhanced correlation methods (Gouédard et al., 2008a) for the estimation of the dispersion curves. The Green's function is estimated by cross-correlation of long term noise recording from a pair of seismic receivers assuming one is the source and the second is the receiver. By sorting the estimated Cross-correlation Green's Function (CGF) with interstation distance (assuming mainly a 1D media), a virtual active seismic data is obtained and processed using the MASW method. The approach is referred to as Interferometric Multichannel Analysis of Surface Waves (IMASW; O'Connell & Turner, 2011). Different other terminologies are used in the literature (see Gouédard et al., 2008a; Feuvre et al., 2015; Cheng et al., 2015; Pan et al., 2016) to refer to the method. The basic principles of the method are therefore of main importance.

Although the application of surface wave methods for subsurface imaging is to date quite advanced as presented hereinabove, a number of research topics, which were investigated in the course of this study are still open. Among others, the list includes:

- The integrated data analysis using the SPAC, f - k, MASW and IMASW for the estimation of a large bandwidth of the dispersion curves;
- The interpretation of the estimated dispersion curves in terms of different surface wave modes;

- The multi-mode inversion of the estimated phase velocity dispersion curves.

Besides the array methods, there is the single station microtremor horizontal-to-vertical (H/V) spectral ratio technique (Nakamura, 1989). The H/V method is famous due to its simplicity, and is globally used since the early 90s. The H/V is primarily used to analyze resonances in unconsolidated sediment structures (Nakamura, 1989; Lermo & Chávez-García, 1993; Bard, 1998; Bonnefoy-Claudet et al., 2006b). Numerical modeling under different assumptions about the nature of the noise wavefield (surface wave or body wave) have in most cases lead to robust estimation of the resonance frequency of the site (Nakamura, 1989; Lachet & Bard, 1994; Bonnefoy-Claudet et al., 2006a,b; Nakamura, 2008). However, ideas diverge on the interpretation of the H/V amplitude at the observed peak frequency as possible signature of site specific amplification factor (compare e.g. Lachet & Bard, 1994; Bonnefoy-Claudet et al., 2006b and Nakamura, 1989, 2008). The interpretation of the H/V spectrum in terms of Rayleigh wave ellipticity allows potentially the derivation of 1D shear wave velocity profiles (Yamanaka et al., 1994; Fäh et al., 2003; Arai & Tokimatsu, 2005; Hobiger et al., 2013).

Interpreting the H/V spectral ratio in terms of Rayleigh wave ellipticity or SH transfer function is actually a strong assumption regarding the noise wavefield composition. For instance, Fäh et al., 2001; Hobiger et al., 2009b; Poggi & Fäh, 2010; Hobiger et al., 2012 suggest to first extract the Rayleigh wave constituent part prior to the inversion. It is further advised to mainly use the right flank around the H/V peak frequency for the shear wave velocity profiling.

Assuming the noise wavefield is diffuse, Sánchez-Sesma et al. (2011a) proposed an improved approach based on the development in the field of seismic interferometry for the interpretation of the full spectrum of the microtremor H/V spectral ratio. The Directional Energy Density (DED) for a given direction is estimated by auto-correlation of the displacement wavefield along the same component. The DED is proportional to the imaginary part of the Green's function assuming the source and the receiver are at the same position (Sánchez-Sesma & Campillo, 2006a; Sánchez-Sesma et al., 2008b).

Bearing in mind the simplicity in the estimation of the H/V from the microtremor data and the new theoretical advances in the interpretation of the full H/V spectrum, another set of research topics, investigated in the course of this study, were raised. Among others, the list includes:

- The full wavefield interpretation of the H/V spectral ratio observed at the surface and at depth on land;
- The inversion of the full microtremor H/V spectral ratio for 1D seismic velocity information;
- The comparison of the estimated velocity information obtained from the H/V inversion with the velocity information estimated from the phase velocity dispersion curves inversion;
- The full wavefield interpretation of the H/V spectral ratio observed in marine environments.

The investigation of research topics related to array method or single station leads to another set of open issues related to the combined analysis of both methods. In this regards mainly two topics have been addressed in the course of this study:

- the differences in the spectral content of the two measures and their implication for structural properties interpretation;
- the combined analysis of the two data set (dispersion curves and H/V(z, f)).

1.2 Work accomplished

In order to investigate the above listed questions, seismic arrays were designed in 1D and 2D configurations to record active (1D) and passive (1D and 2D) seismic data. Three sites, all located in Germany, have

been considered in the course of this study. The following sub-chapters give the thesis overview about the data survey and the new subsurface characterization methodologies presented in chapter two, three, four and five. The different findings are discussed as a whole in Chapter six.

1.2.1 Sites, active and passive seismic data survey

Experiments have been conducted at two sites in Germany. The first is in Horstwalde, located approximately 50 km south of Berlin. The second site is located close to Löbnitz, northern Saxony. For the selected sites, the subsurface geology is mainly composed of quaternary sediment deposits (de Boer, 1995; Juschus, 2001). The very shallow subsurface down to approximately $\sim$ 10 m is known from previous geophysical investigations in Horstwalde (Rumpf & Tronicke, 2014) and Löbnitz (Hausmann et al., 2013). Both, the active and the passive seismic surface wave experiments have been carried out at the above mentioned sites. A 5 kg hammer source and 4.5 Hz vertical geophones are used in the active experiment. Lennartz LE-3D 1s and 5s sensors are used for the passive experiment.

Additional data used in this study, especially for the H/V spectral ratio estimation, at the test site located in Rethem, Germany, were obtained online from the data management center of the Federal Institute for Geosciences and Natural Ressources (BGR; `www.bgr.bund.de`; Last accessed: February 23, 2017).

1.2.2 Surface wave dispersion curve estimation and inversion (presented in Chapter 2)

Here, a combined analysis and interpretation of active, passive and CGF data is performed on seismic recordings from sites at Horstwalde and Löbnitz.

The 1D f - k method, also known as Multichannel Analysis of Surface Waves (MASW; Park et al., 1999), is applied to active data for determining the dispersion characteristic of the surface waves at high frequencies. The 2D f - k method is applied to the raw passive seismic data; the 1D f - k method is also applied to the CGF data, known as Interferometric Multichannel Analysis of Surface Waves (IMASW; O'Connell & Turner, 2011). Following the processing steps by Bensen et al. (2007), the cross-correlation technique is applied to all pairs of stations of the passive seismic data recorded using 1D (Horstwalde) and 2D (Löbnitz) configurations. Daily estimated Correlation Green's Function (CGF) from cross-correlation of receiver-pairs are then stacked (Horstwalde). Assuming a dominantly 1D medium, this allows to create a virtual shot gather by sorting the CGF with inter station distance. The 1D f - k method is then equivalently applied to the rearranged stacked causal and acausal CGF. In this study, picked dispersion curves from the applied methods present a high signal to noise ratio in the frequency range from 0.6 to 35 Hz in Horstwalde and between 1.5 to 25 Hz in Löbnitz. The picked dispersion curves are combined and inverted for the high resolution 1D Vs profile.

This study is published as:
Lontsi, A.M., M. Ohrnberger, F. Krüger, 2016. Shear wave velocity profile estimation by integrated analysis of active and passive seismic data from small aperture arrays, *Journal of applied geophysics*, `http://dx.doi.org/10.1016/j.jappgeo.2016.03.034`.
Publisher: Elsevier

1.2.3 Microtremor H/V estimation and full spectrum inversion for 1D velocity profiling (presented in Chapter 3)

This part of the thesis focuses solely on the use of the single station H/V method for seismic velocity profiling. Using the diffuse wavefield approach, it is shown that the 1D shear and additionally the weaken

compressional wave velocity could be determined using the nonlinear global inversion scheme, when an additional sensor at depth is considered.

The fundamental idea behind the diffuse field theory for the interpretation of the H/V spectral ratio is presented as it applies to receivers at depth. A comparative study performed in the course of this study shows that the obtained H/V(z, f) spectrum computed by the means of the diffuse field assumption could be recovered using the reflectivity method for a medium well illuminated by seismic sources. An inversion for synthetic H/V(z, f) spectral curves is performed for simple and complex structural models corresponding to one, two and seven layer(s) over a half-space. The results allow to potentially use the new theory in a forward computation of the H/V(z, f) to fully invert the experimental H/V spectral ratio at the corresponding depth for the shear velocity profile (Vs) and additionally the compressional velocity profile (Vp). We use seismic ambient noise data for frequencies ranging from 0.2 to 50 Hz recorded at two selected sites in Germany (Horstwalde and Rethem), where borehole information is available.

This study is published as:
Lontsi, A.M., F.J. Sánchez-Sesma, J.C. Molina Villagas, M. Ohrnberger, F. Krüger, 2015. Full microtremor H/V(z, f) inversion for shallow subsurface characterization, *Geophysical Journal International*, `http://dx.doi.org/10.1093/gji/ggv132`.
Publisher: Royal Astronomical Society, Deutsche Geophysikalische Gesellschaft, European Geophysical Society and Oxford University Press.

1.2.4 Microtremor H/V(z, f) modeling in marine sedimentary environment (presented in Chapter 4)

In this section, the propagator (or transfer) matrix is used to relate the displacement and stress field for SH and P-SV waves at two points within an elastic 1D layered media. The approach allows to easily modify the characteristics of the layer on top of a layered 1D media to account for the properties of the water layer and to subsequently estimate the Green's function at the bottom of the water column. For a receiver on land, and for a predefined canonical 1D layered Earth model, the H/V spectral ratio from the current algorithm is compared with the H/V estimated using the global matrix formulation Sánchez-Sesma et al. (2011a).

This study is to be submitted for publication to *Geophysical Journal International* as:
Lontsi, A.M., J.C. Molina-Villegas, F.J. Sánchez-Sesma, M. Ohrnberger, F. Krüger, 2016. Microtremor H/V(z, f) modeling for shallow sedimentary subsurface on land and in marine environment.

1.2.5 Combined analysis of phase velocity dispersion curves and microtremor H/V(z, f) (presented in Chapter 5)

For this part, Rayleigh wave phase velocity dispersion data from the methodology presented in Chapter 2 and the microtremor H/V spectral ratio data presented in Chapter 3 for the test site in Horstwalde are combined and interpreted for frequencies ranging from 0.2 to 50 Hz. The combined interpretation is also performed for data from the Löbnitz test site.

This study is published as:
Lontsi, A.M, Ohrnberger, M, Krüger, F, Sánchez-Sesma, F.J., 2016. Combining surface wave phase velocity dispersion curves and full microtremor horizontal-to-vertical spectral ratio for subsurface sedimentary site characterization, *Interpretation*, `http://dx.doi.org/10.1190/INT-2016-0021.1`.
Publisher: Society of Exploration Geophysics and American Association of Petroleum Geologists.

Chapter 2

Shear wave velocity profile estimation by integrated analysis of active and passive seismic data from small aperture arrays

Lontsi, A. M., Ohrnberger, M., Krüger, F., 2016.
Journal of Applied Geophysics, http://dx.doi.org/10.1016/j.jappgeo.2016.03.034.
Publisher: Elsevier.

Abstract

We present an integrated approach for deriving the 1D shear wave velocity (Vs) information at few tens to hundreds of meters down to the first strong impedance contrast in typical sedimentary environments. We use multiple small aperture seismic arrays in 1D and 2D configuration to record active and passive seismic surface wave data at two selected geotechnical sites in Germany (Horstwalde & Löbnitz). Standard methods for data processing include the Multichannel Analysis of Surface Waves (MASW) methods that exploits the high frequency content in the active data and the sliding window frequency-wavenumber (f - k) as well as the spatial autocorrelation (SPAC) methods that exploit the low frequency content in passive seismic data. Applied individually, each of the passive methods might be influenced by any source directivity in the noise wavefield. The advantages of active shot data (known source location) and passive microtremor (low frequency content) recording may be combined using a correlation based approach applied to the passive data in the so called Interferometric Multichannel Analysis of Surface Waves (IMASW).

In this study, we apply those methods to jointly determine and interpret the dispersion characteristics of surface waves recorded at Horstwalde and Löbnitz. The reliability of the dispersion curves are controlled by applying strict limits on the interpretable range of wavelengths in the analysis and further avoiding potentially biased phase velocity estimates from the passive f - k method by comparing to those derived from the SPatial AutoCorrelation method (SPAC). From our investigation at these two sites, the joint analysis as proposed allows mode extraction in a wide frequency range ($\sim$ 0.6 - 35 Hz at Horstwalde and $\sim$ 1.5 - 25 Hz at Löbnitz) and consequently improving the Vs profile inversion.

To obtain the shear wave velocity profiles, we make use of a global inversion approach based on

the neighborhood algorithm to invert the interpreted branches of the dispersion curves. Within the uncertainty given by the apparent spread of forward models we find that besides a well defined sediment velocity range also a reasonable minimum estimate of bedrock depth and bedrock velocity can be achieved. The Vs estimate for the best model in Horstwalde range from $\sim$ 190 m/s at the surface up to $\sim$ 390 m/s in the bottom of the soft sediment column. The bedrock starts earliest around 200 m depth and bedrock velocities are higher than 1000 m/s. In Löbnitz, we observe slightly lower velocities for the sediments ($\sim$ 165 - 375 m/s for the best model) and a minimum thickness of 75 m.

2.1 Introduction

Estimating the shear wave velocity (Vs) model of the shallow subsurface is of interest for application in seismic hazard assessment and geotechnical engineering (e.g. Dobry et al., 2000; Boore & Atkinson, 2008; Bora et al., 2014, 2015). It relates to the material shear strength and is a sensitive parameter to subsurface lithological changes (see e.g. Mainsant et al., 2012) and thus it is an important parameter for soil classification within the context of earthquake resistant building design as reported in the National Earthquake Hazards Reduction Program (NEHRP) and the Eurocode-EC8 (NEHRP, 1997; EC8, 2004).

Direct shear wave velocity measures can be obtained by laboratory determination of the shear modulus using a triaxial test on soil samples (see Bishop & Henkel, 1962 for details on the procedure). Due to loss of cohesion of soil samples during transport to laboratory (a quantification of the degree of disturbance is given in Braya, 2009), the experiment is usually complimented by in-situ tests, e.g. standard penetration test and cone penetration test (e.g. Mayne, 1997; Akin et al., 2011). All of the above are only scarce in space and thus difficult to generalize or extrapolate to the whole study region.

The application of geophysical techniques, however, allows indirect estimation of shear wave velocities by inverting appropriate observation data. This includes the inversion of the dispersion characteristic of Rayleigh (and Love) waves (e.g. Horike, 1985; Tokimatsu et al., 1992; Asten & Boore, 2005; Cornou et al., 2006; Renalier et al., 2009; Dal Moro & Ferigo, 2011; Puglia et al., 2011), the inversion of the Rayleigh wave ellipticity (e.g. Fäh et al., 2003; Arai & Tokimatsu, 2004) or the combined inversion of both the dispersion curve and the ellipticity (e.g. Scherbaum et al., 2003; Arai & Tokimatsu, 2005; Parolai et al., 2005; Picozzi & Albarello, 2007; Dal Moro, 2010; Hobiger et al., 2013). Here we use the dispersion characteristics of surface waves that provides the basis for estimating the average S-wave velocity profile of the underlying media through inversion assuming a simplified 1D-stratification of physical properties (e.g. Tokimatsu et al., 1992; Wathelet et al., 2004; Socco et al., 2010; Dal Moro et al., 2015). In sedimentary basins with tens to few hundreds of meters thick deposits, the determination of the Vs profile using surface waves methods then requires an accurate estimate of the phase velocity dispersion curve covering the broadest possible frequency range.

The goal of broadband dispersion curve estimation can be achieved by using arrays of increasing apertures (Woods & Lintz, 1973; Asten & Henstridge, 1984) and/or by a combined analysis of active and passive seismic data (Rix et al., 2002; Asten & Boore, 2005; Renalier et al., 2009; Renalier, 2010). A new method known as noise correlation slant-stack technique (Gouédard et al., 2008a) or Interferometric Multichannel Analysis of Surface Waves (IMASW; O'Connell & Turner, 2011) uses the advantages of the passive data (low frequency wavefield) and combines it with signal processing techniques for active data sets, hence knowing the (virtual) source position, for the dispersion curve estimation. Significant interest has been given recently by practitioners to this method (Feuvre et al., 2015; Cheng et al., 2015; Pan et al., 2016).

The combination of all methods then provides a better appraisal of the derived phase velocity dispersion curves as shown in the following. In particular, we investigate the effectiveness of the above mentioned key points (combination of active and passive seismic data, use of multi-processing methods

defined in the next section) to provide a reliable dispersion estimate of the propagating surface waves for a broad frequency range.

We use a set of multi-aperture seismic arrays (1D for active and passive and 2D for passive) together with the frequency - wavenumber (f - k) technique to determine the phase velocity dispersion curve of the propagating surface waves. We assume that the recorded seismic wavefield is dominated by surface waves and of Rayleigh wave type as only data from the vertical component are used. The f - k technique is used to determine the dispersion characteristic of the propagating surface waves for active and passive seismic data sets. We refer to the f - k analysis of the active data sets with the commonly used abbreviation MASW (Multichannel Analysis of Surface Waves; Park et al., 1999). For applying the f - k technique to the passive data sets, we will adopt "passive f - k" in continuation.

Depending on the array aperture and the interstation distance between sensors, the frequency - slowness results for a conventional passive array setup show deficiencies in resolving propagation characteristics of multiple arriving waves in certain frequency (wavelength) bands (Socco & Strobbia, 2004; Poggi & Fäh, 2010; Poggi et al., 2012). As a consequence a clear identification of the dispersion curve branches may be difficult or even not possible (Socco & Strobbia, 2004). In this case, we combine the advantages of active shot data and passive microtremor recording by using the interferometric principle (Snieder, 2004; Curtis et al., 2006; Schuster, 2009; Wapenaar et al., 2010) to estimate the Green's function equivalents from cross-correlating the ambient vibration traces between distinct receiver pairs. The resulting correlograms, assuming the equivalence between the inter-station cross-correlation time derivative pair and the Green's function (Lobkis & Weaver, 2001; Snieder, 2004) can be re-ordered with inter-station distance to build a virtual active experiment setup which is then processed using the MASW method. We refer to the f - k analysis applied to distance sorted correlation Green's function as Interferometric-MASW (IMASW; O'Connell & Turner, 2011). Different terminologies can also be found in the literature (Gouédard et al., 2008a; Feuvre et al., 2015; Cheng et al., 2015; Pan et al., 2016).

The IMASW approach provides a two fold advantage: a) the array response function along the denser 1D virtual receiver array shows better characteristics in terms of resolution and separation of distinct wave numbers in the wavefield; b) the IMASW exploits the frequency band of the ambient vibration wavefield that - compared to active MASW experiments - is enriched in energy at lower frequencies and thus provides the chance to estimate dispersion characteristics for longer wavelengths.

The capability of the array to separate two waves propagating at closely spaced wavelengths/wavenumbers, known as array resolution limit is estimated in the passive experiment from the shape of the respective array response function (ARF) (Woods & Lintz, 1973; Asten & Henstridge, 1984; Di Giulio et al., 2006). For a particular setup, the ARF is defined as the power spectral density evaluated numerically for an incident harmonic wave with infinite apparent horizontal velocity. In the active experiment, the resolution limit is related to the maximum source-to-first-receiver offset that also defines the range for which the plane wave approximation of the recorded surface waves is valid (Stokoe et al., 1994). In both active and passive experiment, the aliasing effects is related to the minimum interstation distance between receivers.

These information (aliasing and resolution limit) need to be taken into account for interpretation of reliable parts of dispersion curve branches (Di Giulio et al., 2006; Cornou et al., 2006; Wathelet et al., 2008b). Following, e.g., Di Giulio et al. (2006), the largest wavelength (or lowest wavenumber) that can be reliably estimated is given by the radius of the main lobe at half-amplitude and the aliasing effect are avoided for wavelengths not smaller (largest wavenumber) than twice the minimum interstation spacing. For the active experiment, the aliasing effect can be related to the minimum geophones spacing. In addition to the nearfield effects, the resolution limit should be taken into account in this case as well. Stokoe et al. (1994) suggest from the Spectral Analysis of Surface Waves methods (SASW) experiment that the offset between the source and the first receiver geophone should be greater than half the maximum interpretable wavelength. For O'Neill (2004), when the distance source-to-first-receiver offset is equal to

the shortest inter-geophone spacing, the maximum interpretable wavelength for the Multichannel Analysis of Surface Waves (MASW) experiment should be less than 0.4L; where L is the overall geophone spread. The two active source methods, SASW and MASW, mainly differ by the spatial setting of the receivers (geophones spread) that also defines the resolution, the seismic source characteristic (harmonic excitation vs spike excitation), and the construction approach of the phase velocity dispersion characteristics of the propagating surface waves. In the virtual MASW experiment (IMASW), the resolution properties are defined equally to the passive experiment. This consideration is useful for the interpretation of the low frequency content in the passive data.

For the appraisal of the derived dispersion curves, we compare the results to independent estimates obtained via the spatial autocorrelation (SPAC) technique. The SPAC method has been initially proposed by Aki (1957) and was modified by several authors (e.g. Ling & Okada 1993; Okada 1994; Bettig et al. 2001) to account for an irregular array geometry and distribution of sensors. The SPAC in comparison to the f - k methods is designed for a wavefield composed of randomly distributed sources. It is theoretically unbiased for this wavefield situation and thus well suited for the analysis of ambient vibration wavefields. The phase velocity dispersion curve is estimated by non-linear inversion of the coherency spectrum (Aki, 1957; Cornou et al., 2006). Within this study, we interpret only the lower lower frequency part (long wavelengths) in comparison to the f - k estimates to reduce the potential bias from f - k.

From the passive experiment, using the passive f - k and the IMASW results, we obtain dispersion curves spanning a lower frequency range (< 1 Hz) in Horstwalde, an intermediate frequency range ($1 < f < 10$ Hz) in Horstwalde and Löbnitz, and a higher frequency range (> 10 Hz) in Horstwalde. From the active experiment, we do process a single shot gather and combine the corresponding intermediate to high frequency dispersion curves with those derived using passive methods. The latter are further inverted to obtain the corresponding 1D Vs profiles.

For the inversion, we use the improved non linear direct search neighborhood algorithm (Wathelet, 2008) to sample the parameter space. The misfit is estimated for each individual model candidate and for each individual mode as the Root Mean Square. We use a simple scheme based on the number of data points to define the contribution of each mode branch to the global misfit.

2.2 Methods

In the following we briefly summarize technicalities of the f - k method as has been applied to both active and passive data. Further, we give a short description of the usage of the cross-correlation and SPAC techniques.

2.2.1 Frequency-wavenumber analysis (f - k)

Assuming an energetically dominant surface wave contribution to the overall composition of the microtremor wavefield, the conventional frequency-wavenumber (f - k) technique (Lacoss et al., 1969; Nolet & Panza, 1976) is applied to the passive data recorded at a spatially distributed set of sensors (2D geometry of array) to obtain the dispersion characteristics of Rayleigh waves (vertical component only).

For a set of narrow frequency bands we perform a sliding window analysis and determine the phase slowness vector that maximizes the beampower by a hierarchical grid search algorithm as implemented in the geopsy software package (freely available at www.geopsy.org; last accessed: February 23, 2017). The analysis results are summarized by evaluating the (azimuthally independent) statistics derived from all time window estimates over all frequency bands (for a full detail on the procedure, see Bonnefoy-Claudet et al., 2005).

For the actively acquired data, the MASW method is applied to the surface wave window recorded

for a hammer shot by equidistantly spaced receivers along a 1D line. The MASW method assumes an in-line plane wave propagation and is computed in frequency domain. In order to improve the signal to noise ratio in the frequency - phase slowness diagram, processing steps as illustrated in Figure 2.1 are implemented. Finally, in both passive and active processing, the dispersion curves are determined by manual picking and analyst interpretation of mode structure from the derived frequency slowness diagrams.

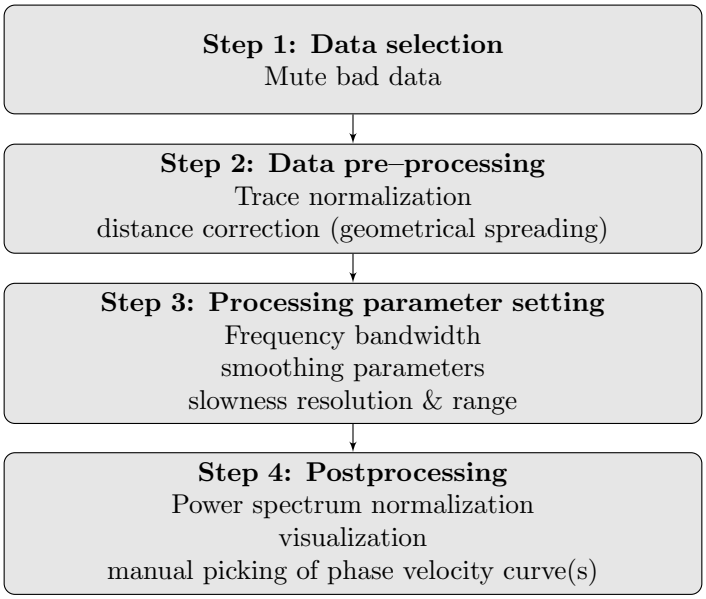

Figure 2.1: Schematic representation of the dispersion curve estimation using active seismic data.

2.2.2 Cross-correlation

The retrieval of the Green's function between a pair of passive receivers from long term cross-correlation has been demonstrated both experimentally (Lobkis & Weaver, 2001) and theoretically (Sánchez-Sesma & Campillo, 2006b; Gouédard et al., 2008b). Equation 2.1 (Gouédard et al., 2008b) gives the general relationship between the Green's function and the long term cross-correlation (CC) in the case of homogeneously distributed white noise sources.

$$\frac{\partial}{\partial t} C_{x_1 x_2}(t) \propto [G(x_1, x_2; t) - G(x_1, x_2; -t)] \tag{2.1}$$

where $G(x_1, x_2; t)$ and $G(x_1, x_2; -t)$ are the causal and acausal Green's function between receivers located at x_1 and x_2 respectively. $C_{x_1 x_2}(t)$ in Equation 2.1 is the long term cross-correlation computed as:

$$C_{x_1 x_2}(t) = \frac{1}{2T} \int_{-T}^{T} u(x_1, \tau) u(x_2, \tau + t) d\tau \tag{2.2}$$

where $u(x_{1,2}, t)$ expresses the displacement recorded at the receiver positions $x_{1,2}$.

This fundamental and powerful principle has been successfully applied in seismology for group/phase velocity estimation and for tomographic purposes (Shapiro et al., 2005; Pilz et al., 2012; Hannemann et al., 2014). In practice, prior to the cross-correlation, the observed data are pre-processed by performing a one bit normalization and then a spectral whitening. This reduces the effect of any transient signal or instrumental irregularities and combats degradation caused by persistent monochromatic sources (see Bensen et al., 2007 for all pre-processing steps and their possible effect on seismic noise cross-correlation).

Within the context of this study, the long term correlation of receiver pairs is rather a pre-processing step for the passive observation of the microtremor wavefield. Once we obtain the correlations and assume their equivalence to Green's functions (in the later referred to as Correlation Green's Functions; CGF) and further assume a laterally homogeneous 1D medium for the region, we can re-order the correlation traces with respect to interstation distance. In this way, we obtain a virtual shot gather with defined shot locations and the frequency content of the natural ambient vibration wavefield. The virtual shot gather is then processed using the f - k method defined above for the active data analysis (see Figure 2.1 for the processing steps). We refer to this procedure as IMASW (O'Connell & Turner, 2011). The same approach has been presented earlier by (Gouédard et al., 2008a).

2.2.3 The SPAC analysis

The spatial autocorrelation method (SPAC) estimates the similarities between stochastic waves assuming that they are stationary in both time and space (Aki, 1957). It follows that the azimuthal average of the correlation $\overline{\rho}$ between multiple receiver-pairs located at a distance r for a given frequency f is given by:

$$\overline{\rho} = J_0(\frac{2\pi fr}{c(f)}) \tag{2.3}$$

where J_0 is the Bessel function of zero order and $c(f)$ is the phase velocity. The ideal situation (as suggested by Aki, 1957) where receivers are all located on a semi-circle of radius r is not easily achievable in the field or in urbanized areas. Bettig et al. (2001) proposed to use the co-array of any 2D array setup to define rings containing stations with inter-station distances between r_1 and r_2. Equation 2.3 then modifies to Equation 2.4.

$$\overline{\rho_{r_1,r_2}} = \frac{2}{r_2^2 - r_1^2}\frac{c(f)}{2\pi f}[r_2 J_1(\frac{2\pi fr_2}{c(f)}) - r_1 J_1(\frac{2\pi fr_1}{c(f)})] \tag{2.4}$$

The phase velocity is obtained through a non-linear inversion of the autocorrelation coefficients. In order to avoid the non-uniqueness related to the non-linear inversion for the phase velocity dispersion curve, Asten et al. (2004) and Wathelet et al. (2005) propose to directly invert the autocorrelation coefficient for structural properties. Here the SPAC method is used as a cross-validation tool for a robust interpretation of the dispersion curves derived using the f - k method in the long wavelength part of the wavefield (Cornou et al., 2006).

2.3 Data and processing

2.3.1 Horstwalde

Site description

The **T**est-site **T**echnical **S**afety (**TTS**) of the Federal Institute for Materials Research and Testing (**BAM**) in Horstwalde (we simply refer to as Horstwalde) is located approximately 50 km south of Berlin (Figure 2.2a). The shallow subsurface is mainly composed of quaternary deposits and characterized by glaciofluvial sediments and densely stratified sand (de Boer, 1995; Juschus, 2001). The very shallow subsurface, with the ground water table at about 3.5 m below the ground (Schmelzbach et al., 2011), is well known from previous geophysical investigations down to $\sim$ 10 m (e.g. Linder et al., 2010; Rumpf & Tronicke, 2014). A sediment characterization down to $\sim$ 330 m is also known from the inversion of the broadband H/V spectral ratio (Lontsi et al., 2015).

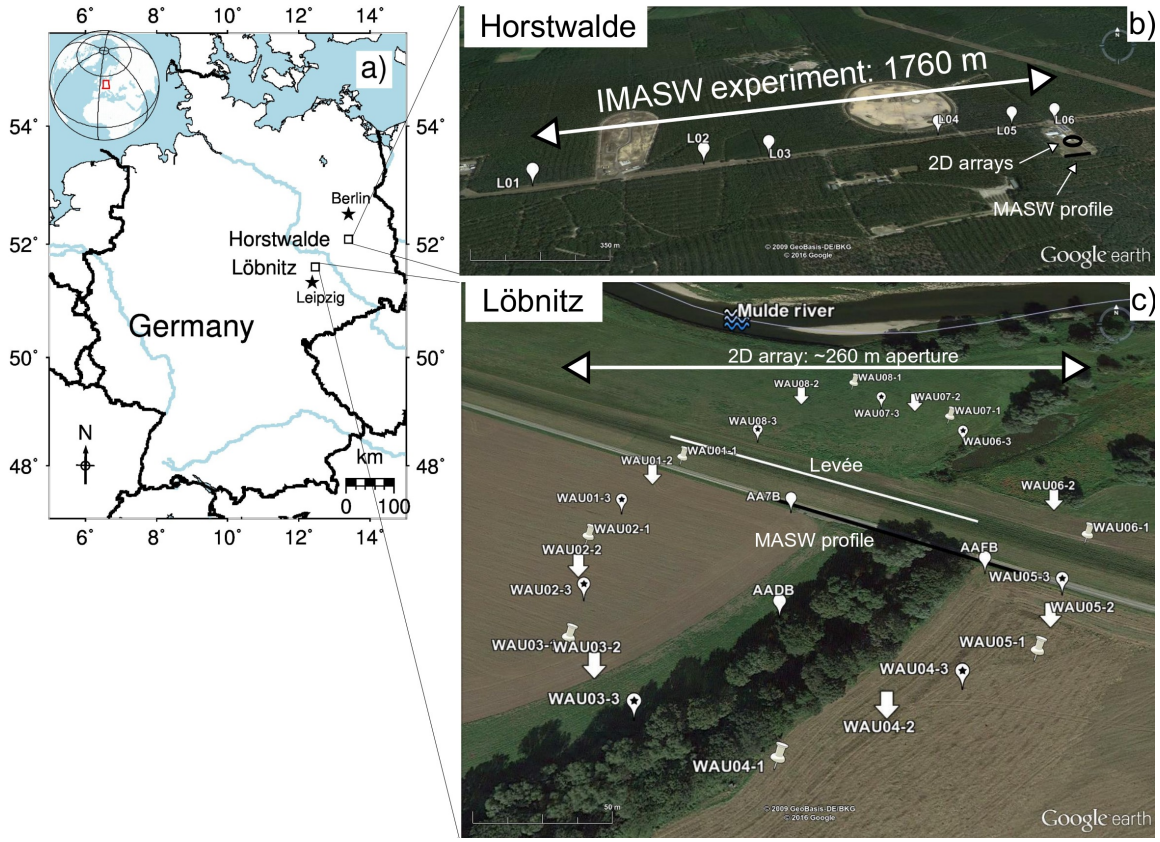

Figure 2.2: a) Test sites locations within Germany. b) & c) present the maps of the survey area together with the array geometries used in Horstwalde and Löbnitz respectively. Active seismic surface wave data were obtained from the profiles represented by the black line; labeled MASW profile in b) & c). Passive seismic data were obtained in Horstwalde using the non-redundant 1.76 km linear array (appropriate for the IMASW analysis) and a set of three small aperture 2D arrays (represented here by a small black circle; see Figures 2.4a-c for the configuration). In Löbnitz, passive seismic data were recorded using a 2D geometry. White pushpin symbols mark stations positions recording during the first day; arrow and white stars symbols mark the stations positions recording during the second and third day respectively. White blank symbols mark stations positions recording permanently during the seismic campaign.

Data surveys

In Horstwalde, we carried out one active seismic experiment (experiment H12A) and four passive seismic surveys (experiments H09B, H10C, H11D, and H11CGF).

In the active experiment H12A, a 5 kg sledgehammer was used as source. The signals were recorded using 96 vertical geophones (f_c = 4.5 Hz) with 1 m spacing and a sampling rate of 4 kHz. The total recording length was 0.75 sec. A sample seismogram section for a shot gather, with 15 m as source to first receiver offset, can be viewed in Figure 2.3a. The traces 64 - 67 were muted in the processing, because the corresponding geophones number were located on an asphalt road and did not record the seismic response to the hammer shot. The gray window in Figure 2.3a shows the development of the surface waves.

In the passive experiment H11D, we used an array of eight sensors (3C Lennartz LE-3D 5s) distributed on two concentric circular rings with an aperture of 10 and 40 m. The data were digitized at 100 Hz sampling rate and recorded the noise wavefield for $\sim$ 3.5 hours. The survey area is represented by the black circle in Figure 2.2b. We further use $\sim$ 12 hours of noise data from the passive experiment H09B. For the passive experiment H10C, 1 hour of noise data was used. Figure 2.4(a-c) present the three array configurations.

Code/ Geometry	# stat.	D_{min} (m)	D_{max} (m)	k_{min} (rad/m)	Recording length	Method	f_{min} (Hz)	f_{max} (Hz)
H09B/2D	6	13.5	31	0.20	12 hours	SPAC	6	16
H10C/2D	114	3	75	0.08	1 hour	SPAC	5	12
H11D/2D	8	5	34	0.18	3.5 hours	SPAC	6	20
H09B/2D	6	13.5	31	0.20	12 hours	passive-fk	6	20
H10C/2D	114	3	75	0.08	1 hour	passive-fk	6	30
H11D/2D	8	5	34	0.18	3.5 hours	passive-fk	6	20
H11CGF/1D	15	165	1760	0.004	3 days / 10 sec	IMASW	0.6	3.4
H12A/1D	96	1	96	0.21	0.75 sec	MASW	8	35

Table 2.1: Array geometry and parameters ranges definition for the dispersion curve analysis at the test site in Horstwalde. The recording length for each seismic experiment is reported. Derived frequency ranges from each method are reported in the last two columns.

In the experiment H11CGF, we used a non-redundant (Haubrich, 1968; Vertatschitsch & Haykin, 1986; Dudgeon & Johnson, 1993) 1D array of 1.76 km length (Figure 2.2b) in which six stations (3C Lennartz LE-3D 1s) are irregularly spaced. In comparison to a common array setup with equidistant spacing, the current configuration allows optimal coverage in the co-array with a minimum number of stations. The data were continuously digitized at 200 Hz over three full days using Reftek 130 digitizers. This configuration appears particularly useful for the IMASW. From the recorded data, we create a virtual active experiment by performing the cross-correlation on a daily basis for all of the 15 receiver pairs combinations. The resulting correlation Green's functions (CGF) are then stacked for three consecutive days of noise recording. Assuming 1D structure, this allows to create a virtual shot gather by sorting the CGF with interstation distance. The causal and acausal part of the CGF, bandpass filtered between 1 and 2 Hz, are presented in Figure 2.3(b). Here we observe (highlighted by the gray window) a dispersive trend of the propagating surface waves with the group and phase velocities averaging 290 m/s.

Phase velocity estimation

To extract the dispersion curves, we applied the f - k method to the 2D small aperture passive seismic arrays deployed between 2009 and 2011 (experiments H09B, H10C & H11D). For statistical analysis, the beampower, for a given centered frequency (f_c), is computed on a variable length (short) time window (t) with a constant time centered-frequency product ($t \cdot f_c = 50$). For the histograms visualization of the frequency slowness diagrams, we use k_{min} (Di Giulio et al., 2006) defined in Table 2.1 for the resolution limit. Figure 2.4(d-f) show in the frequency slowness range the histograms as density plot of the estimated beampower maxima (Ohrnberger et al., 2004; Bonnefoy-Claudet et al., 2005; Wathelet et al., 2008b). The dispersion curve picked in the frequency-slowness histogram plot and its uncertainty derived from the high likelihood region is further constrained in the low frequency range by the array resolution limit being inversely proportional to the overall array aperture. Depending on the specific f - k algorithm, and the data quality, the maximum resolvable wavelength to be reported lies between D_{max} & $3D_{max}$ (e.g. Woods & Lintz, 1973; Asten & Henstridge, 1984; Cornou et al., 2006). Here we use a conservative limit of $2D_{max}$. In the active experiment, the limit as derived for the two-station Spectral Analysis of Surface waves, is set to twice the minimum source-receiver offset (Stokoe et al., 1994; Renalier, 2010).

The obtained frequency-slowness diagrams (Figure 2.4d-f) show a high signal to noise ratio with stable characteristic in the frequency range from 6 to 20 Hz for the three passive seismic campaigns. The dispersion curves are picked within the acceptable range (Di Giulio et al., 2006; Cornou et al., 2006; Wathelet et al., 2008b) delimited here by the dashed curve (k_{min}) or the continuous black curve ($k_{min}/2$). In comparison to frequency-slowness results with few sensors (see setup: Figure 2.4a,c and histograms: Figure: 2.4d,f), additional details in the frequency slowness image are obtained using a dense

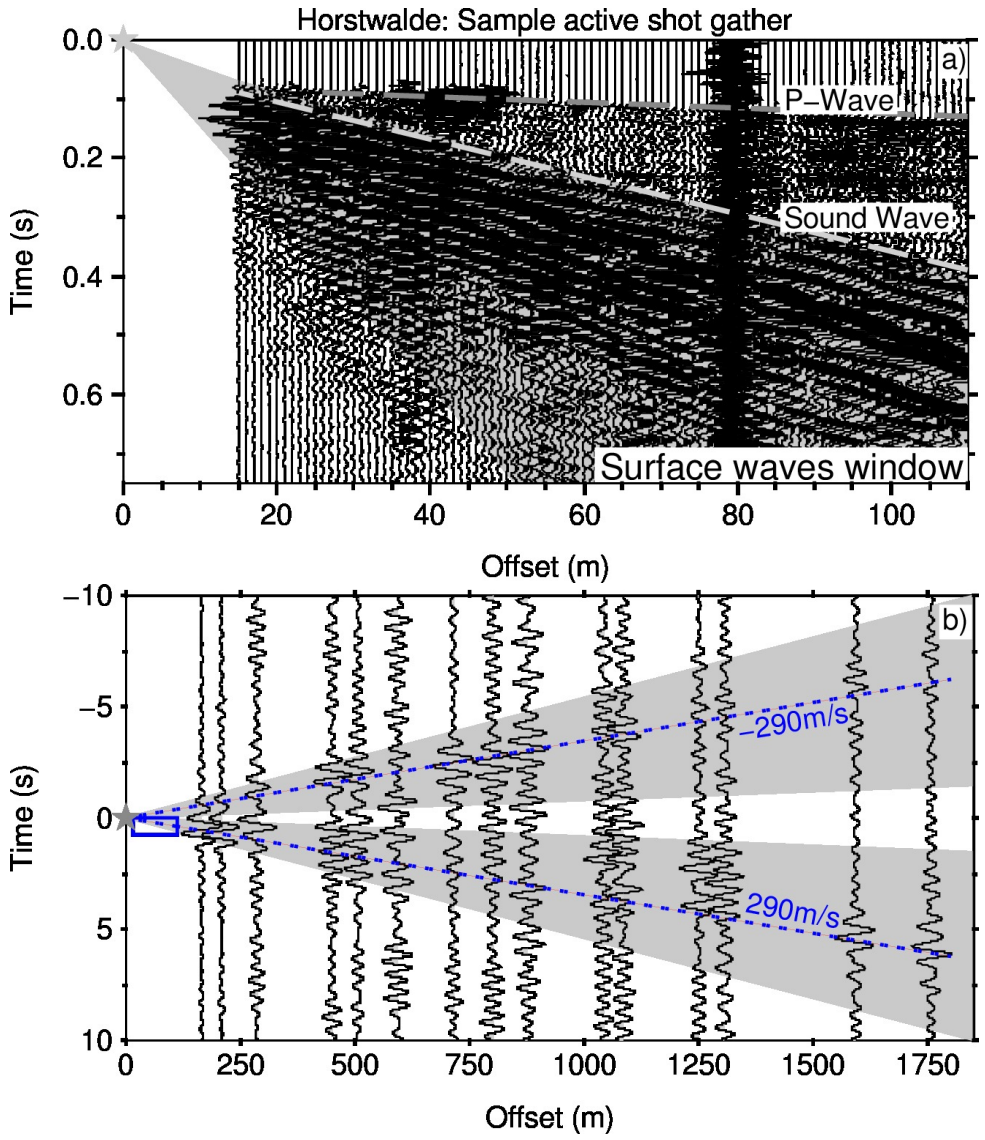

Figure 2.3: a) Sample active shot gather recorded at the test site in Horstwalde. Non-dispersive reflected P and sound waves are marked by dashed gray lines. The gray shading marks the propagating surface waves. b) Resulting cross-correlation Green's functions from the non-redundant linear array resulting from a stack of three days correlograms. The cross-correlation traces are bandpass filtered between 1 and 2 Hz and show a dispersive propagating trend. The gray shading marks the propagating surface waves with 290 m/s as average velocity. The box with reduced size in b) indicates the scale of the active seismic experiment.

array (Figure 2.4b,e). For frequencies above 10 Hz, a non-dispersive branch is observed for a slowness equal to 0.0005 s/m (2000 m/s). This is barely visible in Figure 2.4d,f). The branch corresponds to an average velocity of body P-waves refracted at the top of the water-table boundary at the site (for comparison, see Linder et al., 2010; Rumpf & Tronicke, 2014).

The second set of dispersion curves is extracted by applying the MASW analysis technique to the 1D multichannel seismic data recorded during the experiment H12A. 92 out of 96 channels are processed (uncoupled receivers were removed; see Figure 2.3a). Following the processing steps illustrated by Figure 2.1, the beampower is computed for a given center frequency with a constant frequency bandwidth equal to 0.05 Hz. The beampower is normalized by the maximum power in each frequency bin. The histogram (Figure 2.5d) shows a main dispersion branch, taking into account the resolution limit, between 8 and 35 Hz. Additional branches obtained above 25 Hz are disregarded because no clear mode number could be

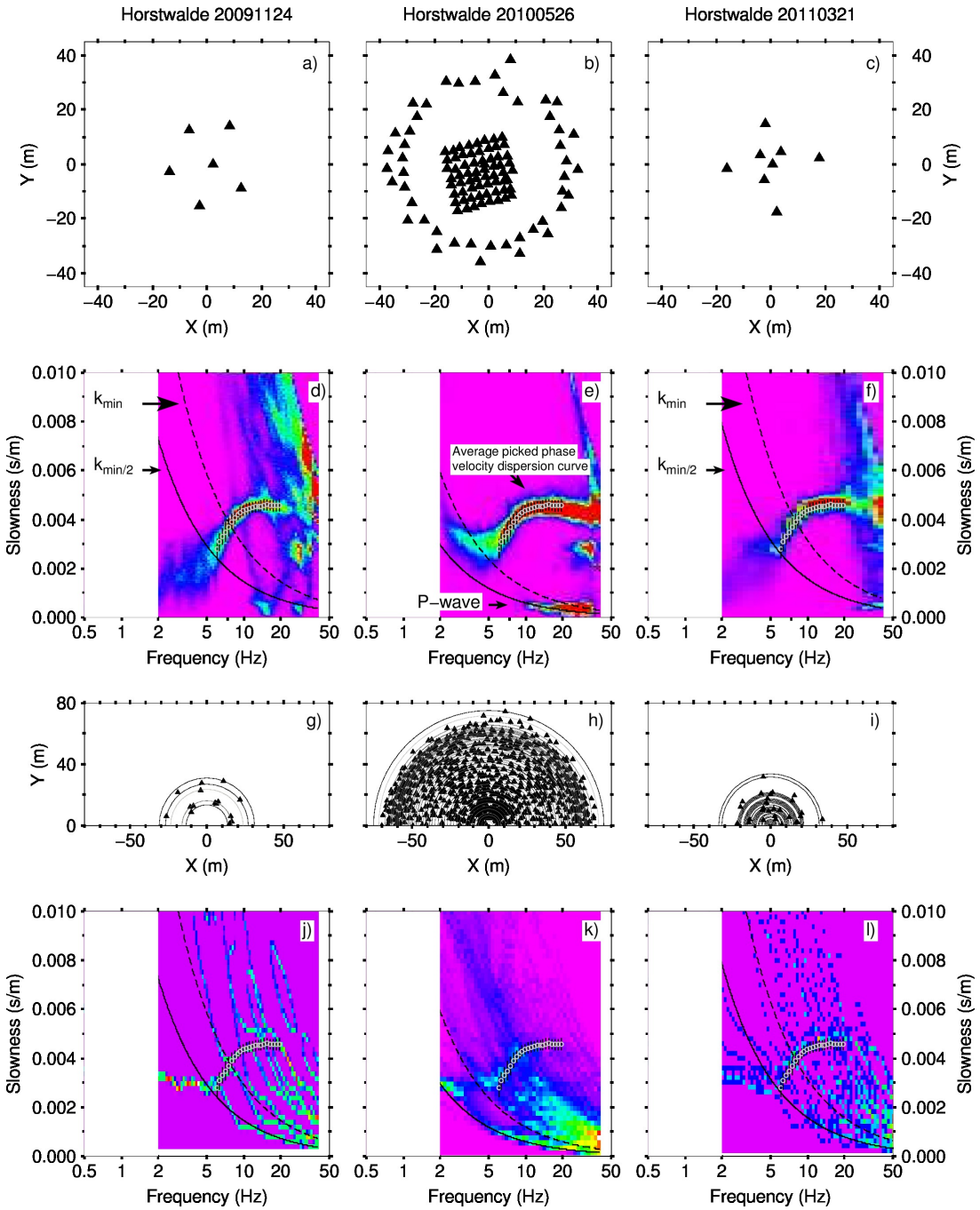

Figure 2.4: Panel 1 (a-c): Small aperture 2D seismic array configuration used in Horstwalde in November 11, 2009; May 26, 2010 and March 21, 2011. Panel 2 (d-f): Frequency-slowness diagram obtained from the passive f - k analysis; presented as density plot of the estimated beampower maxima. Panel 3 (g-i): Co-array maps of the resulting station pairs combination and their azimuthal coverage. Panel 4 (j-l): Frequency-slowness hit counts obtained from the spatial autocorrelation coefficients. The dashed (k_{min}) and the continuous curves ($k_{min}/2$) define the lowest acceptable frequency limits given the maximum array aperture.

associated. In the mode assignment exercise, the corresponding information did not influence the final Vs inversion result.

From the experiment H11CGF, a third set of phase velocity dispersion curves is derived using the resulting CGF. We first stack the causal and the acausal CGF presented in Figure 2.3b. The stacked CGF are then processed as described in the block diagram of Figure 2.1. The first virtual source-receiver offset

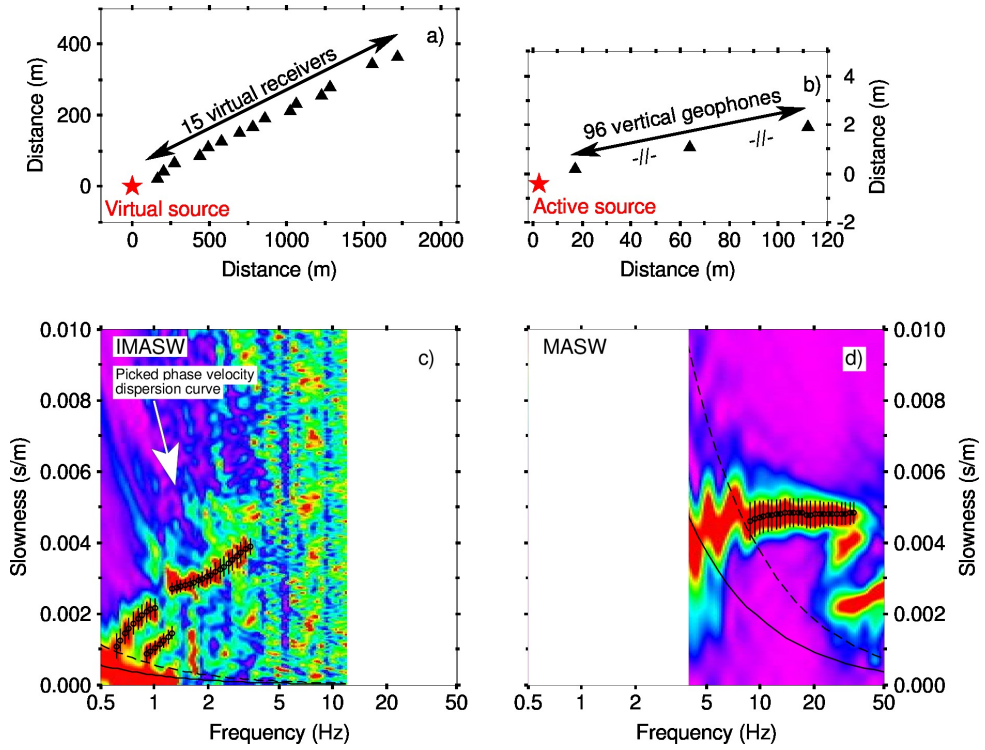

Figure 2.5: IMASW and MASW results in Horstwalde. a) Virtual active experiment array configuration. b) Real active experiment setup. c) Dispersion curve estimate from CGF. d) Dispersion curve estimate from active seismic record.

is $d \sim 165$ m. A distance dependent normalization is applied to the seismic traces. The latter accounts for the geometrical spreading of the surface waves. The beampower is computed using a constant frequency bandwidth equal to 0.1 Hz and further normalized by the maximum power in each frequency bin. The slant-stack diagram (Figure 2.5c) shows two branches with acceptable signal to noise ratio between 0.6 and 3.5 Hz for the first branch and between 0.9 to 1.25 Hz for the second branch. We manually picked the latter respecting the resolving wavelength $\lambda_{max} \simeq D_{max}$; where D_{max} is the maximum aperture of the array.

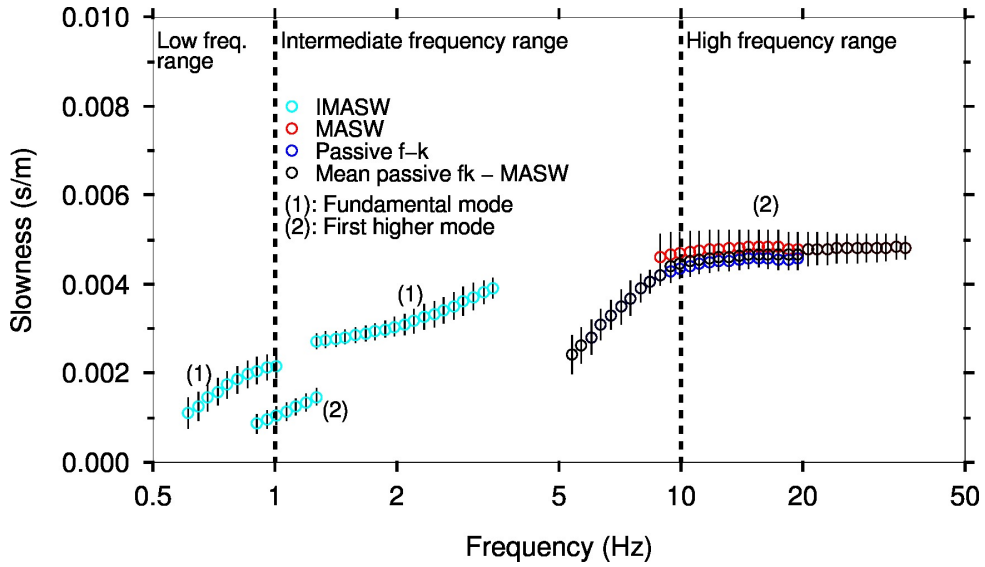

Figure 2.6: Combined dispersion curves from the f - k results at the TTS test site in Horstwalde. The complementarity of the 2D f - k, MASW and IMASW dispersion curves is well illustrated.

In order to prevent a potential bias in the interpretation of the f - k dispersion curves in the low frequency range, we compare the estimations with that from the SPAC method which is less biased for long wavelengths. The dispersion curves are derived for the three 2D arrays deployed in Horstwalde. The co-array map and the corresponding frequency-slowness diagram obtained from inversion of the autocorrelation coefficients are presented in Figure 2.4(g-l). The interpretable phase slowness curves within the array resolution limits are comparable to the f - k analysis results. Furthermore, the phase velocity information in both the passive f - k and the SPAC methods are divergent below $\sim$ 6 Hz which therefore defines our lower frequency limit of interpretation.

The dispersion curves derived from the 2D small aperture passive array, the active data set and the virtual experiment are combined for multiple mode inversion (See Figure 2.6). The dispersion curves range from 0.6 to 35 Hz both for the fundamental and higher modes.

Based on forward modeling using the algorithm reported in SESAME (2004); Wathelet (2005), we test different models with multiple modes (0,1,2,3,4). As a result, we find a best association of the second branch with the first higher mode.

2.3.2 Löbnitz

Site description

The second investigated site is located near Löbnitz, northern Saxony, around an abandoned meander of the Mulde River (Figure 2.2a,c). A levée, constructed for flood protection, crosses the 2D passive array setup (see dashed line in Figure 2.2c). Similar to Horstwalde, the very shallow subsurface is mainly composed of quaternary sediments. The lithological log indicates the presence of a Permian rock, the Rhyolite, at about 80 m below the subsurface. The ground water table is estimated at around 3 m to 5 m below the ground (Linder, 2007). The near subsurface seismic parameters down to approximately 8 m depth are known from active experiments (Hausmann et al., 2013; Steinel et al., 2014).

Data survey

At this site, we carried out one active experiment (experiment L12A) in a 1D configuration and one passive seismic survey with a 2D small aperture array (experiment L12P1). The 2D setup was rotated twice during the seismic campaign (experiments L12P2 and L12P3), leading to a total of three 2D array configurations at this site. The experimental layout is shown on Figure 2.2c where the active and passive seismic configurations are also displayed. In the experiment L12A, a 5 kg sledgehammer was used as source. The generated seismic signals were recorded using 144 vertical geophones ($f_c = 4.5$ Hz) with 1 m spacing at 2 kHz sampling rate. The total recording length was 1.05 sec. Figure 2.7(a) shows a sample seismogram section for a shot gather with 20 m offset. A refracted P-wave and the sound wave are clearly observed. Surface waves are also clearly observed (Figure 2.7a).

For the experiment L12P1, a 2D circular array was deployed with 260 m aperture. Three stations (blue marker in Figure 2.2c) in a circular configuration were set for continuous recording during the seismic campaign. The outer configuration was rotated anticlockwise twice during the seismic campaign to achieve a dense coverage. The experiments L12P2 and L12P3 correspond to the array configuration after the first and the second rotation respectively. Three 1s and eight 5s 3C seismometers of Lennartz LE-3D type sensors were used in the experiment and operated at 100 Hz sampling rate. The total recording lengths, reported in Table 2.2 were $\sim$ 20.5 hours for L12P1, $\sim$ 20.5 hours for L12P2 and $\sim$ 24.5 hours for L12P3.

The data set from the virtual experiment (L12CGF) is obtained from the passive data by correlating the signals from the 165 receiver pairs combinations. With the assumption of a predominantly 1D media,

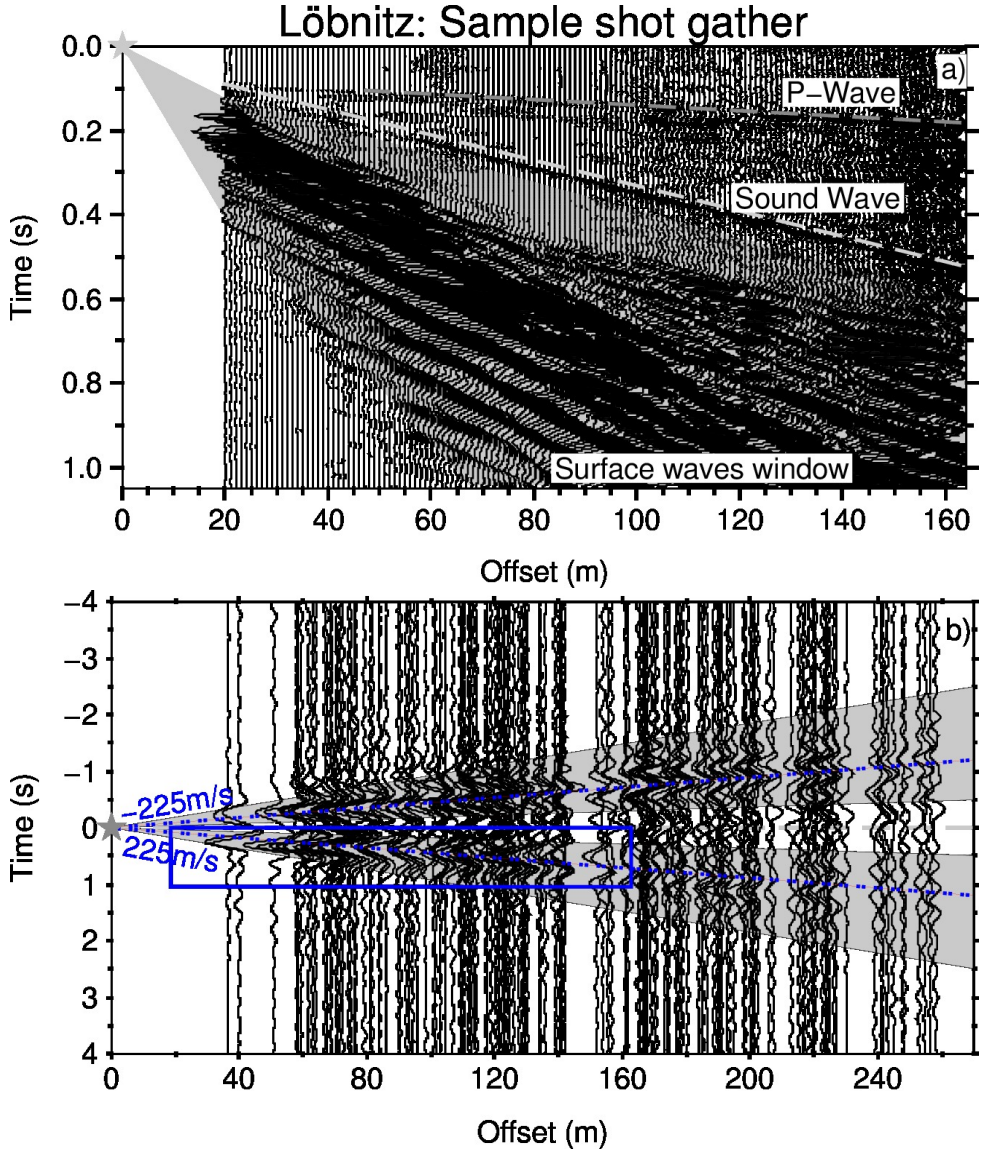

Figure 2.7: a) Sample active seismic seismogram section. Non-dispersive reflected P and sound waves are marked by dashed gray lines. The dispersed surface waves window is highlighted. b) The resulting cross-correlation from 3x55 (Löbnitz) receiver pair combinations (See array setup in Figure 2.2c and the subsequent rotated configurations). The gray star represents the virtual source. The CGF are bandpass filtered between 1 - 4 Hz. The gray window highlights the trend of the propagating surface waves.

Code/ Geometry	# stat.	D_{min} (m)	D_{max} (m)	k_{min} (rad/m)	Recording length	Method	f_{min} (Hz)	f_{max} (Hz)
L12P1/2D	11	62	258	0.024	20.5 hours	SPAC	1.5	3.5
L12P2/2D	11	59	248	0.025	20.5 hours	SPAC	1.5	3.5
L12P3/2D	11	58	243	0.026	24.5 hours	SPAC	1.5	3.5
L12P1/2D	11	62	258	0.024	20.5 hours	passive-fk	1.5	3.5
L12P2/2D	11	59	248	0.025	20.5 hours	passive-fk	1.5	3.5
L12P3/2D	11	58	243	0.026	24.5 hours	passive-fk	1.5	3.5
L12CGF/1D	165	58	258	0.024	$\sim$ 1 day / 4 sec	IMASW	1.6	8
L12A/1D	144	1	144	0.16	1.05 sec	MASW	8	25

Table 2.2: Array geometry and parameters ranges definition for the dispersion curve analysis at the test site in Löbnitz. The recording length for each survey is reported. Derived frequency ranges from each method are reported in the last two columns.

the daily cross-correlation Green's function are sorted with interstation distance. The CGFs bandpass filtered between 1 and 4Hz show a clear propagation and dispersion trend of the surface waves with $\sim$ 225 m/s (Figure 2.7b).

Phase velocity estimation

To determine the dispersion characteristic, we applied the f - k method to the data recorded using the three 2D passive seismic arrays (experiments L12P1, L12P2 & L12P3). Similar to the precedent case (Horstwalde), for a given centered frequency (f_c), the beampower is computed on a variable length short time window (t) with a constant time centered-frequency product ($t \cdot f_c = 50$). Within the array capability (defined here by $k_{min}/2$, with k_{min} given in Table 2.2), the obtained slowness histogram for the three

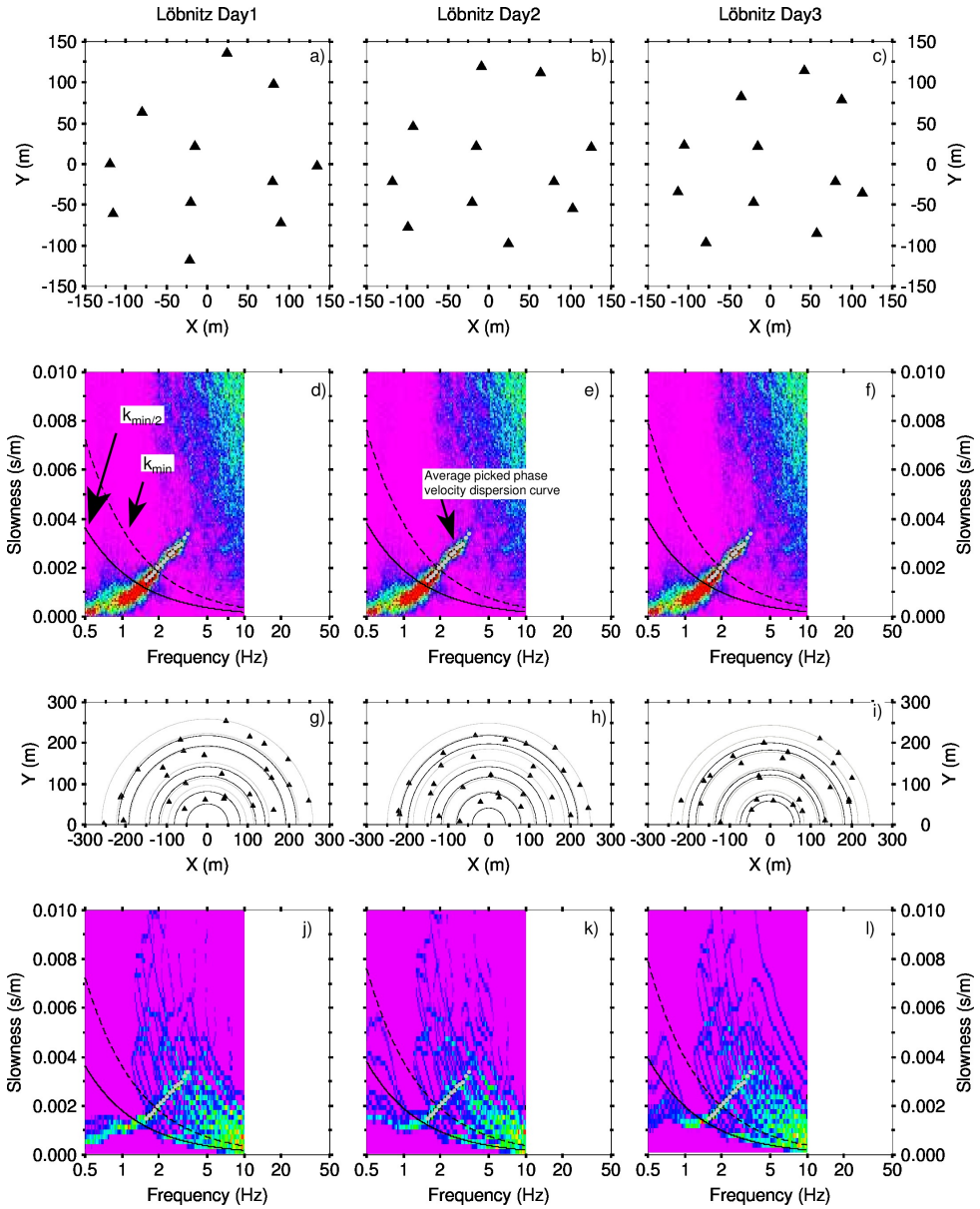

Figure 2.8: Small aperture 2D seismic array configuration used in Löbnitz at different days to monitor the ambient noise. a) The array geometry for the first day of the survey, b) the second day, obtained after anticlockwise rotation of the outer sensors of the initial configuration in a) and c) the third day, obtained after anticlockwise rotation of the configuration shown in b). Panel 2 (d,e,f): Corresponding f - k analysis. Panel 3 & 4 show the co-array and the derived dispersion curves using the spatial autocorrelation method.

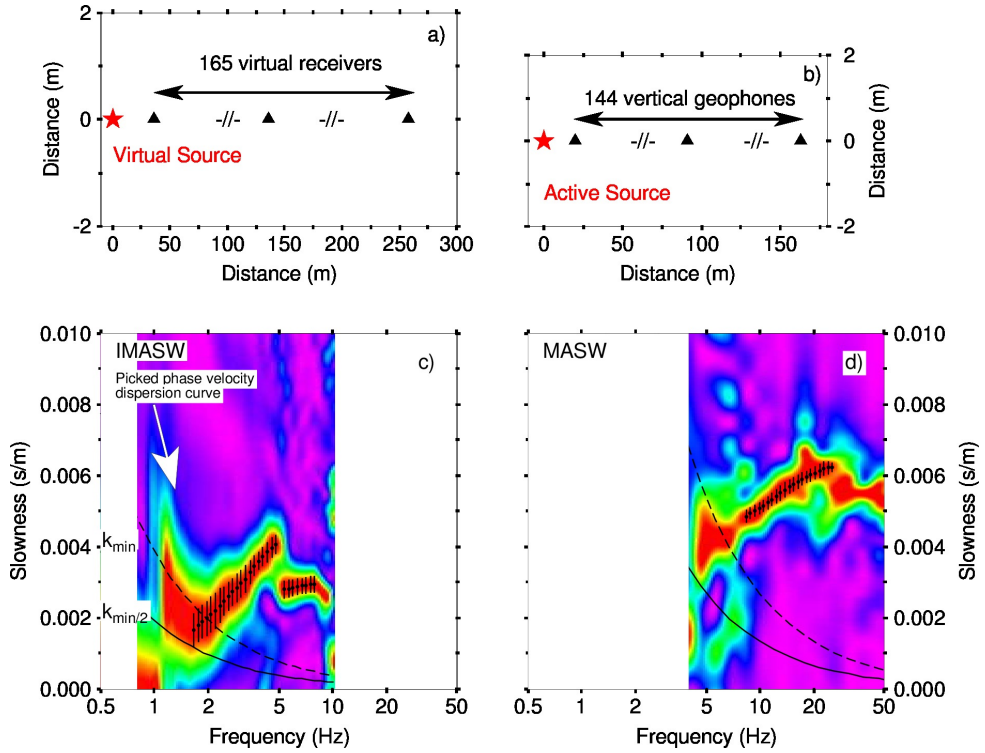

Figure 2.9: IMASW and MASW results obtained in Löbnitz. a) Virtual array configuration. b) Real active array configuration. c) IMASW results from cross-correlation of 55 (8 red + 3 blue stations) station pairs. A clear branch is observed between 1 and 6 Hz. It is picked manually and considered fundamental mode of dispersion. Also picked is the branch between 5 and 8 Hz. d) MASW results from single shot gather.

different days, with array geometries represented by the Figures 2.8(a-c), presents the interpretable area with strong signal to noise ratio between 1.5 and 3.5 Hz (Figures 2.8d-f).

To support the previous interpretation of the obtained dispersion, we applied the SPAC method to the same data set. The co-array maps and the corresponding frequency-slowness diagrams, obtained from

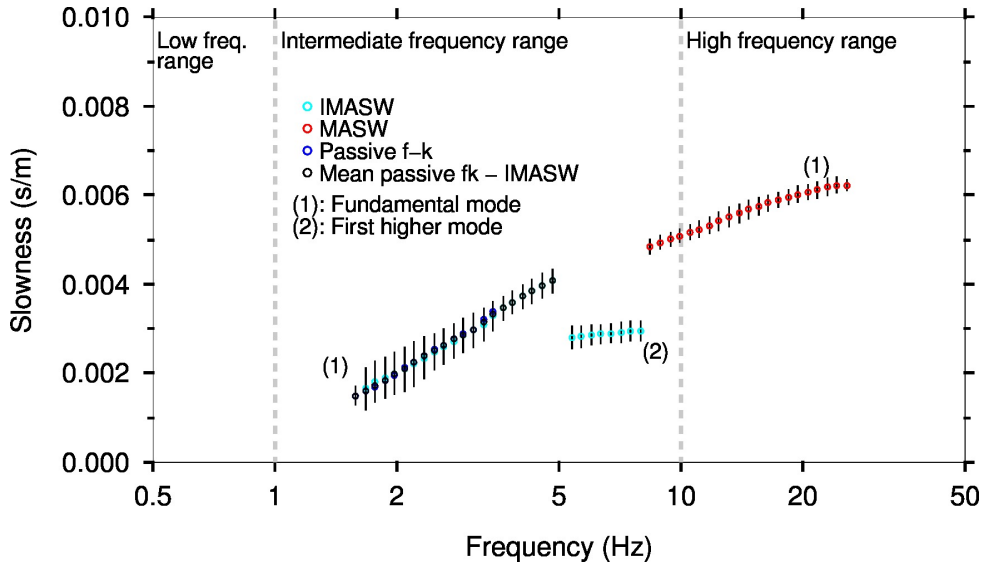

Figure 2.10: Combined f - k results for Löbnitz. The complementarity between the MASW and IMASW is emphasized.

the inversion of the autocorrelation coefficients, are shown in Figure 2.8(g-l). There is a good agreement between the f - k and the SPAC method in deriving the fundamental mode of dispersion. Furthermore, as in the previous case, the dispersion curves information diverges in the low frequency range. This establishes a confidence in the results for the considered frequency band.

Figure 2.10 presents the combined dispersion curves obtained using the passive f - k, the MASW and the IMASW. The dispersion curves range from 1.5 to 25 Hz for the fundamental and higher modes combined. For mode assignment, we repeat the previous exercise by seeking in a pool of possible modes, the mode that best represents each of the picked phase velocity dispersion curve branch. The second dispersion characteristic data set is obtained from processing the 1D active seismic data (experiment L12A). Here again, we follow the processing steps illustrated by Figure 2.1 to compute the beampower. A constant frequency bandwidth equal to 0.1 Hz around the center frequency is used. The beampower is normalized by the maximum power in each frequency bin. The slant-stack diagram (Figure 2.9) shows a main branch with good signal to noise ratio between 5 and 25 Hz. Within the array resolution limit, frequencies between 8 and 25 Hz are considered for inversion.

In the IMASW derived dispersion curves obtained following the above mentioned steps (as in Figure 2.1), two branches in the frequency-slowness diagram with good signal to noise ratio are observable and picked between 1.6 and 5 Hz for the first branch and 5 to 8 Hz for the second branch (Figure 2.9).

2.4 Inversion

2.4.1 Parametrization and inversion scheme

For the parametrization at the TTS site in Horstwalde, we make use of the results obtained from the previous shallow geophysical activities conducted at the site to define the parameter range. A description of the geological structure in the uppermost 15 m has been given in Linder et al., 2010; Schmelzbach et al., 2011; Tronicke et al., 2012; Rumpf & Tronicke, 2014. A geological log down to 577 m depth is also available from a borehole near the test site (referred to as Staakow 159/62). The model parameter range used for the inversion (modified after Lontsi et al., 2015) consists of six layers overlaying a halfspace (see Table 2.3).

In Löbnitz, the shallow information available from previous investigation (Hausmann et al., 2013; Steinel et al., 2014) also allows to constrain the starting parameter range (see Table 2.3).

The improved neighborhood algorithm (Wathelet, 2008) is used to invert the estimated dispersion curves summarized in Figures 2.6 & 2.10 for Horstwalde and Löbnitz respectively. It is a directed search Monte Carlo inversion based on the Voronoi diagram concept, and driven by misfit value evaluated as the standard Root Mean Square (RMS; Equation 2.5). For each sample model, the RMS for the mode m is computed as:

$$dcmisfit_m = \sqrt{\frac{1}{n_m} \sum_{i=0}^{n_m} \frac{(v_{dmi} - v_{cmi})^2}{\sigma_{mi}^2}} \tag{2.5}$$

Where: $dcmisfit_m$ is the misfit value for mode m; m = {0,1}; n_m = number of data points for mode m; v_{dmi} = experimental dispersion curve at frequency f_i; σ_{mi} = standard deviation of v_{dmi}. For each model candidate, the misfit for the fundamental and first higher mode of the dispersion curves are estimated. Different algorithms or assumptions exist to account for the contribution of each individual frequency (Wathelet, 2005; Dal Moro & Pipan, 2007) or energy from each mode (Beaty et al., 2002) to the global misfit. A summary of methods considering higher modes together with their limitations can be found in Socco et al. (2010).

Here we assume a very simple but reasonable weight scheme based on the number of points, n_0 and

Horstwalde		Löbnitz	
Thickness	$Vs(m/s)$	Thickness	$Vs(m/s)$
0.1 - 5	50 - 500	0.1 - 10	50 - 350
0.1 - 10	50 - 500	0.1 - 10	50 - 350
0.1 - 15	100 - 1500	0.1 - 10	50 - 350
0.1 - 20	100 - 1500	0.1 - 10	50 - 350
0.1 - 100	100 - 1500	0.1 - 50	100 - 400
200 - 800	100 - 2500	0.1 - 200	200 - 800
∞	400 - 3500	∞	200 - 3500

Table 2.3: Parameters ranges used in the inversion for the Vs at the sites in Horstwalde and Löbnitz. The background geological/geophysical information (Horstwalde: de Boer, 1995; Juschus, 2001; Löbnitz: Linder, 2007; Hausmann et al., 2013 helped defining the starting parameter range.

n_1 of the fundamental and first higher modes, effectively contributing to the individual misfit evaluation (defined by Equation 2.6), respectively:

$$\begin{aligned} w_0 &= \frac{n_1}{n_0 + n_1} \\ w_1 &= \frac{n_0}{n_0 + n_1} \end{aligned} \tag{2.6}$$

The latter is then used to combine the contribution of each individual mode. This weighting scheme assumes that for equally sampled dispersion curves at discrete frequencies, curves with equal number of points will contribute equally to the global misfit. Misfit values from dispersion curves (fundamental or first higher mode) spanning a broad frequency range are down weighted. In turn, this allows energy balance from each contributing mode and to get information from the shallow to deep subsurface.

The quadratic method defined by Equation 2.7 is appealing for combining the derived misfit. Weighted misfits could then be interpreted in a 2D bi-objective plane as a set of Pareto optimal solutions (Dal Moro, 2010).

$$misfit = \sqrt{(w0 * dcmisfit_0)^2 + (w1 * dcmisfit_1)^2} \tag{2.7}$$

2.4.2 Inversion results and geological interpretation

We performed the inversion described in the previous section using an Intel(R) Core(TM) i7 CPU 870 @ 2.93GHz machine. The computational time effort for a forward model is in the order of milliseconds. For the inversion, we use more than 100 000 effective models both in Horstwalde and Löbnitz in the search.

Using the quadratic misfit combination method, we find for the best model in Horstwalde $\sim$ 190 m/s as shear wave velocity at the surface and a deep sediment cover with an overall thickness of 230 m. The bedrock shear wave velocity for the best model is estimated to 1400 m/s. Obtained results within the uncertainty defined by all models with misfit < 1 in the first 15 m (see Figure 2.11e) correlate well with the previous active experiment (Linder et al., 2010; Rumpf & Tronicke, 2014). The overall Vs profile is also comparable to estimates from an independent study by Lontsi et al. (2015) using the diffuse wavefield approach (DFA; Sánchez-Sesma et al., 2011a) and the H/V spectrum as observable. The authors obtained a Vs ranging from 190 m/s in the very first layer to 1500 m/s in the bedrock.

In light of the obtained results presented in Figure 2.11c and because of the trade-off between the seismic shear wave velocity and the sediment thickness, the minimum bedrock depth (around 200 m) and velocity (1000 m/s) can be guessed from the apparent spread of models.

Figure 2.12 shows the obtained structure in Löbnitz with a bedrock (top strong impedance contrast at bottom of soil column) estimated at approx. 95 m depth. V_S ranges from 165 m/s to 375 m/s in the bottom sediment column and is estimated to 2700 m/s in the bedrock. Within the uncertainties defined

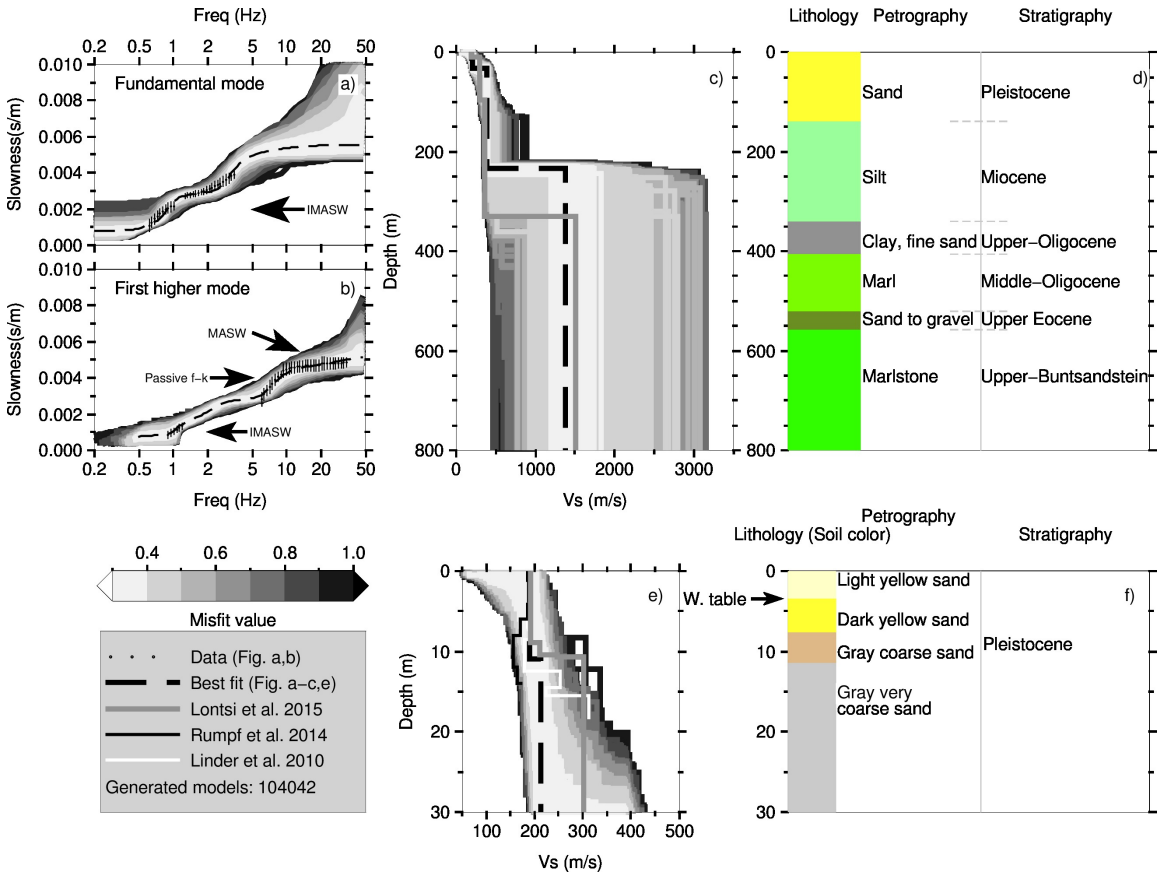

Figure 2.11: Inversion results of a) the fundamental and b) the first higher mode dispersion curves obtained in Horstwalde. c) Obtained Vs profile for the overall sediment column. d) The geological log information. e) A shallow velocity profile for the first 30 m and f) the corresponding geological log information.

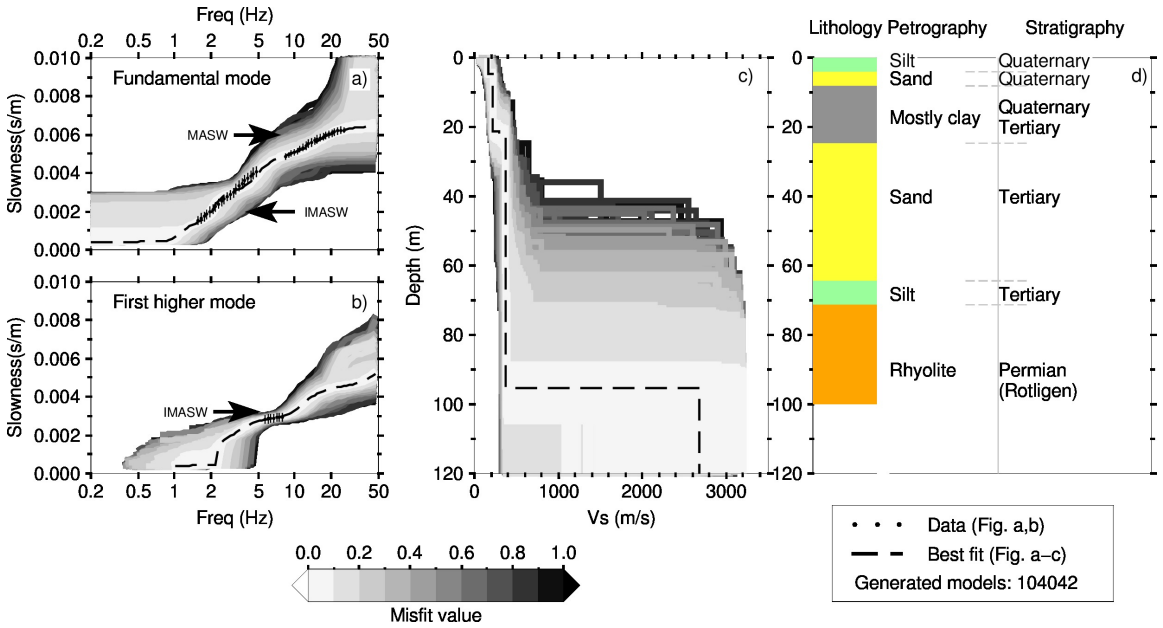

Figure 2.12: Inversion results of a) the fundamental and b) the first higher mode dispersion curves obtained in Löbnitz. c) Obtained Vs profile for the overall sediment column. d) The geological log information.

by all models with misfit < 1, the Vs estimates in the upper 10 m are comparable with estimation by Steinel et al. (2014) where the authors estimate the pseudo 2D average Vs image.

The convergence of the global misfit (Equation 2.7), defined as the euclidean distance for the weighted misfit for each mode, and viewed as the Pareto front evolution (Dal Moro & Pipan, 2007), is presented in Figure 2.13 for the two investigated sites. In comparison to Horstwalde where the overall minimum misfit is 0.35 (estimated using Equation 2.7), that in Löbnitz is estimated to 0.08. These two quantities define the distance to the targeted Utopia point defined in the ideal case as a result of the perfect fitting of the different phase velocity dispersion curve modes. The spread between the misfits may be attributed to the difference in the bandwidth of the observed dispersion curves at each individual site used for inversion. The asymmetry observed at low misfit values presented in the bi-objective plane (Figure 2.13c), may be understood from the spread of models presented in Figure 2.11c and the minimum achieved bedrock depth in comparison to the provided available geological log information. For Löbnitz, a good symmetry is observed for low misfit values (Figure 2.13d). In this case a relatively good match is observed between the minimum estimated bedrock depth (Figure 2.12d) and provided available geological log information.

2.5 Discussion and conclusion

We have presented an integrated approach for determining the 1D shear wave velocity at two selected sites, Horstwalde and Löbnitz in Germany. For the data surveys, we used different seismic arrays in 1D configuration for the active experiments (Horstwalde and Löbnitz). In the passive experiments, 2D arrays were used at both sites. This configuration is useful to minimize any bias introduced by the source directivity (Halliday et al., 2008). We additionally use in Horstwalde a non-redundant 1D array

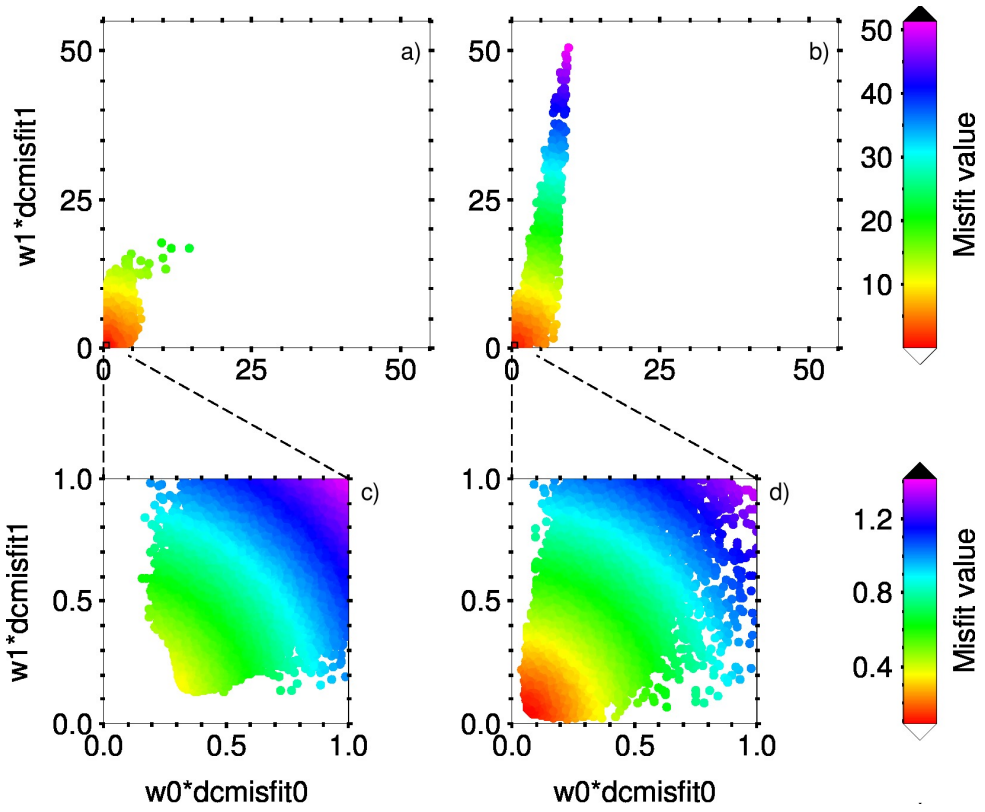

Figure 2.13: Convergence of the global misfit (Equation 2.7) presented as Pareto front evolution optimal solution a) for Horstwalde and b) for Löbnitz. c) Low misfits value ($< \sqrt{2}$) for Horstwalde. d) Low misfits value ($< \sqrt{2}$) for Löbnitz. See text for the interpretation.

of six receivers in the passive experiment. With this configuration we obtain 15 virtual receiver-pair combinations in the cross-correlation process. First, we minimize effects of uneven source contribution (wavefield directivity) in the dispersion curve estimation by stacking the causal and the acausal CGFs.

We mainly used four methods (SPAC, passive f - k, IMASW and MASW), of which the SPAC, passive f - k and MASW are common practice, to estimate the propagation characteristic of Rayleigh waves recorded at the two selected sites.

The dispersion curves derived using the passive f - k are consistent with the repeated seismic noise experiment both in Horstwalde (see Figure 2.4 and the reported frequency ranges in Table 2.1) and in Löbnitz (see Figure 2.8 and the reported frequency ranges in Table 2.2). For the two sites, the passive f - k and the SPAC methods diverge (Figures 2.4 & 2.8) in the low frequency range ($<\sim$ 6 Hz) and converges between 6 to $\sim$12 - 20 Hz. As individual methods might be influenced by the directivity of the noise wavefield (Asten, 2006; Halliday et al., 2008), the combined information in addition to the limits imposed by the array characteristics are useful for a reliable interpretation of the derived dispersion curves.

To obtain dispersion curves for high the frequency range ($>$ 10 Hz), we applied the MASW to active seismic recordings. The results were presented in Figures 2.6 & 2.10 for Horstwalde and Löbnitz respectively. Note however that the nearfield effects remain a problem for the plane wave approximation of the propagating surface waves observed in Figures 2.3 and 2.7.

In this study, the IMASW, which is a relatively new approach for the derivation of dispersion curves from CGFs presents the advantage to provide information regarding the fundamental and higher modes (Figures 2.5 & 2.9). In Horstwalde, application of the passive f - k method to the 1.76 km linear array (with six receivers), did present a smeared frequency-slowness diagram (not shown here). This situation may be improved when having additional sensors evenly spaced along the linear array (Pancha & Pullammanappallil, 2012), but still the possible directivity in the noise wavefield could compromise the final estimation. However the dispersion characteristic is observed (including one higher mode) after we first applied the cross-correlation technique to the noise recordings.

In Löbnitz, the passive f - k and the IMASW give the same results within the error bars between 1.6 and 3.5 Hz (Figure 2.10). The IMASW results (Figure 2.9) also indicates the presence of an additional branch which we interpret as the first higher mode.

Depending on the robustness regarding the source distribution, we sorted the main methods presented in this study as shown in Figure 2.14. The two end members of assumptions about the wavefield are the SPAC method which requires a diffuse wavefield and the MASW method which requires a known source location and the corresponding wavefield propagation direction.

The performance range in terms of wavelength, normalized wavelength (with respect to the maximum array aperture), and achieved frequency range are also presented in Figure 2.14. From the wavelength ranges in Figure 2.14a and using the rule of thumb for which the estimated depth is $\frac{1}{3}\lambda$ (Renalier et al., 2009; Renalier, 2010), we expect a good resolution in Horstwalde between $\sim 2m$ to $\sim 500m$ depth. In Löbnitz, we would expect a good resolution between $\sim 2m$ to $\sim 160m$ depth. From Figure 2.14b, the passive methods (SPAC, passive f - k, and IMASW) resolve structure with wavelength ranging from $\lambda/D_{max} =\sim 0.5$ to 1.5. The active methods (MASW, IMASW), with known (virtual) source location provides the shear wave velocity information for the very short wavelengths ($\lambda/D_{max} < 0.1$). We conclude that the methods presented in this study are complementary for obtaining a broadband phase velocity dispersion curve. The interpretation is reliable in terms of mode of propagation and subsequently the corresponding shear wave velocity profiles.

Our inversion results for the 1D shear wave velocity distribution show a shallower sediment thickness in Löbnitz in comparison to Horstwalde. This can be related to the longer wavelengths interpreted at the site in Horstwalde. Especially in Löbnitz, within the uncertainties, the changes in the estimated Vs profiles correlate well with the changes in the subsurface sediment structure (compare Figure 2.12c-d).

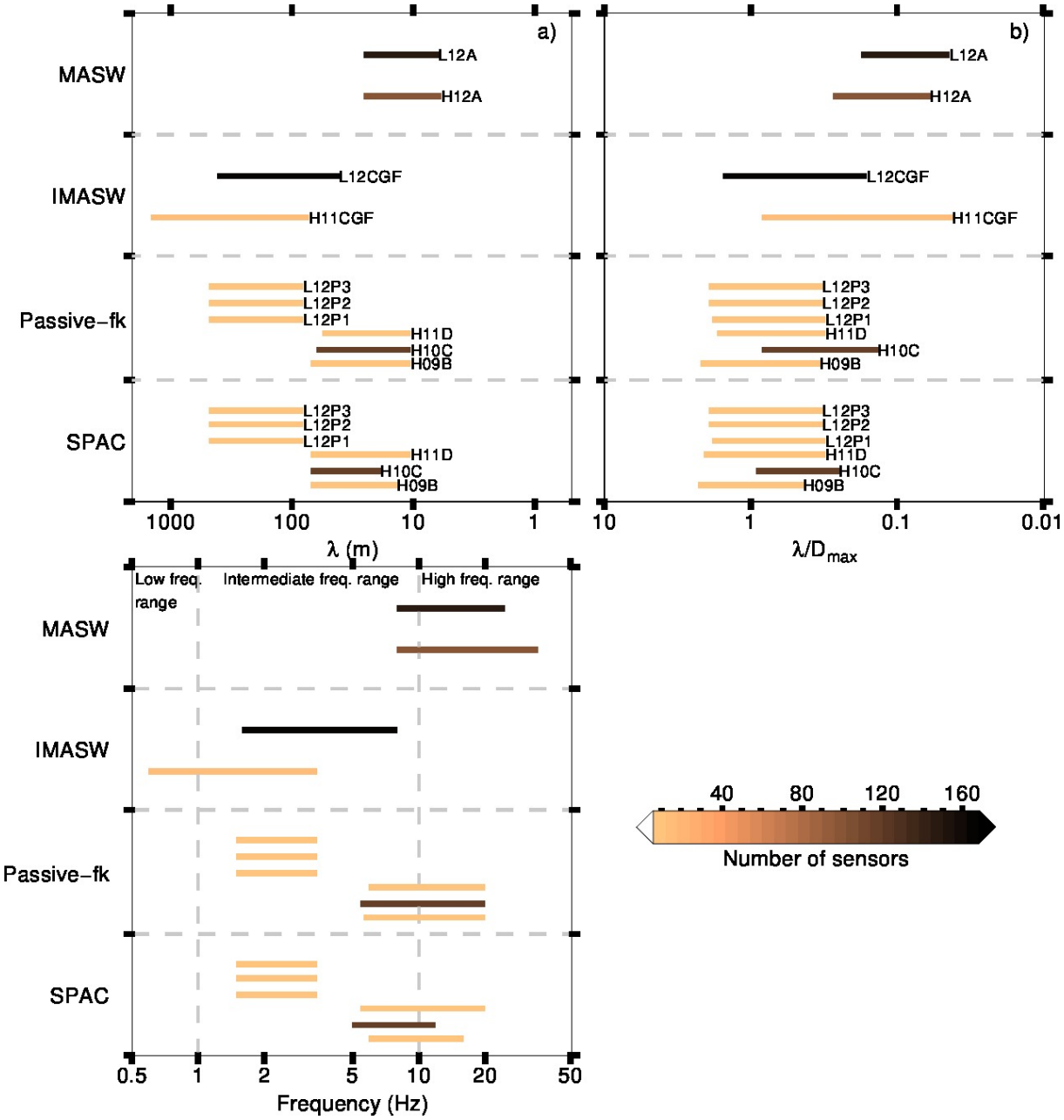

Figure 2.14: Diagram presenting the performance range in terms of normalized (with respect to the maximum array aperture) wavelength of the different methods presented in this study. The performance range in terms of frequency as achieved by each array is also presented. The methods are sorted with respect to consideration regarding the noise source distribution.

Delineating the bedrock depth remains however an issue. In Horstwalde, we obtain a shear wave velocity in the bedrock comparable to the estimate from the inversion of the H/V spectrum when additional sensors at depths are considered (Lontsi et al., 2015). Although the estimated velocity information is reasonable (as in Horstwalde), the estimated bedrock depths do not necessarily match when compared with the available geological log information (Figures 2.11c,e & 2.12d). The mismatch can also be seen as resulting from the freedom introduced in the inversion by the missing phase velocity information (due to the vanishing of the energy close to the resonance frequency; Poggi & Fäh, 2010) below 1.5 Hz (0.6 Hz in Horstwalde).

More studies combining the presented methodologies will allow more comprehensive velocity-depth information to be obtained.

Acknowledgments

This work was funded by Geotechnologien program of the German Federal Ministry of education and Research (BMBF) under grant No. 03G0745A (MuSaWa project, Tomography call), by the DFG Graduiertenkollegs GRK 1364 and by the PhD completion scholarship of the University of Potsdam. I would like to thank, M. Delock for assistance during passive seismic campaign in Löbnitz; Michael Rumpf and Jörg Hausmann for providing active seismic data. We would like to thank Sjoerd de Ridder, Jacopo Boaga and two anonymous reviewers whose comments have helped improving the quality of the manuscript. We also wish to thank the Editor-in-Chief, Jyoti Behura, for answering our queries during the review process.

Chapter 3

Full microtremor H/V(z, f) inversion for shallow subsurface characterization

Lontsi, A. M., Sánchez-Sesma, F. J., Molina, J. C., Ohrnberger, M., Krüger, F., 2015. Geophysical Journal International, http://dx.doi.org/10.1093/gji/ggv132.
Publisher: Royal Astronomical Society; Deutsche Geophysikalische Gesellschaft; European Geophysical Society, Oxford University Press (OUP)

Abstract

The H/V spectral ratio has emerged as a single station method within the seismic ambient noise analysis field by its capability to quickly estimate the frequency of resonance at a site and through inversion the average profile information. Although it is easy to compute from experimental data, its counter theoretical part is not obvious when building a forward model which can help in reconstructing the derived H/V spectrum. This has lead to the simplified assumption that the noise wavefield is mainly composed of Rayleigh waves and the derived H/V often used without further correction. Furthermore only the right (and left) flank around the H/V peak frequency is considered in the inversion for the subsurface 1D shear wave velocity profile. A new theoretical approach for the interpretation of the H/V spectral ratio has been presented by Sánchez-Sesma et al. (2011a). In this paper, the fundamental idea behind their theory is presented as it applies to receivers at depth. A smooth H/V(z, f) spectral curve on a broad frequency range is obtained by considering a fine integration step which is in turn time consuming. We show that for practical purposes and in the context of inversion, this can be considerably optimized by using a coarse integration step combined with the smoothing of the corresponding directional energy density (DED) spectrum. Further analysis shows that the obtained H/V(z, f) spectrum computed by the mean of the imaginary part of Green's function method could also be recovered using the reflectivity method for a medium well illuminated by seismic sources. Inversion of synthetic H/V(z, f) spectral curve is performed for a single layer over a half space. The striking results allow to potentially use the new theory as a forward computation of the H/V(z, f) to fully invert the experimental H/V spectral ratio at the corresponding depth for the shear velocity profile (Vs) and additionally the compressional velocity profile (Vp) using receivers both at the surface and in depth. We use seismic ambient noise data in the frequency range of 0.2 - 50 Hz recorded at two selected sites in Germany where borehole information is also available. The obtained 1D Vs and Vp profiles are correlated with geological log information.

Results from shallow geophysical experiment are also used for comparison.
Keywords: Inverse theory; Interferometry; Site effects.

3.1 Introduction

Characterizing subsurfaces with sediment cover is of importance in seismic hazard analysis, civil engineering and exploration seismology. This is quantitatively done by determining the average 1D shear (Vs) and/or compressional (Vp) wave velocity. Depending of the geological setting, the sediment thickness can vary from few centimeters to hundreds of meters. The determination of the distribution of geophysical parameters down to those depths is thus required for any geotechnical activity (Vs), microzonation (Vs) and exploration seismology (Vs, Vp).

Over the past few decades, seismic ambient noise (SAN) has shown to be a valuable tool for deriving the Vs profile on a broad depth range of the subsurface taking advantage of its broad frequency content. It is primarily done by inversion of the dispersion characteristic of the propagating surface wave. For an overview, see Tokimatsu et al. (1992). When processing the vertical component of the recorded SAN, two factors influence the spectrum of the dispersion curve estimate: The frequency of resonance of the site and the array aperture. Fäh et al. (2008); Poggi & Fäh (2010); Poggi et al. (2012) show that close to the frequency of resonance of the site, the energy on the vertical component is vanishing. This limitation can be overcome using the energy from the horizontal component (Fäh et al., 2008; Poggi & Fäh, 2010; Poggi et al., 2012). For sites with thick sediment cover, a broad spectrum of the dispersion curve can be obtained by using arrays of increasing aperture (Woods & Lintz, 1973; Asten & Henstridge, 1984). Another possibility is to compliment the SAN dispersion curves with those from Multichannel Analysis of Surface Waves (MASW) in a combined inversion (Park et al., 2005).

Using SAN, we can obtain a direct estimate of the frequency of resonance in unconsolidated sediment structures by interpreting the spectrum of the ratio of the horizontal to vertical (H/V) component of the noise wavefield (Nakamura, 1989; Bard, 1998; Bonnefoy-Claudet et al., 2006b). The interpretation of the H/V spectra in terms of Rayleigh wave ellipticity (Yamanaka et al., 1994; Konno & Ohmachi, 1998) also allows potentially the derivation of 1D shear wave velocity profiles (Yamanaka et al., 1994; Fäh et al., 2003; Arai & Tokimatsu, 2004). Given the trade-off between shear wave velocity and depth, additional constraints may be necessary for a unique interpretation of the derived Vs profile.

Recent advances in the use of SAN for site investigation combine the array dispersion curve and the H/V spectral ratio curve in a joint inversion for better estimation of the shear wave velocity profile (e.g. Scherbaum et al., 2003; Arai & Tokimatsu, 2005; Parolai et al., 2005; Picozzi & Albarello, 2007; Hobiger et al., 2013). The latter provides better results but is mainly limited by the assumption about the nature of the noise wavefield and therefore the forward model to compute the H/V spectrum.

Here we focus on the H/V part only and show that, with additional information from the receiver at depth, the H/V method can be used to reliably estimate the seismic velocity profile down to the strong impedance contrast. Although the number of sites with both surface and borehole station is still limited, the number is on the rise (e.g. Kik-Net, International Continental Scientific Drilling Program-ICDP, local sites, etc.). The increase in the availability of seismic data from receivers at the surface and at depth (e.g. Kik-Net, ICDP program and local sites) makes possible a joint interpretation of H/V spectral curves and to jointly invert those data for well resolved shear and compressional wave velocity profile. A joint inversion requires a model which can simulate the H/V spectrum both at the surface and at depth. The model should also take into account the contribution from both the body and surface waves.

By using a diffuse wave field assumption, the initial work by Sánchez-Sesma et al. (2011a) for modeling the microtremor H/V for receivers at the surface is extended to include receivers at depth. A short review of the existing methods for H/V interpretation together with their limitations for simulating the noise

wavefield is presented. The principle idea of the full H/V modeling as it extends to receivers at depth is then presented. Based on the diffuse wavefield theory and assuming the source and the receiver are the same, the energy density of the displacement in each of the orthogonal directions, hereafter referred to as directional energy density (DED), is derived by correlating a component of the displacement field with itself. This has been shown to be proportional to the imaginary part of the Green's function (Sánchez-Sesma et al., 2011a). Perton et al. (2009) showed that in a three dimensional homogeneous elastic half-space, there is an equipartition of the energy for the horizontal components of the displacement, i.e. the radial and transverse component of displacement have energy densities in fixed proportions. This energy corresponds to the medium's response to an impulse load and accounts for energy contribution from all seismic wave types as suggested by Sánchez-Sesma et al. (2011a).

For the virtual sources and receivers located in the deep space, the local structure is mainly illuminated by body waves. Kawase et al. (2011) tested this idea on both theoretical and on observed strong motion data in Japan and concluded that the inversion of a 1D structure could be accomplished by adopting the proposed theory for earthquake H/V spectral ratios. Ducellier et al. (2013) went ahead and inverted those strong motion data for the shallow subsurface structure at selected sites in Japan.

Focusing on the microtremor H/V for a medium illuminated by random sources located at the surface or at shallow depth, we consider a simple one layer over half space earth model and compute the spectral DED for frequencies up to 50 Hz and the corresponding H/V(z, f) spectra. The DED for this model is then compared to the results for a homogeneous half space. A good stability of the derived H/V(z, f) spectrum is obtained for broad frequency range by considering a fine integration wavenumber step. This is in turn time consuming for inversion purposes. We then applied a spectral smoothing to the derived DED using a weighting function proposed by Konno & Ohmachi (1998). Synthetic tests are then performed by inverting the obtained H/V spectrum. We first considered a surface station alone in the inversion. The second test assumes in addition to the surface station spectrum, a spectrum computed at depth. Results indicate more constrain on the final results and an almost perfect recovery of the initial model. Other tests are performed using a two and seven layers over a half-space model. Finally we apply the model to real SAN data from selected sites in Germany where both surface and boreholes data are available.

3.2 H/V(z, f) interpretation

The inversion of geophysical observables for structural properties requires a model which can explain the data and correlate with the geological formation. For the inversion of the microtremor H/V spectral ratio, there are mainly:

1. The inversion of the derived H/V spectrum based on the assumption that it originates purely from surface waves.

2. The complete modeling of the microtremor directional energy density and the inversion of the full H/V wavefield spectrum for the medium properties.

3.2.1 H/V(z, f) interpretation using surface wave assumption

Seismic sources at the origin of the SAN wavefield are usually unknown. They could well be originating from any combination of horizontal and vertical load forces at the Earth surface or at shallow depths. By neglecting the body wave contribution, a forward model which accounts for both Rayleigh and Love wave contribution is required (Arai & Tokimatsu, 2004). This consideration has been applied (e.g. Scherbaum et al., 2003; Arai & Tokimatsu, 2004; Parolai et al., 2005) to derive the shear wave velocity profiles in

sedimentary basins. E.g. Scherbaum et al. (2003) use equal contribution from both Rayleigh and Love wave while Arai & Tokimatsu (2004) use a ratio of 0.7 between Rayleigh and Love waves. Many studies have attempted to quantify the proportion of Rayleigh and Love in the microtremor H/V. Bonnefoy-Claudet et al. (2006b) investigated the origin of the H/V peak frequency and found that at least 50 % of Love waves contribute to the H/V peak amplitude; Endrun (2011) also partially found the same results. Köhler et al. (2006) used a modified 3C spatial autocorrelation method and found that Love waves contribute at least 70 % to the H/V maximum amplitude. Although Rayleigh and Love wave contributions vary with frequency and from site to site, they also lack the quantification of the body wave contribution.

The polarization technique might appear useful in this case because of the possibility to extract the ellipticity of microtremors wavefield. The main motivation lies behind the interpretation of the H/V spectral ratio in terms of Rayleigh wave particle motion (Konno & Ohmachi, 1998) and its potential information content about the underground structure. Basically, three techniques exist for the polarization analysis. The first uses the time frequency analysis method. Here by applying a continuous wavelet transform method to a three component seismic noise time series, mostly Rayleigh waves can be extracted (NERIES, 2010). The second uses the random decrement technique to suppress the energy contribution from waves other than Rayleigh (Hobiger et al., 2013). None of the methods retrieves the very strong amplitude of the ellipticity which in theory is characteristic of the impedance contrast. Additionally, they require a tuning of some parameters to reach a high stability (Wavelet parameters for the time frequency method or the window length for the random decrement technique). The third method on the other hand uses array techniques and the attempt also provides higher modes ellipticity information (Poggi & Fäh, 2010; Maranò et al., 2012; Hobiger et al., 2012). An alternative is to focus on the model which could account for energy contribution from all wave types as suggested by Sánchez-Sesma et al. (2011a).

3.2.2 H/V(z, f) interpretation using the imaginary part of the Green's function

It has been shown that the cross-correlation of random fields recorded at two seismic receivers is proportional to the Green's function between the receivers-pair (e.g. Lobkis & Weaver, 2001; Shapiro & Campillo, 2004; Snieder et al., 2007; Gouédard et al., 2008b; Stehly et al., 2008). Lobkis & Weaver (2001) demonstrates that in the vicinity of a free surface, a diffuse acoustic field may legitimately be regarded as a sum of incoherent, isotropic and homogeneous independent plane waves incident upon the surface together with their respective outgoing reflections. The partition of the energy for the free surface for a homogeneous half-space is studied by Weaver (1985) and compared to the irradiance which now refers to as imaginary part of the Green's function (Sánchez-Sesma et al., 2011b). Prior to this, Miller & Pursey (1955) derived the power radiated by a normal point force acting at the surface and showed that 68 % of the energy consists of Rayleigh waves whereas the S- and P-waves contribution is 26 % and 6 % respectively. Sánchez-Sesma et al. (2011b) summarizes the previous study and complements with the case of a horizontal force acting at the surface of a homogeneous half-space. Here most of the energy is radiated as SH waves (60 %), Rayleigh and SV waves with 18 % and 16 % respectively and only 6 % for body P-wave. Perton et al. (2009) alternatively attempt to derive the energy contribution from each individual wave type using auto-correlation of random field incident at a free surface of a homogeneous half space. Results show that indeed there is equipartition of the directional energy density for P, SV, SH in the deep space.

Sánchez-Sesma et al. (2011a) extended this study to the case of a layered medium and derived the microtremor H/V model for receivers at the surface. This is now modified and applied to receivers at

depths. In comparison to the initial algorithm (surface station only), the in-depth microtremor H/V(z, f) spectral ratio assumes the virtual source located at depth. With the consideration that the source and the receiver are at the same location, the H/V($\mathbf{X}$,f) spectrum at a given point $\mathbf{X} = \mathbf{X}(r, \theta, z)$ can be computed using Equation 3.1 (Sánchez-Sesma & Campillo, 2006a; Sánchez-Sesma et al., 2011a).

$$\begin{aligned} H/V(\mathbf{X}, f) &= \sqrt{\frac{E_1(\mathbf{X}, f) + E_2(\mathbf{X}, f)}{E_3(\mathbf{X}, f)}} \\ &= \sqrt{\frac{Im[G_{11}(\mathbf{X}, \mathbf{X}, f)] + Im[G_{22}(\mathbf{X}, \mathbf{X}, f)]}{Im[G_{33}(\mathbf{X}, \mathbf{X}, f)]}} \end{aligned} \tag{3.1}$$

Where

$$\begin{aligned} E_m(\mathbf{X}, f) &= \rho\omega^2 \langle u_m(\mathbf{X}, f) u_m^*(\mathbf{X}, f) \rangle \\ &= -2\pi\mu E_s k_S^{-1} Im[G_{mm}(\mathbf{X}, \mathbf{X}, f)] \end{aligned} \tag{3.2}$$

is the directional energy density spectrum at a point $\mathbf{X}$ along a polarization direction $m = 1$, 2 or 3. No summation is implied for the repeated indices. ρ is the layer density and ω the angular frequency. $u_m(\mathbf{X})$ is the displacement field at the load point $\mathbf{X}(r, \theta, z)$ in cylindrical coordinates along the polarization direction m; μ is the shear modulus. $E_s = \rho\omega^2 s^2$ is the average energy density of shear waves and is an estimate of the strength of the diffuse illumination. s^2 is the average spectral energy density of shear waves. $k_S = \dfrac{\omega}{V_S}$ is the shear wavenumber. V_S the shear wave velocity of the medium. The asterisk symbol $*$ stands for the complex conjugate and the angular brackets for the azimuthal average. In equation 3.1 and 3.2, G_{mm} represents the medium response in the direction m to an impulse load acting in the same direction.

The analytical expressions for the imaginary part of the Green's function for both the vertical and the horizontal load cases with $r = 0$ and $\theta = 0$ in the j^{th} layer are given by Equation 3.3 for the horizontal component and by Equation 3.4 for the vertical component (see appendix Sánchez-Sesma et al., 2011a).

$$\begin{aligned} Im[G_{11}(0,0,z,f)] \quad = \quad Im \Bigg\{ \int_0^\infty \{ & A_{2j-1} \exp[i\gamma_j(z - z_{j+1})] + A_{2j} \exp[-i\gamma_j(z - z_j)] \\ & + B_{2j-1} i\nu_j \exp[i\nu_j(z - z_{j+1})] - B_{2j} i\nu_j \exp[i\nu_j(z - z_j)] \\ & + \{ C_{2j-1} \exp[-i\nu_j(z - z_j)] + C_{2j} \exp[i\nu_j(z - z_{j+1})] \} \frac{k}{2} dk \Bigg\} \end{aligned} \tag{3.3}$$

$$\begin{aligned} Im[G_{33}(0,0,z,f)] \quad = Im \Big\{ \int_0^\infty \{ & A'_{2j-1} i\gamma_j \exp[i\gamma_j(z - z_{j+1})] - A'_{2j} i\gamma_j \exp[-i\gamma_j(z - z_j)] \\ & + B'_{2j-1} k^2 \exp[i\nu_j(z - z_{j+1})] + B'_{2j} k^2 \exp[-i\nu_j(z - z_j)] \} dk \Big\} \end{aligned} \tag{3.4}$$

$i = \sqrt{-1}$ stands for the unit imaginary number. Within the j^{th} layer, the odd coefficients A_{2j-1}, B_{2j-1}, C_{2j-1}, A'_{2j-1} and B'_{2j-1} represent the amplitudes of up-going waves; the even coefficients A_{2j}, B_{2j} , C_{2j}, A'_{2j} and B'_{2j} represent down-going waves amplitudes. These constants are introduced by solving the Helmholtz equations associated with the displacement potential. The coefficients A_{2j-1} and A_{2j} are associated with the Helmholtz solution for P-waves assuming a horizontal load is applied; B_{2j-1} and B_{2j} to the solution for the corresponding SV-waves. C_{2j-1} and C_{2j} are associated with the SH-wave solution. A'_{2j-1} and A'_{2j} are associated with the Helmholtz solution for P-waves in the case where a vertical load is applied; B'_{2j-1} and B'_{2j} the corresponding Helmholtz solution for SV-waves. All coefficients are obtained

by numerically solving the corresponding boundary value problem, i.e, the displacement and the stress field continuity at the layer interfaces, the free surface condition as well as the radiation condition. γ_j and ν_j are the vertical P- and S-wave wavenumbers in the j^{th} layer. They are given by equations 3.5 and 3.6 respectively.

$$\gamma_j = \sqrt{\frac{\omega^2}{V_{P_j}^2} - k^2} \tag{3.5}$$

$$\nu_j = \sqrt{\frac{\omega^2}{V_{S_j}^2} - k^2} \tag{3.6}$$

k is the radial wavenumber and ω is the angular frequency as given in Equation 3.7. ω is modified by adding a small imaginary constant ω_I (here we use 0.1 throughout the study) in order to shift the poles of the integrand slightly away from the real wavenumber axis k (Bouchon & Aki, 1977).

$$\omega = 2\pi f - \omega_I i \tag{3.7}$$

The attenuation of seismic P- and S-waves energy is quantified by introducing the quality factor Q_P and Q_S for P- and S-waves respectively. Equation 3.8 gives the approximated expression of the seismic velocities taking into account the attenuation (See Equation 135, p165, Müller, 1985). Note that the inverse of the quality factor corresponds to the coefficient of internal friction.

$$\begin{aligned} \frac{1}{V_{P_j}} &= \frac{1}{V_{P0_j}} \left(1 - \frac{i}{2Q_{P_j}}\right) \\ \frac{1}{V_{S_j}} &= \frac{1}{V_{S0_j}} \left(1 - \frac{i}{2Q_{S_j}}\right) \end{aligned} \tag{3.8}$$

For numerical integration, the integral in Equations 3.3 & 3.4 are transformed into a summation by assuming an infinite number of sources distributed along the horizontal axis, at equal interval L (Bouchon & Aki, 1977). L defines the integration step $dk = \frac{2\pi}{L}$ and is subsequently called the integration parameter.

The implementation results for a single layer over half-space are presented in the next section and additional results can be found in the appendix section.

3.2.3 Synthetic inversion: The neighborhood algorithm and the misfit function

We make use of the improved direct search neighborhood algorithm (NA; Wathelet, 2008) to sample the parameter space and to invert the H/V spectral curve. It is a derivative-free (as compared to linearized methods Menke, 1989; Aster et al., 2011) stochastic search method for finding models of acceptable data fit in a multidimensional parameter space (Sambridge, 1999). The NA belongs to the same class of global optimization similar to the genetic algorithm and the simulated annealing (see Sambridge & Mosegaard, 2002 for a review of these two methods, Monte Carlo Methods in general and examples of application in geophysics over the past few decades). The NA differs from other Monte Carlo methods (Uniform Monte Carlo, genetic algorithm, evolutionary programming or simulated annealing) in the sense that it uses information from all previous model samples (Sambridge, 1998).

We start with a set of $n_{s0} = 50$ random samples in the parameter space for which the misfit function defined by Equation 3.9 is known. The NA makes use of the Voronoi concept (Voronoi, 1908) to partition the parameters space into cells, where each cell is the nearest neighbor region in a parameters space subject to an appropriate distance norm. In each step, $n_s = 50$ new models are generated and added to the best previous models. Then, the best $n_r = 50$ are retained as the area in which $n_s = 50$ new models are generated in the next iteration (i.e. inside their Voronoi cells). A total number of 50 steps

$h(m)$	$Vp(m/s)$	$Vs(m/s)$	$\rho(kg/m^3)$	Q_P	Q_S
25	500	200	1900	50	50
∞	2000	1000	2500	100	100

Table 3.1: A one layer over half space earth model used to compute the directional energy density of Figure 3.2 (a)-(d) and the corresponding H/V(z, f) spectra of the Figure 3.2 (e)-(h). It corresponds to Model M2.1 from the SESAME (2004a) project.

(maximum number of iterations) is considered and the complete inversion process repeated at least four time to ensure a good sampling (exploration and exploitation) of the parameter space.

$$hvmisfit = \sum_{j=1}^{M} \frac{1}{M} \sqrt{\frac{1}{N} \sum_{i=1}^{N} \frac{(log(\frac{H}{V}_{m_{ij}}) - log(\frac{H}{V}_{d_{ij}}))^2}{\sigma_{d_{ij}}^2}} \tag{3.9}$$

Where N is the total number of frequency point defining the observed $\frac{H}{V}_d$ and modeled $\frac{H}{V}_m$. $\sigma_{d_{ij}}$ is the standard deviation of observed data at a given frequency point. M is the total number of receivers (surface and at depth). After all iterations have been terminated, a number of best models with given minimum misfit are selected and presented as best possible solution of our inversion.

3.3 Synthetic examples: A one layer over a half-space earth model

3.3.1 Directional energy density and H/V(z, f) modeling

A one layer over a half-space is a simple physical model representative of a soft-soil. The main characteristic is the impedance contrast of S-wave between the surface layer and the bedrock. The soft layer is made up of unconsolidated material and the S- wave particularly has velocity much less compared to that of the bedrock. Any incoming seismic energy is easily trapped in the layer. The physical model we consider here (Table 3.1) has an impedance contrast of approximately 7 for S-waves. This simple model has already been extensively used in site effect related studies (e.g. SESAME, 2004a; Bonnefoy-Claudet et al., 2006a; Poggi & Fäh, 2010; Maranò et al., 2012). and it is represented by a homogeneous layer overlaying a homogeneous half-space. Each layer is characterized by the P- and S-wave velocity, the corresponding attenuation coefficients, the density and the thickness; the latter is infinite for the half space (Table 3.1). The P- and S-wave attenuation parameters are equal for each layer as the effect (not shown here) on the low frequency part of the forward computation of the DED is small for Q values not too low (Qs $>$ 50).

We use the new theoretical model to compute the directional energy density. The latter is plotted against the absolute depth (see Figure 3.1). The Figure 3.1(a) is meant to illustrate the energy density in the different orthogonal directions together with the total energy for a frequency of 3.1 Hz. The energy for the horizontal and vertical directions are also represented at additional frequencies (see Figure 3.B.2 in the appendix). The total energy at all those frequencies is presented in Figure 3.1(b). Here it is interesting to note that with increasing frequency, more surface waves (Rayleigh and Love) modes energy are excited and superimposed to body waves energy. Another interesting feature is that for the considered depth range, and for the chosen layer parameters, the energy is mainly trapped in the soft layer. In comparison to the results for a homogeneous half-space (Weaver, 1985; Perton et al., 2009) considered as a Poisson solid (see Figure 3.B.1 in the appendix) there is very little energy in the deep space for all principal directions. Next we modeled the energy spectrum at different depths for the considered model (Table 3.1). The spectral

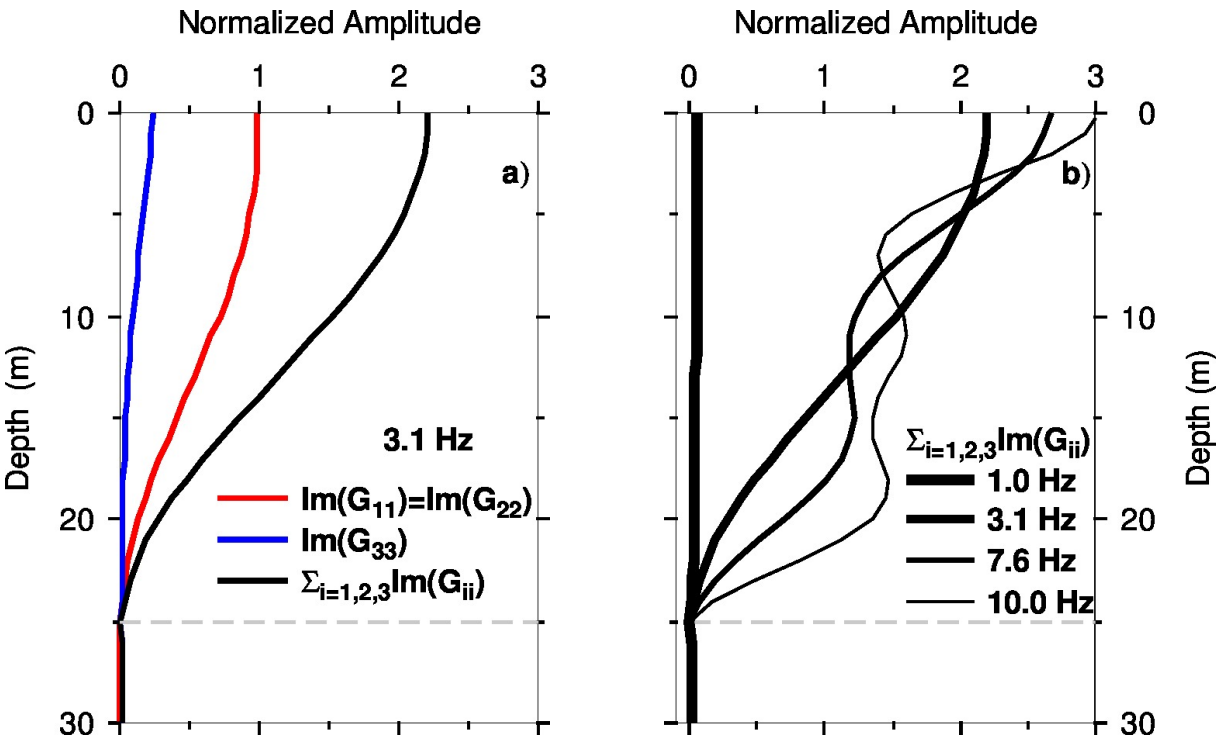

Figure 3.1: Sensitivity of the total directional energy density over depth with changes in frequencies for a one layer over a half-space earth model. a) illustrates the contribution from the horizontal, $\mathrm{Im}(G_{11})$, and vertical , $\mathrm{Im}(G_{33})$, direction to the total energy, $\mathrm{Im}(G_{ii})$, at 3.1 Hz. b) shows the total energy for different frequencies up to 10 Hz. The dashed gray line at 25 m depth represents the sediment-bedrock interface.

seismic energy response for different components of the displacement with L = 1 000 000 are plotted in Figure 3.2(a)-(d). Comparison with the energy density for L = 50 000 indicates small instabilities at low frequencies for small L (in this case mainly for receivers at depth). This is smoothed out using an appropriate spectral smoothing filter (Konno & Ohmachi, 1998). The DED are normalized at each frequency with the energy of the full (homogeneous) elastic space at the corresponding frequency and whose parameters are defined by the first layer.

The corresponding H/V(z, f) spectrum are presented in Figure 3.2(e)-(h). The H/V spectrum at different depths is also compared to the spectrum for a smaller L value. Comparison for L = 1 000 000 and L = 50 000 indicates small instabilities at low frequencies for small L (see also Figures 3.C.5 & 3.C.10 for a two and seven layers over a half space respectively). On the other hand, L = 1 000 000 is stable on a broad frequency but computationally intensive. Figure 3.A.1 shows the computational time for up to 13 layers over a half space. Here we see that the computational time advantage is clear when using a lower L integration parameters. It is considerably reduced by a factor of more than 10. By combining a coarse wave number integration step *dk* (corresponding to a small smoothing (Konno & Ohmachi, 1998), the instability could be suppressed. A more efficient choice of parameters will require further scrutiny.

We further test the new method by comparing the synthetic H/V spectrum for the surface receiver with those obtained using different available seismological tools. Figure 3.3 compares the H/V spectral ratio computed assuming (1) the 1D transfer function (TF) for vertically incident SH-waves, (2) the ellipticity assumption, (3) The arithmetic sum of (1) and (2) labeled TF + Ell, (4) the reflectivity method (Wang, 1999), and (5) the directional energy density approach (Sánchez-Sesma et al., 2011a). For the reflectivity method, a synthetic noise wavefield is obtained assuming a random source distribution to a maximum epicentral distance of 5 km and at a maximum depth of 5 km. As Figure 3.3 (and Figure 3.D.1 for receivers at depth) show there is a close, however not a perfect match between the DED and H/V computation

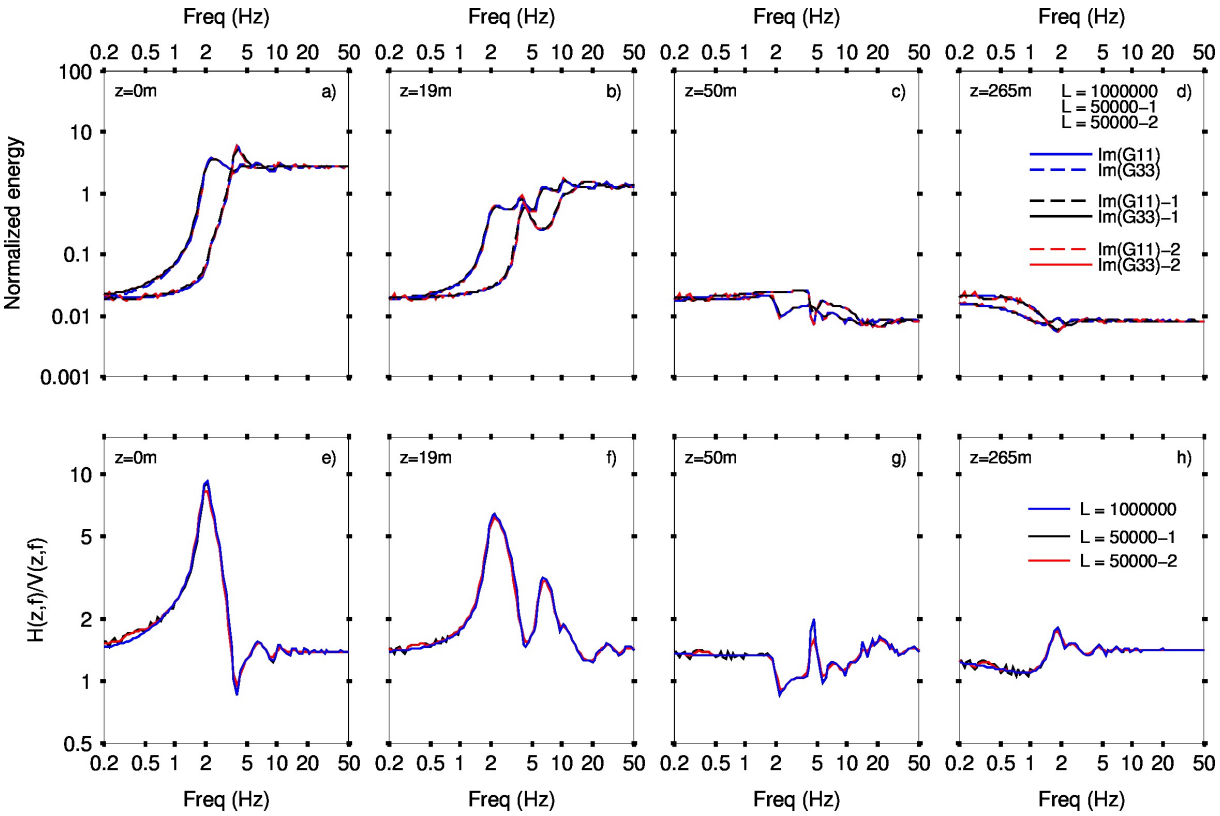

Figure 3.2: a-d) Green's function energy computed using the synthetic model of Table 3.1. The effect of the filter (black curve, L = 50 000) is visible in low frequency in comparison to the unsmoothed with L = 50 000 (red curves) or with L = 1 000 000 (blue curves). e-h) H/V spectral ratio computed at different depths using the synthetic 1LOH model of Table 3.1 (SESAME, 2004a). The smoothed and unsmoothed H/V spectral ratio are plotted together for comparison. L = 50 000 is considered as the integration parameter. Note that in this study L = 50 000 is the value for which the full H/V is recovered after spectral smoothing. The effect of the filter is pronounced around 4 Hz for the receiver at 50 m depth; see g).

from noise synthetics obtained from reflectivity method (Wang, 1999). The differences may be attributed to the assumptions regarding source distribution or possible wave field contributions due to near field terms and will be subject to further investigations.

3.3.2 Inversion of synthetic data

The synthetic inversion is applied on the H/V computed at selected depths (Figures 3.2a & 3.2b) using the model M2.1 (See Table 3.2 for parameters value). For the selected depths, we assume a measurement uncertainty of 20 % in log(H/V) ratio (log normally distributed estimate).

$Thickness(m)$	$Vp(m/s)$	$Vs(m/s)$	$\rho(kg/m^3)$
1-100	200 - 1500	50 - 500	1700 - 2700
∞	1000 - 4500	500 - 3500	1700 - 2700

Table 3.2: Parameter space range used for the inversion of the synthetic H/V(z, f) at selected depths (see Figure 3.2e-h). The synthetic H/V(z, f) were computed using the canonical model M2.1 (SESAME, 2004a).

For the global inversion, the parameter ranges as given in Table 3.2. We first invert the microtremor H/V spectrum computed at the surface and then combine the synthetic surface spectrum together with

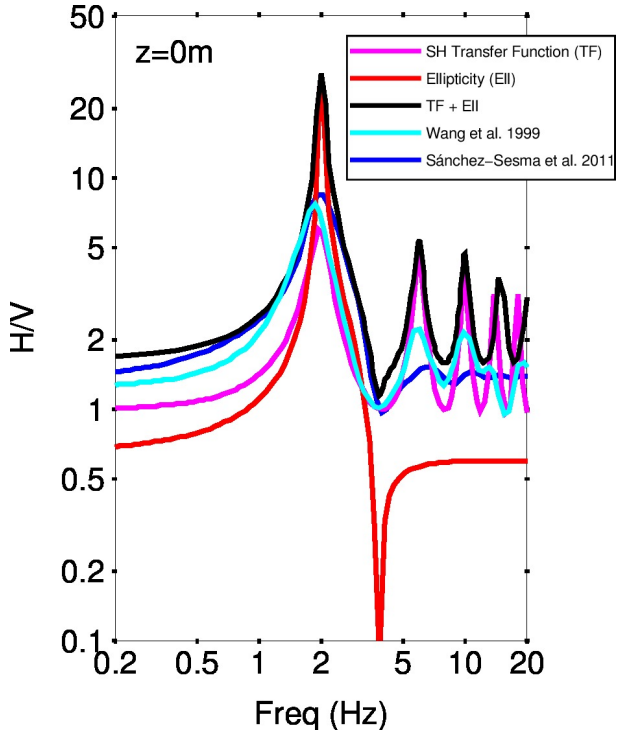

Figure 3.3: H/V spectral ratio computed at the surface using the synthetic model of Table 3.1 (integration parameter L = 50 000). The amplitude spectrum of the energy is smoothed before the ratio is computed. The resulting H/V spectral curves using different techniques are presented. The SH transfer function is calculated with the geopsy software (`http://www.geopsy.org/`; last accessed February 23, 2017), the ellipticity is calculated following Herrmann (2002), full wavefield seismograms are computed with the reflectivity method (Wang, 1999) and the smoothed imaginary part of the Green's function (Sánchez-Sesma et al., 2011a). Note that the fundamental frequency is recovered for all methods. In addition to body waves contributions, higher modes are observed with full wavefield modeling techniques.

the synthetic spectrum for receivers at depth. For the surface station alone, the final best model is off by nearly a factor of 2 for velocity and layer thickness (see Figure 3.4) with respect to the known model. Taking into account a synthetic H/V spectrum for a receiver at depth adds more constraint and provides the expected results (see Figure 3.5). The test performed using the H/V spectrum computed at different depths is able to provide information regarding the sediment-bedrock interface as compared to the single surface station inversion alone. This result shows that additional information for a successful inversion of H/V curves at the surface is needed. Our results indicate that an H/V curve at depth can provide this information. Also of particular interest would be the combination of the full H/V spectrum together with dispersion curves, but this is out of the scope of the current analysis. Another remarkable result in this synthetic study is that the shear wave velocity, Vs, in the bedrock is reasonably well retrieved (Figure 3.5). Also reasonably well retrieved is the compressional wave velocity, Vp, both in the soft layer and in the bedrock. For other inversion techniques (e.g. dispersion curves, ellipticity, autocorrelation coefficient), this is not so straightforward.

The performance of the nonlinear inversion algorithm is illustrated by the convergence to the optimal parameter value (see lower panel Figure 3.4-3.5) . The exception is for the density which shows little or no convergence to the expected value. Inversion for additional depths with the one layer over the half space model at 6 m, 25 m, 50 m and 265 m are presented in the appendix, Figures 3.C.1-3.C.4.
For a receiver as deep as at 6 m depth (Figure 3.C.1), the best seismic parameters are already sensitive to the true sediment-bedrock depth and also to the expected seismic parameters. This can be explained by noting that for the considered frequency range, we do have a significant change in the shape (at high

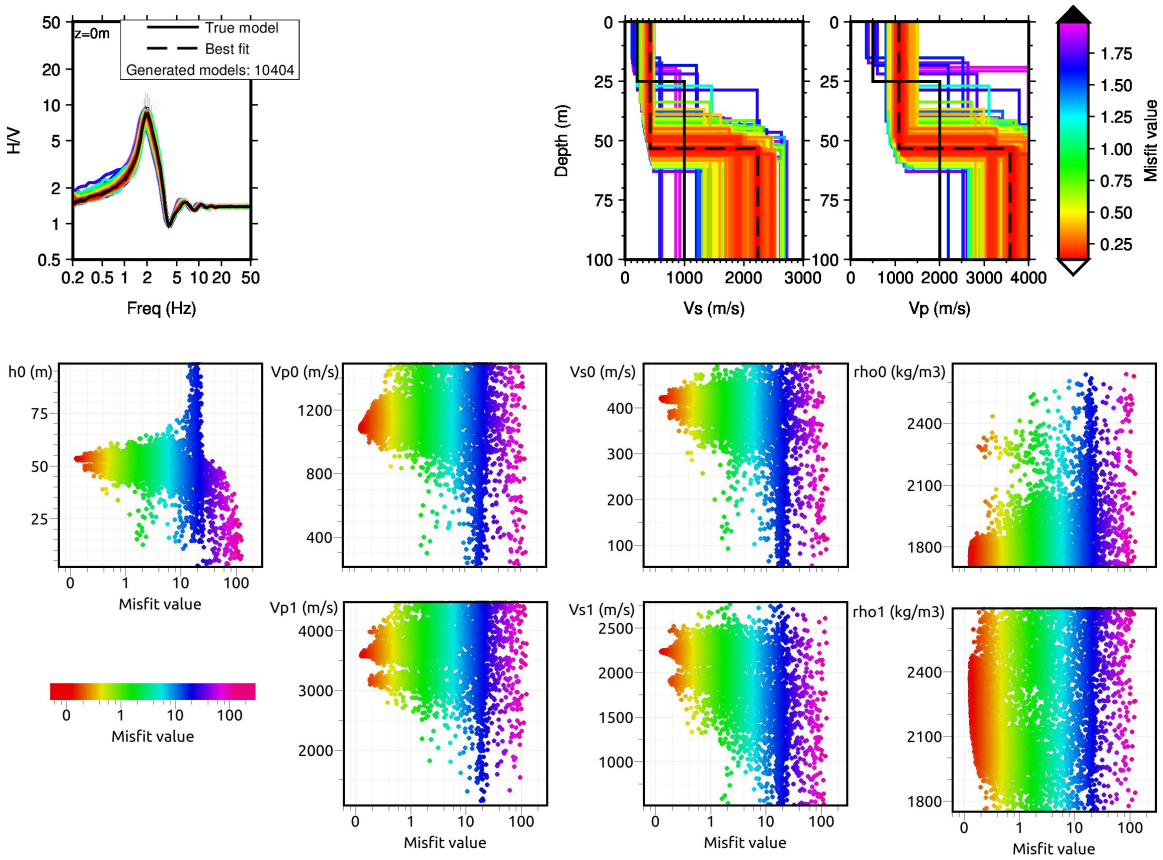

Figure 3.4: Synthetic data inversion assuming a single station located at the surface (z = 0 m). The first panel (first row) shows the fitting of the synthetic model. The initial H/V spectrum assumes an uncertainty of 20 % in the H/V ratio. The best Vp and Vs profiles are off by nearly a factor of 2 as compared to the actual real Vp and Vs profile. The second panel presents the marginal distribution for each individual parameter space (h_0, V_{P0}, V_{S0} and ρ_0 for the first layer and V_{P1}, V_{S1} and ρ_1 for the half space) and simultaneously shows the performance of the used nonlinear inversion approach i.e. the neighborhood algorithm to successfully sample our parameter space.

frequencies) of the H/V spectrum at this depth.
The synthetic test is also performed for a complex model with two and seven layers overlying a half-space. The layers parameters are defined in Table 3.C.1 and Table 3.C.3 respectively.

The Figures 3.C.6-3.C.9 show the results of the synthetic inversion for the two layers over a half-space for receivers at the surface only, the combination of the surface and receiver at 31 m, 150 m and 406 m depth respectively. See Figures 3.C.11-3.C.12 for the seven layers over a half space case. Here again the performance of the single H/V inversion as compared to that with receiver at depth is highlighted.

Based on the synthetic inversion results for the earth models investigated hereinabove, we conclude that improvement of inversion results can be expected if a significant change in the spectral shape of the H/V curve considered at depth, compared to the H/V curve obtained for the surface sensor, is observed. Another feature to point out is the sensitivity analysis of the inversion to the density. The marginal distribution of misfit indicates that the sensitivity to the density is very low. We therefore consider for the practical case a constant density for the different layer.

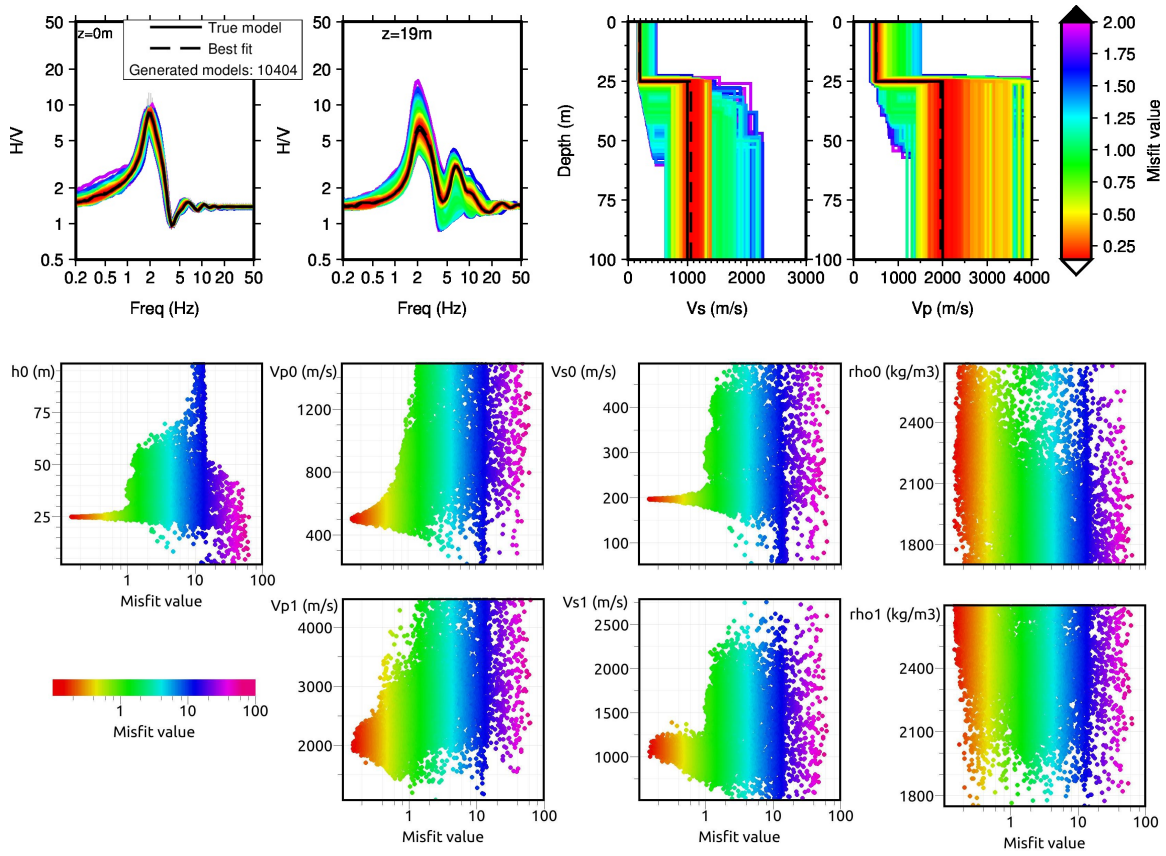

Figure 3.5: Synthetic data inversion for two stations; one at the surface and the second at 19 m depth. The Vp and Vs profiles are well retrieved. Again here the first panel shows the best ensemble solution for the given maximum misfit (see color scale), The second panel shows the performance of the neighborhood algorithm in sampling the parameter space (h_0, V_{P0}, V_{S0} and ρ_0 for the first layer and V_{P1}, V_{S1} and ρ_1 for the half space), the convergence to the true Vp and Vs value and the rather smeared density convergence. Additional synthetic H/V spectrum inversion results with receivers at 6, 25, 50 and 265 m depth can be found in appendix, Figures 3.C.1-3.C.4.

3.4 Test sites, geology, data set and H/V(z, f)

3.4.1 Test sites, geology and Seismic ambient noise data survey

We carried out measurements at the TTS (Testgelände Technische Sicherheit) of the BAM (Federal Institute for Materials Research and Testing) in Horstwalde. It is located approximately 50 km south of Berlin. The very shallow geology consists of glaciofluvial sediments and densely stratified sand with the ground water table at about 3.5 m below the ground. The stations consist of a surface receiver and three permanent 3C boreholes sensors available at the site. Boreholes are at depths of 12 m, 34 m and 41 m for the deepest. The stations names and coordinates are given in Table 3.3 and the site location on Figure 3.6. All sensors are Lennartz LE-3D 1s sensors recording at 1000 Hz. We use Reftek130 as digitizer.

The second selected site is Rethem, located approximately 50 km north of Hannover. The shallow geology also consists of glaciofluvial sediments and densely stratified sand with a sandstone indicated at about 131m below subsurface. The surface station is a 3C Streckeisen STS-2 with a Reftek-130 as digitizer. The borehole sensor, located at 171m depth, is a Guralp CMG-3TB 360s with Guralp CMG-DM24243SEAM as digitizer. Both stations are permanently installed at the site and recording seismic vibration at 100 Hz.

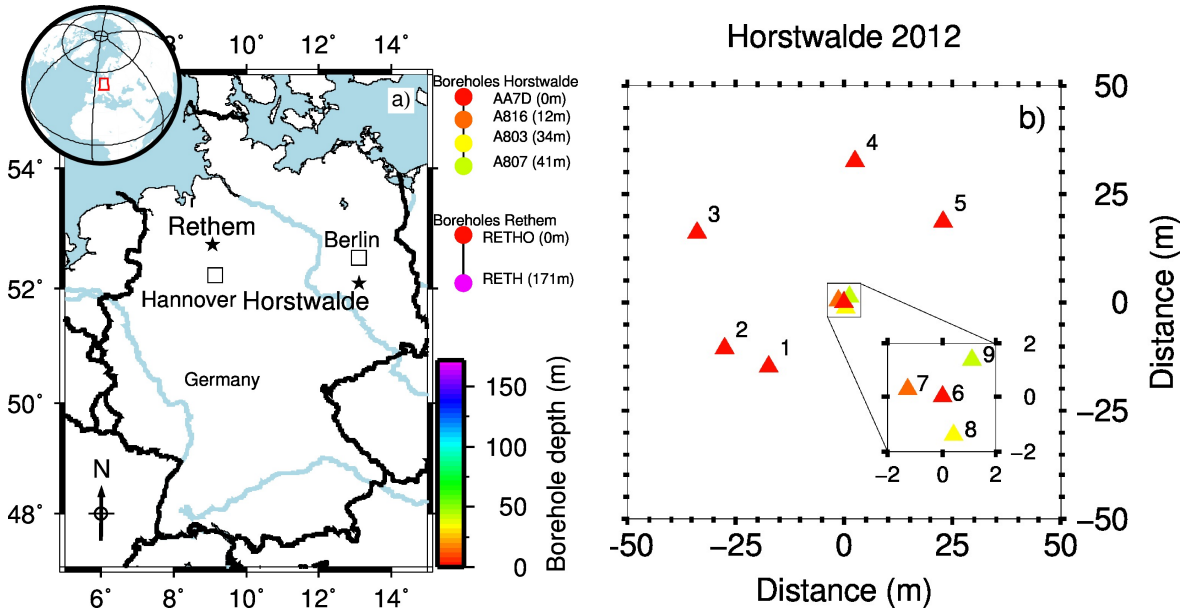

Figure 3.6: a) Map of Germany. The test sites selected for the study are presented. At each test site, the boreholes are presented. The different colors give information regarding the borehole depth. The receivers coordinates are given in Table 3.3. b) Map showing the stations used to compute the spatial variation of the H/V at the test site in Horstwalde during the 2012 seismic campaign. The inset in b) presents the boreholes location around the surface sensor Id 6. The boreholes have sensor Id 7, 8 and 9. They are located at 12, 34 and 41 m depth respectively (see Table 3.3).

Sites	Station	Sensor Id	Net. Code	Lat. (^{o})	Long. (^{o})	Elev. (m)
Horstwalde	AAC0	1	WA	52.09676	13.41795	0
Horstwalde	AADC	2	WA	52.09680	13.41780	0
Horstwalde	AA7B	3	WA	52.09704	13.41771	0
Horstwalde	AADB	4	WA	52.09718	13.41824	0
Horstwalde	AAFB	5	WA	52.09706	13.41854	0
Horstwalde	AA7D	6	WA	52.09689	13.41828	0
Horstwalde	A816	7	WA	52.09689	13.41819	-12
Horstwalde	A803	8	WA	52.09688	13.41824	-34
Horstwalde	A807	9	WA	52.09690	13.41822	-41
Rethem	RETHO		GR	52.738	9.361	0
Rethem	RETH		GR	52.738	9.361	-171

Table 3.3: Test sites name and geographical coordinates (latitude, longitude). The stations names, the sensor Id (used in Figure 3.6b), the network code, the location and the corresponding depth are also given.

3.4.2 Data processing and interpretation

The H/V spectral ratio at each site (see Figure 3.6) is computed for a full day of continuous seismic ambient noise recording. Day and night activities are averaged over the time window to provide a spectral curve which is best representative of the medium under our receiver. Each individual stream is split in windows of 50 periods length. The Fourier spectra are computed for each component of the noise recording followed by a smoothing using the Konno & Ohmachi (1998) with smoothing constant b = 30. Finally the H/V ratio is computed and the average over all windows is presented in Figure 3.7(a)-(b). The comparison of the experimental H/V(z, f) in Horstwalde (Figure 3.7a) and Rethem (Figure 3.7b) shows a significant difference both in the spectral content and with depth. The observed H/V(z, f) curves have a broad peak frequency between 0.5 and 2 Hz for Rethem. A relatively sharp peak frequency is

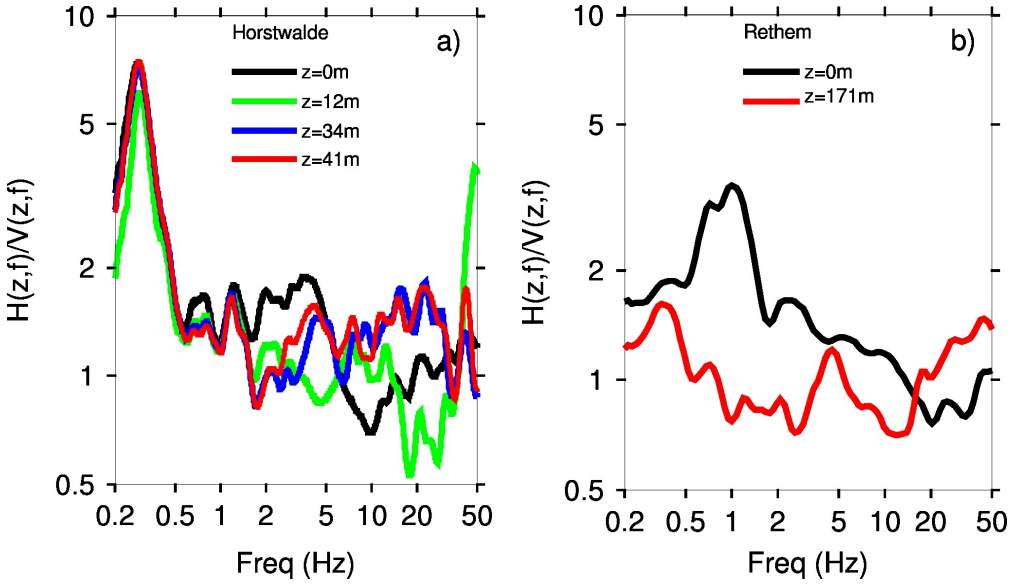

Figure 3.7: H/V spectral ratio for data recorded at the test site in a) Horstwalde and b) Rethem. The standard deviation is omitted for clarity.

instead observed for Horstwalde around 0.3 Hz. The H/V at this site is also well above 2, therefore satisfying the 1D assumption for the interpretation of the observed spectra (SESAME, 2004b). The H/V spectral ratios computed from seismic ambient noise recorded at the TTS site on day 125 of the year 2012 (2012:125) using a small 3C seismic aperture array, 60m, with 6 sensors show on average a high stability (see gray area Figure 3.8a) in the low frequency part (0.2 to 1.5 Hz). At higher frequencies (see Figure 3.8a), between 1.5 and 50 Hz, the mean spectral curves show a significant change in its shape. For a sensor at the surface, we compare the H/V spectrum for one week (2012:125-131 & 2013:184-

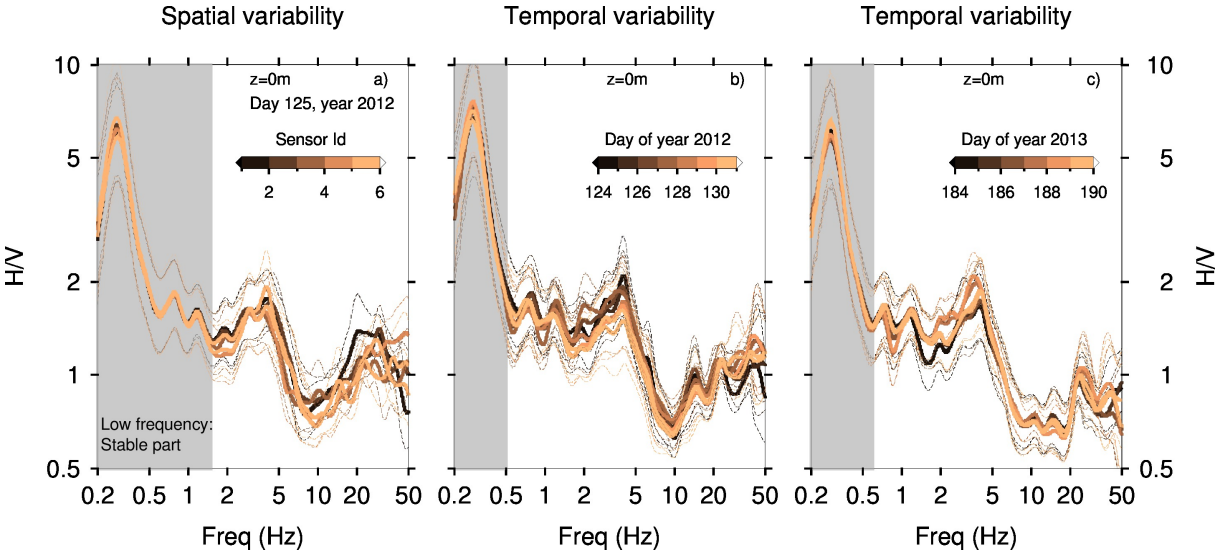

Figure 3.8: Spatial and temporal variation of the H/V spectrum at the TTS, Horstwalde. a) shows the structural variation for the H/Vs spectrum computed from a small, 60m aperture, 3C seismic array of 6 sensors represented here by Id or identity and ranging from 1 to 6. b) and c) show the temporal variations of the H/V spectrum over one week for a station located at the surface, i.e., the H/V computed from 24 hours of SAN measurement and for seven consecutive days, in 2012 & 2013 respectively. The gray area highlights the low frequency and stable part the stable part of the H/V spectrum. The remaining spectrum is associated to the sensitivity to subsurface changes or to the spatial distribution, intensity and typology of the noise sources over time.

190) of the seismic experiment (Figure 3.8b-c). We observe a stable part below 1 Hz (see gray area Figure 3.8b-c). Three possible reasons could explain the changes observed in the H/V spectra. The spatial variation in the subsurface structure (Figure 3.8a), the temporal variation of the structure under the receiver (Figure 3.8b-c), i.e. the ground water table for example, and/or the type and distribution of the noise sources (Figure 3.8b-c). Note that for inversion purposes, an average one day of noise data was stable enough on the considered frequency range given the standard deviation.

3.5 Inversion

3.5.1 Parametrization

At the test site in Horstwalde, shallow active geophysical activities have been conducted and the corresponding geological structure from approx. 4 m (below the ground water table) down to 15 m is well known (e.g. Linder et al., 2010; Schmelzbach et al., 2011; Tronicke et al., 2012; Rumpf & Tronicke, 2014). We considerably lower the possible acceptable range for P-waves velocity in the first meters because of the underlying unconsolidated and dry sand. The geological log down to 577 m depth is also available from a borehole (referred to as Staakow 159/62) located approximately 700m south-east to the site. Using the fundamental frequency of resonance (0.3 Hz) and the empirical relationship available from the literature (e.g. Ibs-von Seht & Wohlenberg, 1999; Gosar & Lenart, 2010) more constraint on the overall sediment thickness can be estimated. The final model considered for the inversion consists of six layers overlaying a half space (see Table 3.4). For the parametrization at the Rethem test site, we also make use of the geological information available from the borehole (referred to as Rethem1). In addition, empirical relationship (e.g. Ibs-von Seht & Wohlenberg, 1999; Gosar & Lenart, 2010) are also used together with the average peak frequency (approx. 1 Hz) for an estimate of the overall sediment thickness. A final parametrization with seven layers over half-space is considered. Table 3.5 shows the final parametrization for this site.

Thickness	$Vp(m/s)$	$Vs(m/s)$
0.1 - 5	500 - 2000	50 - 250
0.1 - 10	500 - 2000	50 - 250
0.1 - 15	1500 - 2000	50 - 250
0.1 - 20	1500 - 2000	50 - 250
0.1 - 100	1500 - 3000	50 - 450
200 - 800	2000 - 3000	50 - 600
∞	2500 - 4500	1500 - 3500

Table 3.4: Parameters range used in the inversion for the Vp and Vs profile at the TTS site in Horstwalde. At this site, 3 3C boreholes seismometers are available at 12 m, 34 m and 41 m depth.

Thickness	$Vp(m/s)$	$Vs(m/s)$
0.1 - 5	200 - 2000	50 - 400
0.1 - 30	500 - 3000	50 - 1000
0.1 - 60	500 - 3000	150 - 2000
0.1 - 100	500 - 3000	150 - 2000
0.1 - 300	500 - 3000	150 - 2000
0.1 - 600	500 - 3000	150 - 2000
100 - 2000	500 - 3000	150 - 2000
∞	1000 - 4000	400 - 3500

Table 3.5: Parameters range used in the inversion for the test site in Rethem. One borehole is available at 171 m depth.

3.5.2 Inversion results

Using the Neighborhood algorithm and the misfit function defined by equation 3.9, the H/V(z, f) curves computed for the test sites in Horstwalde and Rethem (Figure 3.7) are inverted for the subsurface S- and P-wave velocity profiles. The combined inversion for receivers both at the surface and at depth is performed for frequencies ranging from 0.2 to 50 Hz. The set of velocity models explaining our observations at the test site in Horstwalde is presented in the Figure 3.9 and that for Rethem is presented in the Figure 3.10.

Inversion results Horstwalde: geological and geophysical correlation

At this site, the best candidates are plotted for misfit value lower than 1.65 (Figure 3.9). For receivers at 34 and 41m depth, we have a good match of the experimental H/V(z, f) spectra (see Figure 3.9c,d). A noticeable discrepancy is observed around and above 10Hz for the receiver at the surface and at 12 m depth (see Figure 3.9a,b). This could be explained by the restrictive parametrization in the very shallow part. The S- and P-waves velocity profiles indicate a sedimentary cover with an overall thickness of 330 m (see Figure 3.9e,f).

The correlation with the geological log information (Figure 3.9e) indicates that this depth (see Figure 3.9e,f) corresponds to the Miocene silt - upper-Oligocene clay interface. Another interesting outcome is the Pleistocene sand-Miocene silt interface around 100m depth.

The Vp and Vs for the first 30 m are also shown in Figure 3.9(h)-(i). The results indicate a layered structure with the various layers mainly corresponding to sand with color varying from light yellow to dark gray. The structure varies from fine (grain size: 500 μm) to coarse (grain size: 2 mm). The current best profile is compared with the Vs and Vp profiles from inversion of cross-hole P-wave, S-wave, and georadar

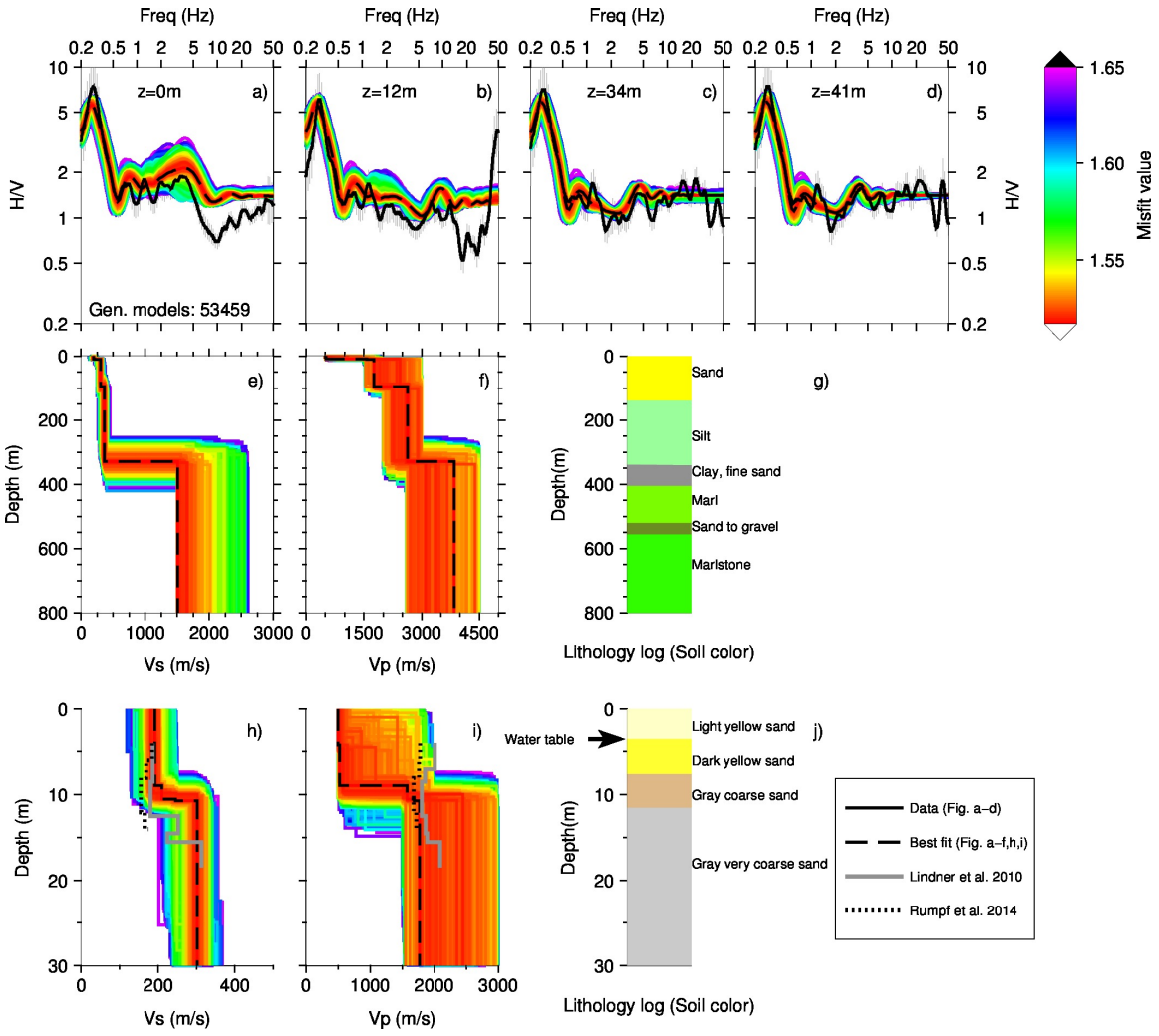

Figure 3.9: Full H/V inversion results for the test site in Horstwalde. An equal weighting factor of (0.25, 0.25, 0.25, 0.25) is used. The set of best models explaining our data are presented for a misfit lower than 1.65. a), b), c) and d) show the best fitting models at 0, 12, 34 and 41 m depth respectively. The corresponding velocity profiles are shown in e) for Vs and in f) for Vp. e) is used for geological correlation. A zoom of e) and f) for the first 30 m are shown in figure h) and i). j) shows the ground truth of the investigated area and is used for geological correlation in the upper 30m.

traveltime data sets (Linder et al., 2010; Rumpf & Tronicke, 2014). For the considered parameters range, we obtain a Vp around 500 m/s for the upper-most surface layer which could well be the velocity in the unconsolidated and dry sand layer.

Inversion results Rethem: geological correlation

At this site, the best candidates are plotted for misfit value lower than 2 (Figure 3.10) and a maximum depth of 300 m. For the receiver at the surface, we have a good match of the experimental H/V(z, f) spectra for frequencies of up to 10 Hz (see Figure 3.10a). For the record at 171 m depth, the fit is less favorable. We note however that for the overall set of acceptable models, a resemblance of the level and trend is observed for frequencies of up to 5 Hz (Figure 3.10). As cause we expect a more complex geological setting at the site deviating from a simple 1D situation. An indication of this may also be seen from looking at the temporal variability of the H/V spectral ratio over a 7 days period (Figure 3.E.1). Results indicate a noticeable change in the complete spectrum of the average H/V curve.

The Vs and Vp velocity profiles indicate a sedimentary cover with an overall thickness of 160 m (see Figure 3.10c). The correlation with the geological log information (Figure 3.10e) indicates that this depth would correspond, based on the Vs velocity information, to the silt - sandstone interface.

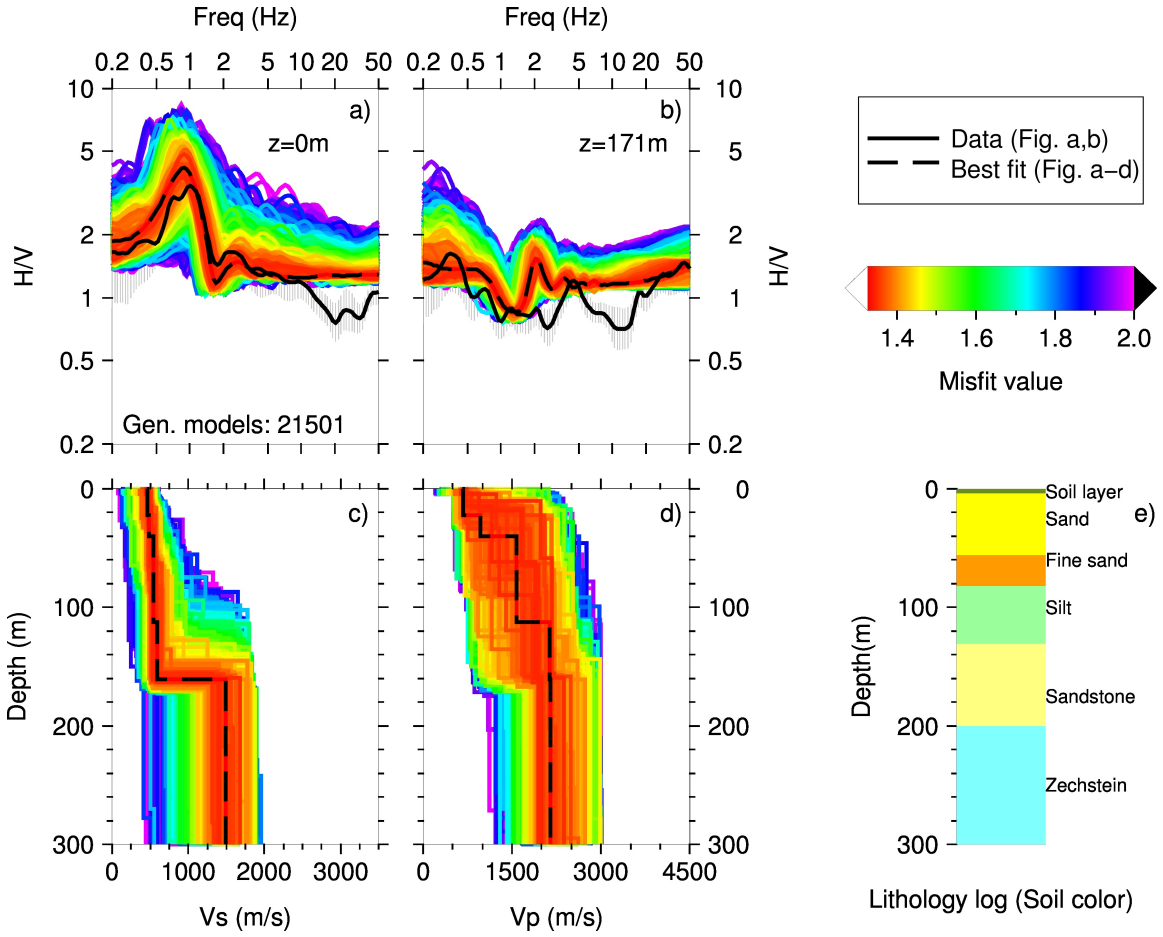

Figure 3.10: Full H/V inversion results for the test site in Rethem. An equal weighting factor of (0.5, 0.5) is used. The set of best models explaining our data are presented for a misfit lower than 2. a) and b) show the best fitting models at 0 and 171 m depth respectively. The corresponding velocity profiles are shown in c) for Vs and in d) for Vp. e) is used for geological correlation.

3.6 Discussion

We have presented the new theoretical development regarding the computation of the full depth dependent microtremor H/V(z, f) spectral ratio as it applies to receivers at depth. Assuming the noise sources are generated at the surface or at shallow depths, we successfully computed the imaginary part of the Green's function at depth with the source and the receiver at the same position. The corresponding directional energy density (DED) helps in deriving the H/V(z, f) for given Earth model parameters.

The modeling of the energy for a one layer over a half-space shows that it is mainly trapped in the shallow subsurface with 25 m thickness. In comparison to the energy profile for the homogeneous case, very little energy propagates in the half-space.

An observation of the H/V spectra at the surface alone does not allow in general situations to retrieve the structure in depth. For simple models like single layer over half-space, the problem is well-known as a trade-off between sediment thickness and average shear wave velocity in the sediment for all wave types (see e.g. Scherbaum et al., 2003; Malischewsky & Scherbaum, 2004). Adding observations from sensors at depth to the inversion problem, however, may significantly reduce this dilemma of non-uniqueness. Whenever the depth observation of the H/V ratio changes significantly in its shape, mostly depending on the fraction of the observation depth versus interface depths, we were able to exploit this additional information to find the underlying model and to reconstruct the subsurface structure. Additional examples for more complex situation with two and seven layers over half-space are shown in the appendix of this paper. Also there we can draw the same conclusion on the value of the H/V observation in depth for finding the true model parameters in the inversion procedure. We note however, that although the final best density profile in this synthetic case looks reasonable, the marginal distribution of misfit shows less sensitivity to the expected density values.

The measured seismic ambient noise in Horstwalde and Rethem show a significant variability in their spectral contents. The H/V spectral curves at different depth in Horstwalde show a strong peak at 0.28 Hz with amplitude well above 2. Here we validated the assumption about the 1D media (SESAME, 2004b). A broad frequency peak between 0.5 to 2 Hz in Rethem shows the heterogeneity of the underlying media and the invalidity of the Rayleigh wave assumption.

In Horstwalde, the overall sediment cover is estimated to be 330 m. Correlation with geological log indicates a Miocene - upper-Oligocene subsurface formation. The shear wave velocity varies between 190 m/s for the surface layer to 1500 m/s below 330 m. The compressional waves velocity varies between 500 m/s to 3850 m/s below 330m.

In Rethem, the overall sediment cover for the first 300 m is presented. The shear wave velocity varies between $\sim$ 500 m/s for the surface layer to 1500 m/s below 160 m. The compressional waves velocity varies between $\sim$ 700 m/s to $\sim$ 2200 m/s below 120 m. The obtained velocity profiles are correlated with geological log information.

The current inversion technique shows a better estimate of the bedrock velocity and depth in comparison to the inversion of dispersion curves only. This can be explained by the broad frequency (0.2 - 50 Hz) spectrum of the H/V been inverted, and also because surface wave inversion very often assume only the fundamental mode of the Rayleigh wave in the inversion.

3.7 Conclusion

Based on the diffuse wavefield theory, this work is the first contribution to our knowledge, of the use of full microtremor H/V(z, f) spectrum for subsurface characterization using an inversion. We successfully obtain the subsurface Vs-profile which is an important parameter in any microzonation study and probabilistic seismic hazard analysis. The method also seems promising to retrieve the P-wave velocity. The

latter potentially provides helpful information necessary to improve the acoustic velocity model building; a key step in any seismic migration. Its high sensitivity to the layering of the medium could then significantly impact on any geotechnical, civil or exploration seismology and precisely the ambiguity related to the layer thickness.

Any drilling program is usually costly, on-site inspection using the current method could help estimate the bedrock interface and help both in the time and the financial cost management. Thus we expect the results of this approach to contribute to studies in geotechnical, civil engineering and seismic exploration applications. As the underground exploration with invasive techniques (drilling) is usually very costly, we can think of the use of H/V(z, f) interpretation as an on-site inspection method that could help to estimate the bedrock interface while drilling and thus contribute to time and financial cost management of drilling operations.

We look forward to applying the method to more test sites to further establish confidence in this approach. Future research will be needed to tackle complex media (including 2D/3D structures).

Acknowledgments

This study was funded by the Geotechnologien program of the BMBF/DFG under grant No. 03G0745A, by the DFG Graduiertenkollegs GRK 1364 and by the Abschluss Promotionsstipendiums of the University of Potsdam. Figures were drawn using the Generic Mapping Tools (`http://gmt.soest.hawaii.edu/`; last accessed February 23, 2017) and a drawing plugging incorporated into geopsy (`http://www.geopsy.org/`; last accessed February 23, 2017). Data from Rethem were obtained from the BGR data archive center and requested via Arclink implemented in the SeisComp3 software. I am thankful to Daniel Vollmer, Lutz Ehlert and Christian Hillemann for assistance during field trip in Horstwalde. Thanks to Michael Krause for his assistance in obtaining the deep geological log information for the test site in Horstwalde. We would like to thank Valerio Poggi and one anonymous reviewer whose comments have helped to improve the quality of the article.

Appendices

3.A Computational time

Figure 3.A.1 gives a comparison of the computational time effort for different layers number over a half-space.

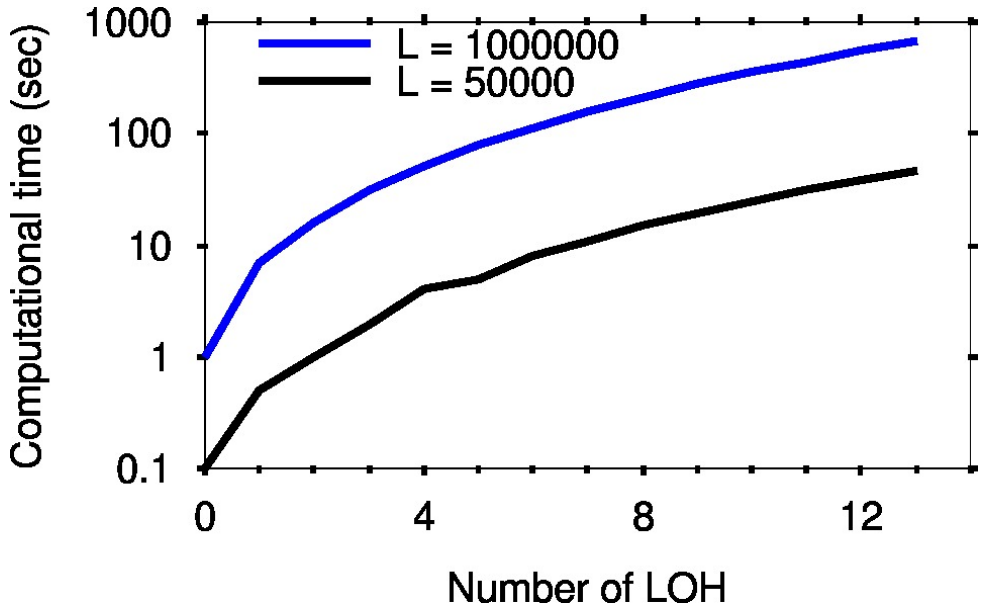

Figure 3.A.1: Computational time for different layers number over a half space. Different L parameters and the corresponding run time. For 13 layers over a half space, the time required for the H/V computation to complete is reduced by a factor of more than 10. The combined use of L = 50 000 with the spectral filter is presented in Figure 3.2e-h and compared with unsmoothed H/V for L = 1 000 000.

3.B Directional energy density: Homogeneous half-space and one layer over a half space

The new theoretical model is applied to a homogeneous half space earth model whose parameters are given in Table 3.B.1. The Vp and Vs are defined such that the Poisson ratio $\nu = 0.25$. For a receiver at

$h(m)$	$Vp(m/s)$	$Vs(m/s)$	$\rho(kg/m^3)$	Q_P	Q_S
∞	1732	1000	2000	50	50

Table 3.B.1: Homogeneous half-space earth model used for modeling the directional energy density. A constant attenuation or quality factor is used for both P and S waves.

the Earth's surface, the directional energy density (DED) is computed and plotted against the normalized depth (Figure 3.B.1). The normalization is with respect to the Rayleigh wave wavelength. For depths larger than $\sim$ 1.5 times the Rayleigh wavelength, there is no contribution from surface waves. At this depth, we obtain an equal energy contribution for all the three directions. These results compare with the previous work on the energy partitioning (Weaver, 1985; Perton et al., 2009).

We also applied the new model to the case of a one layer over a half space model defined in the Table 3.1. The corresponding horizontal, vertical and total energy density plotted against the absolute

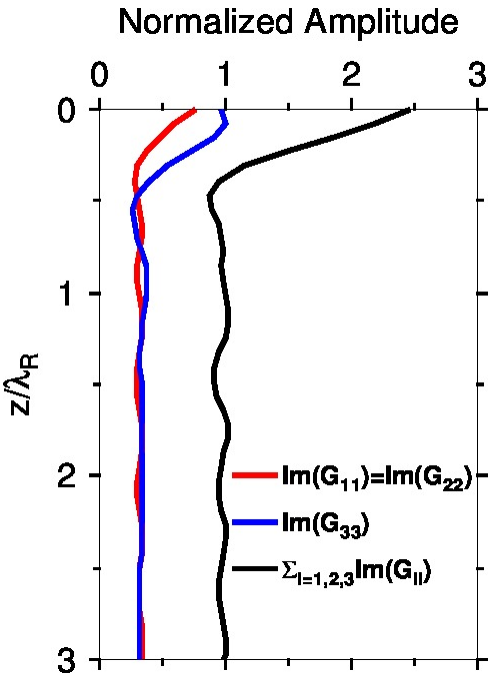

Figure 3.B.1: Normalized energy amplitude over normalized depth for a homogeneous half-space. For depths larger than 1.5 times the Rayleigh wavelength, the energy is equal for the three orthogonal direction.

depth are presented in the Figure 3.B.2. With the increase in the frequency, more surface wave eigenfunctions are excited and their energy superimposed on that of body waves (see also the Figure 3.1-right)

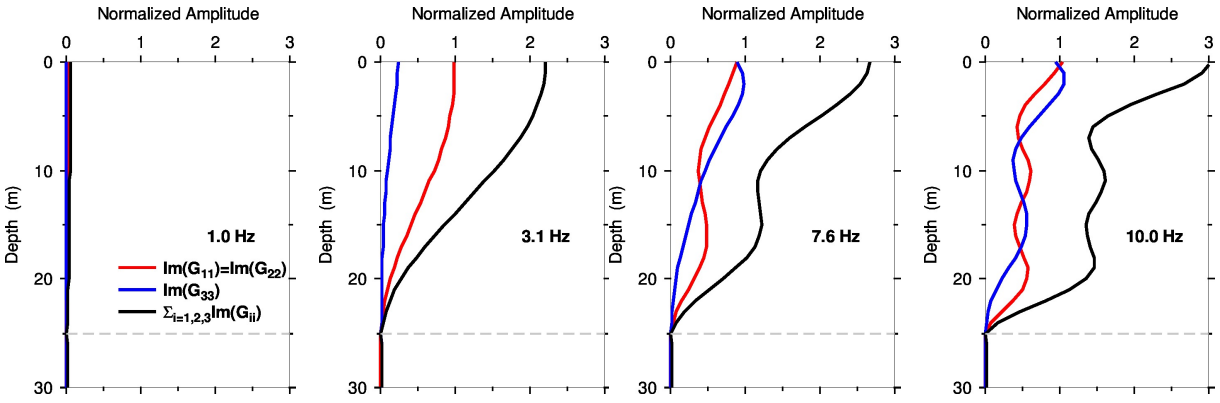

Figure 3.B.2: Normalized energy amplitude over the absolute depth for a one layer over a half-space model defined in the Table 3.1.

For the considered model of the Table 3.1, we modeled the corresponding dispersion curves. The latter indicates that for frequencies below 3 Hz, the surface waves (Rayleigh and Love waves) contribute to the total energy mainly with that of their fundamental and first higher mode and for higher frequencies, higher modes are also excited.

3.C Sensitivity to P and S wave velocities and density (Electronic supplement)

3.C.1 1LOH: model M2.1 with constant density

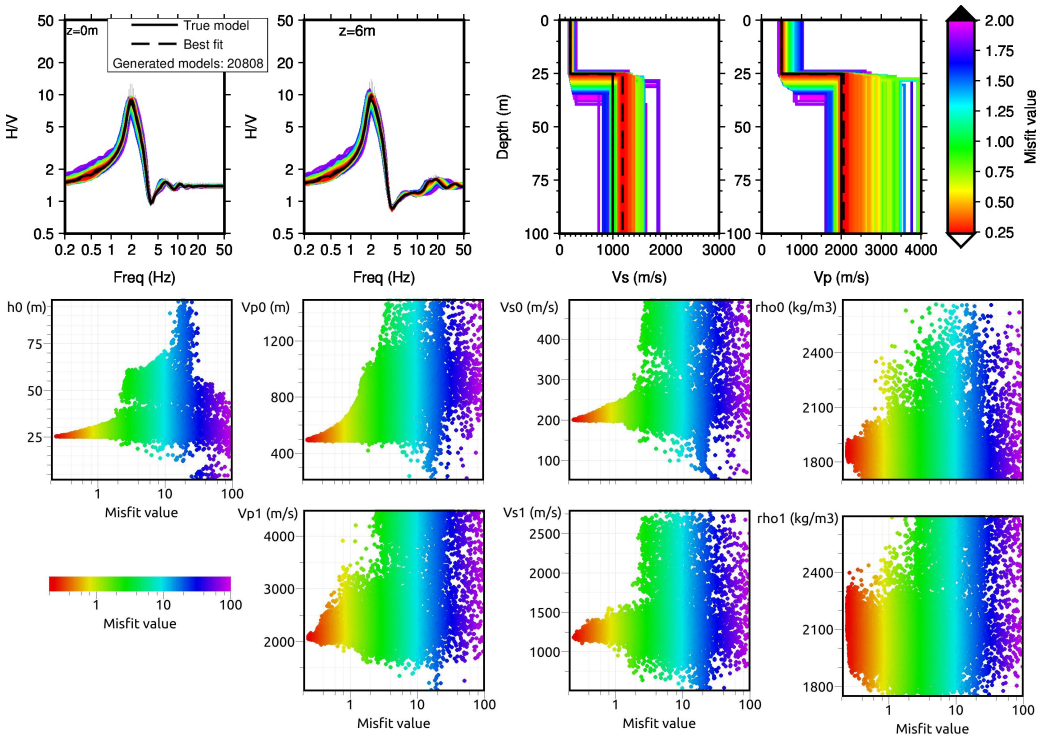

Figure 3.C.1: Synthetic data inversion. Sensitivity analysis for receiver at 6 m depth.

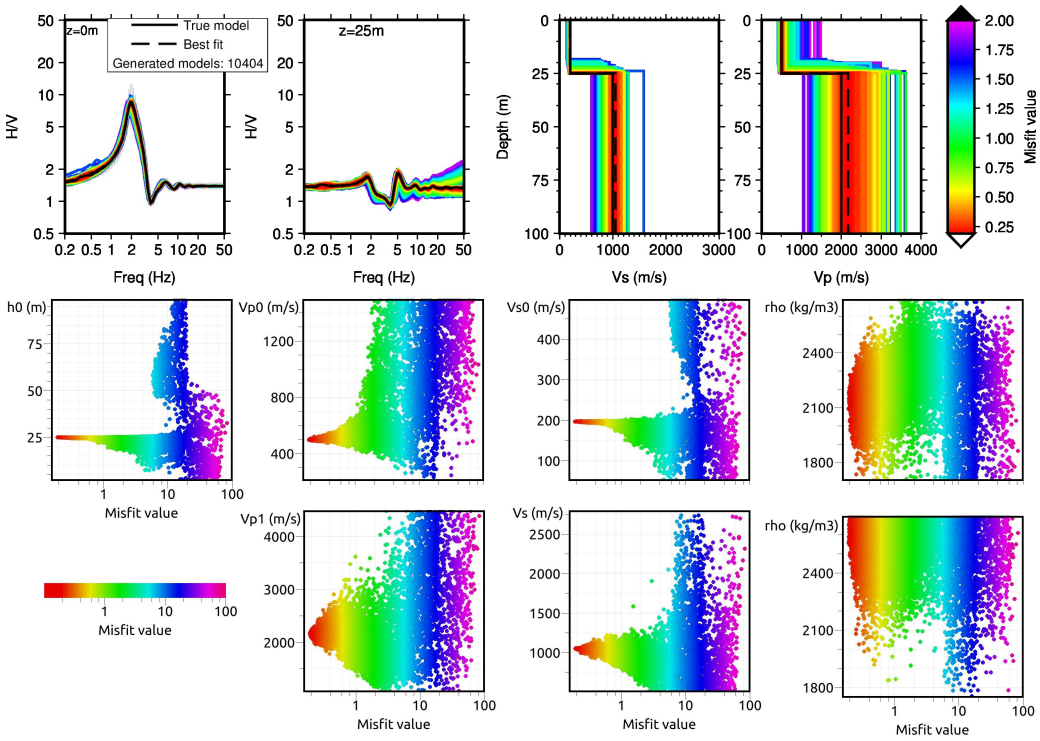

Figure 3.C.2: Synthetic data inversion. Sensitivity analysis for receiver at 25 m depth.

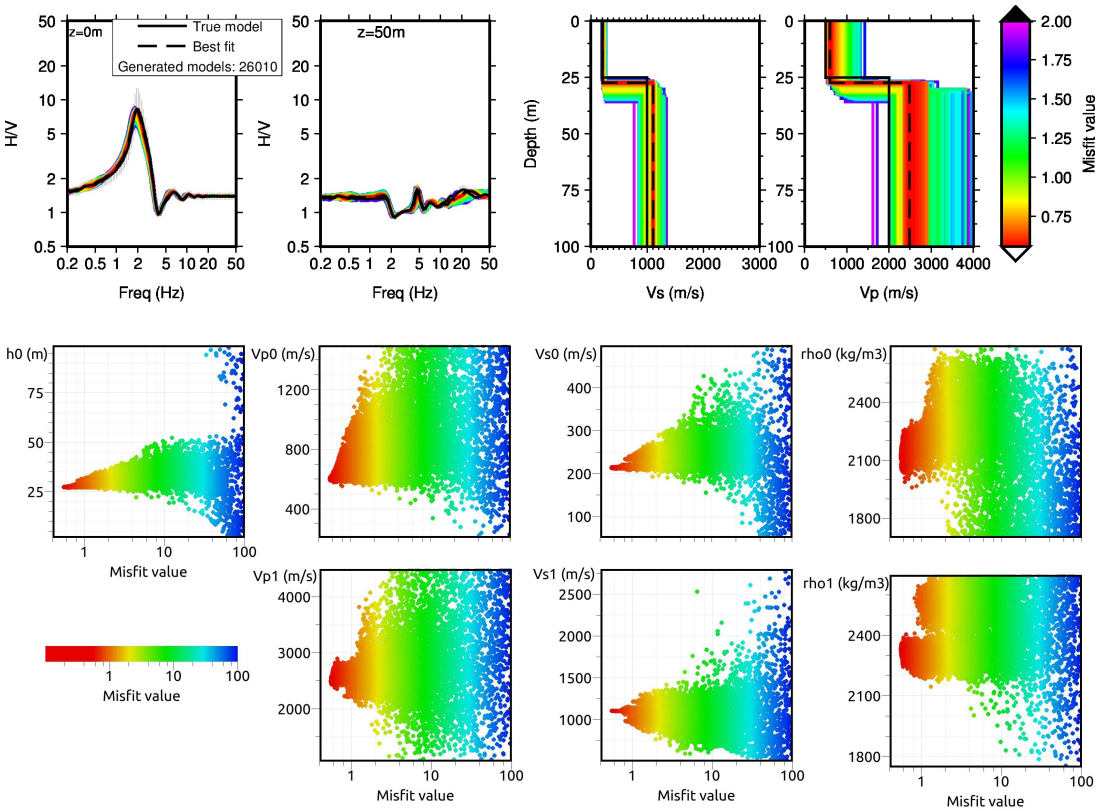

Figure 3.C.3: Synthetic data inversion. Sensitivity analysis for receiver at 50 m depth.

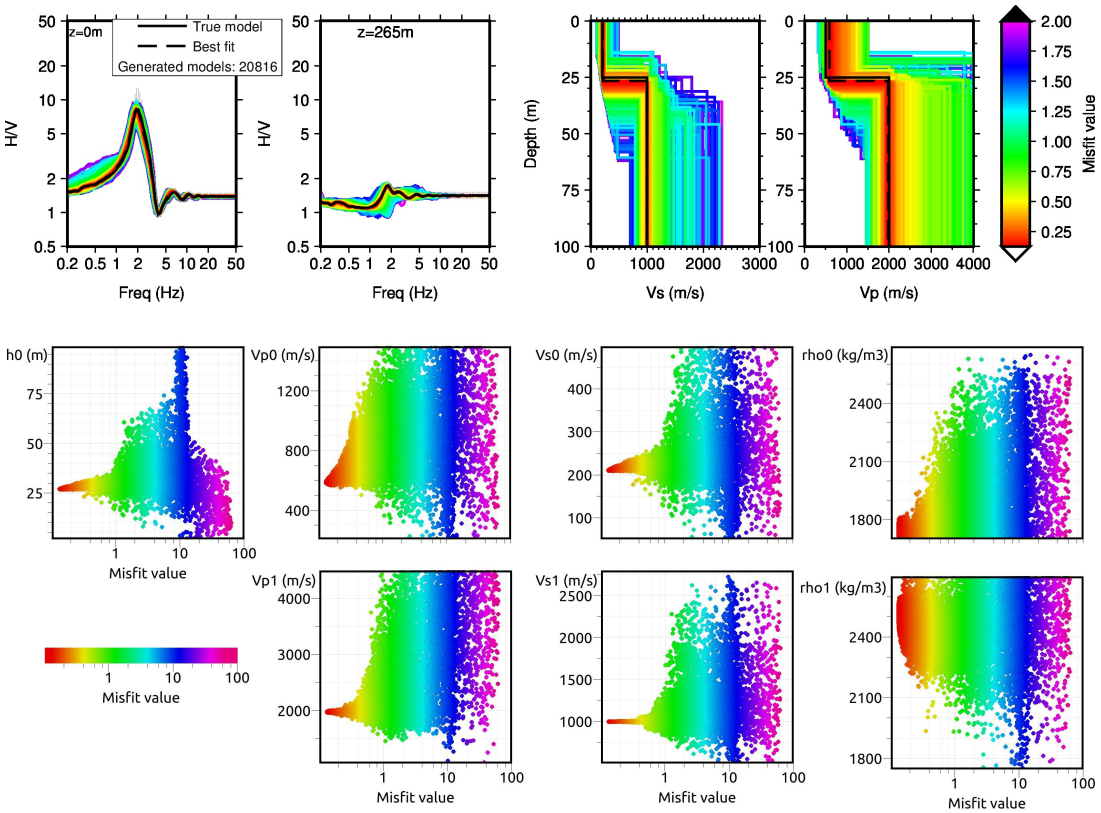

Figure 3.C.4: Synthetic data inversion. Sensitivity analysis for receiver at 265 m depth.

3.C.2 Two layers over a half space model: model M10.1

$Thickness(m)$	$Vp(m/s)$	$Vs(m/s)$	$\rho(kg/m^3)$	Q_P	Q_S
31	500	250	1900	50	50
375	1800	750	2100	100	100
∞	3500	2000	2500	200	200

Table 3.C.1: Parameters definition for a two layers over a half-space model used in the second synthetic inversion test.

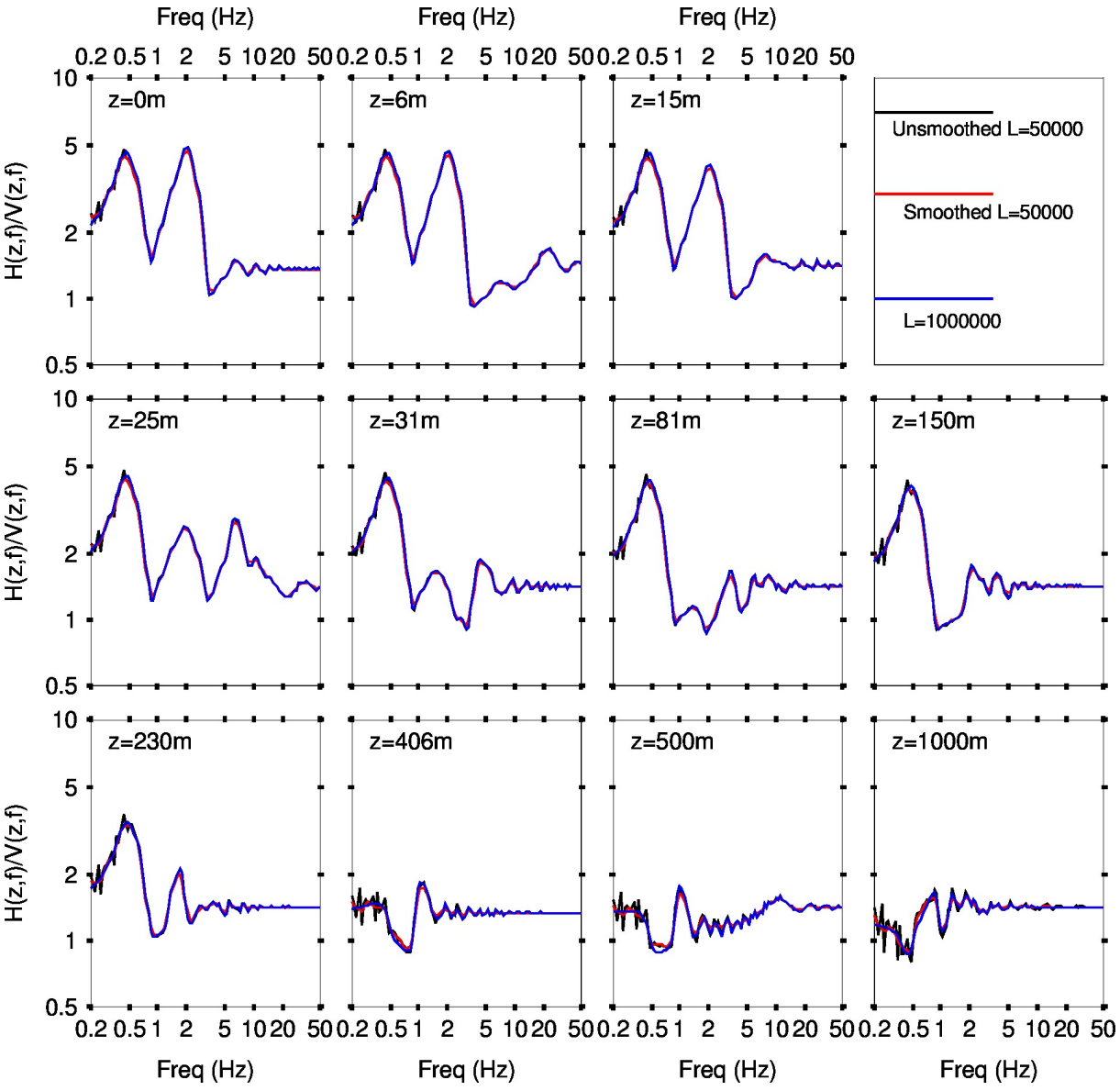

Figure 3.C.5: H/V spectral ratio computed at different depths using the synthetic 2LOH model of Table 3.C.2 (SESAME, 2004a). The smoothed and unsmoothed H/V spectral ratios are plotted together for comparison. L = 50 000 is considered as the integration parameter. Note that in this study L = 50 000 is the value for which the full H/V is recovered after spectral smoothing.

$Thickness(m)$	$Vp(m/s)$	$Vs(m/s)$	$\rho(kg/m^3)$
1 - 100	200 - 1500	50 - 700	1700 - 2700
1 - 1000	200 - 4000	50 - 2000	1700 - 2700
∞	1000 - 5500	500 - 3500	1700 - 2700

Table 3.C.2: Parameters definition for a two layers over a half-space model used in the second synthetic inversion test.

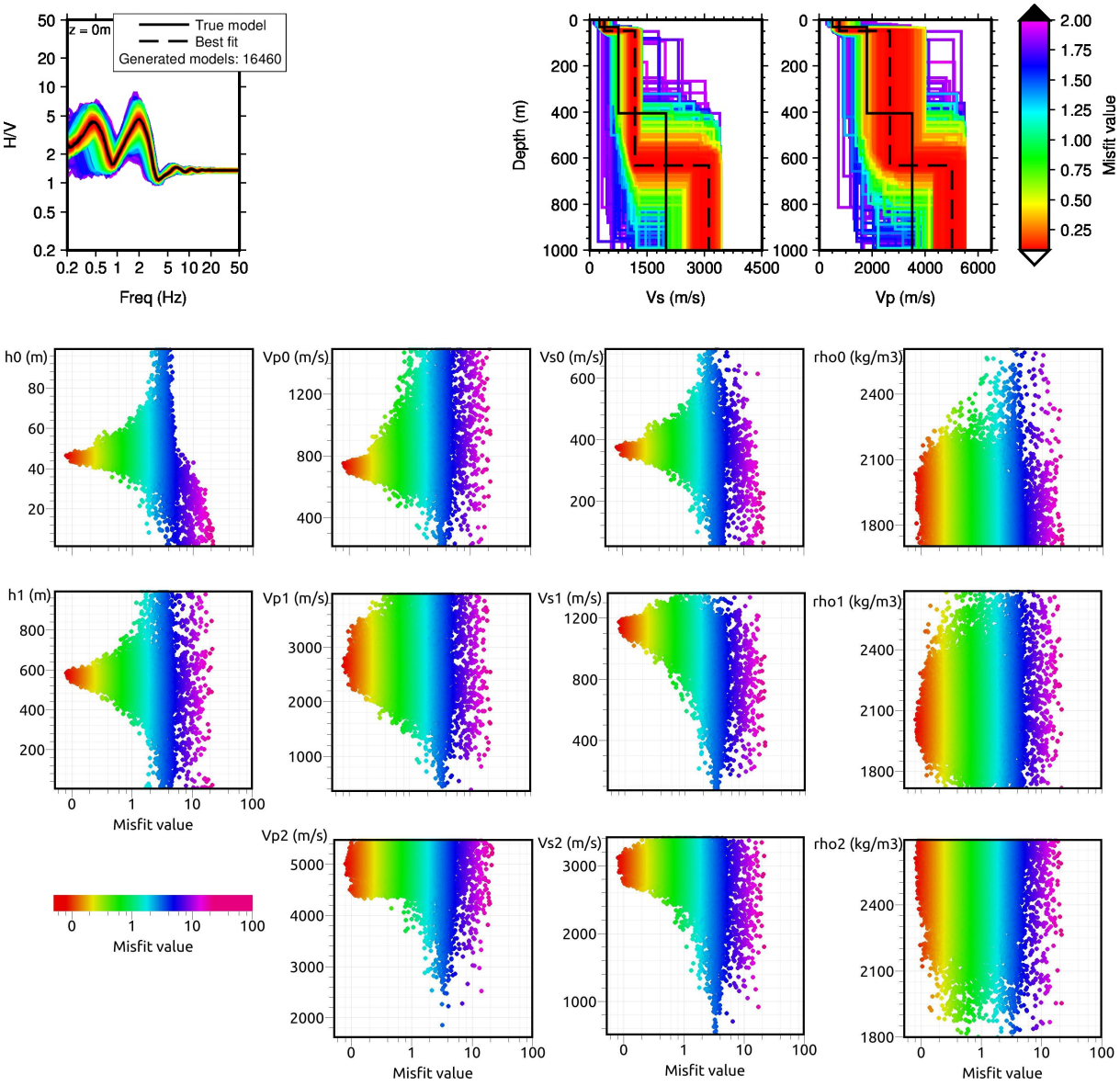

Figure 3.C.6: Synthetic data inversion. Sensitivity analysis for receiver at the surface.

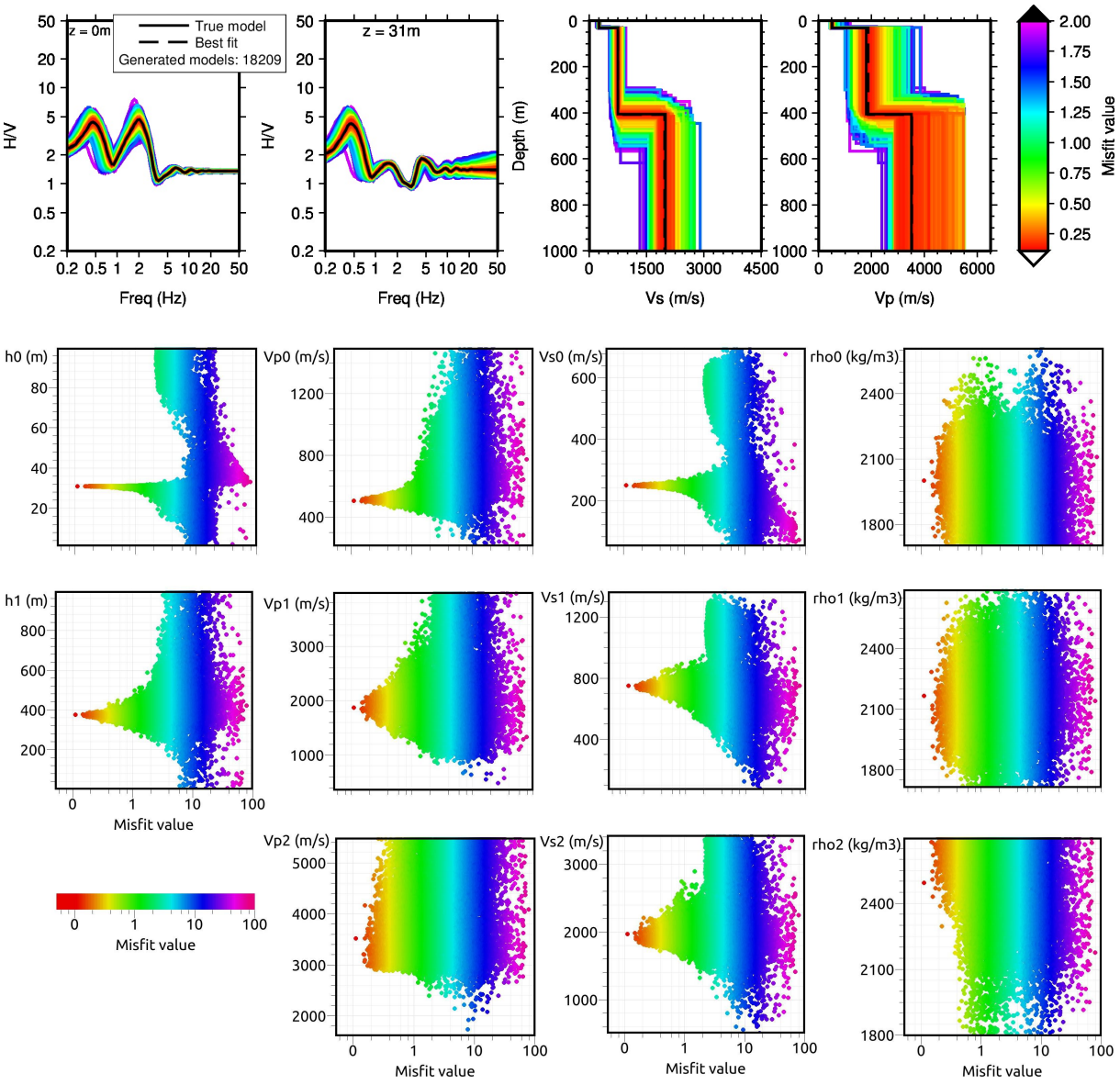

Figure 3.C.7: Synthetic data inversion. Sensitivity analysis for receiver at the 31 m depth.

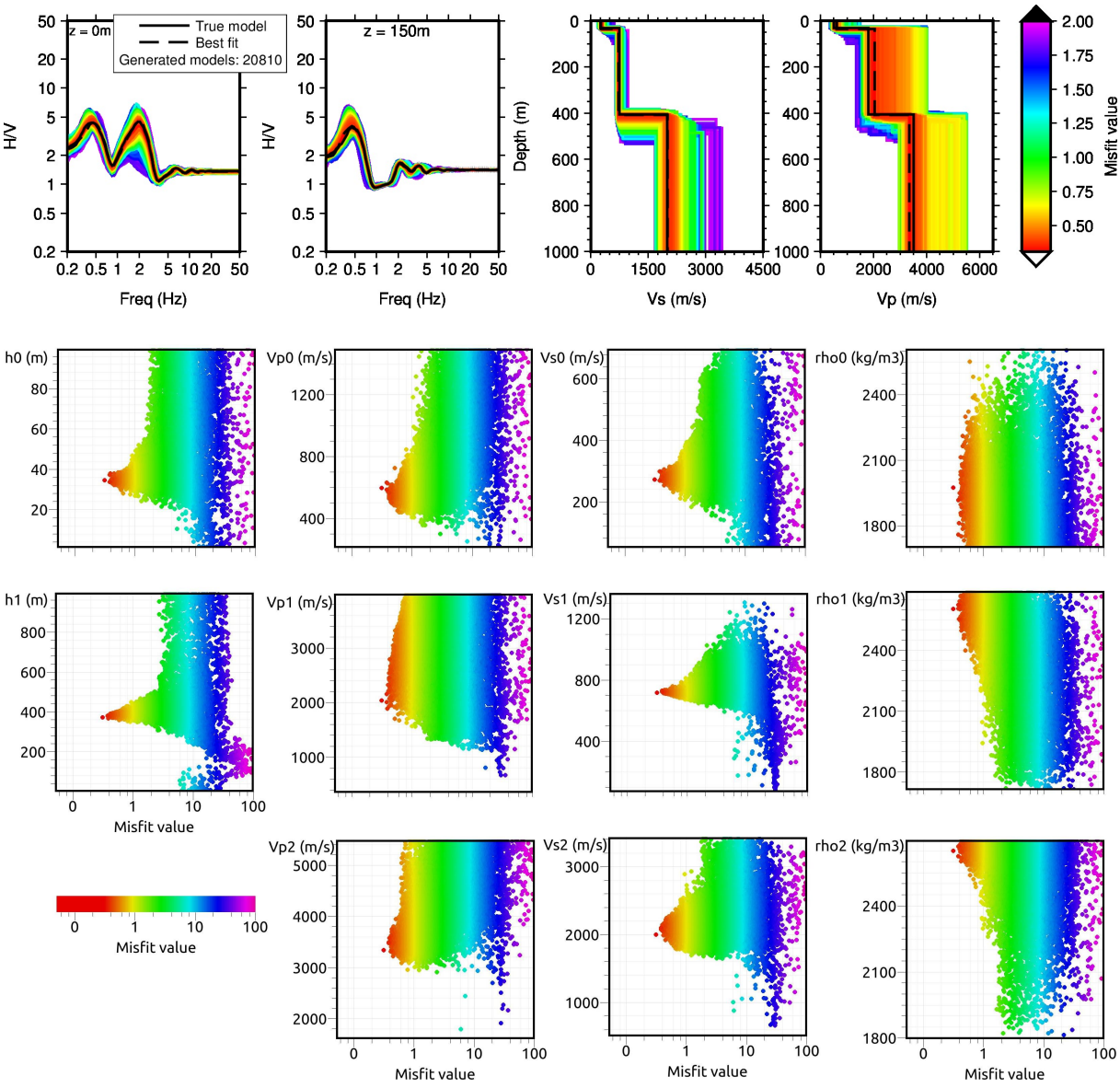

Figure 3.C.8: Synthetic data inversion. Sensitivity analysis for receiver at 150 m depth.

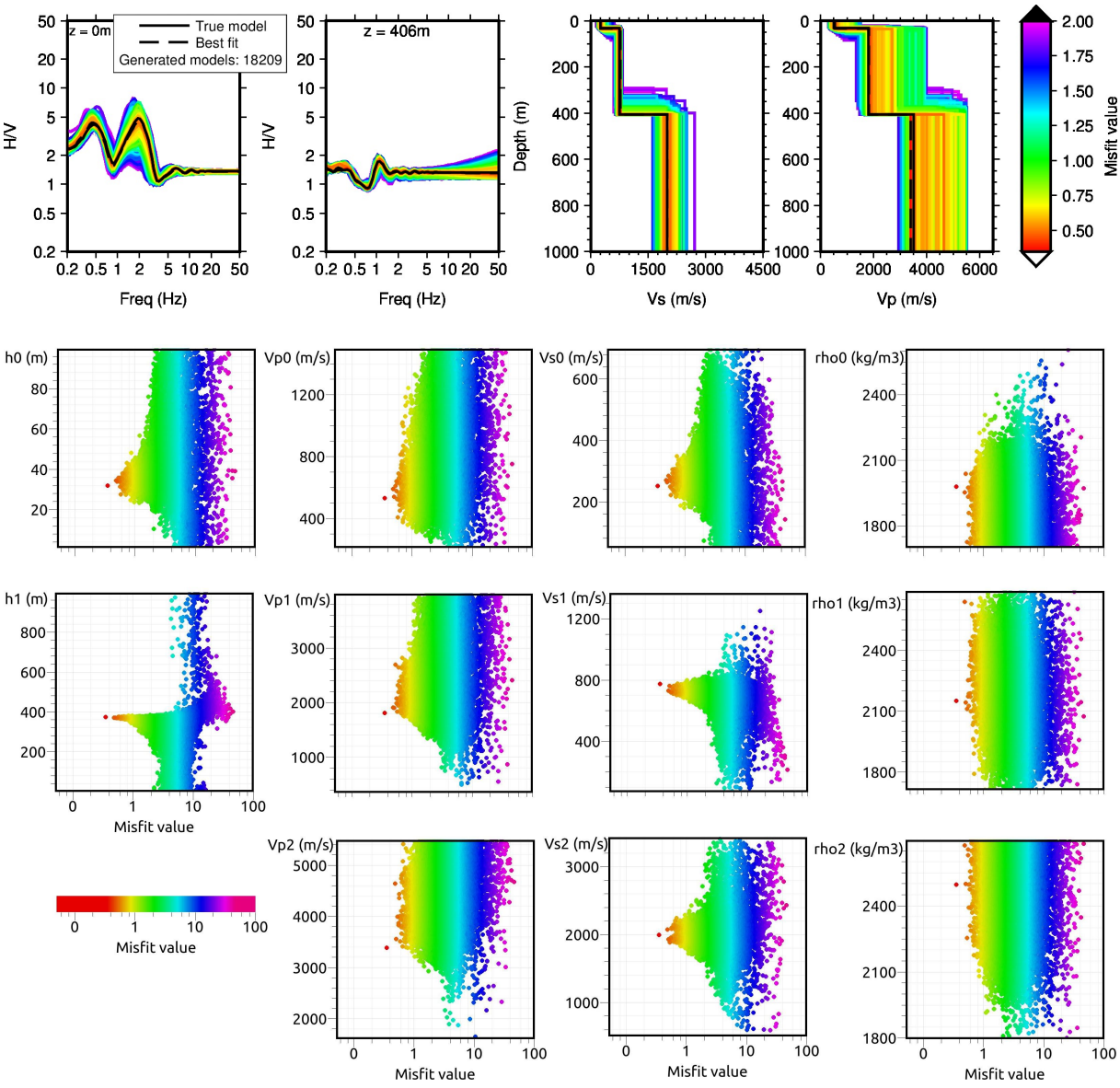

Figure 3.C.9: Synthetic data inversion. Sensitivity analysis for receiver at 406 m depth.

3.C.3 Seven layers over a half space model: model M12.1

$Thickness(m)$	$Vp(m/s)$	$Vs(m/s)$	$\rho(kg/m^3)$	Q_P	Q_S
3	296	104	2050	50	50
16	1160	166	2150	50	50
30	1322	227	2080	50	50
31	1458	315	2100	50	50
50	1764	455	2160	100	100
55	2160	560	2200	100	100
10	2482	875	2500	100	100
∞	3920	2868	2600	100	100

Table 3.C.3: Parameters definition for a seven layers over a half-space model used in the third synthetic inversion test. The model is derived from the study by Chavez-Garcia & Raptakis (2008) for the Volvi Graben test site in Greece.

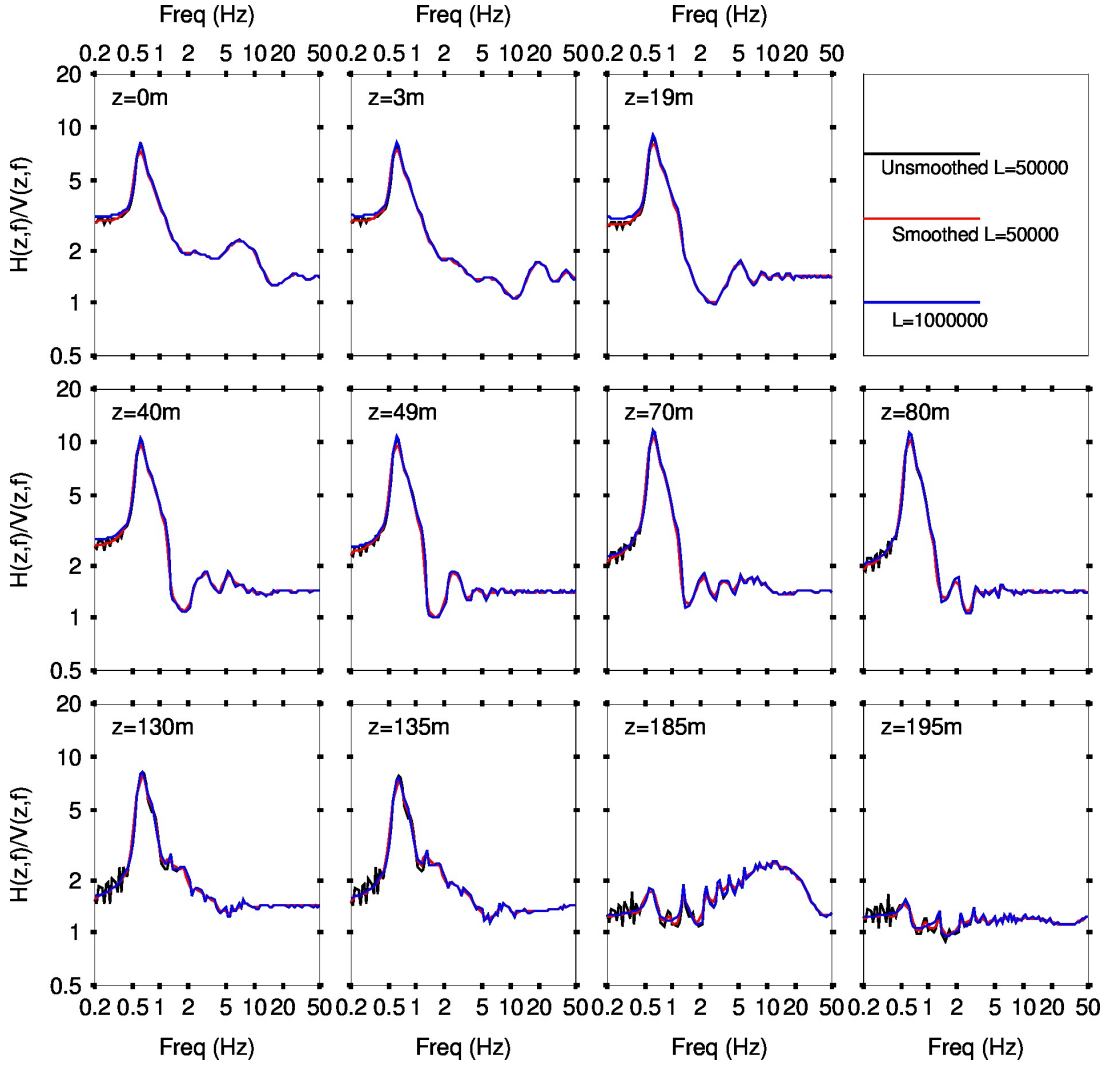

Figure 3.C.10: H/V spectral ratio computed at different depths using the synthetic 7LOH model of Table 3.C.3. The smoothed and unsmoothed H/V spectral ratio are plotted together for comparison. L = 50 000 is considered as the integration parameter. Note that in this study L = 50 000 is the value for which the full H/V is recovered after spectral smoothing.

$Thickness(m)$	$Vp(m/s)$	$Vs(m/s)$
0.1 - 5	200 - 2000	10 - 1000
0.1 - 100	200 - 3500	50 - 2000
0.1 - 100	200 - 3500	50 - 2000
0.1 - 100	200 - 3500	50 - 2000
0.1 - 100	200 - 3500	50 - 2000
0.1 - 100	200 - 4000	50 - 3000
0.1 - 40	200 - 4000	50 - 3000
∞	200 - 6000	50 - 4000

Table 3.C.4: Parameters definition for a seven layers over a half-space model used in the third synthetic inversion test.

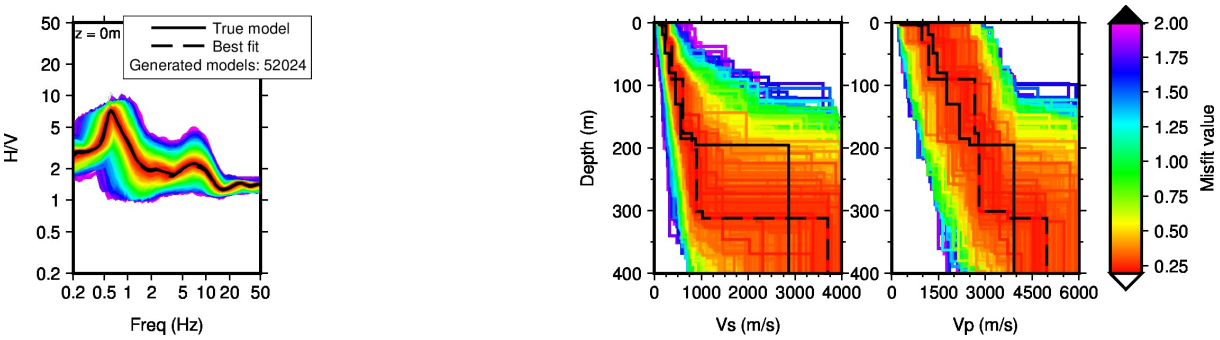

Figure 3.C.11: Synthetic data inversion. Sensitivity analysis for receiver at the surface.

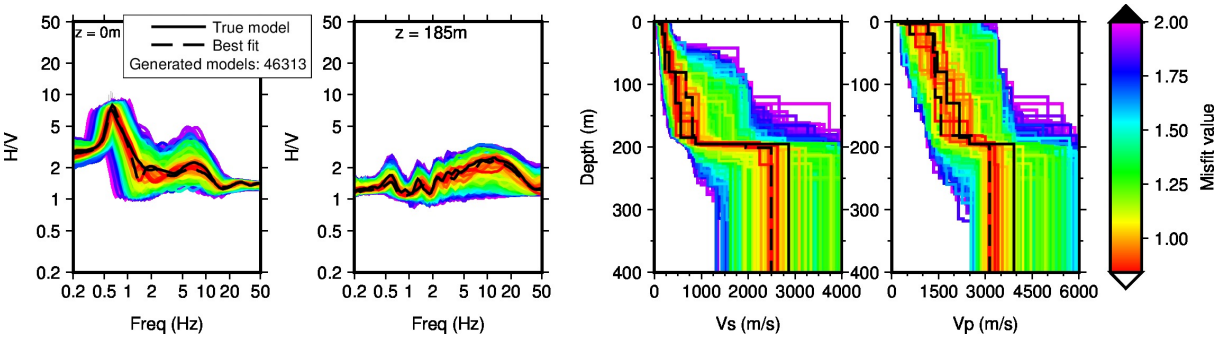

Figure 3.C.12: Synthetic data inversion. Sensitivity analysis for receiver at the 185 m depth.

3.D H/V(z, f) modeling using the full wavefield method

In addition to the H/V computed at the surface (Figure 3.3) using the full wavefield method by Wang (1999), we investigated the potential of the method to estimate the H/V(z, f) at depth. Different receivers depths range have also been considered for the single one layer over half space used hereinabove. Results show that one needs an appropriate source distribution to simulate the diffuse wavefield.

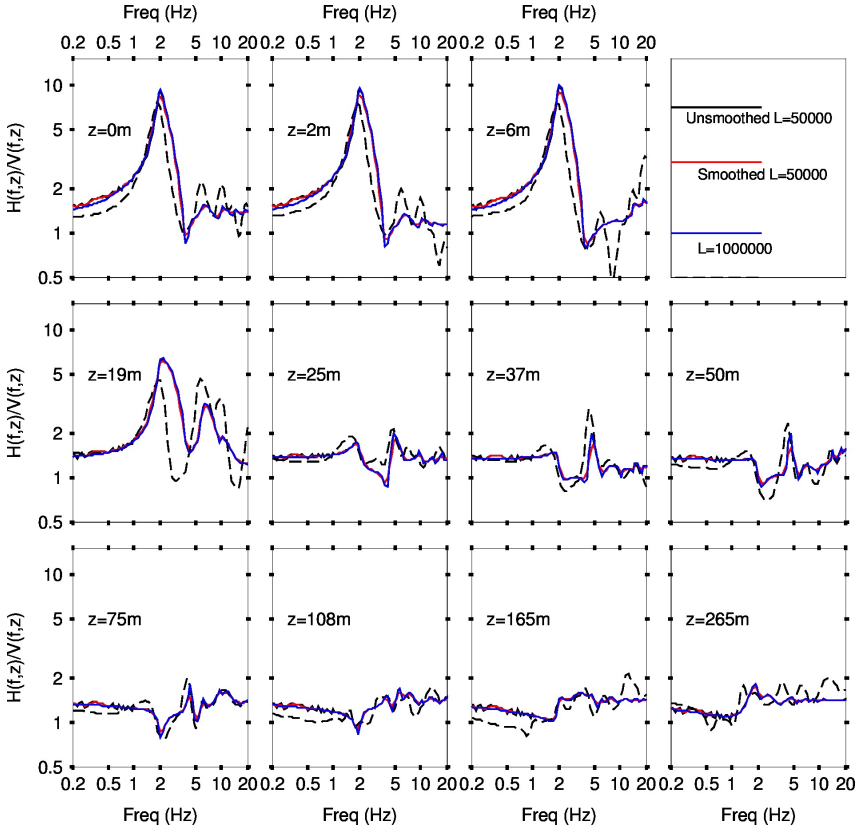

Figure 3.D.1: The synthetic 1LOH model of Table 3.1 (SESAME, 2004a) is used. The maximum source depth is at 5 km The smoothed and unsmoothed H/V spectral ratio are plotted together for comparison.

3.E H/V temporal variation at Rethem

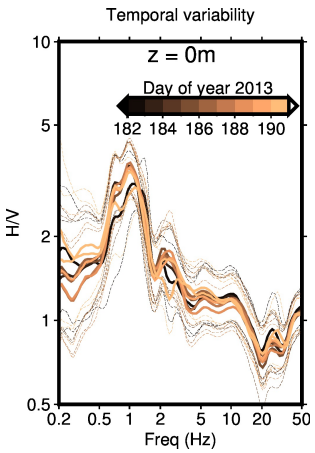

Figure 3.E.1: Temporal variation of the H/V spectrum at the test site in Rethem.

Chapter 4

Microtremor H/V(z, f) modeling for shallow sedimentary subsurface in marine environment

Lontsi, A.M., J.C. Molina-Villegas, F.J. Sánchez-Sesma, M. Ohrnberger, F. Krüger, 2016. To be submitted to *Geophysical Journal International*.

Abstract

Recent advances in the field of seismic interferometry aided in providing a basic theoretical interpretation to the full spectrum of the microtremor H/V(z, f) spectral ratio estimated from ambient noise data. The interpretation applies to both recordings at the surface and/or at depth. The ambient noise wavefield contains information regarding the underlying subsurface structure due to multiple scattering and therefore is used to image the underlying structure. The new algorithm, based on the diffuse wavefields assumption, has been used in an inversion scheme to estimate the seismic shear wave velocity profile that is a useful input parameters in engineering seismology for hazard estimation and in earthquake seismology for removing the effect of near surface sediment layer. However, at present, the algorithm is only suitable to sedimentary environments on land.

Here, the microtremor H/V(z, f) spectral ratio forward modeling algorithm is extended for applications to marine sedimentary environments. This is accomplished by computing the directional energy density in a 1D media by using the layer propagator matrix formulation. Therefore, in the presence of a water layer on top, the properties of the propagator matrix for the surface layer are modified to account for water column properties.

For application, the analysis is performed on four simple canonical layered Earth models having each 25 m of soft soil cover and the second, third, and fourth model having respectively 8-, 16-, and 25 m of water column overlaying the soft soil layer. Frequencies ranging from 0.2 to 50 Hz are considered as they cover a broad wavelength spectrum and aid in practice to investigate subsurface structures in the depth range from few tens to few hundreds of meters.

While limiting ourselves to shallow marine environments with a maximum of 25 m of water cover, the modeled H/V(z, f) results indicate that the theoretical formulation is valid for the interpretation of microtremor H/V(z, f) estimated from 3C ambient noise data recorded on land as well as for the interpretation of the microtremor H/V(z, f) estimated from 3C ambient noise data recorded in marine environment. From the modeling results, the fundamental frequency of the site remained unchanged

with the presence of a water layer. The main changes in the modeled H/V spectral ratio are observed in the high frequencies part ($\sim>$ 10 Hz) when the water layer is present. Relative variations in the H/V amplitude in this high frequency range ($\sim>$ 10 Hz) indicate an amplitude decrease down to $\sim$ 24% in the first 50 cm below the water column and an amplitude increase up to $\sim$ 10% below $\sim$ 1 m. This relative increase in the H/V amplitude is observed down to the main strong impedance contrast (at 25 m below water column).

4.1 Introduction

The single station microtremor horizontal-to-vertical (H/V) spectral ratio as a method for shallow subsurface characterization has attracted over the past few decades a number of site investigation studies both on land (e.g. Nakamura, 1989; Bard, 1998; Bonnefoy-Claudet et al., 2006a; Fäh et al., 2003; Scherbaum et al., 2003; Hobiger et al., 2013; Lontsi et al., 2015 and in marine environment (e.g. Huerta-Lopez et al., 2003; Muyzert, 2007; Overduin et al., 2015). The interest in the method is mainly due to its practicability, its cost efficiency, and the minimum investment effort during microtremor (ambient noise or passive seismic) survey campaign. Generic engineering parameters directly estimated from the spectrum of the microtremor H/V spectral ratio include the amplification factor of the site (Nakamura, 1989; Konno & Ohmachi, 1998; Nakamura, 2008) and the site fundamental frequency (e.g. Nakamura, 1989; Lachet & Bard, 1994; Konno & Ohmachi, 1998; Bonnefoy-Claudet et al., 2006a; Nakamura, 2008). The fundamental frequency corresponds to the frequency for which the microtremor H/V reaches its maximum amplitude.

Although the peak frequency is relatively well understood, this is not straightforward for secondary peaks as they could represent higher modes or materialize the presence of more than one strong contrast in the subsurface lithology. With this limitation (lack in the full H/V interpretation), mainly part of the microtremor H/V spectral ratio curve between the peak and the first trough are often used in the inversion (e.g. Fäh et al., 2003) or in combination with the surface waves phase velocity dispersion curves (e.g. Scherbaum et al., 2003) to estimate the 1D Vs profile. With the recent advances in the computation of the full spectrum of the microtremor H/V spectral ratio using seismic interferometric principles under the diffuse fields assumption (Sánchez-Sesma et al., 2011a), Lontsi et al. (2015) suggest to use additional H/V information from a receiver at depth in the inversion. This approach provides meaningful results for the shear wave velocity and to some extend for the compressional wave velocity but the model applies only to sedimentary environments on land with no consideration about marine environments where, with the evolving technology in boreholes acquisition seismic instrument and data transmission (e.g. Stephen et al., 1994), there is a growing need for efficient subsea exploration and geohazard estimation as reported by Djikpesse et al. (2013).

Here we present a model that is valid for the interpretation of the H/V(z, f) both on land and in marine sedimentary environment. A similar study has been performed by Huerta-Lopez et al. (2003). The main differences with the current work reside in the background assumption regarding the nature of the noise wavefield and the possibility to interpret the H/V spectral ratio estimated below the seafloor. First, the propagator (transfer) matrix is used to relate the displacement and stress for SH and P-SV waves at two points within an elastic 1D layered media. In comparison to the global matrix formulation (Knopoff, 1964) used by Sánchez-Sesma et al. (2011a) for the Green's function estimation, the propagator matrix formulation (Thomson, 1950; Haskell, 1953) allows to easily modify the characteristics of the layer on top to account for the properties of the water layer and to subsequently estimate the Green's function at the bottom of the water layer.

A synthetic analysis is performed on four simple canonical Earth models. The models differ by the presence of a water column with varying depth at the top of a one layer over a halfspace soft soil model.

The H/V spectral ratio is estimated for frequencies ranging from 0.2 to 50 Hz. The effect of the water column and the variations in the H/V spectrum at randomly selected depths are interpreted.

4.2 Microtremor H/V spectral ratio in 1D layered media: A physical interpretation

Here, the main steps linking the microtremor H/V(z, f) spectral to the subsurface Green's function are presented. The basic equations for SH and P-SV wave contributions to the Green's function are also presented (the key theoretical development steps are left in the Appendix 4.B). Considerations for numerical integration are then presented.

4.2.1 H/V(z, f) estimation and interpretation

Starting from a three-component ambient vibration data, the microtremor H/V spectral ratio at a given depth for a known frequency is estimated using Equation 4.1

$$H/V(z,f) = \sqrt{\frac{E_1(z,f) + E_2(z,f)}{E_3(z,f)}} \tag{4.1}$$

where $E_m(z,f) = \rho\omega^2\langle u_m(z,f){u_m}^*(z,f)\rangle$ is the Directional Energy Density (DED), ρ is the mass density, ω is the angular frequency and u_m (m=1,2,3) is the recorded wavefield in the orthogonal direction m. Using interferometric principles under the diffuse field assumption, it was shown that in the farfield (Sánchez-Sesma & Campillo, 2006b; Sánchez-Sesma et al., 2008; Snieder et al., 2009, see a summary in Appendix 4.A)

$$\langle u_m(z,f)u_m^*(z,f)\rangle \propto Im[G_{mm}(z,z,f)] \tag{4.2}$$

where the symbol $*$ stands for the complex conjugate, the angular brackets stand for the azimuthal average and G_{mm} represents the medium response in the direction m to a harmonic concentrated load acting in the same direction. The physical formulation of the H/V in terms of the Green's function is therefore given by Equation 4.3.

$$H/V(z,f) = \sqrt{\frac{Im[G_{11}(z,z,f)] + Im[G_{22}(z,z,f)]}{Im[G_{33}(z,z,f)]}} \tag{4.3}$$

We are therefore left with the estimation of the Green's functions G_{11}, G_{22} and G_{33}. In linear elasticity, the elastodynamic Green's function in a 1D layered medium is the set of responses for unit harmonic loads in the three directions. Using cylindrical coordinates the contribution of the radial-vertical (P-SV) and transverse (SH) motions are uncoupled. Therefore, it suffices to solve each case separately using the horizontal wavenumber.

4.2.2 SH and P-SV contribution to the Green's function

Assuming the subsurface can be approximated with a 1D layered media, ImG_{11}, ImG_{22} and ImG_{33} are given by:

$$
\begin{aligned}
ImG_{11} &= ImG_{22} \\
&= Im\left[G_{11}^{SH}(z,f)\right] + Im\left[G_{11}^{P-SV}(z,f)\right] \\
&= Im\left[G_{22}^{SH}(z,f)\right] + Im\left[G_{22}^{P-SV}(z,f)\right] \\
&= \frac{1}{4\pi}\int_0^\infty Im\left[g_{22}\right] kdk + \frac{1}{4\pi}\int_0^\infty Im\left[g_{11}\right] kdk
\end{aligned}
\tag{4.4}
$$

$$
\begin{aligned}
ImG_{33} &= Im\left[G_{33}^{P-SV}(z,f)\right] \\
&= \frac{1}{2\pi}\int_0^\infty Im\left[g_{33}\right] kdk
\end{aligned}
\tag{4.5}
$$

It is important to notice that the Green's function for the 3D media are obtained from the 2D counterpart through a multiplicative factor. This multiplicative factor equals $\frac{k}{4\pi}$ for the radial and transverse components of the Green's function and equals $\frac{k}{2\pi}$ for the vertical component.

The explicit analytical expressions for g_{11}, g_{22}, and g_{33} are given in Appendix 4.B.

4.2.3 Considering a water layer on top of the layered half-space

In the particular case the top layer is a non-gravitating water layer, the shear stress and the corresponding shear velocity equal zero. By introducing these quantities in the 4x4 propagator matrix for P-SV waves, the latter becomes singular. An alternative approach is used to estimate the corresponding 2x2 propagator matrix which is that of the pressure at the bottom of the water column. It is therefore possible to define a pseudo 4x4 matrix (see Appendix 4.D) and to treat the problem as in the P-SV case (Herrmann, 2008).

4.2.4 Numerical implementation and testing

For the numerical integration, Equations 4.4 and 4.5 are transformed into a summation assuming virtual sources along the horizontal wavenumber with spacing L (Bouchon & Aki, 1977). L defines the integration step $dk = \frac{2\pi}{L}$. The vertical wavenumber γ_j and ν_j for, respectively, P- and S- waves in the j^{th} layer relate to the horizontal wavenumber k by:

$$
\gamma_j = \sqrt{k^2 - \frac{\omega^2}{V_{P_j}^2}} \tag{4.6}
$$

$$
\nu_j = \sqrt{k^2 - \frac{\omega^2}{V_{S_j}^2}} \tag{4.7}
$$

Because of the singularity of the kernel, introduced by the poles on the real axis, a correction term ω_I is added to the frequency to shift the poles of the kernel from the real axis so that the effective frequency is:

$$
\omega = 2\pi f + \omega_I i \tag{4.8}
$$

P- and S-wave energy attenuation are considered by defining complex seismic wave velocities.

For testing the presented algorithm, the directional energy density profile for a homogeneous halfspace and the H/V spectral ratio for a one layer over a halfspace are estimated and compared with results from the model presented by Sánchez-Sesma et al. (2011a). The authors (Sánchez-Sesma et al., 2011a) used the global matrix formulation for the estimation of the Green's functions. Their model has now been extended to include the interpretation of the H/V spectral ratio at depth. Table 4.1 presents the model

$h(m)$	$Vp(m/s)$	$Vs(m/s)$	$\rho(kg/m^3)$	Q_P	Q_S
Homogeneous halfspace					
∞	1732	1000	2000	100	100
A sedimentary layer on land (modified after SESAME, 2004a)					
25	500	200	1900	200	200
∞	2000	1000	2500	200	200

Table 4.1: Seismic parameters for a homogeneous halfspace and a single layer over a halfspace. The first model is used to estimate the Directional Energy Density (DED) profile with normalized depth and the second model is used to model the DED and the corresponding H/V spectral ratio at three randomly selected depths (Figure 4.2). The H/V spectral ratio has been investigated in the work by Lontsi et al. (2015) and the current results allow for comparison of the approaches (See text).

parameter for the homogeneous halfspace defined as a Poisson solid. The energy variation with depth (Figure 4.1) shows a good agreement with known theory regarding the energy partition for a diffuse wavefield (e.g. Weaver, 1985; Perton et al., 2009). For depths larger than approximately 1.5 times the Rayleigh wavelength, there is almost no energy contribution from Rayleigh waves and the energy is equal for the three orthogonal direction (Figure 4.1). The parameters for the one layer (25 m thick) over a halfspace model used in the second algorithm testing are defined in Table 4.1. The model represents a very simple soft-soil structure and it is characterized by constant shear wave velocities (200 m/s for the soft-layer and 1000 m/s for the bedrock), compressional wave velocities (500 m/s for the soft-layer and 2000 m/s for the bedrock), densities (1900 kg/m^3 for the soft-layer and 2500 kg/m^3 for the bedrock) and quality factors Qp and Qs for the shear- and compressional waves respectively (Qp is assumed equal to Qs for both the soft layer and the half-space). The impedance contrast approximates 7. Figure 4.2a presents the velocity profiles. This model has been extensively investigated for site effect related studies (e.g. SESAME, 2004a; Bonnefoy-Claudet et al., 2006a; Poggi & Fäh, 2010; Maranò et al., 2012; Lontsi et al., 2015).

The two approaches (propagator matrix and global matrix formulations) provide H/V spectral ratio

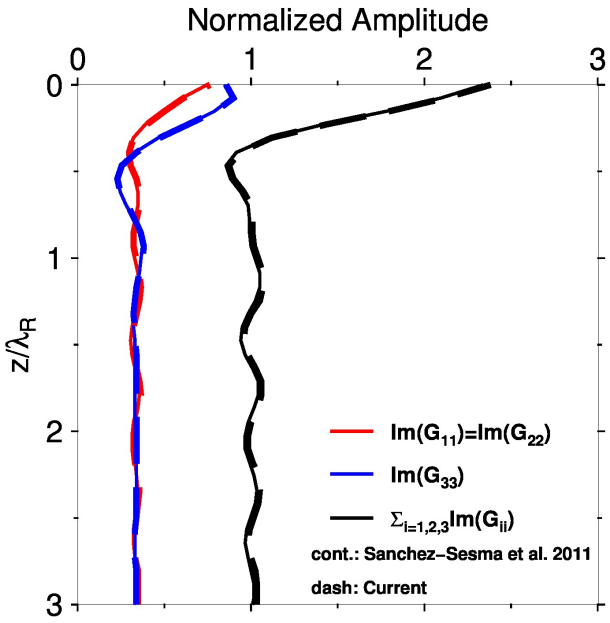

Figure 4.1: Comparison between normalized energy profiles estimated using the propagator matrix (current) and the global matrix formulation (Sánchez-Sesma et al., 2011a). The depth is normalized with the Rayleigh wavelength. There is a good agreement between the two formulations.

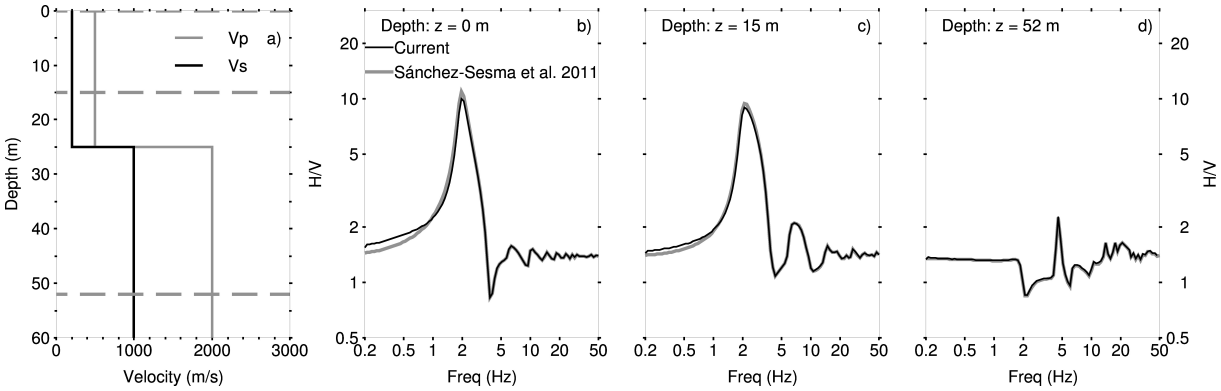

Figure 4.2: a) Seismic parameters for a very simple soft soil layer over a halfspace. Dashed gray lines indicate depths at which the H/V information have been compared. b) Comparison between H/V spectral ratios at the surface (z = 0 m). c) Comparison between H/V spectral ratios at 15 m depth (z = 15 m). d) Comparison between H/V spectral ratios at 52 m depth (z = 52 m).

that agree with each other for a receiver in the half-space (Figure 4.2d). While for receivers in the soft soil there were discrepancies in the H/V spectral ratios for frequencies below 2 Hz, a good agreement was observed for frequencies above 2 Hz. The (almost) good agreement as presented in Figure 4.2b,c for the full frequency range between 0.2 and 50 Hz was obtained after the attenuation parameters have been changed from 100 to 200. Although this agreement between the two approaches (Figure 4.2b-d) gives confidence to move forward for further synthetic analysis, the sensitivity of the algorithm to the attenuation parameters in the low frequencies will require further scrutiny.

4.3 Synthetic analysis (four additional models)

Four synthetic models are defined and the algorithm presented hereinabove is used to model the H/V spectral ratios at depths. To obtain the first model (Table 4.2), the P-wave velocity from the previously investigated one layer over a halfspace (for a recall see Table 4.1) has been modified from 500 m/s to 1750 m/s. This P-wave velocity is characteristic of water saturated sediments. The attenuation parameters for P- and S-wave are taken equal to 50 for the soft soil and the halfspace (Table 4.2). The second, third and fourth models are obtained by considering an a water column with respectively 8, 16 and 25 m on top of the soft soil. For the appraisal of the effect of the water layer on the H/V(z, f), the P-wave velocities on land and in water saturated sediment are kept equal.

The H/V is computed at 50 points distributed on a logarithmic scale between 0.001 m (0 m) and 50 m depth. The resulting H/V spectral ratio curves are used to generate a 2D plot (x,y,z) = (frequency,

$h(m)$	$Vp(m/s)$	$Vs(m/s)$	$\rho(kg/m^3)$	Q_P	Q_S
Model 2: A sedimentary layer on land					
25	1750	200	1900	50	50
∞	2000	1000	2500	50	50
Model 3: A sedimentary layer on land and a sedimentary layer in marine environment					
8 (or 16, or 25)	1500	0	1000	9999	9999
25	1750	200	1900	50	50
∞	2000	1000	2500	50	50

Table 4.2: Definition of two synthetic models. Model 2 is representative of sedimentary environments on land and Model 3 is representative of a shallow marine environment. All models are modified after SESAME, 2004a.

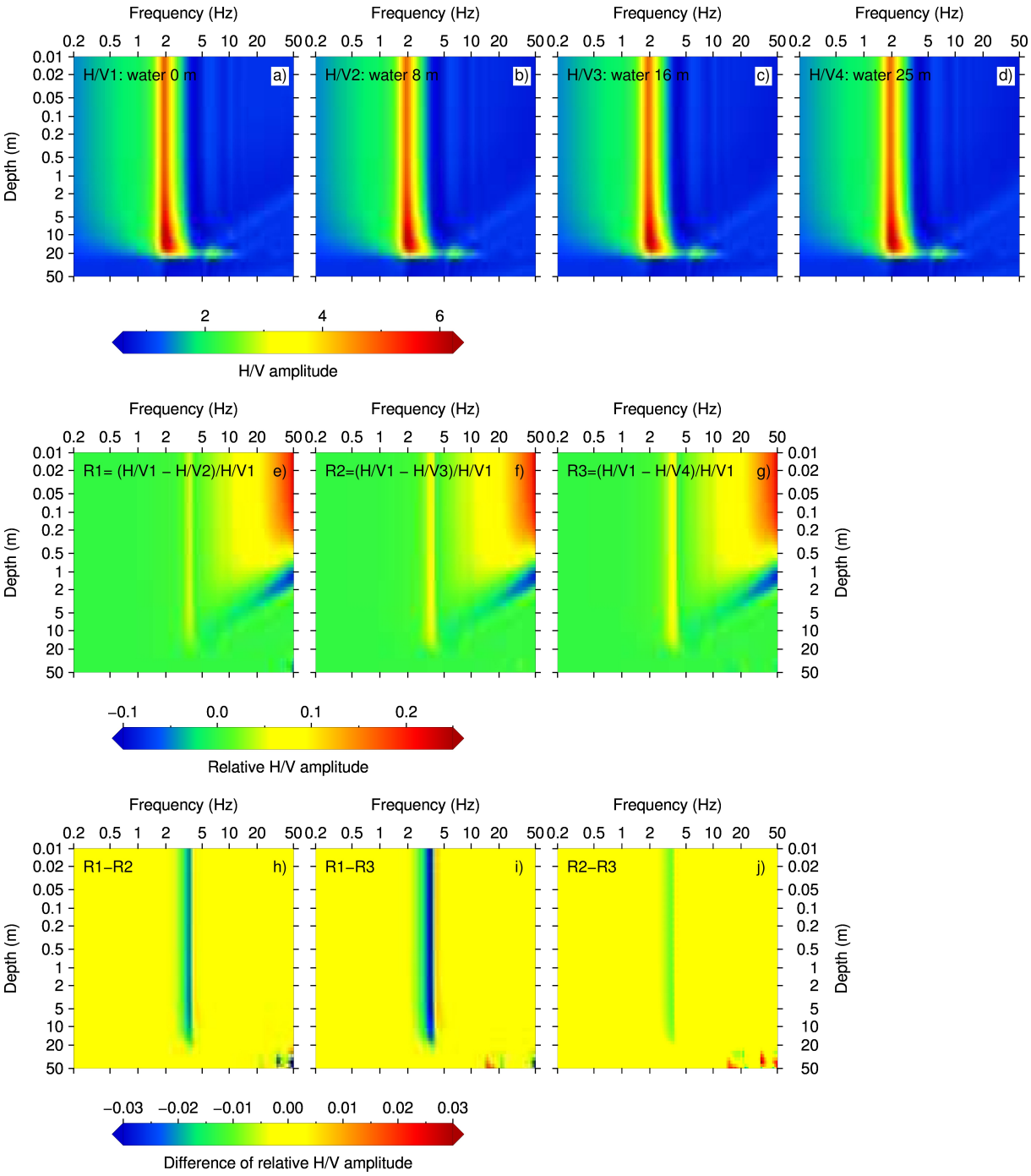

Figure 4.3: a) to d) represent the H/V spectral ratio amplitude variation with depth for a one-layer-over-a-halfspace model with no water layer, with 8 m water layer, with 16 m water layer and with 25 m water layer respectively. e) to g) represent the relative change in the H/V spectral ratio amplitude between a) and b), a) and c), and a) and d). h) to j) indicate the differences in the relative H/V amplitude variation.

depth, H/V amplitude) represented by Figures 4.3a-d for the four models. In this representation, no clear difference is observed between the four figures. Nevertheless, relative variation in the H/V amplitude, represented by Figures 4.3e-g, indicates that there is a sensitivity of the model to the overlying water layer. From 0. to approximately 0.5 m depth, there is a positive relative change in the H/V amplitude of up to 24% for frequencies larger than 10 Hz (Figure 4.3e-g). For receiver-depths larger than approximately 1 m, a negative relative change in the H/V amplitude reaching approximately 10% for frequencies larger than 5 Hz is observed (Figures 4.3e-g). The three figures also indicate changes in the H/V spectral ratio at

$\sim$ 4 Hz (H/V trough). The range of this change slightly broadens with the increase of the water column depth (from 8 to 25 m). These observations are well visible in Figures (Figures 4.3h-j) where differences between the relative variations for all frequencies have been represented.

For both the synthetic soft soil on land and in marine environment, it is important to notice the large amplitude difference in the maximum H/V spectral ratio amplitude in the soft soil and in the halfspace. One important remark is that, for all models, the peak frequencies satisfy the relationship $f_n = \frac{V_S}{4h}(2n+1)$ often used in practical applications.

4.4 Conclusion

The propagator matrix (PM) method is used to estimate the Green's function in a 1D layered media. Modeled H/V spectral curves are compared with estimation from the global matrix (GM) approach. For a receiver at the surface, the main differences are observed in the H/V spectral ratio at low frequencies. Tuning the attenuation parameters for P- and S-waves allowed to obtain a good agreement between the two formulations in the whole investigated frequency range (0.2 - 50 Hz). In comparison to the GM method, the PM provides an efficient approach for modeling the H/V spectral ratio within marine environments. Modeling results indicate the H/V spectral ratio in the halfspace is not sensitive to the presence of the water column on top if an amplitude variation of up to 24% is neglected. It is to be noted that all models presented in this study are very simple and lead to H/V estimation in the frequency range of interest (up to 50 Hz). Instabilities appear in the high frequencies when the structure include, e.g., a deep water column or a thick sediment layer cover (see Figure 4.E.1 in the Appendix 4.E).

Appendices

4.A Ambient noise - Green's function - representation theorem - cross-correlation - Directional Energy Density - Equipartition

Seismic sources at the origin of the ambient noise wavefield are located at surface or at depth. Generated seismic waves are back-scattered in the subsurface. The recorded noise wavefield at a seismic station after a lapse time large enough compared to the mean travel time of ballistic waves (e.g direct waves, first reflected waves) contains information regarding the underlying subsurface structure.

Equation 4.9 relates the Directional Energy Density (DED), E_m, for a given orthogonal direction m to the auto-correlation of the recorded displacement wavefield and to the Green's function of the underlying structure assuming the source and the receiver are at the same location.

$$\begin{aligned} E_m(\mathbf{X}, f) &\propto \langle u_m(\mathbf{X}, f) u_m^*(\mathbf{X}, f) \rangle \\ &\propto Im[G_{mm}(\mathbf{X}, \mathbf{X}, f)] \end{aligned} \tag{4.9}$$

In practice, the DED is estimated from the auto-correlation (power spectrum) of the recorded ambient noise wavefield. For subsurface imaging purposes, the DED is estimated from the imaginary part of the Green's function.

To demonstrate the validity of Equation 4.9 and estimate the corresponding proportionality constants, a simple homogeneous, isotropic, elastic medium for which the analytical expression to the Green's function to the Navier's equation, in the farfield is known is considered (Sánchez-Sesma & Campillo, 2006b; Sánchez-Sesma et al., 2008). (The Green's functions for a layered elastic media are estimated in sections 4.B and 4.C.)

The displacement field $u_i(\mathbf{x}, \omega)$ produced by a body force f_i at a given point $\mathbf{x}$ of an elastic solid is described by the wave Equation 4.10.

$$\frac{\partial}{\partial x_j} \left(c_{ijkl} \frac{\partial u_l(\mathbf{x}, \omega)}{\partial x_k} \right) + \omega^2 \rho u_i(\mathbf{x}, \omega) = -f_i(\mathbf{x}, \omega) \tag{4.10}$$

where c_{ijkl} is the stiffness tensor, ρ is the mass density and ω the angular frequency. The Einstein summation index is assumed, i.e repeated index implies summation over all indices.

From Equation 4.10, it is possible to show that in the particular case of a concentrated harmonic unit load at the position $\mathbf{x_A}$ in the direction m, defined by Equation 4.11,

$$f_i(\mathbf{x} - \mathbf{x_A}, \omega) = \delta_{im} \delta(\mathbf{x} - \mathbf{x_A}) \exp(i\omega t) \tag{4.11}$$

the displacement at a point $\mathbf{x_A}$ can be written as (e.g. Wapenaar & Fokkema, 2006; van Manen et al., 2006; Snieder et al., 2007; Sánchez-Sesma et al., 2008):

$$u_m(x_A, \omega) = \int_\Gamma \{ G_{im}(\mathbf{x}, \mathbf{x_A}, \omega) t_i(\mathbf{x}, \omega) - T_{im}(\mathbf{x}, \mathbf{x_A}, \omega) u_i(\mathbf{x}, \omega) \} d\Gamma_x + \int_V f_i(\mathbf{x}, \omega) G_{im}(\mathbf{x_A}, \mathbf{x}, \omega) dV_x \tag{4.12}$$

where $t_i(\mathbf{x}, \omega)$ and $T_{im}(\mathbf{x_A}, \mathbf{x}, \omega)$ are given by Equation 4.13.

$$
\begin{aligned}
t_i(\mathbf{x},\omega) &= n_j(\mathbf{x})\left(c_{ijkl}\frac{\partial u_l(\mathbf{x},\omega)}{\partial x_k}\right) \\
T_{im}(\mathbf{x_A},\mathbf{x},\omega) &= n_j(\mathbf{x})\left(c_{ijkl}\frac{\partial G_{lm}(\mathbf{x},\mathbf{x_A},\omega)}{\partial x_k}\right)
\end{aligned}
\tag{4.13}
$$

Using the reciprocity theorem of the Green's function with the following considerations: $x_A \leftrightarrow x$ and $i \leftrightarrow n$), we obtain

$$
u_m(x,\omega) = \int_\Gamma \{G_{im}(\mathbf{x},\mathbf{x_A},\omega)t_i(\mathbf{x_A},\omega) - T_{im}(\mathbf{x},\mathbf{x_A},\omega)u_i(\mathbf{x_A},\omega)\}d\Gamma_x + \int_V f_i(\mathbf{x_A},\omega)G_{im}(\mathbf{x},\mathbf{x_A},\omega)dV_x \tag{4.14}
$$

The time reverse is given by:

$$
u^*_m(x,\omega) = \int_\Gamma \{G_{im}(\mathbf{x},\mathbf{x_A},\omega)t^*_i(\mathbf{x_A},\omega) - T_{im}(\mathbf{x},\mathbf{x_A},\omega)u^*_i(\mathbf{x_A},\omega)\}d\Gamma_x + \int_V f^*_i(\mathbf{x_A},\omega)G_{im}(\mathbf{x},\mathbf{x_A},\omega)dV_x \tag{4.15}
$$

Using Equations 4.14 and 4.15 together with the reciprocity theorem for a point load, Equation 4.16 is obtained (e.g. Wapenaar & Fokkema, 2006; van Manen et al., 2006; Snieder et al., 2007; Sánchez-Sesma et al., 2008).

$$
\begin{aligned}
G^*_{im}(\mathbf{x_A},\mathbf{x_B},\omega) - G_{im}(\mathbf{x_A},\mathbf{x_B},\omega) &= -2iIm\left[G^*_{im}(\mathbf{x_A},\mathbf{x_B},\omega)\right] \\
&= \int_\Gamma \{G_{im}(\mathbf{x_A},\zeta,\omega)T^*_{in}(\zeta,\mathbf{x_B},\omega) - T_{im}(\zeta,\mathbf{x_A},\omega)G^*_{ni}(\mathbf{x_B},\zeta;\omega)\}d\Gamma_x
\end{aligned}
\tag{4.16}
$$

Starting from the analytical expressions for G_{im} and T_{im} in the farfield (Sánchez-Sesma & Campillo, 2006b; Sánchez-Sesma et al., 2008; see, e.g., Domínguez & Abascal, 1984 for the full expression of G_{im} and T_{im}), it can be demonstrated, under the assumption of equipartitioned diffuse field, the right hand side of Equation 4.16 is proportional to the azimuthal average of the autocorrelation of the displacement field assuming the source and the receiver are at the same location (Sánchez-Sesma et al., 2008). An alternative approach linking the azimuthal average of cross-correlation to the imaginary part of the Green's function under diffuse assumption in the farfield, and without prior knowledge of the full analytical expression of the Green's function was presented by Snieder et al. (2009). We are now left with the estimation of the Green's function in a 1D layered media.

4.B Estimating the SH waves contribution to the imaginary part of the Green's function

Receiver at the surface

The wave equation in Layer 1 is (linear elasticity):

$$
\frac{\partial^2 v}{\partial t^2} = \frac{\mu}{\rho}\left(\frac{\partial^2 v}{\partial x^2} + \frac{\partial^2 v}{\partial z^2}\right) \tag{4.17}
$$

A solution to the Equation 4.17 can be of the form:

$$
v = l_1(z,w,k)\exp i(kx - \omega t) \tag{4.18}
$$

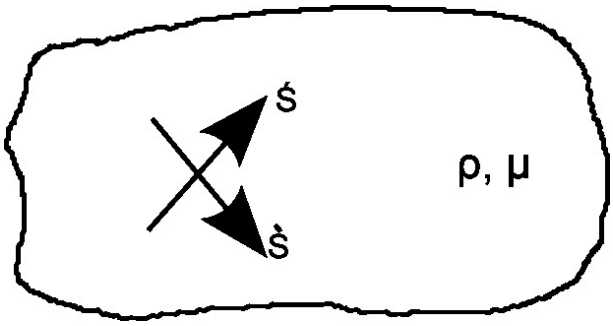

Figure 4.B.1: Schematic representation of the 2D SH wave propagation.

and the associated stresses:

$$\begin{aligned} \tau_{xx} = \tau_{yy} = \tau_{zz} = 0 \\ \tau_{yz} &= \mu \frac{\partial l_1}{\partial z} \exp i(kx - \omega t) \\ &= l_2 \exp i(kx - \omega t) \\ \tau_{xy} &= ik\mu l_1 \exp i(kx - \omega t) \end{aligned} \tag{4.19}$$

From Equation 4.19, the differential Equation 4.20 is obtained.

$$\frac{dl_1}{dz} = \frac{1}{\mu} l_2 \tag{4.20}$$

From Newton's second law, one gets:

$$\frac{\partial \tau_{xy}}{\partial x} + \frac{\partial \tau_{yz}}{\partial z} = \rho \frac{\partial^2 v}{\partial t^2} \tag{4.21}$$

This leads to

$$\frac{dl_2}{dz} = (\mu k^2 - \rho\omega^2) l_1 \tag{4.22}$$

Equations 4.20 and 4.22 leads to the system of first order differential equation 4.23.

$$\frac{d}{dz}\begin{pmatrix} l_1 \\ l_2 \end{pmatrix} = \begin{pmatrix} 0 & \frac{1}{\mu} \\ \mu k^2 - \rho\omega^2 & 0 \end{pmatrix} \begin{pmatrix} l_1 \\ l_2 \end{pmatrix} \tag{4.23}$$

This equation is of the form:

$$\frac{d\mathbf{l}}{dz} = \mathbf{A}\mathbf{l} \tag{4.24}$$

where $\mathbf{l} = \begin{pmatrix} l_1 \\ l_2 \end{pmatrix}$ and $\mathbf{A} = \begin{pmatrix} 0 & \frac{1}{\mu} \\ -k^2 - \omega^2\rho & 0 \end{pmatrix}$.

The solution to Equation 4.24 at two points z_1 and z_2 is (Gantmacher, 1959; Gilbert & Backus, 1966; Aki & Richards, 2002):

$$\begin{pmatrix} l_1 \\ l_2 \end{pmatrix}_{z_2} = \mathbf{P} \begin{pmatrix} l_1 \\ l_2 \end{pmatrix}_{z_1} \tag{4.25}$$

where

$$P = \begin{pmatrix} \cosh \nu(z_2 - z_1) & \frac{1}{\mu\nu} \sinh \nu(z_2 - z_1) \\ -\mu\nu \sinh \nu(z_2 - z_1) & \cosh \nu(z_2 - z_1) \end{pmatrix} \tag{4.26}$$

Without loss of generality, we have:

$$\begin{pmatrix} l_1 \\ l_2 \end{pmatrix}_{z_{n+1}} = \mathbf{P}_n \begin{pmatrix} l_1 \\ l_2 \end{pmatrix}_{z_n} \tag{4.27}$$

where

$$P_n = \begin{pmatrix} \cosh \nu_n(z_{n+1} - z_n) & \dfrac{1}{\mu_n \nu_n} \sinh \nu_n(z_{n+1} - z_n) \\ -\mu_n \nu_n \sinh \nu_n(z_{n+1} - z_n) & \cosh \nu_n(z_{n+1} - z_n) \end{pmatrix} \tag{4.28}$$

For a n-layer over half-space system, we obtain:

$$\begin{pmatrix} l_1 \\ l_2 \end{pmatrix}_{z_{n+1}} = \mathbf{P}_n \mathbf{P}_{n-1} ... \mathbf{P}_1 \begin{pmatrix} l_1 \\ l_2 \end{pmatrix}_{z_1} \tag{4.29}$$

By introducing Equation 4.18 into Equation 4.21, a second order differential equation is obtained for l_1 where the solution can be written on the form:

$$l_1 = \acute{S}_1 \exp -\nu_1 z + \grave{S}_1 \exp \nu_1 z \tag{4.30}$$

where $\acute{S}_1$ and $\grave{S}_1$ are constant.
Equation 4.20 and 4.30 lead to

$$l_2 = -\mu_1 \nu_1 \acute{S}_1 \exp -\nu_1 z + \mu_1 \nu_1 \grave{S}_1 \exp \nu_1 z \tag{4.31}$$

Equation 4.30 and 4.31 combine to

$$\begin{pmatrix} \acute{S}_1 \\ \grave{S}_1 \end{pmatrix} = \begin{pmatrix} \frac{1}{2} \exp \nu_1 z & \frac{-1}{2\mu_1 \nu_1} \exp \nu_1 z \\ \frac{1}{2} \exp -\nu_1 z & \frac{1}{2\mu_1 \nu_1} \exp -\nu_1 z \end{pmatrix} \begin{pmatrix} l_1 \\ l_2 \end{pmatrix} \tag{4.32}$$

Without loss of generality, we have:

$$\begin{pmatrix} \acute{S}_{n+1} \\ \grave{S}_{n+1} \end{pmatrix} = \begin{pmatrix} \frac{1}{2} \exp \nu_{n+1} z & \frac{-1}{2\mu_{n+1} \nu_{n+1}} \exp \nu_{n+1} z \\ \frac{1}{2} \exp -\nu_{n+1} z & \frac{1}{2\mu_{n+1} \nu_{n+1}} \exp -\nu_{n+1} z \end{pmatrix} \begin{pmatrix} l_{n+1} \\ l_{n+1} \end{pmatrix} \tag{4.33}$$

For a n-layer over a half-space, it is obtained:

$$\begin{pmatrix} \acute{S}_{n+1} \\ \grave{S}_{n+1} \end{pmatrix} = \begin{pmatrix} \frac{1}{2} \exp \nu_{n+1} z & \frac{-1}{2\mu_{n+1} \nu_{n+1}} \exp \nu_{n+1} z \\ \frac{1}{2} \exp -\nu_{n+1} z & \frac{1}{2\mu_{n+1} \nu_{n+1}} \exp -\nu_{n+1} z \end{pmatrix} \mathbf{P}_n \mathbf{P}_{n-1} ... \mathbf{P}_1 \begin{pmatrix} l_1 \\ l_2 \end{pmatrix}_{z_1} \tag{4.34}$$

$$\begin{pmatrix} \acute{S}_{n+1} \\ \grave{S}_{n+1} \end{pmatrix} = \mathbf{B} \begin{pmatrix} l_1 \\ l_2 \end{pmatrix}_{z_1} \tag{4.35}$$

where

$$\begin{aligned} \mathbf{B} &= \begin{pmatrix} \frac{1}{2} \exp \nu_{n+1} z & \frac{-1}{2\mu_{n+1} \nu_{n+1}} \exp \nu_{n+1} z \\ \frac{1}{2} \exp -\nu_{n+1} z & \frac{1}{2\mu_{n+1} \nu_{n+1}} \exp -\nu_{n+1} z \end{pmatrix} \mathbf{P}_n \mathbf{P}_{n-1} ... \mathbf{P}_1 \\ &= \begin{pmatrix} B_{11} & B_{12} \\ B_{21} & B_{22} \end{pmatrix} \end{aligned} \tag{4.36}$$

At the surface load point (z=0), $l_1 = v = g_{22}$ (g_{22} is the Green's function of interest) and $l_2 = -1$. In the half-space, there is no upgoing waves, i.e. $\acute{S}_{n+1} = 0$. This leads to

$$\begin{pmatrix} 0 \\ \grave{S}_{n+1} \end{pmatrix} = \mathbf{B} \begin{pmatrix} g_{22} \\ -1 \end{pmatrix}_{z_1} \tag{4.37}$$

$$g_{22} = \frac{B_{12}}{B_{11}} \tag{4.38}$$

The Green's function in 3D is therefore:

$$Im\left[G_{22}^{SH}(z,f)\right] = Im\left[G_{11}^{SH}(z,f)\right] = \frac{1}{4\pi}\int_0^\infty Im\left[g_{22}\right] kdk \tag{4.39}$$

Receiver at depth

$$\begin{pmatrix} \acute{S}_{n+1} \\ \grave{S}_{n+1} \end{pmatrix} = \begin{pmatrix} \frac{1}{2}\exp\nu_{n+1}z & \frac{-1}{2\mu_{n+1}\nu_{n+1}}\exp\nu_{n+1}z \\ \frac{1}{2}\exp-\nu_{n+1}z & \frac{1}{2\mu_{n+1}\nu_{n+1}}\exp-\nu_{n+1}z \end{pmatrix} \mathbf{P}_n\mathbf{P}_{n-1}...\mathbf{P}_j \begin{pmatrix} l_1 \\ l_2 \end{pmatrix}_{z_j} \tag{4.40}$$

$$\begin{pmatrix} l_1 \\ l_2 \end{pmatrix}_{z_j} = \mathbf{P}_{j-1}\mathbf{P}_{j-2}...\mathbf{P}_1 \begin{pmatrix} l_1 \\ l_2 \end{pmatrix}_{z_1} \tag{4.41}$$

Let

$\mathbf{P}^d = \mathbf{P}_n\mathbf{P}_{n-1}...\mathbf{P}_j$

$\mathbf{P}^u = \mathbf{P}_{j-1}\mathbf{P}_{j-2}...\mathbf{P}_1$

and $B = \mathbf{F}^{-1}\mathbf{P^d}$

Where $\mathbf{F}^{-1} = \begin{pmatrix} \frac{1}{2}\exp\nu_{n+1}z & \frac{-1}{2\mu_{n+1}\nu_{n+1}}\exp\nu_{n+1}z \\ \frac{1}{2}\exp-\nu_{n+1}z & \frac{1}{2\mu_{n+1}\nu_{n+1}}\exp-\nu_{n+1}z \end{pmatrix}$

Boundary conditions:

at the surface, z = 0,

Displacement: $l_1 = v_s$;

Stress: $l_2 = 0$

At the load point at depth:

Displacement in the layer on top: $l_{1-} = g_{22}$;

Stress: $l_{2-} = \tau_-$

Displacement in the layer at bottom: $l_{1+} = g_{22}$;

Stress: $l_{2+} = \tau_+$

and

$\tau_+ - \tau_- = 1$

This leads to

$$g_{22} = \frac{1}{\frac{P_{21}^u}{P_{11}^u} + \frac{B_{21}}{B_{22}}} \tag{4.42}$$

Again, the Green's function in 3D is therefore:

$$Im\left[G_{22}^{SH}(z,f)\right] = Im\left[G_{11}^{SH}(z,f)\right] = \frac{1}{4\pi}\int_0^\infty Im\left[g_{22}\right] kdk \tag{4.43}$$

4.C Estimating the P-SV waves contribution to the imaginary part of the Green's function

Following, e.g., Aki & Richards, 2002 (Chap5, Chap7):

$$\begin{pmatrix} r_1 \\ r_2 \\ r_3 \\ r_4 \end{pmatrix} = Fw = F \begin{pmatrix} \grave{P} \\ \grave{S} \\ \acute{P} \\ \acute{S} \end{pmatrix} \tag{4.44}$$

where **r** is the displacement-stress vector and

$$F = \frac{1}{\omega} \begin{pmatrix} \alpha k & \beta\nu & \alpha k & \beta\nu \\ \alpha\gamma & \beta k & -\alpha\gamma & -\beta k \\ -2\alpha\mu k\gamma & -\beta\mu(k^2+\nu^2) & 2\alpha\mu k\gamma & \beta\mu(k^2+\nu^2) \\ -\alpha\mu(k^2+\nu^2) & -2\beta\mu k\nu & -\alpha\mu(k^2+\nu^2) & -2\beta\mu k\nu \end{pmatrix} \times \begin{pmatrix} e^{-\gamma z} & 0 & 0 & 0 \\ 0 & e^{-\nu z} & 0 & 0 \\ 0 & 0 & e^{\gamma z} & 0 \\ 0 & 0 & 0 & e^{\nu z} \end{pmatrix} \tag{4.45}$$

The inverse matrix F^{-1} of the matrix F is given by:

$$F^{-1} = \begin{pmatrix} e^{\gamma z} & 0 & 0 & 0 \\ 0 & e^{\nu z} & 0 & 0 \\ 0 & 0 & e^{-\gamma z} & 0 \\ 0 & 0 & 0 & e^{-\nu z} \end{pmatrix} \times \frac{\beta}{2\alpha\nu\gamma\mu\omega} \times \begin{pmatrix} 2\beta\mu k\gamma\nu & -\beta\mu\nu(k^2+\nu^2) & -\beta k\nu & \beta\gamma\nu \\ -\alpha\mu\gamma(k^2+\nu^2) & 2\alpha\mu k\gamma\nu & \alpha\gamma\nu & -\alpha k\gamma \\ 2\beta\mu k\gamma\nu & \beta\mu\nu(k^2+\nu^2) & \beta k\nu & -\beta\gamma\nu \\ -\alpha\mu\gamma(k^2+\nu^2) & -2\alpha\mu k\gamma\nu & -\alpha\gamma\nu & -\alpha k\gamma \end{pmatrix} \tag{4.46}$$

The parameters α, β, μ, ν are layer dependent. For a n-layers over a half-space system, we can write

$$\begin{pmatrix} \grave{P} \\ \grave{S} \\ \acute{P} \\ \acute{S} \end{pmatrix}_{n+1} = F_{n+1}^{-1} \begin{pmatrix} r_1 \\ r_2 \\ r_3 \\ r_4 \end{pmatrix}_{n+1} \tag{4.47}$$

$$\begin{pmatrix} r_1 \\ r_2 \\ r_3 \\ r_4 \end{pmatrix}_{n+1} = \mathbf{P}_n \begin{pmatrix} r_1 \\ r_2 \\ r_3 \\ r_4 \end{pmatrix}_{n} \tag{4.48}$$

Receiver at the surface

Harmonic horizontal load: For a receiver at the surface, the boundary conditions for a harmonic horizontal load are the following:

$$\begin{pmatrix} r_1 \\ r_2 \\ r_3 \\ r_4 \end{pmatrix}_1 = \begin{pmatrix} g_{11} \\ g_{31}/i \\ -1 \\ 0 \end{pmatrix} \tag{4.49}$$

Harmonic vertical load: For a receiver at the surface, the boundary conditions for a harmonic vertical load are the following:

$$\begin{pmatrix} r_1 \\ r_2 \\ r_3 \\ r_4 \end{pmatrix}_1 = \begin{pmatrix} g_{13} \\ g_{33}/i \\ 0 \\ -1/i \end{pmatrix} \tag{4.50}$$

In the half-space, we have the following boundary conditions:

$$\begin{pmatrix} \grave{P} \\ \grave{S} \\ \acute{P} \\ \acute{S} \end{pmatrix} = \begin{pmatrix} \grave{P} \\ \grave{S} \\ 0 \\ 0 \end{pmatrix} \tag{4.51}$$

For the harmonic horizontal load we then have:

$$\begin{pmatrix} \grave{P} \\ \grave{S} \\ 0 \\ 0 \end{pmatrix} = F^{-1}\mathbf{P}_n\mathbf{P}_{n-1}...\mathbf{P}_1 \begin{pmatrix} g_{11} \\ g_{31}/i \\ -1 \\ 0 \end{pmatrix} = \mathbf{B} \begin{pmatrix} g_{11} \\ g_{31}/i \\ -1 \\ 0 \end{pmatrix} \tag{4.52}$$

and for the harmonic vertical load:

$$\begin{pmatrix} \grave{P} \\ \grave{S} \\ 0 \\ 0 \end{pmatrix} = F^{-1}\mathbf{P}_n\mathbf{P}_{n-1}...\mathbf{P}_1 \begin{pmatrix} g_{13} \\ g_{33}/i \\ 0 \\ -1/i \end{pmatrix} = \mathbf{B} \begin{pmatrix} g_{13} \\ g_{33}/i \\ 0 \\ -1/i \end{pmatrix} \tag{4.53}$$

The following equations are therefore obtained for g_{11} and g_{33}:

$$g_{11} = \frac{B_{33}B_{42} - B_{32}B_{43}}{B_{31}B_{42} - B_{32}B_{41}} \tag{4.54}$$

and

$$g_{33} = \frac{B_{31}B_{44} - B_{34}B_{41}}{B_{31}B_{42} - B_{32}B_{41}} \tag{4.55}$$

The Green's function in 3D are then given by:

$$Im\left[G_{22}^{P-SV}(z,f)\right] = Im\left[G_{11}^{P-SV}(z,f)\right] = \frac{1}{4\pi}\int_0^\infty Im\left[g_{11}\right]kdk \tag{4.56}$$

$$Im\left[G_{33}^{P-SV}(z_F,f)\right] = \frac{1}{2\pi}\int_0^\infty Im\left[g_{33}\right]kdk \tag{4.57}$$

Receiver at depth

The displacement-stress vector can be decomposed as:

$$\begin{aligned}
\begin{pmatrix}\grave{\mathbf{W}}\\ \mathbf{0}\end{pmatrix} = \begin{pmatrix}\grave{P}\\ \grave{S}\\ 0\\ 0\end{pmatrix} = \begin{pmatrix}r_1\\ r_2\\ r_3\\ r_4\end{pmatrix}_{n+1} &= F^{-1}\mathbf{P}_n\mathbf{P}_{n-1}...\mathbf{P}_j \begin{pmatrix}r_1\\ r_2\\ r_3\\ r_4\end{pmatrix}_{j_+} = F^{-1}\mathbf{P}^d \begin{pmatrix}r_1\\ r_2\\ r_3\\ r_4\end{pmatrix}_{j_+} = \mathbf{B}\begin{pmatrix}r_1\\ r_2\\ r_3\\ r_4\end{pmatrix}_{j_+}\\
&= \begin{pmatrix}B11 & B12 & B13 & B14\\ B21 & B22 & B23 & B24\\ B31 & B32 & B33 & B34\\ B41 & B42 & B43 & B44\end{pmatrix}\begin{pmatrix}r_1\\ r_2\\ r_3\\ r_4\end{pmatrix}_{j_+} = \begin{pmatrix}\mathbf{B_{dd}} & \mathbf{B_{ds}}\\ \mathbf{B_{sd}} & \mathbf{B_{ss}}\end{pmatrix}\begin{pmatrix}r_1\\ r_2\\ r_3\\ r_4\end{pmatrix}_{j_+}\\
&= \begin{pmatrix}\mathbf{B_{dd}} & \mathbf{B_{ds}}\\ \mathbf{B_{sd}} & \mathbf{B_{ss}}\end{pmatrix}\begin{pmatrix}g_{11}\\ g_{31}/i\\ -\sigma_{h+}\\ 0\end{pmatrix}_{j_{+horizontalload}}\\
&= \begin{pmatrix}\mathbf{B_{dd}} & \mathbf{B_{ds}}\\ \mathbf{B_{sd}} & \mathbf{B_{ss}}\end{pmatrix}\begin{pmatrix}\mathbf{g_h}\\ \sigma_{\mathbf{h}+}\end{pmatrix}_{j_{+horizontalload}}
\end{aligned} \tag{4.58}$$

$$\begin{pmatrix}r_1\\ r_2\\ r_3\\ r_4\end{pmatrix}_{j_-} = \begin{pmatrix}g_{11}\\ g_{31}/i\\ -\sigma_{h-}\\ 0\end{pmatrix}_{j_{-horizontalload}}$$

$$= \begin{pmatrix}\mathbf{g_h}\\ \sigma_{\mathbf{h}-}\end{pmatrix}_{j_{-horizontalload}}$$

$$= \mathbf{P}_{j-1}...\mathbf{P}_1\begin{pmatrix}r_1\\ r_2\\ r_3\\ r_4\end{pmatrix}_1 = \mathbf{P}_{j-1}...\mathbf{P}_1\begin{pmatrix}u_s\\ w_s/i\\ 0\\ 0\end{pmatrix} = \mathbf{P}^u\begin{pmatrix}u_s\\ w_s/i\\ 0\\ 0\end{pmatrix} = \mathbf{P}^u\begin{pmatrix}\mathbf{D_s}\\ \mathbf{0_s}\end{pmatrix}$$

For a receiver at depth, the boundary conditions for the horizontal harmonic load are the following:

Boundary conditions at the surface:

$$\begin{pmatrix}r_1\\ r_2\\ r_3\\ r_4\end{pmatrix}_1 = \begin{pmatrix}u_s\\ w_s/i\\ 0\\ 0\end{pmatrix} = \begin{pmatrix}\mathbf{D_s}\\ \mathbf{0_s}\end{pmatrix} \tag{4.59}$$

horizontal harmonic load: Top layer at load

$$\begin{pmatrix}r_1\\ r_2\\ r_3\\ r_4\end{pmatrix}_{z_-} = \begin{pmatrix}g_{11}\\ g_{31}/i\\ -\sigma_-\\ 0\end{pmatrix} \tag{4.60}$$

Vertical harmonic load: For a receiver at the surface, the boundary conditions for the vertical harmonic load are the following:

$$\begin{pmatrix} r_1 \\ r_2 \\ r_3 \\ r_4 \end{pmatrix}_{z_-} = \begin{pmatrix} g_{13} \\ g_{33}/i \\ 0 \\ -\sigma_-/i \end{pmatrix} \tag{4.61}$$

horizontal harmonic load: bottom layer at load

$$\begin{pmatrix} r_1 \\ r_2 \\ r_3 \\ r_4 \end{pmatrix}_{z_+} = \begin{pmatrix} g_{11} \\ g_{31}/i \\ -\sigma_+ \\ 0 \end{pmatrix} \tag{4.62}$$

Vertical harmonic load: bottom layer at load

$$\begin{pmatrix} r_1 \\ r_2 \\ r_3 \\ r_4 \end{pmatrix}_{z_+} = \begin{pmatrix} g_{13} \\ g_{33}/i \\ 0 \\ -\sigma_+/i \end{pmatrix} \tag{4.63}$$

with

$$\sigma_{h+} - \sigma_{h-} = 1 \tag{4.64}$$

$$\sigma_{v+} - \sigma_{v-} = 1/i \tag{4.65}$$

Vertical harmonic force: For a receiver at the surface, the boundary conditions for the vertical load are the following:

In the half-space, we have the following boundary conditions:

$$\begin{pmatrix} \grave{P} \\ \grave{S} \\ \acute{P} \\ \acute{S} \end{pmatrix} = \begin{pmatrix} \grave{P} \\ \grave{S} \\ 0 \\ 0 \end{pmatrix} = \begin{pmatrix} \grave{\mathbf{W}} \\ \mathbf{0} \end{pmatrix} \tag{4.66}$$

The boundary conditions above lead to the equation:

$$\mathbf{g} = [\mathbf{B_{ss}^{-1}B_{sd}} + \mathbf{P_{sd}^{u}P_{dd}^{u-1}}]^{-1}\mathbf{J} \tag{4.67}$$

where

$$\mathbf{g} = \begin{pmatrix} g_{11} & g_{13} \\ g_{31} & g_{33} \end{pmatrix} \tag{4.68}$$

and

$$\mathbf{J} = \begin{pmatrix} -1 & 0 \\ 0 & -1/i \end{pmatrix} \tag{4.69}$$

The explicit relationships for g_{11} and g_{33} are therefore:

$$g_{11} = \frac{\frac{d}{det(\mathbf{B_{ss}})} + \frac{h}{det(\mathbf{P^u_{dd}})}}{\left(\frac{a}{det(\mathbf{B_{ss}})} + \frac{e}{det(\mathbf{P^u_{dd}})}\right) \times \left(\frac{d}{det(\mathbf{B_{ss}})} + \frac{h}{det(\mathbf{P^u_{dd}})}\right) - \left(\frac{c}{det(\mathbf{B_{ss}})} + \frac{g}{det(\mathbf{P^u_{dd}})}\right) \times \left(\frac{b}{det(\mathbf{B_{ss}})} + \frac{f}{det(\mathbf{P^u_{dd}})}\right)} \tag{4.70}$$

and

$$g_{33} = \frac{\frac{a}{det(\mathbf{B_{ss}})} + \frac{e}{det(\mathbf{P^u_{dd}})}}{\left(\frac{a}{det(\mathbf{B_{ss}})} + \frac{e}{det(\mathbf{P^u_{dd}})}\right) \times \left(\frac{d}{det(\mathbf{B_{ss}})} + \frac{h}{det(\mathbf{P^u_{dd}})}\right) - \left(\frac{c}{det(\mathbf{B_{ss}})} + \frac{g}{det(\mathbf{P^u_{dd}})}\right) \times \left(\frac{b}{det(\mathbf{B_{ss}})} + \frac{f}{det(\mathbf{P^u_{dd}})}\right)} \tag{4.71}$$

Where

$$\begin{aligned}
det(\mathbf{B_{ss}}) &= B_{ss11}B_{ss22} - B_{ss12}B_{ss21} = B_{33}B_{44} - B_{34}B_{43} \\
det(\mathbf{P^u_{dd}}) &= P^u_{dd11}P^u_{dd22} - P^u_{dd12}P^u_{dd21} = P^u_{11}P^u_{22} - P^u_{12}P^u_{21} \\
a &= B_{ss22}B_{sd11} - B_{ss21}B_{sd21} = B_{44}B_{31} - B_{43}B_{41} \\
b &= B_{ss22}B_{sd12} - B_{ss21}B_{sd22} = B_{44}B_{32} - B_{43}B_{42} \\
c &= -B_{ss12}B_{sd11} + B_{ss11}B_{sd21} = -B_{34}B_{31} + B_{33}B_{41} \\
d &= -B_{ss12}B_{sd12} + B_{ss11}B_{sd22} = -B_{34}B_{32} + B_{33}B_{42} \\
e &= P^u_{dd22}P^u_{sd11} - P^u_{dd12}P^u_{sd12} = P^u_{22}P^u_{31} - P^u_{12}P^u_{32} \\
f &= -P^u_{sd11}P^u_{dd21} + P^u_{sd12}P^u_{dd11} = -P^u_{31}P^u_{21} + P^u_{32}P^u_{11} \\
g &= P^u_{sd21}P^u_{dd22} - P^u_{sd22}P^u_{dd12} = P^u_{41}P^u_{22} - P^u_{42}P^u_{12} \\
h &= -P^u_{sd21}P^u_{dd21} + P^u_{sd22}P^u_{dd11} = -P^u_{41}P^u_{21} + P^u_{42}P^u_{11}
\end{aligned} \tag{4.72}$$

The Green's function in 3D are then given by:

$$Im\left[G^{P-SV}_{22}(z,f)\right] = Im\left[G^{P-SV}_{11}(z,f)\right] = \frac{1}{4\pi}\int_0^\infty Im\left[g_{11}\right] kdk \tag{4.73}$$

$$Im\left[G^{P-SV}_{33}(z_F,f)\right] = \frac{1}{2\pi}\int_0^\infty Im\left[g_{33}\right] kdk \tag{4.74}$$

4.D Pseudo 4x4 propagator matrix for a water layer on top of a layered elastic media

In presence of a water layer, characterized by a shear stress $\mu = 0$, only P-waves contribute to the Green's function estimation.

Starting from the wave equation for the P-SV case, it can be demonstrated that:

$$r_1 = \frac{k}{\rho\omega^2} r_4 \tag{4.75}$$

and

$$\begin{aligned}\frac{\partial r_4}{\partial z} &= -\rho\omega^2 r_2 \\ \frac{\partial r_2}{\partial z} &= \frac{1}{\rho\omega^2}\,(-k^2+\frac{\omega^2}{\alpha^2}\,)r_4\end{aligned} \tag{4.76}$$

$$\frac{d}{dz}\begin{pmatrix} r_2 \\ r_4 \end{pmatrix} = \begin{pmatrix} 0 & \frac{1}{\rho\omega^2}\,(-k^2+\frac{\omega^2}{\alpha^2}\,) \\ \mu k^2 - \rho\omega^2 & 0 \end{pmatrix}\begin{pmatrix} r_2 \\ r_4 \end{pmatrix} \tag{4.77}$$

This equation is of the form:

$$\frac{d\mathbf{r}}{dz} = \mathbf{A}\mathbf{r} \tag{4.78}$$

where $\mathbf{r} = \begin{pmatrix} r_2 \\ r_4 \end{pmatrix}$ and $\mathbf{A} = \begin{pmatrix} 0 & \frac{1}{\rho\omega^2}\,(-k^2+\frac{\omega^2}{\alpha^2}\,) \\ -k^2-\omega^2\rho & 0 \end{pmatrix}$.

The solution to Equation 4.78 at two points z_1 (at the water surface) and z_2 (at the ocean floor) is (Gantmacher, 1959; Gilbert & Backus, 1966; Aki & Richards, 2002):

$$\begin{pmatrix} r_2 \\ r_4 \end{pmatrix}_{z_2} = \mathbf{P}\begin{pmatrix} r_2 \\ r_4 \end{pmatrix}_{z_1} \tag{4.79}$$

where

$$P = \begin{pmatrix} \cosh\nu(z_2-z_1) & -\frac{\nu}{\rho\omega}\sinh\nu(z_2-z_1) \\ -\frac{\rho\omega^2}{\nu}\sinh\nu(z_2-z_1) & \cosh\nu(z_2-z_1) \end{pmatrix} \tag{4.80}$$

To obtain the pseudo 4x4 matrix, we rewrite Equation 4.79 as follow (Herrmann, 2008)

$$\begin{pmatrix} r_1|_{z_2} \\ r_2|_{z_2} \\ r_3|_{z_2} \\ r_4|_{z_2} \end{pmatrix} = \begin{pmatrix} 1 & 0 & 0 & 0 \\ 0 & \cosh\nu(z_2-z_1) & 0 & -\frac{\nu}{\rho\omega}\sinh\nu(z_2-z_1) \\ 0 & 0 & 1 & 0 \\ 0 & -\frac{\rho\omega^2}{\nu}\sinh\nu(z_2-z_1) & 0 & \cosh\nu(z_2-z_1) \end{pmatrix}\begin{pmatrix} r_1|_{z_2} \\ r_2|_{z_1} \\ r_3|_{z_2} \\ r_4|_{z_1} \end{pmatrix} \tag{4.81}$$

From this point, the algebra is again similar to the derivations presented earlier.

4.E H/V modeling using real Earth models: High frequency instability

In this section, Earth models obtain at two different marine sites are used to estimate the H/V spectral ratio. The first model is represented by a two-layer (one water layer - 10 m and one sedimentary layer - 60 m) over a halfspace (Table 4.E.1). This model is a very coarse one in comparison to the structure obtained by Ritzwoller & Levshin (2002). The exact location for this site was not provided because data were from an oil field. The second site is represented by a four-layer (one water later - 1475 m and three soft soil layers) overlaying a halfspace (Table 4.E.1). This model is obtained from Huerta-Lopez et al. (2003) and was obtained in the Golf of Mexico.

The H/V modeling results at four randomly selected depths for the two sites are represented in Figure 4.E.1a and Figure 4.E.1b. present the H/V modeling results at four randomly selected depths for the two models.

$h(m)$	$Vp(m/s)$	$Vs(m/s)$	$\rho(kg/m^3)$	Q_P	Q_S
Coarse model defined from Ritzwoller & Levshin (2002)					
10	1500	0	1000	9999	9999
60	1600	300	1500	50	50
∞	1710	400	1700	50	50
Model defined from Huerta-Lopez et al. (2003)					
1475	1500	0	1000	9999	9999
5	1300	90	1300	50	50
10	1400	190	1400	50	50
35	1700	400	1700	50	50
∞	3000	2100	2000	50	50

Table 4.E.1: Seismic parameters defining the two structures derived from Ritzwoller & Levshin (2002) and Huerta-Lopez et al. (2003).

For the coarse model derived from Ritzwoller & Levshin (2002), no clear identification of the H/V peak is observed. This is because there is no strong impedance contrast between the sediment layer and the assumed halfspace. For the receivers at 70 and 100 m depth, the instability issue is manifested for frequencies above approximately 25 Hz.

For the model derived from Huerta-Lopez et al. (2003), the algorithm collapses for frequencies larger than approximately 4 Hz. In comparison to H/V modeling results for the receiver at the seafloor, the discrepancies in the low frequency may be attributed to the actual attenuation parameters of the site.

The observed instability at high frequencies for estimating P-SV Green's function using the propagator matrix formulation is a well known situation in computation seismology (Dunkin, 1965). Two methods have been proposed to address this high frequencies instability issue (e.g. Dunkin, 1965; Wang, 1999). As pointed out by Dunkin (1965), his method can be computationally intensive. For the next step, we intend to use the approach by Wang (1999) who suggest to insert an additional numerical procedure into the matrix propagation loop. The numerical procedure makes the displacement vector in situ orthogonal and consequently leading to a non-vanishing subdeterminant.

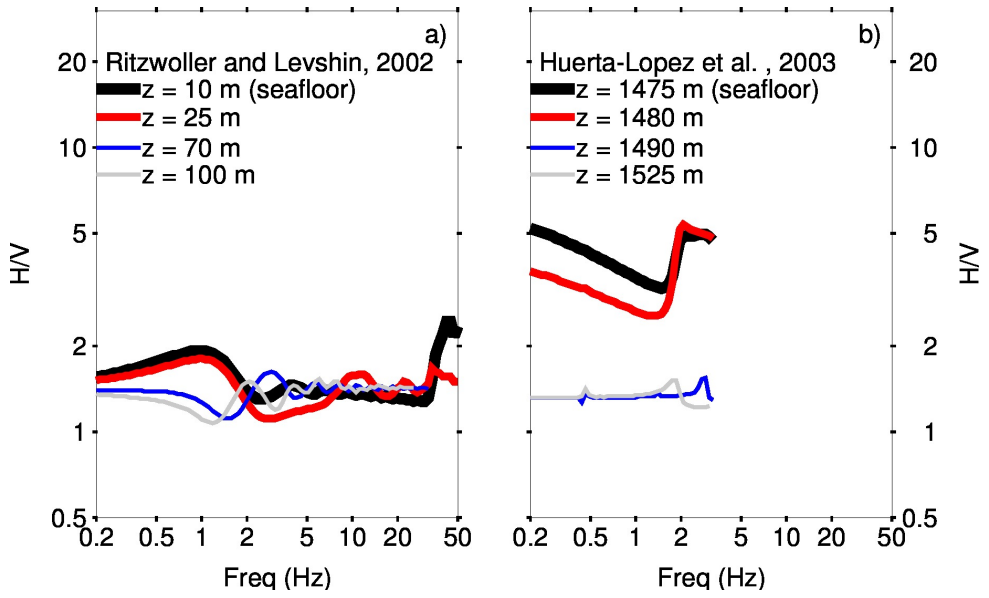

Figure 4.E.1: a) H/V spectral ratio estimated at four depths from the coarse model derived from Ritzwoller & Levshin (2002). The test site location is unknown. b) H/V spectral ratio estimated at four depths from the coarse model derived from Huerta-Lopez et al. (2003). The test site is located in the Golf of Mexico.

Chapter 5

Combining surface wave phase velocity dispersion curves and full microtremor horizontal-to-vertical spectral ratio for subsurface sedimentary site characterization

Lontsi, A.M, M. Ohrnberger, F. Krüger, F.J. Sánchez-Sesma, 2016. *Interpretation*, `http://dx.doi.org/10.1190/INT-2016-0021.1`.
Publisher: Society of Exploration Geophysics and American Association of Petroleum Geologists.

5.1 Abstract

Seismic velocity profiles are computed by a combined inversion of surface-wave phase-velocity dispersion curves together with the full spectrum of the microtremor horizontal-to-vertical (H/V) spectral ratio at two sediment-covered sites in Germany. The sediment deposits are $\sim$ 100 m thick at the first test site and $\sim$ 400 m thick at the second test site. We used an extended physical model based on the diffuse wavefield assumption for the interpretation of the observed microtremor H/V spectral ratio. The extension includes the interpretation of the microtremor H/V spectral ratio observed at depth (in boreholes). This full wavefield approach accounts for the energy contribution from both body and surface waves and thus allows for inverting the properties of the shallow subsurface. The multi-mode phase velocity dispersion curves are obtained from an independent study and a description of the extracted branches and their interpretation is presented. The inversion results indicate that the combined approach using seismic ambient noise and actively generated surface-wave data will improve the accuracy of the reconstructed near-surface velocity model, a key step in microzonation, geotechnical engineering, seismic statics corrections and reservoir imaging.

5.2 Introduction

Characterizing the subsurface down to depths of tens to few hundreds of meters is of particular interest in geotechnical engineering, seismic exploration and engineering seismology. The often low-velocity

characteristics of the sediments overlying the bedrock can be a waveguide that can promote strong site effects (see e.g. Aki, 1993; Parolai, 2012). The determination of physical parameters for those depth ranges is important in global seismology observations at high frequencies where site effects are often neglected in seismic waveform modeling. In exploration seismology the interest of the shallow environment is in obtaining starting acoustic velocity models for static seismic corrections and its impact on reservoir imaging.

Using seismic ambient-noise recordings at small aperture arrays and the a priori assumption of a dominant Rayleigh-wave contribution to the seismic wavefield, the local shear-wave velocity (Vs) can be derived by the inversion of spatial autocorrelation curves (Aki 1957; Asten et al. 2004; Wathelet et al. 2005) or phase-velocity dispersion curves in the frequency-wavenumber ($f-k$) domain (e.g. Tokimatsu et al., 1992; Cornou et al., 2006; Garofalo et al., 2016b; Lontsi et al., 2016a). A broad spectrum and a better interpretation of the dispersion curve branches can be obtained by complementing seismic ambient noise (also known as passive seismic or microtremor) data with actively acquired seismic data (e.g. Rix et al., 2002; Asten & Boore, 2005; Renalier et al., 2009; Lontsi et al., 2016a) and more recently with the Greens' functions data estimates from the ambient noise wavefield (Lontsi et al., 2016a). The $f-k$ analysis applied to active seismic data is also known as Multichannel Analysis of Surface Waves method (MASW; Park et al. 1999), whereas the same technique applied to the estimated cross-correlation Green's functions is termed Interferometric MASW (IMASW; O'Connell & Turner, 2011).

Although surface wave methods are widely used for determining the local shear-wave velocity profile there is a high probability of misinterpretation of the inversion results due to the nonlinearity and the non-uniqueness of the inverse problem. A remedy for improving upon the non-uniqueness of the problem consists in taking additional information into account. Using microtremor data, the single station H/V spectral ratio (Nakamura, 1989; Bard, 1998; Bonnefoy-Claudet et al., 2006a) appears to be of particular interest.

The interpretation of parts of the microtremor H/V spectral ratio in terms of Rayleigh wave ellipticity has been adapted to derive 1D shear-wave velocity profiles (e.g. Fäh et al., 2003; Arai & Tokimatsu, 2004). Scherbaum et al. (2003) suggested to combine the microtremor H/V spectral ratio and the dispersion curve in a joint inversion. This approach is sound, but is mainly limited by the model for the interpretation of the microtremor H/V spectral ratio. When trying to fit the microtremor H/V spectral ratio shape, the approach requires assigning a frequency-dependent percentage of Rayleigh and Love contributions to the wavefield resulting in the observed microtremor H/V spectrum.

Methodologies have been developed to extract the Rayleigh wave constituent part from the observed microtremor H/V spectral ratio (Hobiger et al., 2009a; NERIES, 2010). The extraction methodology also provides information on higher-mode ellipticity (Poggi & Fäh, 2010; Maranò et al., 2012; Hobiger et al., 2012). This practical aspect is very important for the understanding of the structure of the observed microtremor H/V spectral ratio and for the analysis of the recorded microtremor data purely from the surface-wave view.

As opposed to partial wavefield interpretation of the estimated microtremor H/V spectral ratio, i.e, Rayleigh wave ellipticity, percentage of Rayleigh and Love waves, SH-response, or Rayleigh wave extraction, there is the full wavefield (FW) technique which is a relatively new approach for site investigation. Using the FW technique we seek the interpretation of the complete spectrum of the observed microtremor H/V spectral ratio. The approach presents the advantage that there is no background assumption regarding the noise wavefield composition.

Under the diffuse field approximation and assuming the source and the receiver are at the same location, it is possible to estimate the Directional Energy Density (DED) by correlating a component of the displacement wavefield with itself (Sánchez-Sesma & Campillo, 2006a; Sánchez-Sesma et al., 2006, 2008a). The DED is proportional to the imaginary part of the Green's function and therefore accounts

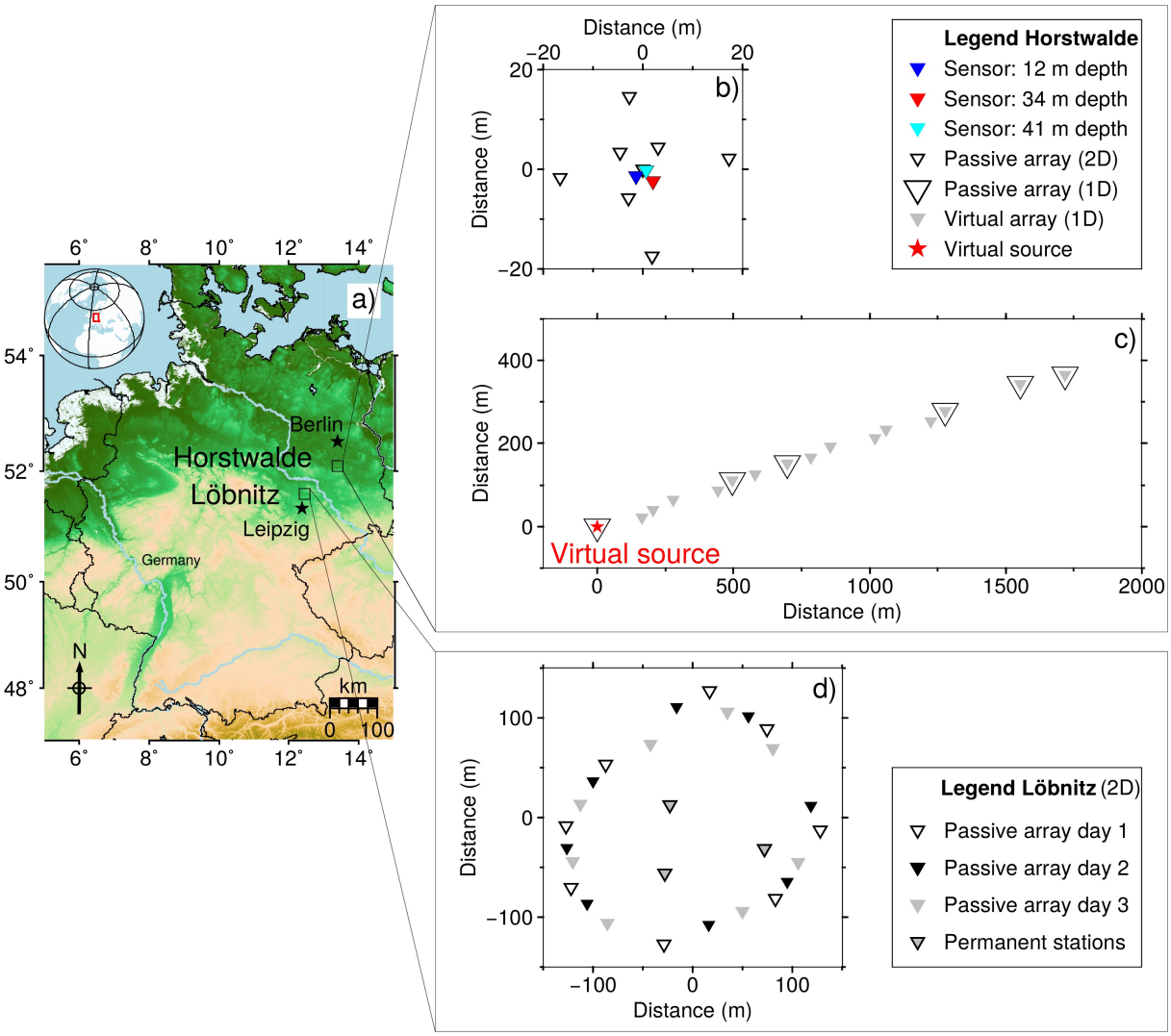

Figure 5.1: a) Test sites location within Germany. b) Small aperture 2D seismic array with borehole locations. The colored station positions mark borehole sensors used for the estimation of the H/V spectral ratio at depths. c) Non-redundant 1D seismic array (empty triangles) and corresponding virtual array (filled triangles). d) Final array configuration at the Löbnitz test site where there is no borehole sensor.

for the energy contributions from both body and surface waves. This "full wavefield" model has now been extended for the interpretation of the microtremor H/V spectral ratio from borehole observations (Lontsi et al., 2015).

Here we propose a combined inversion of the dispersion curves (including higher modes) together with the full microtremor H/V(z,f) spectral ratio computed at the surface and at depth to determine the velocity profiles at the test sites in Löbnitz and Horstwalde, Germany. We expect the results of this investigation to have some significant implications in the development of techniques using actively generated surface waves and/or ambient-noise data for deriving high-quality near-surface velocity models.

5.3 Test sites, data sets and processing

To obtain a broad spectrum and interpretable range of dispersion curves, active and passive seismic experiments were conducted at two test sites within Germany. The first site is at Löbnitz, located approximately 30 km north of Leipzig, and the second site is at the Technical Safety Test site (TTS) of the Federal Institute for Materials Research and Testing (BAM) in Horstwalde, located approximately

Code/ Geometry	# stat.	D_{min} (m)	D_{max} (m)	k_{min} (rad/m)	Recording length	Method	f_{min} (Hz)	f_{max} (Hz)
Löbnitz								
L12P1/2D	11	62	258	0.024	20.5 hours	passive-fk	1.5	3.5
L12P2/2D	11	59	248	0.025	20.5 hours	passive-fk	1.5	3.5
L12P3/2D	11	58	243	0.026	24.5 hours	passive-fk	1.5	3.5
L12CGF/1D	165	58	258	0.024	$\sim$ 1 day / 4 sec	IMASW	1.6	8
L12A/1D	144	1	144	0.16	1.05 sec	MASW	8	25
Horstwalde								
H11D/2D	8	5	34	0.18	3.5 hours	passive-fk	6	20
H11CGF/1D	15	165	1760	0.004	3 days / 10 sec	IMASW	0.6	3.4
H12A/1D	96	1	96	0.21	0.75 sec	MASW	8	35

Table 5.1: Characteristics of the arrays deployed at the test sites in Löbnitz and Horstwalde. The recording length and the estimated phase-velocity frequency ranges are reported (modified after Lontsi et al., 2016a).

50 km south of Berlin (Figure 5.1a). The very shallow sub-subsurface at both sites is mainly composed of quaternary sediment deposits.

5.3.1 Löbnitz: Data survey and processing

At the test site in Löbnitz, one active seismic experiment (L12A) and three passive seismic experiments (L12P1, L12P2, L12P3) were conducted. A 5 kg sledgehammer served as a source in the active experiment. 144 vertical geophones, with a 4.5 Hz corner frequency, were used to record the generated surface waves. Geophones were deployed with 1 m spacing and recorded at 2 kHz for 1.05 s. The source-to-first-receiver offset was set to 20 m. This was important to reduce the nearfield effects and to ensure the validity of plane-wave approximation of the recorded surface waves (Stokoe et al., 1994). From this setting, the maximum estimated wavelength in the active experiment was $\sim$ 25 m (Figure 5.2a), well within the interpretable range limits (Stokoe et al., 1994).

For the ambient-noise experiment, a total of 11 three-component Lennartz LE-3D type sensors were used. Eight stations with 5 s corner frequency were placed in a circular geometry (see outer circle in Figure 5.1d) with $\sim$ 260 m aperture. Three stations with a 1 s corner frequency were arranged in a triangular geometry, but with a smaller aperture of $\sim$ 110 m as the permanent backbone (Figure 5.1d). The outer configuration, L12P1, was rotated anticlockwise twice during the seismic campaign to obtain the experiments L12P2 and L12P3, respectively. The recordings were digitized at 100 Hz sampling rate for $\sim$ 24 hrs in each experiment. Table 5.1 gives a summary of the seismic experiment (array geometry, number of stations, recording length, minimum and maximum apertures) together with the array properties (aliasing and resolution limits). The aliasing is related to the minimum receiver pair spacing (D_{min}) and the resolution limit, defined by the capability of the array to separate waves propagating at close wavenumbers, is related to the array aperture. We refer to this resolution limit as κ_{min} that can be estimated from the array response function (Woods & Lintz, 1973; Asten & Henstridge, 1984; Cornou et al., 2006; Di Giulio et al., 2006).

A virtual active seismic experiment (L12CGF) is obtained from the passive recordings L12P1, L12P2 and L12P3 by applying interferometric principles (Snieder, 2004; Curtis et al., 2006; Gouédard et al., 2008b; Schuster, 2009; Wapenaar et al., 2010) to estimate the correlation Green's function between the different interstation pairs. In the pre-processing steps, a one bit normalization (Bensen et al., 2007) was used to remove the effect of any possible transient signal and a simulation filter (Seidl, 1980) was used to homogenize the instrument responses of the two distinct sensors.

The frequency - wavenumber ($f - k$) method was then applied to the active, passive and virtual

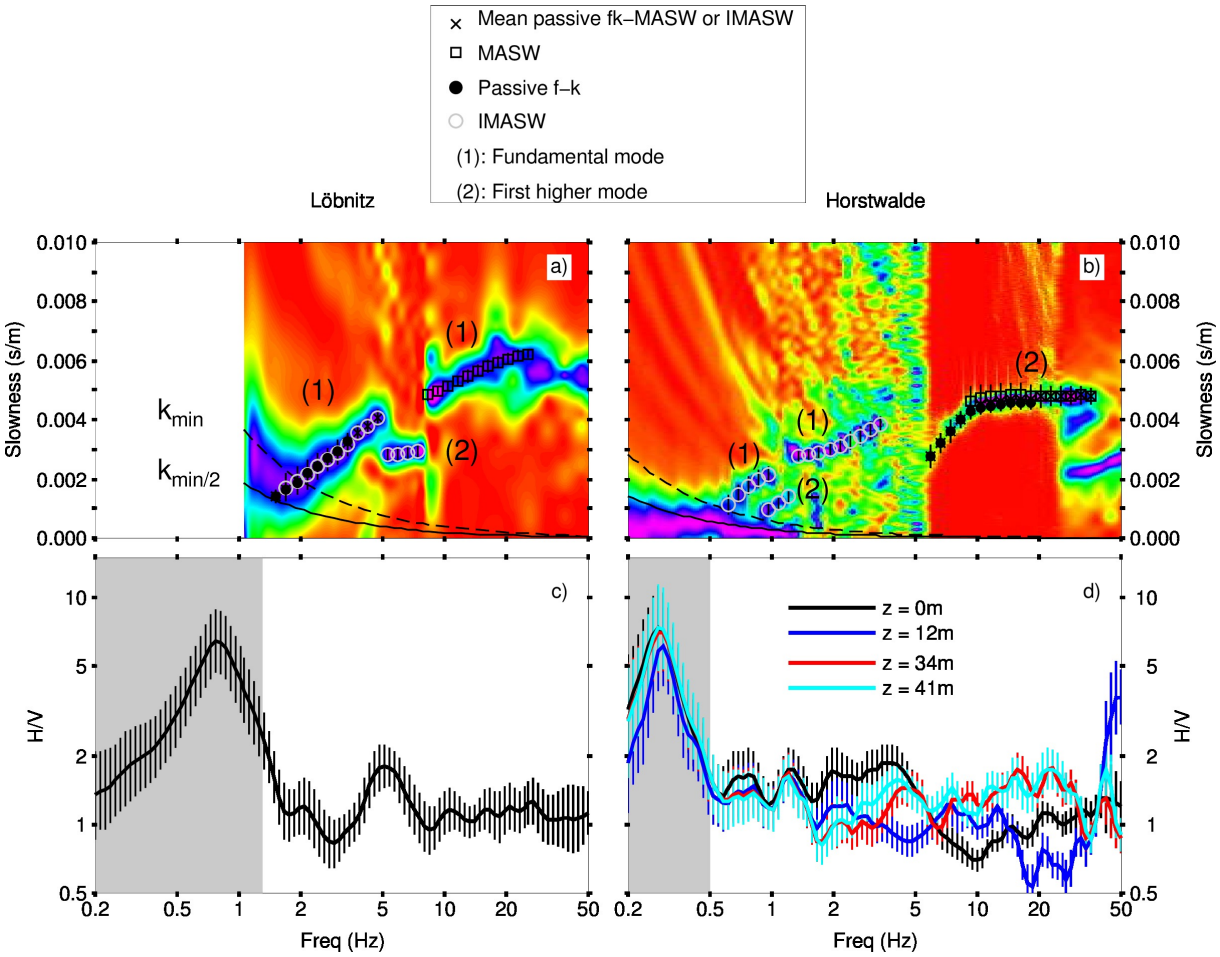

Figure 5.2: a) Dispersion curve estimates at the test site in Löbnitz. b) Dispersion curve estimates at the test site in Horstwalde. c) Average microtremor H/V spectral ratio estimated from a single station located at the surface at Löbnitz. d) Average microtremor H/V spectral ratio estimated from a single station at Horstwalde. The receivers are located at the surface, and at depths of 12 m, 34 m and at 41 m. (1) and (2) in a) and b) indicate the interpreted fundamental and first-higher modes, respectively. Vertical bars in the picked dispersion curves and the average microtremor H/V spectral ratio curves standard deviation of the data errors. The gray area around the microtremor H/V peak at low frequencies indicates additional information that is useful for bedrock depth interpretation.

active seismic (obtained from the estimated correlation Green's functions) data sets to obtain the partial dispersion curve branches of the propagating surface waves (Lontsi et al., 2016a). We interpret the fundamental and first higher modes spanning the frequency range from 1.5 to 25 Hz (Figure 5.2a).

At the Löbnitz site, no borehole information is available and the microtremor H/V spectral ratio was estimated for a surface receiver only (Figure 5.2c).

5.3.2 Horstwalde: Data survey and processing

At the site in Horstwalde, a 5 kg sledgehammer was used as a source in the active experiment (H12A) to generate surface waves. The generated signal was recorded using 96 vertical component geophones (with 4.5 Hz corner frequency) at a 4 kHz sampling rate for 0.75 s. The geophones were spaced 1 m apart and 16 m was the source-to-first-receiver offset. From this setting the maximum interpretable wavelength was $\sim$ 26 m (Figure 5.2b), and therefore also well within the interpretable range limits (Stokoe et al., 1994).

For the passive survey, a small aperture 2D seismic array with approximately 40 m in width was deployed in March 2011 (Figure 5.1b; colored stations indicate borehole locations). The array was

equipped with a set of eight wireless acquisition units (Ohrnberger et al., 2006), each composed of a 3C Lennartz LE-3D 5 s sensor and a datalogger digitizing at 100 Hz. After applying the passive $f-k$ method, an average dispersion curve for the 2D array setup is obtained between 6 and 20 Hz (Figure 5.2b).

In the second passive survey, we use a non-redundant 1D array (e.g. Johnson & Dudgeon, 1992), with a 1760 m aperture (Figure 5.1c), consisting of six 3C Lennartz LE-3D 1 s sensors recording at 200 Hz. This geometry was used to approximate a virtual-shot gather with approximately equidistant (virtual) sensor spacing of $\sim$ 100 to 150 m. Given the real test-site environment, equidistant of the virtual positions could not be achieved, but a rather homogeneous spatial sampling of the co-array is evident (Figure 5.1c). The noise recordings were obtained for three consecutive days and the recordings digitized using Reftek 130. We then obtain the corresponding 15 cross-correlation Green's functions, which, assuming a 1D media, are sorted with the interstation distance in a virtual array setup and processed in a way similar to the MASW method, referred to as Interferometric Multichannel Analysis of Surface Waves (IMASW). The obtained dispersion curves, ranging from $\sim$ 0.6 to $\sim$ 3.4 Hz, are represented by the gray dots in Figure 5.2b.

The estimated dispersion curve branches from the different data sets are combined and interpreted as the fundamental mode and the first-higher mode (Lontsi et al., 2016a). They are marked with (1) and (2) in Figure 5.2a-5.2b, respectively.

In comparison to Löbnitz where only the surface-microtremor H/V spectral-ratio information is available, there are microtremor H/V spectral-ratio results from three shallow boreholes located at the site in addition to the surface sensor (Figure 5.1b). From the observations, the fundamental peak frequency of the microtremor H/V spectral ratio is $\sim$ 0.8 Hz at Löbnitz (Figure 5.2c) and $\sim$ 0.28 Hz at Horstwalde (Figure 5.2d). For both sites, no clear surface-wave energy is observed around the fundamental frequency in the obtained dispersion curves. Additional information from the low-frequency part of the observed microtremor H/V spectral-ratio (gray area in Figure 5.2c,d) could therefore be useful for improving the bedrock depth resolution.

5.4 Inversion procedure

We briefly describe the algorithms used for the interpretation of both the dispersion curves and the microtremor H/V spectrums. This description of methods is followed by a short explanation of the combined inversion procedure applied to the two data sets.

5.4.1 Rayleigh wave phase velocity physical interpretation

The clear identification of the dispersion curve branches over large frequency ranges (Figure 5.2a-5.2b) suggests that the 1D media approximation, consisting of a stack of homogeneous layers, for the investigated sites could be considered valid.

Given the layers seismic properties (compressional-wave velocity, shear-wave velocity, attenuation parameters, density and thickness for each layer), the Rayleigh-wave phase-velocity-dispersion curves are obtained by solving the eigenvalue problem associated with the radiation condition in the half-space and the stress-free motion at the surface for the propagating P-SV wavefield. The approach using the propagator matrix (Thomson, 1950; Haskell, 1953; Dunkin, 1965; Aki & Richards, 2002, Chapter 7) was used to obtain the secular equation. For a given frequency, the roots of the secular equation for distinct modes provide the dispersion curves of interest. The algorithm as implemented in the software package geopsy (Wathelet, 2005), available at `http://www.geopsy.org/` (Last accessed: February 23, 2017), is used to compute the dispersion curves.

5.4.2 Full microtremor H/V(z,f) physical interpretation

Assuming the source and the receiver positions are the same, the microtremor H/V(z,f) spectrum for a given position (surface or depth), is computed using equation 5.1 (Sánchez-Sesma et al., 2011a).

$$H/V(z,f) = \sqrt{\frac{E_1(z,f)+E_2(z,f)}{E_3(z,f)}}, = \sqrt{\frac{Im[G_{11}(z,z,f)]+Im[G_{22}(z,z,f)]}{Im[G_{33}(z,z,f)]}}, \tag{5.1}$$

where

$$E_m(z,f) \propto \langle u_m(z,f) {u_m}^*(z,f) \rangle, \tag{5.2}$$

is the directional energy density spectrum along a polarization direction m ($m \in 1,2,3$) and

$$\langle u_m(z,f) u_m^*(z,f) \rangle \propto Im[G_{mm}(z,z,f)]. \tag{5.3}$$

The symbol $*$ stands for the complex conjugate and the angular brackets for the azimuthal average. In equations 5.1 and 5.3, G_{mm} represents the medium response in the direction m to a harmonic concentrated load acting in the same direction. In the time domain it corresponds to an impulsive load.

5.4.3 Inversion algorithm

We use the improved non-linear direct search neighborhood algorithm (Wathelet, 2008), modified after Sambridge (1999) to account for complex boundaries and parameter conditions. The parameter space is densely sampled in orded to simultaneously invert both the fundamental and first higher modes of the dispersion curves together with the full microtremor H/V spectral curves.

As compared to linearized methods (Menke, 1989; Aster et al., 2011), the neighborhood algorithm (NA) is a derivative-free stochastic method for obtaining models of acceptable data fit in the parameter space (Sambridge, 1999). Different from the Uniform Monte Carlo, genetic algorithm, evolutionary programming or simulated annealing (for a review of these algorithms and their application to geophysical problems, see Sambridge & Mosegaard, 2002), the NA uses information from all previous model samples (states) to guide the space sampling.

The inversion starts with an ensemble of $n_{s0} = 50$ random samples in the parameter space. The Voronoi concept (Voronoi, 1908) is used by the neighborhood algorithm to partition the parameters space into cells, where cells are the nearest neighbor regions in the parameter space subject to an appropriate distance norm. In each step, $n_s = 50$ new models are generated and added to the best previous models. Then, the best $n_r = 50$ are retained as the next sampling area in which new $n_s = 50$ models are generated in the next iteration (Wathelet, 2008). We consider a total of 50 steps as the maximum number of iterations. The complete inversion process is repeated at least four times to ensure a good exploration and exploitation of the parameter space (Sambridge, 1998). A total of 30460 models have been generated for the test site in Löbnitz and 10408 for the test site in Horstwalde.

A number of similar models, defined qualitatively from the trend between modeled and experimental data and quantitatively for models fitting the data within one standard deviation, are selected and presented as the best solution of our inversion.

The misfit between the current model sample and the actual data is computed using the following equations 5.4-5.7.

$$misfit = \sqrt{(\eta \cdot dcmisfit)^2 + ((1-\eta) \cdot hvmisfit)^2}, \tag{5.4}$$

where

$$hvmisfit = \sum_{j=1}^{M} \frac{1}{M} \sqrt{\frac{1}{N} \sum_{i=1}^{N} \frac{(ln(\frac{H}{V}_{m_{ij}}) - ln(\frac{H}{V}_{d_{ij}}))^2}{\sigma_{d_{ij}}^2}}, \tag{5.5}$$

$$dcmisfit = \sqrt{\sum_{m=0,1} w_m^2 \sum_{i=1}^{n_m} \frac{(v_{dmi} - v_{cmi})^2}{n_m \sigma_{mi}^2}} \ , \tag{5.6}$$

$$\begin{aligned} w_0 &= n_1/(n_0 + n_1), \\ w_1 &= n_0/(n_0 + n_1). \end{aligned} \tag{5.7}$$

N in equation 5.5 is the total number of frequency points defining the observed $\frac{H}{V}_d$ and modeled $\frac{H}{V}_m$. $\sigma_{d_{ij}}$ is the standard deviation of observed data for j^{th} receiver of i^{th} frequency. M is the total number of receivers used in the computation of the microtremor H/V spectral ratio at each site. For Löbnitz $M = 1$ (one receiver at the surface only) and for Horstwalde $M = 4$ (one receiver at surface and three at depth). The use of the natural logarithm (ln) in equation 5.5 is important to avoid overweighting strong peaks in the microtremor H/V spectral ratio. n_m, with $m = (0, 1)$, in equation 5.6 is the number of effective frequency points for the mode m contributing to the inversion. Both n_0 and n_1 are used to define the weight w_m for the mode m (equation 5.7). σ_{mi} is the standard deviation of observed data for m^{th} dispersion curve mode of i^{th} frequency. An overall weighting factor (η), equal to 0.6 in Löbnitz and 0.5 in Horstwalde, is considered for the overall global misfit.

5.5 Inversion results

Starting with the phase velocity dispersion curves and the microtremor H/V spectral ratio data estimated at Löbnitz and Horstwalde (Figure 5.2), we inverted for the seismic S- and P-wave velocity profiles. The density, and the quality factor for P- and S-waves in each layer were set constant during the inversion.

5.5.1 Löbnitz

For this site, we obtain a good match between the actual dispersion curves and the modeled synthetic ones within the range of acceptable models (Figures 5.3a-5.3b). This is especially true for the first higher mode and to a less extent for the fundamental mode. A good agreement is observed for the microtremor H/V spectral ratio estimated at the surface (Figure 5.3c).

Results indicate smooth S- and P-wave velocity profiles down to the estimated bedrock depth (strong impedance contrast) at $\sim$ 105 m below the surface with higher uncertainty. The Vs estimates range from $\sim$ 190 m/s in the very shallow layer to $\sim$ 900 m/s below 105 m and the Vp estimates range from $\sim$ 500 m/s in the very shallow layer to $\sim$ 2200 m/s below 105 m.

Results from the inversion of the dispersion curves (Lontsi et al., 2016a), independently of the microtremor H/V spectral ratio observation, are overlaid as solid gray lines for comparison and show good agreement down to $\sim$ 100 m. Below this depth, the S-wave velocity information is more accurately estimated with the combined inversion and the estimated values are characteristic of sedimentary environments.

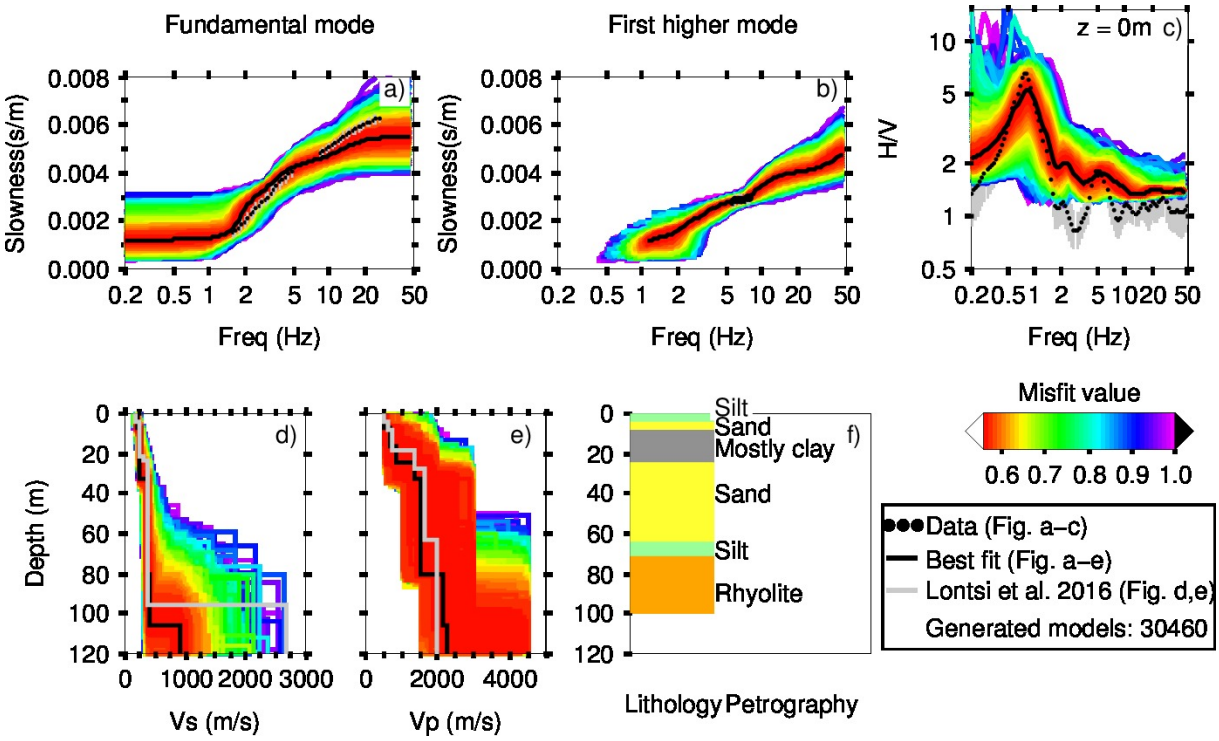

Figure 5.3: Inversion results at the test site in Löbnitz. For all models with a misfit value lower than 1, the Vs and Vp profiles are presented. a) and b) provide the best fit for the fundamental and first higher modes of the dispersion curves, respectively. c) presents the best solutions for the microtremor H/V spectral ratio at the surface. d) and e) present the resulting best Vs and Vp velocity profiles. f) presents the geological-log information available for the site.

5.5.2 Horstwalde

At the Horstwalde site, a good agreement is found between the measured dispersion curves and the modeled ones. Here, the match is better for the fundamental mode. Good agreement is also observed for the microtremor H/V spectral ratio shape at the lower frequencies for receivers at the surface and at 12 m depth. The models present very good agreement with data recorded at the depths of 34 m and 41 m (see Figure 5.4). Results indicate smooth S- and P-wave velocity profiles down to the bedrock (strong impedance contrast) at about 420 m. This corresponds to the clay - marl interface. The Vs values estimated at this site range from $\sim$ 160 m/s in the very shallow layer to $\sim$ 2400 m/s below 420 m. For Vp, the range varies from $\sim$ 260 m/s in the very shallow layer and $\sim$ 4030 m/s below 420 m. The results from this experiment are used to compare with estimates in the upper 12 m for Horstwalde (Linder et al., 2010; Tronicke et al., 2012; Rumpf & Tronicke, 2014) and Lontsi et al. (2015) for the overall sediment column down to approximately 400 m. The comparison with estimates by Lontsi et al. (2015) shows promising results for delineating the deep-sediment cover.

5.6 Suggestions for further study

Currently we are working on a detailed investigation of the high-frequency part of the microtremor H/V spectral ratio for receivers at the surface (Löbnitz and Horstwalde) and at 12 m depth (Horstwalde). We approach this by combining the results of this study and a linearized local search method. This study is the first for jointly inverting the phase-velocity dispersion curves and the microtremor H/V spectral ratios under full wavefield consideration to estimate the S- and P-velocity profiles. Both test sites are 1D and thus more field examples from well-studied sediment-covered environments, including 2D and 3D

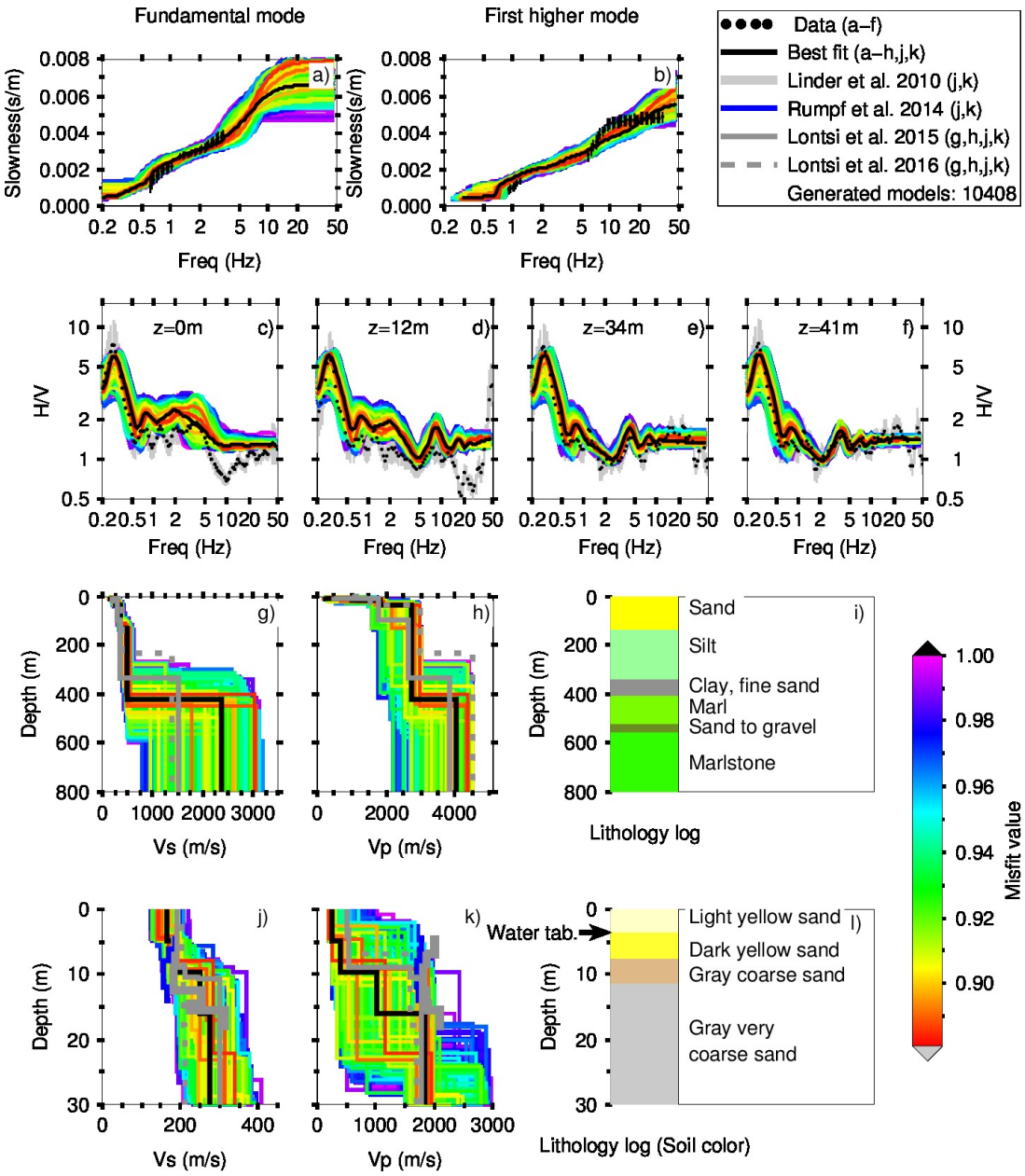

Figure 5.4: Inversion results for Horstwalde. Vs and Vp profiles are displayed when the misfit value is lower than 1. a) and b) show the best fit for the fundamental and first-higher modes, respectively. c)-f) are the best solutions for the microtremor H/V spectral ratio at the depths of 0 m, at 12 m, at 34 m and at 41 m. g) and h) are judged to be the most reliable Vs and Vp velocity profiles. The first 30 m is presented in j) for Vs and in k) for Vp. i) and l) present the available geological-log information.

geological features (e.g. dipping layer, fault, cavity), would be helpful in establishing confidence in this method. The weight contribution from the different data types deserves further scrutiny.

5.7 Conclusion

Starting with dispersion curve estimates using both active and ambient seismic noise data from arrays in 1D and 2D configurations, we were able to invert for the average Vs and Vp profiles. As indicated by the geological-log information, an improved depth resolution is obtained when considering microtremor H/V spectral ratio data in the inversion. The diffuse-field assumption allows for modeling the microtremor

H/V spectral ratio at any depth.

Acknowledgments

This study was partly funded by the Geotechnologien program of the BMBF/DFG under grant No. 03G0745A-C, by the UP Transfer GmbH, by University of Potsdam initiative: Research Focus in Earth Science, by the AXA Research Fund and by DGAPA-UNAM under Project IN104712. Thanks are given to E. Plata, G. Sánchez and their team of the Unidad de Servicios de Información (USI) of the Institute of Engineering-UNAM for locating useful references. We are thankful to three anonymous reviewers, the Associate Editor, Ge Zhan and the Assistant Editor, Gerard Schuster whose comments and suggestions helped to improve the quality of the manuscript.

Chapter 6

Discussion

As summarized in the introduction, a number of research topics are open regarding the use of active and/or passive seismic (microtremor or ambient noise) data for estimating the subsurface 1D velocity information. They can be sorted depending on the methods - array or/and single station - used for data processing.

As a recall:

- **Research topics using array methods (also known as surface wave methods) include:**

  1a. The integrated data analysis using the SPAC, f-k, MASW and IMASW for the estimation of a large bandwidth of the dispersion curves;

  1b. The interpretation of the estimated dispersion curves in terms of different surface wave modes;

  1c. The multi-mode inversion of the estimated phase velocity dispersion curves.

- **Research topics using the single station microtremor H/V spectral ratio method include:**

  2a. The full wavefield interpretation of the H/V spectral ratio observed at the surface and at depth;

  2b. The inversion of the full microtremor H/V spectral ratio for 1D seismic velocity information;

  2c. The comparison of the estimated velocity information obtained from the H/V inversion with the velocity information estimated from the phase velocity dispersion curves inversion;

  2d. The full wavefield interpretation of the H/V spectral ratio observed in marine environments.

- **Research topics using array methods and the single station microtremor H/V spectral ratio method include:**

  3a. The interpretation of the spectral contain of the two measures (dispersion curve and H/V) and their implication for structural properties estimation;

  3b. The combined analysis of the two data set (dispersion curves and H/V(z,f));

  3c. The comparison of the velocity profile information from individual approaches (dispersion curves inversion, H/V inversion and joint dispersion curves and H/V inversion).

In the sections hereafter, the main findings of this thesis with respect to those topics are discussed. The focus is mainly turned on the research topics using array methods or the single station microtremor H/V spectral ratio. When the discussion involves the combined analysis, the corresponding research topic

is clearly indicated. The strengths and limitations of the presented methodologies with respect to the above listed questions and the overall findings are then presented. Encountered difficulties are stated and, when possible, an approach to solve the problem is proposed.

6.1 Array methods for subsurface characterization

6.1.1 Achieved array configuration

The topics related to array methods for site characterization were investigated after arrays in 1D and 2D configurations have been designed. This pre-planning phase determined the quality of the array output. For geotechnical scale investigation, the capability to detect signal incoming from different directions was enhanced by using array in 2D configuration. A straightforward optimum array configuration in 2D (circular, triangular, rectangular, T, or L shape) given a number of sensors for site specific investigation remains an open issue.

The passive seismic array configurations achieved in this study at the two investigated sites, Horstwalde and Löbnitz, both in Germany were presented in Chapter 2 (Figures 2.2bc and Figures 2.4a-c). Except Figure 2.2b which was a "particular" 1D array as explained in the next paragraph, Figure 2.2c and Figures 2.4a-c were 2D small aperture (max. aperture: $\sim 260m$) arrays. In Horstwalde, three different array geometries, with different sensor numbers, were tested from a repeated ambient noise campaign. For the dense array (Figures 2.4b), it was obtained in this study that the spatial aliasing, defined by the minimum receiver interstation distance was significantly reduced in the high frequency range (compare Figures 2.4d-f).

Figure 2.2b was a non-redundant (Haubrich, 1968; Vertatschitsch & Haykin, 1986; Dudgeon & Johnson, 1993) 1D array of 1.76 km in which six stations (3C Lennartz LE-3D 1s) are irregularly spaced. This array configuration with six sensors was "particular", because it allowed optimal coverage in the co-array with a minimum number of stations (Figure 2.5a). The quality of the estimated phase velocity dispersion curves as presented in Chapter 2, Figure 2.5c, suggested that the site investigation with scaled array maximum aperture (always six stations, but with a reduced maximum aperture in this case) may aid in obtaining a broad dispersion spectrum especially in the high frequency. But this has not been explored in the course of this study.

The configuration achieved in the active experiment was a traditional 1D setup. A 5 kg hammer shot was used as a source and 4.5 Hz vertical geophones were used as receivers. Both the source and the receivers were inline to improve the signal to noise ratio and the energy signal estimation. The source-to-first receiver offset (15 m in Horstwalde and 20 m in Löbnitz) was set as to reduce the nearfield effect and to ensure the validity of the plane wave assumption.

Stokoe et al. (1994) suggested from the Spectral Analysis of Surface Waves methods (SASW) experiment that this offset should be greater than half the maximum interpretable wavelength or conversely the maximum interpretable wavelength should be less than twice the source - first receiver spacing.

At Horstwalde, the maximum estimated wavelength in the active experiment was $\sim$ 26 m (Figure 2.14a). These observations are in agreement with the recommendations from Stokoe et al. (1994) with 26 m $<$ 2x15 m = 30 m. At Löbnitz, the maximum estimated wavelength in the active experiment was $\sim$ 25 m (Figure 2.14a). Again at this site, the finding satisfied the requirement (25.57 m $<$ 2x20 m = 40 m).

6.1.2 Research topic 1a: The integrated data analysis (Chapter 2)

It was found from the analysis of the recorded ambient vibration and active seismic data that a large spectrum of the dispersion characteristic of the propagating surface waves was obtained by an integrated

analysis of different data sets. The outcome of the analysis in terms of phase velocity dispersion curves were summarized in Figure 2.6 for the test site at Horstwalde and in Figure 2.10 for the test site at Löbnitz both in Chapter 2. Figure 6.1 compared the achieved frequency ranges, as they combined for Vs profiling. They were classified from low (less than 1 Hz) to intermediate (between 1 and 10 Hz) or from intermediate to high frequency range (above 10 Hz). The broad dispersion curves coverage provided a unique opportunity to obtain a high resolution 1D shear wave velocity image of the subsurface ranging from few meters to $\sim$ 400 m.

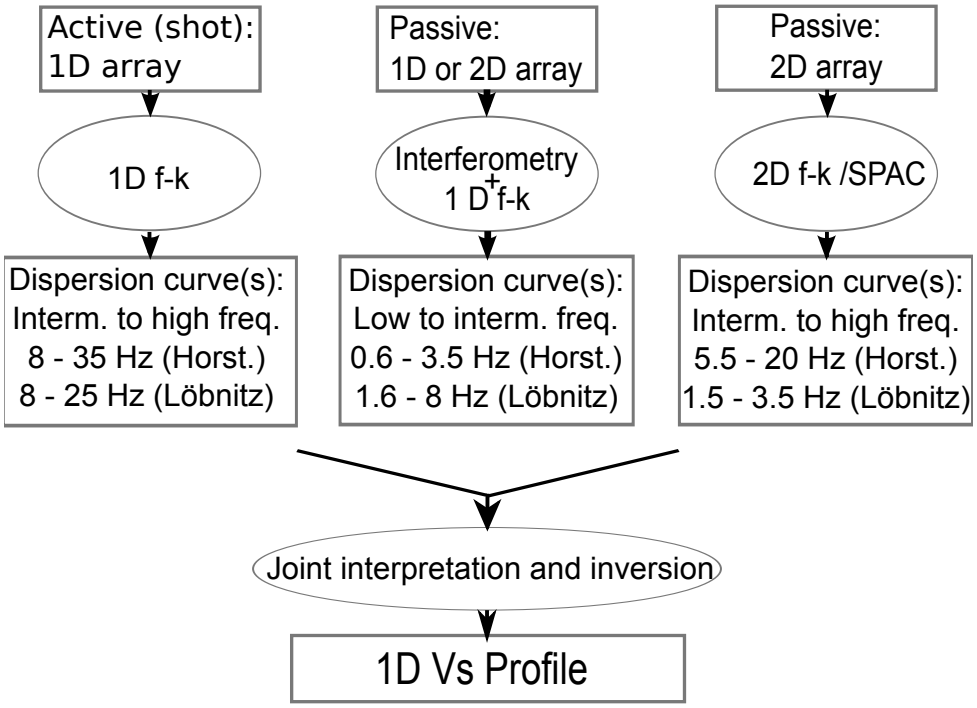

Figure 6.1: Schematic diagram representing the processing steps of the recorded data. The achieved frequency range from each method is reported.

Within the resolution limit, the interpretable phase velocity dispersion curve, estimated from the processing of the shot gather using the 1D frequency - wavenumber (f - k) technique, commonly referred to as MASW, ranged from 8 to 35 Hz in Horstwalde (Figure 2.5d) and from 8 to 25 Hz in Löbnitz (Figure 2.9d). Dispersion curve information with frequencies well above 40 - 50 Hz could also be observed. The upper limit at $\sim$ 35 Hz is related to the interpretation and relevance of additional dispersion curve branches spanning the higher frequencies. This interpretation issue was part of the key topics addressed in this study and could be found in the section 6.1.4.

From the analysis of ambient noise data from small aperture 2D array, the interpretable phase velocity dispersion curve ranged from 6 to 20 Hz (Figures 2.4d-f,j-l and Figures 2.8d-f,j-l). The information was obtained using two approaches: the 2D f - k and the (modified) SPatial AutoCorrelation (SPAC) techniques. The two processing techniques mainly differ in the consideration regarding the noise source distribution below or above a certain frequency. These two properties were supported by the findings of this thesis:

- For frequencies lower than $\sim$ 5 Hz at Horstwalde (Figures 2.4d-f) or lower than 1.5 Hz at Löbnitz (Figures 2.8d-f), the f - k technique overestimated the phase velocities due to their insufficient resolution capabilities;
- For the same frequency range, i.e, lower than $\sim$ 5 Hz at Horstwalde or lower than 1.5 Hz at Löbnitz, the SPAC technique, Figures 2.4j-l and Figures 2.8d-f, was advantageous with respect to

the inherent resolution limits;

- From the SPAC estimates, the lack of information in the high frequency part (above $\sim$ 10 Hz) in Horstwalde (Figures 2.4jk) may result from situations with dominant source contribution from a single direction in the noise wavefield.

One technique that was not so common, but yet powerful in the estimation of the dispersion curves employs the use of the estimated Correlation Green's Function (Gouédard et al., 2008a; O'Connell & Turner, 2011; Feuvre et al., 2015; Cheng et al., 2015; Pan et al., 2016; Lontsi et al., 2016a). Using the interferometric principles, the mathematical cross-correlation technique was used to estimate the Green's function between distinct receiver pairs. With the basic assumption of a 1D media, the estimated correlation Green's function were sorted with the interstation distance in a virtual active experiment. This was followed by the application of the 1D f - k (MASW) technique for the estimation of the dispersion curves. Throughout this study the approach has been referred to as Interferometric-MASW (IMASW; O'Connell & Turner, 2011. At Horstwalde, the observations obtained from processing the non-redundant linear array data using the IMASW technique compliment the dispersion curves estimates in the low to intermediate frequency range ($\sim$ 0.6 to 3.4 Hz). At the site in Löbnitz, the observations obtained from processing the 2D passive array data by means of the IMASW method provides confidence in the phase velocity dispersion curves branches estimated using the 2D f - k or the SPAC method. At this site, the IMASW further provided information on a broader frequency range in comparison to the 2D f - k or the SPAC method. This observation was previously obtained by Gouédard et al. (2008a). In comparison to the 2D f - k and SPAC, the IMASW at either site further provided information regarding overtones (Horstwalde: Figures 2.5c; Löbnitz: Figures 2.9c). The overall findings for the phase velocity dispersion of Rayleigh wave range from 0.6 to 35 Hz at the first test site in Horstwalde and from 1.5 to 25 Hz at the second test site in Löbnitz. The observed difference in the minimum achieved frequencies (0.6 Hz in Horstwalde and 1.5 Hz in Löbnitz) can be related to the maximum array aperture (resolution limit) used for the ambient noise data surveys ($\sim$ 1760 m in Horstwalde and $\sim$ 260 m in Löbnitz). Another limiting factor may be related to the vanishing of the seismic energy close to the resonance frequency estimated at $\sim$ 0.28 Hz at Horstwalde and at $\sim$ 0.8 Hz at Löbnitz.

The difference in the maximum achieved frequencies on the other hand (35 Hz in Horstwalde and 25 Hz in Löbnitz) was obtained from the interpretable range of the estimated dispersion curve as discussed in Subsection 6.1.4.

6.1.3 Research topic 1b: Array methods classification considering end-member assumptions about the noise wavefield (Chapter 2)

The findings for this research topic were highly dependent on the outcome of the Research topic 1a (Subsection 6.1.2). From the minimum and maximum estimates of the interpreted frequency-slowness curves (Figures 2.6 and 2.10), the minimum wavelength (λ_{min}) and maximum wavelength (λ_{max}) were estimated (Figure 2.14a). No linear relationship exists between the estimated wavelength and the basement depth. Using the rule of thumb (1/3 of the maximum estimated wavelength) , the minimum and maximum resolvable depth were respectively 2 and 500 m at Horstwalde and 2 and 160 m at Löbnitz.

The normalized wavelength ranges, with respect to the array aperture, were further obtained (Figure 2.14b). This information, together with the assumptions regarding the nature of the noise wavefield, were valuable for the classification of the applied methods (Figure 6.2). The unique classification as obtained from this study led to the conclusion that a robust estimation of the dispersion curves requires a complementary use of the different array techniques.

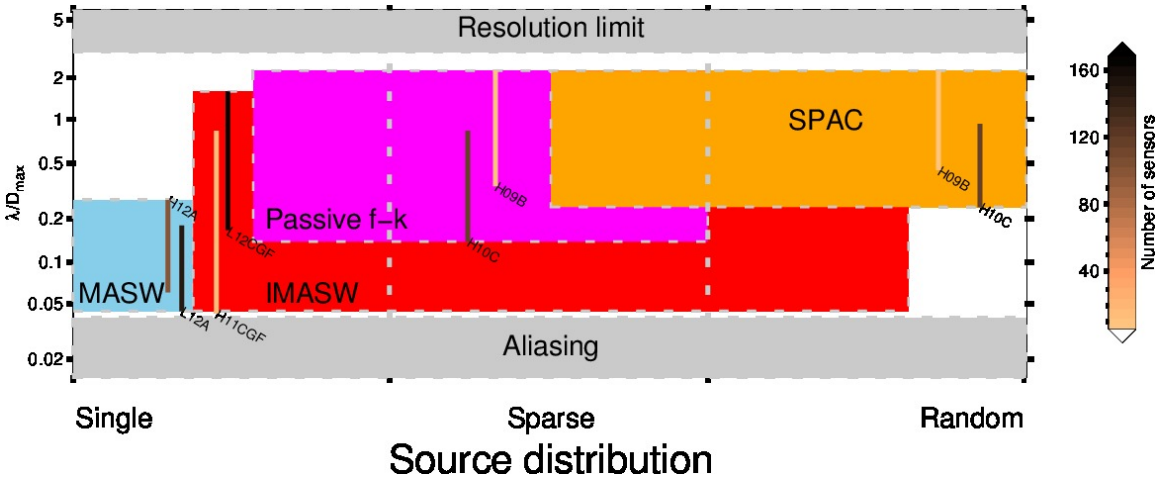

Figure 6.2: Diagram representing the overlap between methods used in the dispersion curves estimation. The sorting is based on considerations about the source distribution and the frequency (wavelength) content. Vertical lines indicate the range, in normalized wavelength unit, achieved using each method. The vertical lines are color coded with the sensor numbers.

6.1.4 Research topic 1c: Phase velocity dispersion curve branch interpretation (Chapter 2)

The estimated phase velocity dispersion curve branches were classified as fundamental and first higher mode. The interpretation of the different branches in terms of Rayleigh wave modes was an important step and probably the most difficult towards an unbiased inversion of the estimated dispersion curves. Using each of the applied methods as stand alone techniques, the first branch in the literature is very often interpreted as the fundamental mode and additional branches are interpreted as higher modes. This rule did work for the investigated site in Löbnitz, but was not the case for the site in Horstwalde. Here the first branch, for example in the passive f - k in comparison to that in the IMASW could not be considered as fundamental mode as explained by the mode search exercise below. As indicated by the integrated analysis (Figures 2.6 and 2.10), doing so in the interpretation of the 2D f - k results would have led to the inversion of a wrong mode number. The work reported in this thesis aids in reducing uncertainties by interpreting dispersion curves spanning a large frequency range. It is still worth noticing that opinions diverge on the systematic mode assignment procedure. The task was accomplished in this study by performing a blind mode search. This is possible using the software package *geopsy* (Freely available at www.geopsy.org; Last accessed: February 23, 2017). To achieve this exercise, different mode numbers (e.g 0,1,2,3,4) were assigned to each branch. Through a forward modeling, the first branch was associated with the fundamental Rayleigh wave mode and the second branch with the first higher mode. It was observed that after the first and the second mode have been determined, difficulties arose when assigning a particular mode number to any additional branch.

For the high frequency signal (MASW), a different viewpoint as proposed by Forbriger (2003) consists of inverting directly the observations in the frequency - phase slowness diagram by using the full waveform approach for given hypothetical Earth models. The approach avoids dealing with dispersion in terms of normal modes, and exploits the full signal-content, including the dispersion of higher modes, leaky modes and their true amplitudes (Forbriger, 2003). The application for the interpretation of the low frequency signal generated by ambient vibration will most probably make the approach more appealing for near subsurface investigation (down to few hundreds of meters).

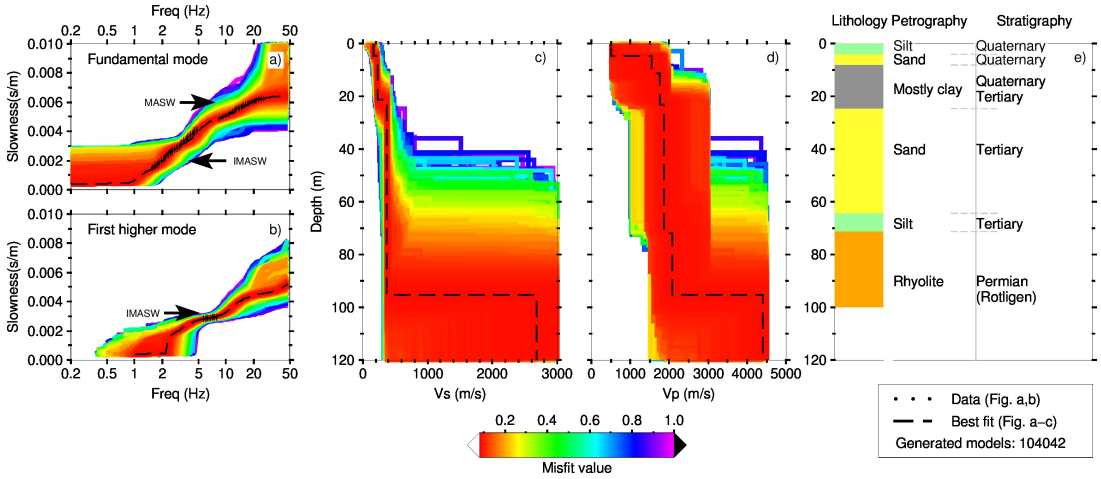

Figure 6.3: Dispersion curve inversion at the test site in Löbnitz. The resulting Vp velocity is also presented.

6.1.5 Research topics 1d, 2c, 3a, 3b, 3c: Multi-mode phase velocity dispersion curve inversion and comparison with H/V inversion results (Chapters 2, 3 and 5)

The interpreted dispersion curve branches were successfully inverted to estimate the subsurface shear (Vs) velocity profile. While the depth resolution was low at Horstwalde in comparison to geological log information, a reasonable depth information was obtained at Löbnitz.

The inversion results were partly presented in Chapter 2 for the shear velocity profiles at the two investigated sites (Figures 2.11 and 2.12). The combined interpretation of the estimated dispersion curves and the corresponding overtones enabled the exploration not only of the Vs and the geological formation delineation, but also the robustness in estimating the Vp profile information.

The complete inversion results (including the Vp information) are presented in Figures 5.3 and 6.3

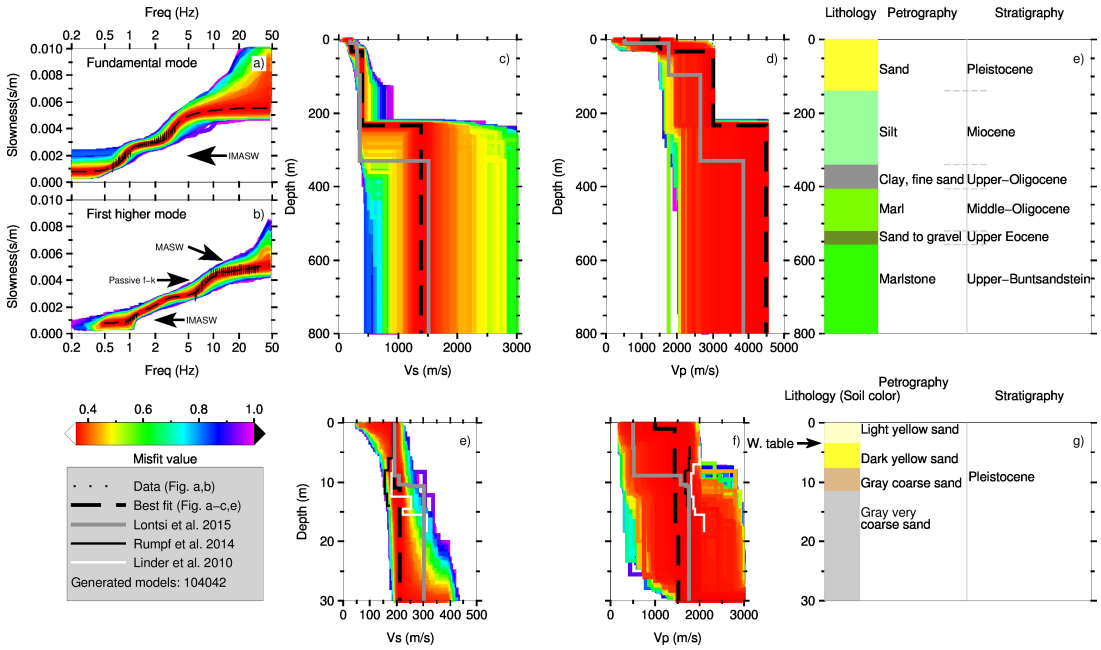

Figure 6.4: Dispersion curves inversion at the test site in Horstwalde. The resulting Vp velocity is also presented.

for Löbnitz and in Figures 5.4 and 6.4 for Horstwalde. At first, the overall sediment thickness estimated to 230 m at Horstwalde is less comparable to the borehole information that indicates a possible strong impedance contrast at about 350 m depth (silt - clay, fine sand) formation or 400 m depth (clay, fine sand - marl). The depth difference might be attributed to the achievable low frequency limit of the estimated phase velocity dispersion curves. It is important to notice that close to the resonance frequency of a site, estimated at ∼0.28 Hz in Horstwalde and at ∼0.8 Hz in Löbnitz, the energy on the vertical component vanishes (Lontsi et al., 2016b). The lack of dispersion curve information in the low frequency range below this natural threshold therefore may have reduced the depth resolution. On the other hand, as pointed out for example by Cornou et al. (2006), considering higher modes may improve the depth resolution of the estimated velocity profiles and enhance the resolution of the inverted model. Obtained results presented in this thesis, at least at Horstwalde do not fully corroborate with this statement.

Besides the depth correlation, the shear wave velocity information down to ∼ 230 m at Horstwalde or down to ∼ 95 m depth at Löbnitz characterize observations in sedimentary environments. The Vs profile for the very near subsurface down ∼ 10 m at Horstwalde correlated well with estimations from previous active geophysical investigations. Although higher mode information was considered in the inversion, the interpretation of the observed Vp profiles information was very difficult. For a minimum misfit set to 1 in either case, almost all Vp profiles were good potential candidates. This finding did not fully support the assertion for which higher modes may improve the resolution of the Vp profile information (Ernst, 2008).

6.2 Microtremor H/V method for site characterization

Array methods for deriving the dispersion curves as reported in Chapter 2 are costly in terms of equipment and manpower. Ideas emerged for deriving, in an inversion scheme, the structural parameters using the microtremor H/V spectral ratio (e.g. Yamanaka et al., 1994; Fäh et al., 2003). The approach used in this thesis overcomes the limitations of the Rayleigh wave ellipticity that considers only certain frequency range for the estimation of the velocity profile information (Fäh et al., 2003; Hobiger et al., 2012). An inversion methodology that exploits the full spectrum of the microtremor H/V(z,f) spectral ratio to retrieve the subsurface shear and additionally the compressional wave velocity information was proposed in the course of this study.

6.2.1 Research topic 2a and 2d: Full wavefield interpretation of the H/V spectral ratio observed at the surface and at depth (Chapter 3 and 4)

The new physical approach proposed by Sánchez-Sesma et al. (2011a) for the interpretation of the full microtremor H/V spectral ratio was extended in the course of this study to include the interpretation of the H/V observed in boreholes.

The H/V spectral ratio is a relatively simple method for the interpretation of recorded three-component microtremor data. The sources at the origin of the noise wavefield are in general both of natural and anthropogenic origin. Noise sources can be located at close or far distances to the receiver; they can also be located at surface or at depth. All sources contribute to the noise wavefield with both body and surface waves in proportions that are not well known. With this background knowledge, algorithms that interpret the H/V spectrum as surface waves (ellipticity) only/mostly or as body waves only (transfer function) were discarded or sparingly used in this study for comparison (Figure 3.3).

The question **"surface and/or body waves?"** has led to a new research topic about the real nature of the noise wavefield and the quantification of the respective proportion (e.g. Chouet et al., 1998; Yamamoto, 2000; Bonnefoy-Claudet, 2004; Köhler et al., 2006; Endrun, 2011).

With the assumption that the noise wavefield is diffuse, Sánchez-Sesma et al. (2011a) proposed a theory for the computation of the Directional Energy Density (DED) and subsequently for the interpretation of the full spectrum of the microtremor H/V spectral ratio. The approach does not require any background knowledge regarding the percentage of Love- and Rayleigh-wave.

For very simple canonical soft soil structure (one layer over a halfspace), the modeled H/V(z,f) using the diffuse field approach was compared with estimations using the reflectivity method by Wang (1999). The partial match between the two algorithms as observed for example in Figure 3.D.1 for the receivers at 19 m depth suggests that considerations regarding the noise source distribution needs further investigation. The reliability of the diffuse field assumption (DFA) to model the H/V spectral ratio for sites as presented in this study is further supported by the recent investigation by (Kawase et al., 2015) at selected known sites.

With the increased availability of the noise data at surface or at the bottom of a water column and at depth the existing algorithm based on the DFA was enhanced in the course of this study to include observations at depth both on land and in marine environment. Depth information for observations on land were proven to significantly reduce the non-uniqueness problem associated with the inversion of the H/V spectral ratio (see Research topic 2b).

6.2.2 Research topic 2b: Inversion of the full microtremor H/V spectral ratio for 1D seismic velocity information - Global search (Chapter 3)

Using both synthetic and real microtremor data, the estimated H/V curves have been inverted to estimate the 1D Vs and Vp velocity information.

Inversion results are discussed in light of estimates from an independent approach that uses empirical relationship available from the literature (e.g. Ibs-von Seht & Wohlenberg, 1999; Hinzen et al., 2004).

Table 6.1: Estimation of the overall sediment thickness at the test sites in Horstwalde and Rethem using an empirical relationship. The fundamental frequency at Horstwalde is estimated to 0.28 ± 0.03 Hz and at Rethem it is estimated to 1.0 ± 0.16 Hz. The parameters a and b of inverse power frequency-thickness relationship are taken from the literature ($z = af^b \pm b\frac{z}{f}\Delta f$). Interpreted quantities are in **bold**.

Basin (Reference)	a	b	$z_{Horst.}$ (m)	$z_{Löb.}$ (m)
Lower Rhine-west (Germany) (Ibs-von Seht & Wohlenberg, 1999)	96.0	-1.388	**562 ± 84**	96 ± 21
Segura river (Spain) (Delgado et al., 2000)	55.1	-1.256	273 ± 37	55 ± 11
Cologne (Germany) (Parolai et al., 2002)	108.0	-1.551	778 ± 129	108 ± 26
Lower Rhine-east (Germany) (Hinzen et al., 2004)	137.0	-1.190	**623 ± 79**	**137 ± 26**
Zafarraya (Spain) (García-Jerez et al., 2006)	194.6	-1.140	831 ± 101	**194 ± 35**
Bam (Iran) (Motamed et al., 2007)	135.2	-1.979	1679 ± 356	**135 ± 42**
Florence basin (Italy) (D'Amico et al., 2008)	140.0	-1.172	622 ± 78	**140 ± 26**
Ljubljana Moor (Slovenia) (Gosar & Lenart, 2010)	105.5	-1.250	518 ± 69	105.5 ± 21
L'Aquila (Italy) (Del Monaco et al., 2013)	53.5	-1.010	194 ± 21	53 ± 9

The estimated depth with the corresponding uncertainty, knowing the site fundamental frequency at Horstwalde and Rethem, are reported in Table 6.1.

For Horstwalde ($f_0 \sim 0.28$ Hz), only information derived from Ibs-von Seht & Wohlenberg, 1999; Hinzen et al., 2004 were used for comparison because the relationship was obtained from data covering the frequency of interest. The overall sediment thickness at Horstwalde estimated from the empirical relationship differs significantly from the inversion of the H/V spectrum. The information remains however all plausible, because when compared with borehole log information available at the site, they all correspond to changes in the material properties.

In contrast to Horstwalde where the comparison was established with two sites only, a large number of proposed relationships do cover the fundamental frequency at Rethem ($f_0 \sim 1$ Hz). Estimates comparable to the inversion of the full spectrum of the H/V(z,f), i.e. 160 m, are observed for this site (see Table 6.1).

In comparison to the empirical relationship, the inversion of the full H/V spectrum of the microtremor H/V further provides additional information regarding the detailed velocity and geological structure of the overlaying sediment column.

6.3 Strengths, limitations and encountered problems

6.3.1 Strengths

After reading the methodologies presented in this thesis and their applications at sites in Horstwalde, Löbnitz and Rethem, the reader is expected to be able to approach with ease the following geotechnical engineering or exploration seismic problems:

- The estimation and interpretation of a large frequency range of the phase velocity dispersion curve of the propagating Rayleigh waves;
- The multi-modal inversion of the Rayleigh wave phase velocity dispersion curve for the shear wave velocity profile information;
- The modeling and interpretation of the H/V observation at the surface, in boreholes, and in marine environment;
- The inversion of the full H/V spectral ratio for seismic velocity information.

6.3.2 Limitations and problems encountered

Identified limitations of this thesis are defined as weaknesses of the assumptions underlying the physical model for the interpretation of the noise wavefield. Also defined as limitations, thesis ideas not fully investigated and therefore not explicitly included in the open research topics listed earlier.

Using an array configuration, in 1D or 2D, with increasing aperture and applying all array methods (SPAC, passive f-k, IMASW, MASW), would help in determining the applicability limit of each method. This is of particular interest for the new IMASW method.

The application of the data analysis and inversion procedures (array method and single station methods) presented in this thesis to additional sites will definitely establish confidence in the approach for routine applications. The classification of surface wave methods (SPAC, f - k, MASW and IMASW) considering background end-member assumptions regarding the noise source distribution has briefly been approached (Appendix 6.1.3) and would require a more elaborated work.

The proposed algorithm based on the DFA for the interpretation of the H/V spectral ratio in its current development state assumes a farfield approximation. With this approximation, the model is mainly sensitive to shear waves. The application to H/V modeling in marine environment is, in the

current development state, is successful in a broad frequency range (up to 50 Hz for to shallow water environment with up to 25 m of water cover). However, with an increase of the sediment thickness and/or the water column, and/or the layer seismic properties, instabilities occur (Figure 4.E.1a,b). This situation is well known and it is caused by large numbers that result from matrix multiplication (Dunkin, 1965). The substraction of two large numbers (see Equation 4.72) results in a loss of significant digits. This situation has not been investigated here and may be subject to future analysis. Furthermore, the algorithm presents a long computational time (full waveform modeling; see Figure 3.A.1) and therefore requires a Central Processing Unit (CPU) cost optimization. The application of the developed inversion methodology at complex sites that include 2D/3D geology is also of interest. Sites with low noise azimuthal coverage where the diffuse field assumption fails would also be of interest.

For the investigated sites, issues related to the quantification of the proportion of each wave type has not been addressed, neither the interpretation of the amplitude of the H/V at the peak frequency has been addressed. Not investigated were ideas regarding the use of the simultaneous observation of the ambient noise wavefield with a 2D surface array and 1D vertical array (borehole sensors) towards a high resolution wavefield decomposition in Rayleigh, Love and body wavefield constituent parts.

Chapter 7

Conclusion

In the course of this research work, aimed at characterizing shallow subsurface sedimentary environments by Vs determination, new methodologies have been developed and proposed for high resolution 1D shear wave (Vs) and possible 1D compressional wave (Vp) velocity imaging of the subsurface. The methodological development is based on array data (phase velocity dispersion curves estimation) and single station data (H/V spectral ratio) processing. An integrated analysis that exploits the advantages of the SPAC, passive f-k, MASW and IMASW methods was used for the estimation of the large bandwidth of phase velocity dispersion curves. The dispersion curves were interpreted based on a forward modeling as fundamental and first higher mode. From a multi-mode inversion of the estimated dispersion curves at two selected sites in Germany, robust information regarding the Vs depth profile was obtained. Further interpretation of the phase velocity dispersion curves inversion results indicated that the estimated Vp and the bedrock of the sediment were not well recovered at Horstwalde.

Next to array methods, it was shown that using an improved model for the interpretation of the microtremor H/V spectral ratio, the 1D Vs profile and possibly the 1D Vp could be estimated. The farfield assumption in the theoretical development makes the model more suitable for Vs profiling. From this study, a good practice using the single station approach would be to consider, when available, H/V spectral ratio at a depth for which changes at least in the high frequency part are observed. As the single station H/V method easily provides a broad frequency content (in this case from 0.2 to 50 Hz) and therefore covering a broad wavelength for the investigated sites, the inversion approach developed in the course of this thesis is expected to be of common practice in the near future.

Based on the diffuse wavefield approach, the work in this thesis is the first contribution to our knowledge to model the H/V spectral ratio at the surface and at depth for both the sedimentary subsurface on land and in marine environments. The innovation to our knowledge also resides in the use of the full microtremor H/V(z, f) spectral ratio for subsurface characterization using an inversion. The application to additional sites with 1D geological structure will allow establishing confidence in this approach. Future research will also be needed to tackle subsurface structures that include 2D or 3D geological features.

Finally, for the investigated 1D sites at Horstwalde and Löbnitz, the phase velocity dispersion curves (DC) and the H/V(z, f) were combined and jointly inverted. The overall estimated depth from the joint inversion (DC + H/V) was comparable to information from the H/V(z, f) inversion. Looking at the available geological log for the sites, velocity profiles from H/V(z, f) and DC + H/V(z, f) inversion better corroborated with changes in the subsurface lithology in comparison to the DC inversion alone.

Appendix A

Full H/V inversion: A tutorial

Introduction

The following presents a description of the steps for deriving the subsurface parameters using the microtremor H/V method. The forward modeling is based on the diffuse wavefield approach as proposed by Sánchez-Sesma et al. (2011a). The material can be cited as (Lontsi et al., 2015):
Agostiny Marrios Lontsi, Francisco José Sánchez-Sesma, Juan Camillo Molina-Villegas, Matthias Ohrnberger, and Frank Krüger. Full microtremor H/V(z, f) inversion for shallow subsurface characterization, Geophys. J. Int. (July, 2015) 202 (1): 298-312 doi:10.1093/gji/ggv132

A.1 Dependency

- Operating System: Linux (The scripts as presented here were tested on a Linux (Ubuntu 14.04) system.
- geopsy/dinver (A sofware dedicated to ambient vibrations analysis: freely available at `www.geopsy.org`)

A.2 Necessary files for the inversion

The files/scripts described below are available on request.

A.2.1 Receiver at the surface only: change the directory to z00

- **b4inv.bash**: Script for preparing the files for saving the outputs.
  Example run from the shell: **./b4inv.bash test 00**
  The following files will be generated: **test.txt** for saving the output model; **test-00.txt** for saving the H/V spectral ratio computed at the surface; and **counter.txt** this file is used for counting the number of iterations.
- **parameters**: Sample vector file generated at random in the sampling process.
- **lontsi_HVDEPTH_loglin**: Executable file for the computation of the synthetic Directional Energy Density. The file can be executed from a shell as follow:
  ./lontsi_HVDEPTH_loglin INPUT.DAT OUTPUT.RES

- **konnoohmachismoothing**: Executable file for the smoothing of the estimated Directional Energy Density.
- **hv-greens-full-misfit-4log.bash** script for computing the misfit between the estimated H/V spectral ratio and the real data. The script can be executed as follow:
  ./hv-greens-full-misfit-4log.bash <thfile> <ofile> <fmin> <fmax> <rsamp>
- **inv-hvgreen-full.bash** takes as argument a vector of parameters generated at random and compute the corresponding misfit. The script can be executed as:
  ./inv-hvgreen-full.bash parameters ttt
- **hvdepth-2stations.bash** & **get-parameters.bash** are utility files.
- **test-5LOH.param** a sample parametrization for a 5 Layers over a half-space model.

A.2.2 Receiver at the surface and a second receiver at 19m depth: change the directory to z15

In the directory z15, the files are similar to those in the directory z00.

- **b4inv.bash**: Script for preparing the files for saving the outputs.
  Example run from the shell: ./b4inv.bash test 15
  The following files will be generated: **test.txt** for saving the output model; **test-00.txt** for saving the H/V spectral ratio computed at the surface; and **counter.txt** this file is used for counting the number of iterations.
- **parameters**: Sample vector file generated at random in the sampling process.
- **lontsi_HVDEPTH_loglin**: Executable file for the computation of the synthetic Directional Energy Density. The file can be executed from a shell as follow:
  ./lontsi_HVDEPTH_loglin INPUT.DAT OUTPUT.RES
- **konnoohmachismoothing**: Executable file for the smoothing of the estimated Directional Energy Density.
- **hv-greens-full-misfit-4log.bash** script for computing the misfit between the estimated H/V spectral ratio and the real data. The script can be executed as follow:
  ./hv-greens-full-misfit-4log.bash <thfile> <ofile> <fmin> <fmax> <rsamp>
- **inv-hvgreen-full.bash** takes as argument a vector of parameters generated at random and compute the corresponding misfit. The script can be executed as:
  ./inv-hvgreen-full.bash parameters ttt
- **hvdepth-2stations.bash** & **get-parameters.bash** are utility files.
- **test-5LOH.param** a sample parametrization for a 5 Layers over a half-space model.

A.3 Visualization

A.3.1 Directory z00

Assuming the output files from the inversion are: test.txt and text-00.txt,

- Vs visualization from the command line:
  cat test.txt | **gpprofile -vs** | **figue -mc**
- Vp visualization from the command line:
  cat test.txt | **gpprofile -vp** | **figue -mc**
- Density (ρ) visualization from the command line:
  cat test.txt | **gpprofile -rho** | **figue -mc**
- H/V (for z=0m) visualization from the command line:
  cat test-00.txt | **figue -mc**

A.3.2 Directory z15

Assuming the output files from the inversion are: test.txt, text-00.txt and text-15.txt,

- Vs visualization from the command line:
  cat test.txt | **gpprofile -vs** | **figue -mc**
- Vp visualization from the command line:
  cat test.txt | **gpprofile -vp** | **figue -mc**
- Density (ρ) visualization from the command line:
  cat test.txt | **gpprofile -rho** | **figue -mc**
- H/V (for z=0m) visualization from the command line:
  cat test-00.txt | **figue -mc**
- H/V (for z=15m) visualization from the command line:
  cat test-15.txt | **figue -mc**

Bibliography

Aki, K., 1957. Space and time spectra of stationary stochastic waves, with special reference to microtremors., *Bull. Earthq. Res. Inst.*, **35**, 415–456.

Aki, K., 1993. Local site effects on weak and strong ground motion, *Tectonophysics*, **218**(1–3), 93–111.

Aki, K. & Richards, P. G., 2002. *Quantitative Seismology*, University Science Books, 2nd edn.

Akin, M. K., Kramer, S. L., & Topal, T., 2011. Empirical correlations of shear wave velocity (vs) and penetration resistance (spt-n) for different soils in an earthquake-prone area (erbaa-turkey), *Engineering Geology*, **119**(1–2), 1 – 17.

Arai, H. & Tokimatsu, K., 2004. S-Wave Velocity Profiling by Inversion of Microtremor H/V Spectrum, *Bulletin of the Seismological Society of America*, **94**(1), 53–63.

Arai, H. & Tokimatsu, K., 2005. S-Wave Velocity Profiling by Joint Inversion of Microtremor Dispersion Curve and Horizontal-to-Vertical (H/V) Spectrum, *Bulletin of the Seismological Society of America*, **95**(5), 1766–1778.

Asten, M. & Henstridge, J., 1984. Array estimators and the use of microseisms for reconnaissance of sedimentary basins, *GEOPHYSICS*, **49**(11), 1828–1837.

Asten, M. W., 2006. On bias and noise in passive seismic data from finite circular array data processed using spac methods, *GEOPHYSICS*, **71**(6), V153–V162.

Asten, M. W. & Boore, D. M., 2005. Comparison of shear-velocity profiles of unconsolidated sediments near the Coyote borehole (CCOC), measured with fourteen invasive and non-invasive methods, *in: Blind comparisons of shear-wave velocities at closely spaced sites in San Jose, California, eds M. W. Asten and D. M. Boore*, **Report 2005-1169**, part 1, 35pp.(http://pubs.usgs.gov/of/2005/1169/)., US Geological Survey, Open-File.

Asten, M. W., Dhu, T., & Lam, N., 2004. Optimized array design for microtremor array studies applied to site classification; comparison of results with scpt logs, *In Proc. 13th World Conf. on Earthquake Engineering, Vancouver, 1–6 August*, p. paper no. 1120.

Aster, R. C., Borchers, B., & Thurber, C. H., 2011. *Parameter estimation and inverse problems; 2nd ed.*, Elsevier Science, [S.l.].

Bard, P.-Y., 1998. Microtremor measurements: a tool for site effect estimation? State-of-the-art paper, *Effects of Surface Geology on Seismic Motion*, **3**, 1251–1279.

Beaty, K. S., Schmitt, D. R., & Sacchi, M., 2002. Simulated annealing inversion of multimode rayleigh wave dispersion curves for geological structure, *Geophysical Journal International*, **151**(2), 622–631.

Bensen, G. D., Ritzwoller, M. H., Barmin, M. P., Levshin, A. L., Lin, F., Moschetti, M. P., Shapiro, N. M., & Yang, Y., 2007. Processing seismic ambient noise data to obtain reliable broad-band surface wave dispersion measurements, *Geophysical Journal International*, **169**(3), 1239–1260.

Bettig, B., Bard, P. Y., Scherbaum, F., Riepl, J., Cotton, F., Cornou, C., & Hatzfeld, D., 2001. Analysis of dense array noise measurements using the modified spatial auto-correlation, *Boll. Geof. Teor. Appl.*, **42**, 281–304.

Bishop, A. W. & Henkel, D., 1962. *The measurement of soil properties in the triaxial test*, Edward Arnold, London, 2nd edn.

Bonnefoy-Claudet, S., 2004. *Nature of seismic noise wavefield: implications for site effects studies*, Theses, Université Joseph-Fourier - Grenoble I.

Bonnefoy-Claudet, S., Cornou, C., Di Giuglio, G., Guillier, B., Jongmans, D., Köhler, A., Ohrnberger, M., Savvaidis, A., Roten, D., Scherbaum, F., Schissele, E., Vollmer, D., & Wathelet, M., 2005. Report on the fk/spac capabilities and limitations, *SESAME Deliverable D19.06*.

Bonnefoy-Claudet, S., Cornou, C., Bard, P.-Y., Cotton, F., Moczo, P., Kristek, J., & Fäh, D., 2006a. H/V ratio: a tool for site effects evaluation. Results from 1-D noise simulations, *Geophysical Journal International*, **167**(2), 827–837.

Bonnefoy-Claudet, S., Cotton, F., Bard, P.-Y., Cornou, C., Ohnrberger, M., & Wathelet, M., 2006b. Robustness of the H/V ratio peak frequency to estimate 1D resonance frequency, *in Proc. 3rd Int. Symp. on the Effects of Surface Geology on Seismic Motion, Grenoble, 30 August - 01 September, 2006*, LCPC Editions.

Boore, D. M. & Atkinson, G. M., 2008. Ground-Motion Prediction Equations for the Average Horizontal Component of PGA, PGV, and 5%-Damped PSA at Spectral Periods between 0.01 s and 10.0 s, *Earthquake Spectra*, **24**(1), 99–138.

Bora, S. S., Scherbaum, F., Kuehn, N., & Stafford, P., 2014. Fourier spectral- and duration models for the generation of response spectra adjustable to different source-, propagation-, and site conditions, *Bulletin of Earthquake Engineering*, **12**(1), 467–493.

Bora, S. S., Scherbaum, F., Kuehn, N., Stafford, P., & Edwards, B., 2015. Development of a Response Spectral Ground-Motion Prediction Equation (GMPE) for Seismic-Hazard Analysis from Empirical Fourier Spectral and Duration Models, *Bulletin of the Seismological Society of America*, **105**(4), 2192–2218.

Bouchon, M. & Aki, K., 1977. Discrete wave-number representation of seismic-source wave fields, *Bulletin of the Seismological Society of America*, **67**(2), 259–277.

Braya, M. D., 2009. *Principles of geotechnical engineering*, Cengage Learning, Stamford, USA, 7th edn.

Capon, J., 1969. High-resolution frequency-wavenumber spectrum analysis, *Proc. IEEE*, **57(8)**, 1408–1419.

Chavez-Garcia, F. J. & Raptakis, D., 2008. Inversion of soil structure and analysis of the seismic wavefield from vertical array, *14th World Conference of Earthquake Engineering, Beijing*.

Cheng, F., Xia, J., Xu, Y., Xu, Z., & Pan, Y., 2015. A new passive seismic method based on seismic interferometry and multichannel analysis of surface waves, *Journal of Applied Geophysics*, **117**, 126–135.

Chouet, B., De Luca, G., Milana, G., Dawson, P., Martini, M., & Scarpa, R., 1998. Shallow velocity structure of stromboli volcano, italy, derived from small-aperture array measurements of strombolian tremor, *Bulletin of the Seismological Society of America*, **88**(3), 653–666.

Cornou, C., Ohrnberger, M., Boore, D. M., Kudo, K., & Bard., P.-Y., 2006. Derivation of structural models from ambient vibration arrays recordings: Results from an international blind test, *Third International Symposium on the Effects of Surface Geology on Seismic Motion*, p. 92pp, Grenoble, France, 30 August - 1 September 2006.

Curtis, A., Gerstoft, P., Sato, H., Snieder, R., & Wapenaar, K., 2006. Seismic interferometry—turning noise into signal, *The Leading Edge*, **25**(9), 1082–1092.

Dal Moro, G., 2010. Insights on surface wave dispersion and HVSR: Joint analysis via Pareto optimality, *Journal of Applied Geophysics*, **72**(2), 129 – 140.

Dal Moro, G. & Ferigo, F., 2011. Joint analysis of Rayleigh- and Love-wave dispersion: Issues, criteria and improvements, *Journal of Applied Geophysics*, **75**(3), 573 – 589.

Dal Moro, G. & Pipan, M., 2007. Joint inversion of surface wave dispersion curves and reflection travel times via multi-objective evolutionary algorithms, *Journal of Applied Geophysics*, **61**(1), 56 – 81.

Dal Moro, G., Ponta, R., & Mauro, R., 2015. Unconventional optimized surface wave acquisition and analysis: Comparative tests in a perilagoon area, *Journal of Applied Geophysics*, **114**, 158 – 167.

de Boer, W. M., 1995. Äolische und landschaftsformen im mittleren baruther urstromtal seit dem hochglazial der weichselkaltzeit, *Humboldt University Berlin,*, **Ph.D. Thesis**, 274pp.

Del Monaco, F., Tallini, M., Rose, C. D., & Durante, F., 2013. HVNSR survey in historical downtown l'aquila (central italy): Site resonance properties vs. subsoil model, *Engineering Geology*, **158**, 34 – 47.

Delgado, J., López Casado, C., Giner, J., Estévez, A., Cuenca, A., & Molina, S., 2000. Microtremors as a geophysical exploration tool: Applications and limitations, *pure and applied geophysics*, **157**(9), 1445–1462.

Di Giulio, G., Cornou, C., Ohrnberger, M., Wathelet, M., & Rovelli, A., 2006. Deriving wavefield characteristics and shear-velocity profiles from two- dimensional small-aperture arrays analysis of ambient vibrations in a small-size alluvial basin, colfiorito, italy, *Bulletin of the Seismological Society of America*, **96**(5), 1915–1933.

Djikpesse, H., Sobreira, J. F. F., Hill, A., Wrobel, K., Stephen, R., Fehler, M., Campbell, K., Carrière, O., & Ronen, S., 2013. Recent advances and trends in subsea technologies and seafloor properties characterization, *The Leading Edge*, **32**(10), 1214–1220.

Dobry, R., Borcherdt, R. D., Crouse, C. B., Idriss, I. M., Joyner, W. B., Martin, G. R., Power, M. S., Rinne, E. E., & Seed, R. B., 2000. New Site Coefficients and Site Classification System Used in Recent Building Seismic Code Provisions, *Earthquake Spectra*, **16**(1), 41–67.

Domínguez, J. & Abascal, R., 1984. On fundamental solutions for the boundary integral equations method in static and dynamic elasticity, *Engineering Analysis*, **1**(3), 128–134.

Ducellier, A., Kawase, H., & Matsushima, S., 2013. Validation of a New Velocity Structure Inversion Method Based on Horizontal-to-Vertical (H/V) Spectral Ratios of Earthquake Motions in the Tohoku Area, Japan, *Bulletin of the Seismological Society of America*, **103**(2A), 958–970.

Dudgeon, D. E. & Johnson, D. H., 1993. Array signal processing: concepts and techniques, *PRT Prentice Hall, Englewood Cliffs, NJ*.

Dunkin, J. W., 1965. Computation of modal solutions in layered, elastic media at high frequencies, *Bulletin of the Seismological Society of America*, **55**(2), 335–358.

D'Amico, V., Picozzi, M., Baliva, F., & Albarello, D., 2008. Ambient noise measurements for preliminary site-effects characterization in the urban area of florence, italy, *Bulletin of the Seismological Society of America*, **98**(3), 1373–1388.

EC8, 2004. Eurocode 8, design of structures for earthquake resistance – part 1: General rules, seismic actions and rules for buildings, *Brussels: European Committee for Normalization*, **EN 1998-1:2004**.

Endrun, B., 2011. Love wave contribution to the ambient vibration H/V amplitude peak observed with array measurements, *Journal of Seismology*, **15**(3), 443–472.

Ernst, F. E., 2008. *Multi-mode inversion for P-wave velocity and thick near-surface layers*.

Fäh, D., Kind, F., & Giardini, D., 2001. A theoretical investigation of average H/V ratios, *Geophysical Journal International*, **145**(2), 535–549.

Fäh, D., Kind, F., & Giardini, D., 2003. Inversion of local S-wave velocity structures from average H/V ratios, and their use for the estimation of site-effects, *Journal of Seismology*, **7**(4), 449–467.

Fäh, D., Stamm, G., & Havenith, H.-B., 2008. Analysis of three-component ambient vibration array measurements, *Geophysical Journal International*, **172**(1), 199–213.

Feuvre, M. L., Joubert, A., Leparoux, D., & Côte, P., 2015. Passive multi-channel analysis of surface waves with cross-correlations and beamforming. Application to a sea dike, *Journal of Applied Geophysics*, **114**, 36–51.

Forbriger, T., 2003. Inversion of shallow-seismic wavefields: I. wavefield transformation, *Geophysical Journal International*, **153**(3), 719–734.

Gantmacher, F., 1959. *The Theory of Matrices: Vol.: 1*, Chelsea Publishing Company.

García-Jerez, A., Luzón, F., Navarro, M., & Pérez-Ruiz, J. A., 2006. Characterization of the sedimentary cover of the zafarraya basin, southern spain, by means of ambient noise, *Bulletin of the Seismological Society of America*, **96**(3), 957–967.

Garofalo, F., Foti, S., Hollender, F., Bard, P. Y., Cornou, C., Cox, B. R., Dechamp, A., Ohrnberger, M., Perron, V., Sicilia, D., Teague, D., & Vergniault, C., 2016a. InterPACIFIC project: Comparison of invasive and non-invasive methods for seismic site characterization. Part II: Inter-comparison between surface-wave and borehole methods, *Soil Dynamics and Earthquake Engineering*, **82**, 241–254.

Garofalo, F., Foti, S., Hollender, F., Bard, P. Y., Cornou, C., Cox, B. R., Ohrnberger, M., Sicilia, D., Asten, M., Giulio, G. D., Forbriger, T., Guillier, B., Hayashi, K., Martin, A., Matsushima, S., Mercerat, D., Poggi, V., & Yamanaka, H., 2016b. InterPACIFIC project: Comparison of invasive and non-invasive methods for seismic site characterization. Part I: Intra-comparison of surface wave methods, *Soil Dynamics and Earthquake Engineering*, pp. –.

Gilbert, F. & Backus, G. E., 1966. Propagator matrices in elastic wave and vibration problems, *GEOPHYSICS*, **31**(2), 326–332.

Gosar, A. & Lenart, A., 2010. Mapping the thickness of sediments in the Ljubljana Moor basin (Slovenia) using microtremors, *Bulletin of Earthquake Engineering*, **8**(3), 501–518.

Gouédard, P., Cornou, C., & Roux, P., 2008a. Phase–velocity dispersion curves and small-scale geophysics using noise correlation slantstack technique, *Geophysical Journal International*, **172**(3), 971–981.

Gouédard, P., Stehly, L., Brenguier, F., Campillo, M., Colin de Verdière, Y., Larose, E., Margerin, L., Roux, P., Sánchez-Sesma, F. J., Shapiro, N. M., & Weaver, R. L., 2008b. Cross-correlation of random fields: mathematical approach and applications, *Geophysical Prospecting*, **56**(3), 375–393.

Halliday, D., Curtis, A., & Kragh, E., 2008. Seismic surface waves in a suburban environment: Active and passive interferometric methods, *The Leading Edge*, **27**(2), 210–218.

Hannemann, K., Papazachos, C., Ohrnberger, M., Savvaidis, A., Anthymidis, M., & Lontsi, A. M., 2014. Three-dimensional shallow structure from high-frequency ambient noise tomography: New results for the Mygdonia basin-Euroseistest area, northern Greece, *Journal of Geophysical Research: Solid Earth*, **119**(6), 4979–4999.

Haskell, N. A., 1953. The dispersion of surface waves on multilayered media, *Bulletin of the Seismological Society of America*, **43**(1), 17–34.

Haubrich, R. A., 1968. Array design, *Bulletin of the Seismological Society of America*, **58**(3), 977–991.

Hausmann, J., Steinel, H., Kreck, M., Werban, U., Vienken, T., & Dietrich, P., 2013. Two-dimensional geomorphological characterization of a filled abandoned meander using geophysical methods and soil sampling, *Geomorphology*, **201**(0), 335 – 343.

Herrmann, R. B., 2002. Computer programs in seismology: an overview of synthetic seismogram computation, pp. 733–741, Version 3.30.

Herrmann, R. B., 2008. Seismic waves in layered media, pp. 1–335, ftp://ftp.eas.slu.edu/pub/rbh/PDF/all.pdf, Last accessed: February 23, 2017.

Hinzen, K.-G., Weber, B., & Scherbaum, F., 2004. On the resolution of h/v measurements to determine sediment thickness, a case study across a normal fault in the lower rhine embayment, germany, *Journal of Earthquake Engineering*, **08**(06), 909–926.

Hobiger, M., Bard, P.-Y., Cornou, C., & Le Bihan, N., 2009a. Single station determination of Rayleigh wave ellipticity by using the random decrement technique (RayDec), *Geophysical Research Letters*, **36**(14), n/a—-n/a.

Hobiger, M., Bard, P.-Y., Cornou, C., & Le Bihan, N., 2009b. Single station determination of Rayleigh wave ellipticity by using the random decrement technique (RayDec), *Geophysical Research Letters*, **36**(14), n/a–n/a, L14303.

Hobiger, M., Le Bihan, N., Cornou, C., & Bard, P., 2012. Multicomponent signal processing for rayleigh wave ellipticity estimation: Application to seismic hazard assessment, *Signal Processing Magazine, IEEE*, **29**(3), 29–39.

Hobiger, M., Cornou, C., Wathelet, M., Giulio, G. D., Knapmeyer-Endrun, B., Renalier, F., Bard, P.-Y., Savvaidis, A., Hailemikael, S., Le, B. N., Ohrnberger, M., & Theodoulidis, N., 2013. Ground structure imaging by inversions of rayleigh wave ellipticity: sensitivity analysis and application to european strong-motion sites, *Geophysical Journal International*, **192**(1), 207–229.

Horike, M., 1985. Inversion of phase velocity of long-period microtremors to the S-wave velocity structure down to the basement in urbanised areas., *Journal of Physics of the Earth*, **33**(2), 59–96.

Huerta-Lopez, C., Pulliam, J., & Nakamura, Y., 2003. In situ evaluation of shear-wave velocities in seafloor sediments with a broadband ocean-bottom seismograph, *Bulletin of the Seismological Society of America*, **93**(1), 139–151.

Ibs-von Seht, M. & Wohlenberg, J., 1999. Microtremor measurements used to map thickness of soft sediments, *Bulletin of the Seismological Society of America*, **89**(1), 250–259.

Johnson, D. H. & Dudgeon, D. E., 1992. *Array Signal Processing: Concepts and Techniques*, Simon & Schuster.

Juschus, O., 2001. Das Jungmoränenland südlich von Berlin – Untersuchungen zur jungquartären Landschaftsentwicklung zwischen Unterspreewald und Nuthe [The young moraine area to the south of Berlin – Investigations on the Quaternary landscape between Unterspreewald and Nuthe], *Humboldt University Berlin,*, **Ph.D. Thesis**, 251pp.

Kawase, H., Sánchez-Sesma, F. J., & Matsushima, S., 2011. The optimal use of horizontal-to-vertical spectral ratios of earthquake motions for velocity inversions based on diffuse-field theory for plane waves, *Bulletin of the Seismological Society of America*, **101**(5), 2001–2014.

Kawase, H., Matsushima, S., Satoh, T., & Sánchez-Sesma, F. J., 2015. Applicability of theoretical horizontal-to-vertical ratio of microtremors based on the diffuse field concept to previously observed data, *Bulletin of the Seismological Society of America*.

Knopoff, L., 1964. A matrix method for elastic wave problems, *Bulletin of the Seismological Society of America*, **54**(1), 431–438.

Köhler, A., Ohrnberger, M., & Scherbaum, F., 2006. The relative fraction of rayleigh to love waves in ambient vibration wavefields at different european sites, *in Proc. 3rd Int. Symp. on the Effects of Surface Geology on Seismic Motion, Grenoble, August 30–September 1, 2006*, **1**, 351–360.

Konno, K. & Ohmachi, T., 1998. Ground-motion characteristics estimated from spectral ratio between horizontal and vertical components of microtremor, *Bulletin of the Seismological Society of America*, **88**(1), 228–241.

Lachet, C. & Bard, P.-Y., 1994. Numerical and Theoretical Investigations on the Possibilities and Limitations of Nakamura's Technique, *Journal of Physics of the Earth*, **42**(5), 377–397.

Lacoss, R. T., Kelly, E. J., & Toksöz, M. N., 1969. Estimation of seismic noise structure using arrays, *GEOPHYSICS*, **34**(1), 21–38.

Lermo, J. & Chávez-García, F. J., 1993. Site effect evaluation using spectral ratios with only one station, *Bulletin of the Seismological Society of America*, **83**(5), 1574–1594.

Linder, S., 2007. Vergleich seismischer Verfahren zur Erkundung des oberflächennahen Untergrundes, *Diploma thesis, Universität Tübingen*, p. pp. 60S.

Linder, S., Paasche, H., Tronicke, J., Niederleithinger, E., & Vienken, T., 2010. Zonal cooperative inversion of crosshole P-wave, S-wave, and georadar traveltime data sets, *Journal of Applied Geophysics*, **72**(4), 254 – 262.

Ling, S. & Okada, H., 1993. An extended use of the spatial autocorrelation method for the estimation of structure using microtremors, *in Proc. of the 89th SEGJ Conference, Nagoya, Japan, 12–14 October 1993, Society of Exploration Geophysicists of Japan (in Japanese)*, p. 44–48.

Lobkis, O. I. & Weaver, R. L., 2001. On the emergence of the Green's function in the correlations of a diffuse field, *The Journal of the Acoustical Society of America*, **110**(6), 3011–3017.

Lontsi, A., Ohrnberger, M., & Krüger, F., 2016a. Shear wave velocity profile estimation by integrated analysis of active and passive seismic data from small aperture arrays, *Journal of Applied Geophysics*, **130**, 37 – 52.

Lontsi, A. M., Sánchez-Sesma, F. J., Molina-Villegas, J. C., Ohrnberger, M., & Krüger, F., 2015. Full microtremor H/V(z, f) inversion for shallow subsurface characterization, *Geophysical Journal International*, **202**(1), 298–312.

Lontsi, A. M., Ohrnberger, M., Krüger, F., & Sánchez-Sesma, F. J., 2016b. Combining surface wave phase velocity dispersion curves and full microtremor horizontal-to-vertical spectral ratio for subsurface sedimentary site characterization, *Interpretation*, **4**(4).

Mainsant, G., Jongmans, D., Chambon, G., Larose, E., & Baillet, L., 2012. Shear-wave velocity as an indicator for rheological changes in clay materials: Lessons from laboratory experiments, *Geophysical Research Letters*, **39**(19), n/a–n/a, L19301.

Malischewsky, P. G. & Scherbaum, F., 2004. Love's formula and H/V-ratio (ellipticity) of Rayleigh waves, *Wave Motion*, **40**(1), 57 – 67.

Maranò, S., Reller, C., Loeliger, H.-A., & Fäh, D., 2012. Seismic waves estimation and wavefield decomposition: application to ambient vibrations, *Geophysical Journal International*, **191**(1), 175–188.

Mayne, P. W., 1997. Cone penetration testing: A synthesis of highway practice, *NATIONAL COOPERATIVE HIGHWAY RESEARCH PROGRAM, SYNTHESIS 368*, Report FEMA-273, Washington, DC.

Menke, W., 1989. Geophysical data analysis: discrete inverse theory, *rev. edn, Academic Press, San Diego*.

Miller, G. F. & Pursey, H., 1955. On the partition of energy between elastic waves in a semi-infinite solid, *Proceedings of the Royal Society of London A: Mathematical, Physical and Engineering Sciences*, **233**(1192), 55–69.

Motamed, R., Ghalandarzadeh, A., Tawhata, I., & Tabatabaei, S. H., 2007. Seismic microzonation and damage assessment of bam city, southeastern iran, *Journal of Earthquake Engineering*, **11**(1), 110–132.

Müller, G., 1985. The reflectivity method: a tutorial, *J. Geophys.*, **58**, 153–174.

Muyzert, E., 2007. Seabed property estimation from ambient-noise recordings: Part 2 — scholte-wave spectral-ratio inversion, *GEOPHYSICS*, **72**(4), U47–U53.

Nakamura, Y., 1989. A method for dynamic characteristics estimations of subsurface using microtremors on the ground surface, *Q. Rept. RTRI Jpn.*, **30**, 25–33.

Nakamura, Y., 2008. On the h/v spectrum, *Proceedings of the 14th World Conference on Earthquake Engineering, Beijing, China*.

NEHRP, 1997. Nehrp guidelines for the seismic rehabilitation of buildings, *Federal Emergency Management Agency,*, Report FEMA-273, Washington, DC.

NERIES, 2010. Report: Using Ellipticity Information for Site Characterisation., p. pp54, NERIES (NEtwork of Research Infrastructures for European Seismology), Deliverable, D4, JRA4 Task B2, Sixth Framework Program, EC project number: 026130; D. Fäh and M. Wathelet and M. Kristekova and H. Havenith and B. Endrun and G. Stamm and V. Poggi and J. Burjanek and C. Cornou.

Nolet, G. & Panza, G., 1976. Array analysis of seismic surface waves: Limits and possibilities, *pure and applied geophysics*, **114**(5), 775–790.

O'Connell, D. R. H. & Turner, J. P., 2011. Interferometric Multichannel Analysis of Surface Waves (IMASW), *Bulletin of the Seismological Society of America*, **101**(5), 2122–2141.

Ohrnberger, M., Schissele, E., Cornou, C., Wathelet, M., Savvaidis, A., Scherbaum, F., Jongmans, D., & Kind, F., 2004. Microtremor array measurements for site effect investigations: comparison of analysis methods for field data crosschecked by simulated wavefields, *Proceedings of the 13th World Conference on Earthquake Engineering*, Vancouver, Canada, paper 946.

Ohrnberger, M., Vollmer, D., & Scherbaum, F., 2006. Waran-a mobile wireless array analysis system for in-field ambient vibration dispersion curve estimation, *Proceedings of the 1st ECEES*, p. 284.

Okada, H., 1994. A research on the practical application of microtremor exploration technique to a wide area survey of a underground structure under 3,000 m in depth, *report of a Grant-in-Aid for Co-operative Research (B) No. 03554009 supported by the Scientific Research Fund in 1993 (in Japanese)*.

O'Neill, A., 2004. *Shear velocity model appraisal in shallow surface wave inversion*, chap. 140, pp. 539–546.

Overduin, P. P., Haberland, C., Ryberg, T., Kneier, F., Jacobi, T., Grigoriev, M. N., & Ohrnberger, M., 2015. Submarine permafrost depth from ambient seismic noise, *Geophysical Research Letters*, **42**(18), 7581–7588, 2015GL065409.

Pan, Y., Xia, J., Xu, Y., Xu, Z., Cheng, F., Xu, H., & Gao, L., 2016. Delineating shallow S-Wave velocity structure using multiple ambient-noise surface-wave methods: An example from western junggar, china, *Bulletin of the Seismological Society of America*.

Pancha, A. & Pullammanappallil, S., 2012. Determination of 3d-velocity structure across the deepest portion of the reno area basin, *U.S. Geological Survey, External Grant Award No. G12AP20026, 54 pp. http://earthquake.usgs.gov/research/external/reports/G12AP20026.pdf*.

Park, C., Miller, R., Ryden, N., Xia, J., & Ivanov, J., 2005. Combined use of active and passive surface waves, *Journal of Environmental & Engineering Geophysics*, **10**(3), 323–334.

Park, C. B., Miller, R. D., & Xia, J., 1999. Multichannel analysis of surface waves, *Geophysics*, **64**(3), 800–808.

Parolai, S., 2012. Investigation of site response in urban areas by using earthquake data and seismic noise. - in: Bormann, p. (ed.), new manual of seismological observatory practice 2 (nmsop-2), potsdam : Deutsches geoforschungszentrum gfz, pp. 1–38.

Parolai, S., Bormann, P., & Milkereit, C., 2002. New Relationships between Vs, Thickness of Sediments, and Resonance Frequency Calculated by the H/V Ratio of Seismic Noise for the Cologne Area (Germany), *Bulletin of the Seismological Society of America*, **92**(6), 2521–2527.

Parolai, S., Picozzi, M., Richwalski, S. M., & Milkereit, C., 2005. Joint inversion of phase velocity dispersion and H/V ratio curves from seismic noise recordings using a genetic algorithm, considering higher modes, *Geophysical Research Letters*, **32**(1), n/a–n/a.

Perton, M., Sánchez-Sesma, F. J., Rodríguez-Castellanos, A., Campillo, M., & Weaver, R. L., 2009. Two perspectives on equipartition in diffuse elastic fields in three dimensions, *The Journal of the Acoustical Society of America*, **126**(3), 1125–1130.

Picozzi, M. & Albarello, D., 2007. Combining genetic and linearized algorithms for a two-step joint inversion of Rayleigh wave dispersion and H/V spectral ratio curves, *Geophysical Journal International*, **169**(1), 189–200.

Pilz, M., Parolai, S., Picozzi, M., & Bindi, D., 2012. Three-dimensional shear wave velocity imaging by ambient seismic noise tomography, *Geophysical Journal International*, **189**(1), 501–512.

Poggi, V. & Fäh, D., 2010. Estimating rayleigh wave particle motion from three-component array analysis of ambient vibrations, *Geophysical Journal International*, **180**(1), 251–267.

Poggi, V., Fäh, D., Burjanek, J., & Giardini, D., 2012. The use of rayleigh-wave ellipticity for site-specific hazard assessment and microzonation: application to the city of lucerne, switzerland, *Geophysical Journal International*, **188**(3), 1154–1172.

Puglia, R., Tokeshi, K., M. Picozzi, E. D. A., Parolai, S., & Foti, S., 2011. Interpretation of microtremor 2D array data using Rayleigh and Love waves: the case study of Bevagna (central Italy), *Near Surf. Geophys.*, **9(6)**, 529–540.

Renalier, F., 2010. Caracterisation sismique de sites heterognes partir de methodes actives et passives : variations laterales et temporelles., *Earth Sciences. Universite Joseph-Fourier - Grenoble*, p. pp235.

Renalier, F., Endrun, B., & et al, 2009. Comparative analysis of classical measurements and newly developed methods, *Delivrable D6, pp39 & 2 Appendix, NERIES project*.

Ritzwoller, M. H. & Levshin, A. L., 2002. Estimating shallow shear velocities with marine multicomponent seismic data, *GEOPHYSICS*, **67**(6), 1991–2004.

Rix, G. J., Hebeler, G. L., & Orozco, M. C., 2002. Near-surface Vs Profiling in the New Madrid Seismic Zone Using Surface-wave Methods, *Seismological Research Letters*, **73**(3), 380–392.

Rumpf, M. & Tronicke, J., 2014. Predicting 2D geotechnical parameter fields in near-surface sedimentary environments, *Journal of Applied Geophysics*, **101**(0), 95 – 107.

Sambridge, M., 1998. Exploring multidimensional landscapes without a map, *Inverse Problems*, **14**(3), 427.

Sambridge, M., 1999. Geophysical inversion with a neighbourhood algorithm—i. searching a parameter space, *Geophysical Journal International*, **138**(2), 479–494.

Sambridge, M. & Mosegaard, K., 2002. Monte carlo methods in geophysical inverse problems, *Reviews of Geophysics*, **40**(3), 3–1–3–29.

Sánchez-Sesma, F. J. & Campillo, M., 2006a. Retrieval of the Green's Function from Cross Correlation: The Canonical Elastic Problem, *Bulletin of the Seismological Society of America*, **96**(3), 1182–1191.

Sánchez-Sesma, F. J. & Campillo, M., 2006b. Retrieval of the green's function from cross correlation: The canonical elastic problem, *Bulletin of the Seismological Society of America*, **96**(3), 1182–1191.

Sánchez-Sesma, F. J., Pérez-Ruiz, J. A., Luzón, F., Campillo, M., & Rodríguez-Castellanos, A., 2008. Diffuse fields in dynamic elasticity, *Wave Motion*, **45**, 641–654.

Sánchez-Sesma, F. J., Rodríguez, M., Iturrarán-Viveros, U., Luzón, F., Campillo, M., Margerin, L., García-Jerez, A., Suarez, M., Santoyo, M. A., & Rodríguez-Castellanos, A., 2011a. A theory for microtremor h/v spectral ratio: application for a layered medium, *Geophysical Journal International*, **186**(1), 221–225.

Sánchez-Sesma, F. J., Weaver, R. L., Kawase, H., Matsushima, S., Luzón, F., & Campillo, M., 2011b. Energy partitions among elastic waves for dynamic surface loads in a semi-infinite solid, *Bulletin of the Seismological Society of America*, **101**(4), 1704–1709.

Scherbaum, F., Hinzen, K.-G., & Ohrnberger, M., 2003. Determination of shallow shear wave velocity profiles in the Cologne, Germany area using ambient vibrations, *Geophysical Journal International*, **152**(3), 597–612.

Schmelzbach, C., Tronicke, J., & Dietrich, P., 2011. Three-dimensional hydrostratigraphic models from ground-penetrating radar and direct-push data, *Journal of Hydrology*, **398**(3–4), 235 – 245.

Schuster, G., 2009. Seismic interferometry, *Cambridge University Press*.

Seidl, D., 1980. The simulation problem for broad-band seismograms, *J. Geophys. Res.*, **48**, 84–93.

SESAME, 2004. Final report of the inversion of velocity profile, *SESAME Deliverable D14.07*.

SESAME, 2004a. Report on parameter studies, *SESAME EVG1-CT-2000-00026 project*, **WP9, Deliverable D12.09**, 39.

SESAME, 2004b. Guideleines for the implimentation of the H/V spectral ration technique on ambient vibrations measurements, processing and interpretation, *SESAME EVG1-CT-2000-00026 project*, **WP12, Deliverable D23.12**, 62.

Shapiro, N. M. & Campillo, M., 2004. Emergence of broadband rayleigh waves from correlations of the ambient seismic noise, *Geophysical Research Letters*, **31**(7), n/a–n/a.

Shapiro, N. M., Campillo, M., Stehly, L., & Ritzwoller, M. H., 2005. High resolution surface wave tomography from ambient seismic noise, *Science*, **307**, 1615 – 1618.

Snieder, R., 2004. Extracting the Green's function from the correlation of coda waves: A derivation based on stationary phase, *Phys. Rev. E*, **69**, 046610.

Snieder, R., Wapenaar, K., & Wegler, U., 2007. Unified Green's function retrieval by cross-correlation; connection with energy principles, *Phys. Rev. E*, **75**, 036103.

Snieder, R., Sánchez-Sesma, F. J., & Wapenaar, K., 2009. Field fluctuations, imaging with backscattered waves, a generalized energy theorem, and the optical theorem, *SIAM Journal on Imaging Sciences*, **2**(2), 763–776.

Socco, L. V. & Strobbia, C., 2004. Surface wave methods for near-surface characterisation: A tutorial, *Near Surface Geophysics*, **2**, 165–185.

Socco, L. V., Foti, S., & Boiero, D., 2010. Surface-wave analysis for building near-surface velocity models — established approaches and new perspectives, *Geophysics*, **75**(5), 75A83–75A102.

Stehly, L., Campillo, M., Froment, B., & Weaver, R. L., 2008. Reconstructing Green's function by correlation of the coda of the correlation (C3) of ambient seismic noise, *Journal of Geophysical Research: Solid Earth*, **113**(B11), n/a–n/a.

Steinel, H., Hausmann, J., Werban, U., & Dietrich, P., 2014. Reliability of MASW profiling in near-surface applications, *Near Surface Geophysics*, **12**, pp. 731–737.

Stephen, R. A., Koelsch, D. E., Berteaux, H., Bocconcelli, A., Bolmer, S., Cretin, J., Etourmy, N., Fabre, A., Goldsborough, R., Gould, M., Kery, S., Laurent, J., Omnes, G., Peal, K., Swift, S., Turpening, R., & Zani, C., 1994. The seafloor borehole array seismic system (seabass) and vlf ambient noise, *Marine Geophysical Researches*, **16**(4), 243–286.

Stokoe, K. H., Wright, S. G., Bay, J. A., & Roesset, J. M., 1994. Characterization of Geotechnical Sites by SASW Method, *ISSMFE Technical Committee 10 for XIII ICSMFE, Geophysical Characterization of Sites, A. A. Balkema Publishers/Rotterdam & Brookfield, Netherlands*, pp. pp. 15–25.

Sánchez-Sesma, F. J., Pérez-Ruiz, J. A., Campillo, M., & Luzón, F., 2006. Elastodynamic 2d green function retrieval from cross-correlation: Canonical inclusion problem, *Geophysical Research Letters*, **33**(13), n/a–n/a, L13305.

Sánchez-Sesma, F. J., Pérez-Ruiz, J. A., Luzón, F., Campillo, M., & Rodríguez-Castellanos, A., 2008a. Diffuse fields in dynamic elasticity, *Wave Motion*, **45**(5), 641 – 654, Special Issue on Selected Papers Presented at the International Symposium on Mechanical Waves in Solids - Volume 2.

Sánchez-Sesma, F. J., Pérez-Ruiz, J. A., Luzón, F., Campillo, M., & Rodríguez-Castellanos, A., 2008b. Diffuse fields in dynamic elasticity, *Wave Motion*, **45**(5), 641 – 654, Special Issue on Selected Papers Presented at the International Symposium on Mechanical Waves in Solids - Volume 2.

Thomson, W. T., 1950. Transmission of elastic waves through a stratified solid medium, *Journal of Applied Physics*, **21**(2), 89–93.

Tokimatsu, K., Shinzawa, K., & Kuwayama, S., 1992. Use of Short-Period Microtremors for Vs Profiling, *Journal of Geotechnical Engineering*, **118**(10), 1544–1558.

Toksöz, M. N., 1964. Microseisms and an attempted application to exploration, *GEOPHYSICS*, **29**(2), 154–177.

Tronicke, J., Paasche, H., & Böniger, U., 2012. Crosshole traveltime tomography using particle swarm optimization: A near-surface field example, *Geophysics*, **77**(1), R19–R32.

van Manen, D.-J., Curtis, A., & Robertsson, J. O., 2006. Interferometric modeling of wave propagation in inhomogeneous elastic media using time reversal and reciprocity, *GEOPHYSICS*, **71**(4), SI47–SI60.

Vertatschitsch, E. & Haykin, S., 1986. Nonredundant arrays, *Proc. IEEE*, **74**, p. 217.

Voronoi, M. G., 1908. Nouvelles applications des paramétres continus à la théorie des formes quadratiques, *J. Reine Angew. Math.*, **134**, 198–287.

Wang, R., 1999. A simple orthonormalization method for stable and efficient computation of Green's functions, *Bulletin of the Seismological Society of America*, **89**(3), 733–741.

Wapenaar, K. & Fokkema, J., 2006. Green's function representations for seismic interferometry, *GEOPHYSICS*, **71**(4), SI33–SI46.

Wapenaar, K., Draganov, D., Snieder, R., Campman, X., & Verdel, A., 2010. Tutorial on seismic interferometry: Part 1 — basic principles and applications, *Geophysics*, **75**(5), 75A195–75A209.

Wathelet, M., 2005. Array recordings of ambient vibrations: surface-wave inversion, *Universite de Liege, Belgium*, p. 177pp.

Wathelet, M., 2008. An improved neighborhood algorithm: Parameter conditions and dynamic scaling, *Geophysical Research Letters*, **35**(9).

Wathelet, M., Jongmans, D., & Ohrnberger, M., 2004. Surface wave inversion using a direct search algorithm and its application to ambient vibration measurements, *Near Surf. Geophys.*, **2**, 211–221.

Wathelet, M., Jongmans, D., & Ohrnberger, M., 2005. Direct inversion of spatial autocorrelation curves with the neighborhood algorithm, *Bulletin of the Seismological Society of America*, **95**(5), 1787–1800.

Wathelet, M., Jongmans, D., Ohrnberger, M., & Bonnefoy-Claudet, S., 2008b. Array performances for ambient vibrations on a shallow structure and consequences over Vs inversion, *Journal of Seismology*, **12**(1), 1–19.

Weaver, R. L., 1985. Diffuse elastic waves at a free surface, *J. Acoust. Soc. Am.*, **78**, 131–136.

Woods, J. & Lintz, P., 1973. Plane waves at small arrays, *GEOPHYSICS*, **38**(6), 1023–1041.

Yamamoto, H., 2000. Estimation of shallow s-wave velocity structures from phase velocities of love and rayleigh waves in microtremors.

Yamanaka, H., Takemura, M., Ishida, H., & Niwa, M., 1994. Characteristics of long-period microtremors and their applicability in exploration of deep sedimentary layers, *Bulletin of the Seismological Society of America*, **84**(6), 1831–1841.